DEPARTAMENT D'ASTRONOMIA

MULTIWAVELENGTH STUDY OF ACCRETION-POWERED PULSARS.

ELISA NESPOLI

UNIVERSITAT DE VALÈNCIA
Servei de Publicacions
2010

Aquesta Tesi Doctoral va ser presentada a València el dia 18 de juny de 2010 davant un tribunal format per:

- Dr. Josep Maria Paredes Roy
- Dr. Pere Blay Serrano
- Dr. Jorge Casares Velázquez
- Dr. José Miguel Torrejón Vázquez
- Dra. Silvia Martínez Núñez

Va ser dirigida per:
Dr. Juan Fabregat Llueca
Dr. Pablo Reig Torres

Dipòsit legal: V-2053-2011
I.S.B.N.: 978-84-370-7913-4
Edita: Universitat de València
Servei de Publicacions
C/ Arts Gràfiques, 13 baix
46010 València
Spain
Telèfon:(0034)963864115

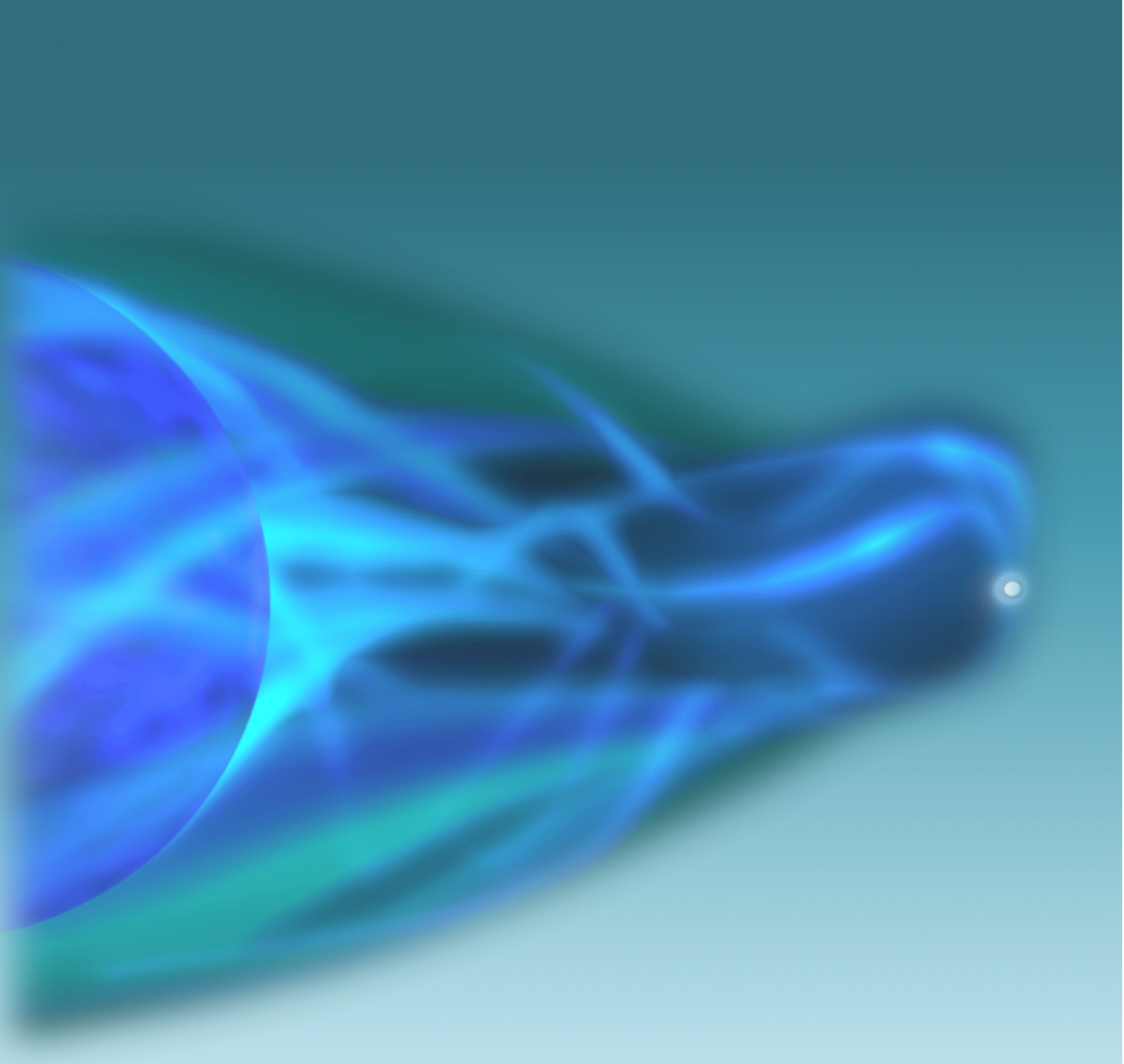

MULTIWAVELENGTH STUDY OF ACCRETION-POWERED PULSARS

Elisa Nespoli

PhD Thesis

Observatori Astronòmic
VNIVERSITAT DE VALÈNCIA

Valencia – 2010

DEPARTAMENT D'ASTRONOMIA I ASTROFÍSICA

VNIVERSITAT DE VALÈNCIA

Dr. Juan Fabregat Llueca,

Profesor titular del Departamento de Astronomía y Astrofísica de la Universidad de Valencia,

CERTIFICA

Que la presente memoria, "Multiwavelength study of accretion-powered pulsars", ha sido realizada bajo su dirección por Elisa Nespoli, y que constituye su tesis doctoral para optar al grado de Doctor en Física.

Y para que quede constancia y tenga los efectos oportunos, firmo el presente documento en Paterna, a 13 de Abril de 2010.

Firmado: Juan Fabregat Llueca

Dr. Pablo Reig Torres,

Investigador del Foundation for Research & Technology – HELLAS (FORTH), Grecia

CERTIFICA

Que la presente memoria, "Multiwavelength study of accretion-powered pulsars", ha sido realizada bajo su dirección por Elisa Nespoli, y que constituye su tesis doctoral para optar al grado de Doctor en Física.

Y para que quede constancia y tenga los efectos oportunos, firmo el presente documento en Paterna, a 13 de Abril de 2010.

Firmado: Pablo Reig Torres

ai miei genitori

Contents

Felix qui potuit rerum cognoscere causam

Virgilio

1 Introduction: X-Ray Binaries

1.1 Scientific context

X-ray binaries are among the brightest extra-solar objects in the sky and are characterized by dramatic variability in brightness on timescales ranging from milliseconds to months and years. Their main source of power is the gravitational energy released by matter accreted from a companion star and falling onto a neutron star (NS) or a black hole (BH) in a close binary system. X-ray binaries therefore serve as rich sources of information about compact stellar objects, and, once understood, could be used as unique natural laboratories for the properties of matter under extreme conditions. In recent years, the launching of a number of X-ray observatories has marked the beginning of a new era in X-ray astronomy. These include BeppoSAX, RXTE, Chandra X-ray observatory, XMM-Newton and INTEGRAL. These facilities provided unprecedented sensitivity, all-sky coverage and timing resolution, and led to a range of new discoveries related to X-ray binaries, such as millisecond-oscillations, superbursts, quiescent luminosity measurements in transients, and the discovery of new classes of sources as well.

We are now aware that in our galaxy there are more than 200 bright X-ray sources with fluxes well above 10^{-10} erg cm^{-2} s^{-1} in the energy range 1–10 keV (above the Earth's atmosphere) (see Liu et al. 2006, 2007, for recent catalogues). The distribution of these sources shows a clear concentration towards the Galactic

center and also towards the Galactic plane, indicating that the majority belong indeed to our galaxy. Furthermore, several dozen strong sources are found in Galactic globular clusters and in the Magellanic Clouds.

In the 40 years since the first X-ray binary was optically identified (ScoX-1), the basic division of X-ray binaries into the high-mass (HMXBs) and low-mass (LMXBs) systems has become firmly established. The nomenclature refers to the nature of the mass donor, with HMXBs normally taken to be $\geq 10\ M_{\odot}$, and LMXBs $\leq 1\ M_{\odot}$. However, the last decade has seen the identification and measurement of a significant number of X-ray binaries whose masses are intermediate between these limits. Nevertheless, the nature of the mass-transfer process (stellar wind dominated in HMXBs, Roche lobe overflow in LMXBs), together with differences in the accreting compact stars (i.e. strongly magnetic NS in HMXBs versus weakly magnetic NS in LMXBs), produces quite different properties in the two groups (see Fig. 1.1 and Table 1.1).

Table 1.1: The two main classes of Galactic X-ray sources

	HMXB	LMXB
X-ray spectra:	$kT \geq 15$ keV (hard)	$kT \leq 10$ keV (soft)
Type of time variability:	regular X-ray pulsations no X-ray bursts	only a very few pulsars often X-ray bursts
Accretion process:	wind (or incipient RLO)	Roche-lobe overflow
Timescale of accretion:	10^5 yr	$10^7 - 10^9$ yr
Accreting compact star:	high $\vec{B}$-field NS (or BH)	low $\vec{B}$-field NS (or BH)
Spatial distribution:	Galactic Plane	Galactic center and spread around the plane
Stellar population:	young, age $< 10^7$ yr	old, age $> 10^9$ yr
Companion stars:	luminous, $L_{opt}/L_{\rm X} > 1$ early-type O(B)-stars $> 10 M_{\odot}$ (Pop. I)	faint, $L_{opt}/L_{\rm X} \ll 0.1$ late-type G-M stars $\leq 1 M_{\odot}$ (Pop. I and II)

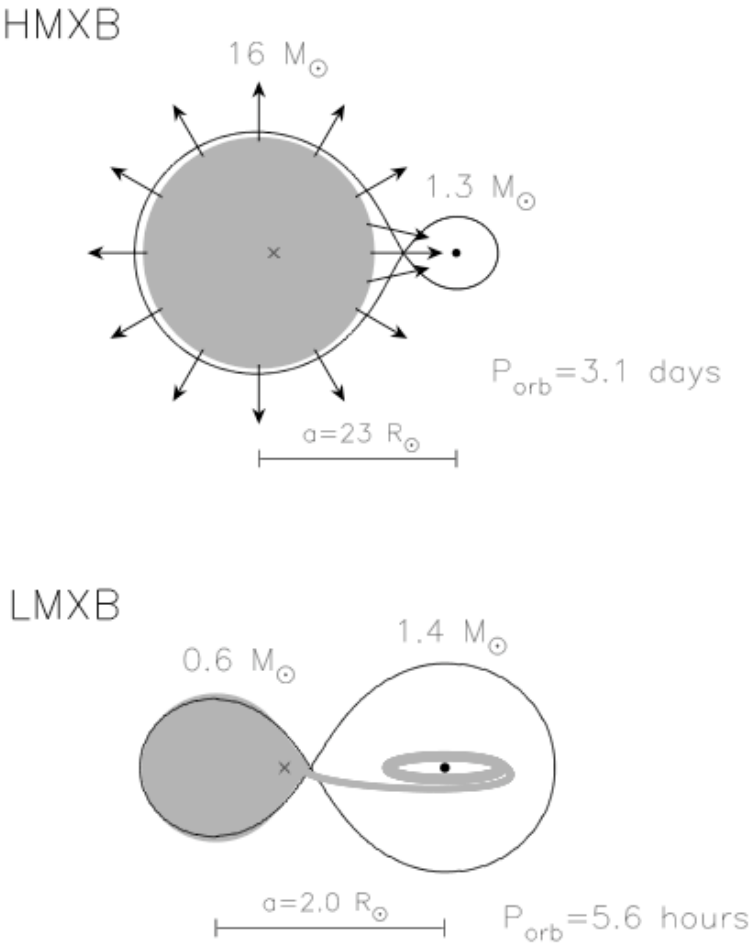

Figure 1.1: Examples of a typical HMXB (top) and LMXB (bottom). The compact objects in the HMXB is fed by a strong, high-velocity stellar wind and/or by beginning atmospheric Roche-lobe overflow. The compact object in a LMXB is surrounded by an accretion disk which is fed by Roche-lobe overflow. In this schematic representation, the compact object is thought to be a neutron star, but there is also observational evidence for HMXBs and LMXBs harboring black holes.

1.2 A brief historical review

The X-ray fluxes measured for these systems correspond to typical source luminosities of 10^{34} – 10^{38} erg s^{-1}(which is more than 25 000 times the total energy output of our Sun). Table 1.2 lists the rates of accretion ($\dot{M} = dm/dt$) required to generate a typical X-ray luminosity of 10^{37} erg s^{-1}. Also listed is the amount of gravitational potential energy released per unit mass ($\Delta U/m = GM/R$) by accretion onto a 1 $M_\odot$ stellar (compact) object, as well as the column density towards the stellar surface (or Schwarzschild radius) in the case of spherical accretion, $\sigma = L_{\rm X} 4\pi\sqrt{R/(GM)^3}$. The table shows that only for accreting neutron stars and black holes is the column density low enough to allow X-rays to escape, as X-rays are stopped at column densities larger than a few g cm^{-2} (see, for instance, Frank et al. 2002). Hence, the brightest Galactic X-ray sources cannot be accreting white dwarfs.

Table 1.2: Energetics of accretion

Stellar object	Radius	$\Delta U/mc^2$	$\Delta U/m$	dm/dt^a	Column density^a
$1M_\odot$	(km)		(erg/g)	$(M_\odot/yr)$	(g/cm^2)
Sun	7×10^5	2×10^{-6}	2×10^{15}	1×10^{-4}	140
White dwarf	6000	2×10^{-4}	1×10^{17}	1×10^{-6}	16
Neutron star	10	0.15	1×10^{20}	1×10^{-9}	0.5
Black hole	3	$0.1 \sim 0.4$	4×10^{20}	4×10^{-10}	0.3

^{a} required to power $L_{\rm x} = 10^{37}$ erg/s

The recognition that neutron stars and black holes can exist in close binary systems came at first as a surprise. It was known that the initially more massive star should evolve first and explode in a supernova (SN). However, as a simple consequence of the virial theorem, the orbit of the post-SN system should be disrupted if more than half of the total mass of the binary is suddenly ejected. For X-ray binaries like Cen X-3 it was soon realized (van den Heuvel & Heise 1972) that the survival of the system was due to the effects of large-scale mass

transfer that must have occurred prior to the SN.

The formation of LMXBs ($M_{donor} \leq 1.5 M_{\odot}$) with observed orbital periods mostly between 11 min and 12 hr, as well as the discovery of the double neutron star system PSR 1913+16 with an orbital period of 7.75 hr, was an even harder problem to solve since the progenitor star of the neutron star must have had a radius much larger than the current separation. It was clear that such systems must have lost a large amount of orbital angular momentum. The first models to include large loss of angular momentum were made by van den Heuvel & de Loore (1973) for the later evolution of HMXBs, showing that in this way very close systems like Cyg X-3 can be formed; on the other hand, Sutantyo (1975) proposed the same mechanism for the origin of LMXBs.

Furthermore, the important concept of a "common envelope" (CE) evolution was introduced by Paczyǹski (1976) and Ostriker et al. (1976). In this scenario a neutron star is captured by the expansion of a giant companion star and is forced to move through the giant's envelope. The resulting frictional drag will cause its orbit to shrink rapidly while, at the same time, ejecting the envelope before the naked core of the giant star explodes to form another neutron star.

It was suggested by Smarr & Blandford (1976) that it is an old "spun-up" neutron star what is observed as a radio pulsar in PSR 1913+16. The magnetic field of this pulsar is relatively weak ($\sim 10^{10}$ Gauss, some two orders of magnitude lower than the average pulsar magnetic field) and its spin period is very short (59 ms). Hence, this pulsar is most likely spun-up (or "recycled") in an X-ray binary where mass and angular momentum from an accretion disk is fed to the neutron star. The other neutron star in the system was then produced by the second supernova explosion and must be a young, strong $\vec{B}$-field neutron star (it is not observable, either because it has already rapidly spun-down, due to dipole radiation; or because the Earth is not hit by the pulsar beam; or because of centrifugal inhibition, if the drag exerted by the rotating magnetosphere on the accreting matter gives rise to a centrifugal force that is locally stronger than gravity).

The idea of recycling pulsars was given a boost by the discovery of the first millisecond radio pulsar (Backer et al. 1982). As a result of the long accretion phase in LMXBs, millisecond pulsars are believed to be formed in such systems

(Alpar et al. 1982; Radhakrishnan & Srinivasan 1982). This model was beautifully confirmed by the discovery of the first millisecond X-ray pulsar in the LMXB SAX 1808.4-3658 (Wijnands & van der Klis 1998).

Finally, another ingredient which has important consequences for close binary evolution is the event of a "kick" imparted to newborn neutron stars as a result of an asymmetric SN and/or the sudden loss of matter ejected in a symmetric SN explosion (the so-called Blaauw kick). There is now ample evidence for the occurrence of such kicks inferred from the space velocities of pulsars and from dynamical effects on surviving binaries.

This work will concentrate on results from HMXBs observations: in the next two sections an overview of the two single components of these systems is presented, compact objects, including white dwarfs for completeness, in Sect. 1.3, and hot OB stars in Sect. 1.4. In Sect. 1.5 their observational properties will be explored.

1.3 The primary star: a compact object

The gravitational collapse of normal matter produces the most exotic objects in the Universe – neutron stars and black holes. Proving that these objects exist in Nature occupied theoretical and observational astrophysicists for much of the 20th century. As the endpoint states of stellar evolution, they form today fundamental constituents of galaxies. As a class of astronomical objects, compact objects include white dwarfs, neutron stars and black holes. For a complete and recent review of compact objects, see, for example, Camenzind (2007).

A study of compact objects begins when normal stellar evolution ends. These objects differ from normal stars in at least three aspects:

- They are not burning nuclear fuel, and they cannot support themselves against gravitational collapse by means of thermal pressure. Instead white dwarfs are supported by the pressure of the degenerate electrons, and neutron stars are largely supported by the pressure of the degenerate neutrons and quarks. Only black holes represent completely collapsed stars, assembled by mere self-graviting forces.

- The second characteristic property of compact stars is their compact size. They are much smaller than normal star, thus have much stronger surface gravitational fields.

- Often compact objects carry strong magnetic fields.

White dwarfs

White dwarfs are stars of about one solar mass with a characteristic radius of 5000 km, corresponding to a mean density of 10^6 g cm^{-3}. They are no longer burning nuclear fuel but are steadily cooling away their internal heat since in their interior gravitation forces are balanced by electron degeneracy pressure. In 1926, only three white dwarfs were firmly detected. In that year, Dirac formulated the Fermi-Dirac statistics, which was used by Fowler in the same year to explain the puzzling nature of white dwarf stars. He identified the pressure holding up the stars from gravitational collapse with the electron degeneracy pressure.

Actual models of white dwarfs, taking into account the special relativistic effects in the degenerate electron equation of state, were constructed by Chandrasekhar (1931). He made the fundamental discovery of a maximum mass, the *Chandrasekhar limit*, of (about) 1.4 $M_\odot$, above which a white dwarf would undergo gravitational collapse.

Many nearby young white dwarf have been discovered as sources of soft X-rays; recently, soft X-ray and extreme ultraviolet observations have become a powerful tool in the study of the composition and structure of the thin atmosphere of these stars. As shown before, white dwarfs do not take part in the formation of X-ray binaries (see Table 1.2).

Neutron stars

Neutron stars are about 20 km in diameter and have a mass of about 1.4 times that of our Sun. Because of its small size and high density, a neutron star possesses a very strong surface gravitational field. Neutron stars are one of the possible end states for a massive star ($M > 6$–$8\ M_\odot$). After these stars have finished burning their nuclear fuel, they undergo a supernova explosion. This explosion

blow off the outer layers of a star in a supernova remnant. The central region of the star collapses under gravity so much that protons and electrons combine to form neutrons.

Massive stars at the end of their lives are believed to consist of a white dwarf-like iron core of mass (1.2 - 1.4) $M_\odot$, having low entropy, and surrounded by layers of less processed material from nuclear shell burning. The effective Chandrasekhar mass is dictated by the lepton number Y_L believed to be around 0.41 - 0.43. As mass is added to the core by shell Si-burning, the core becomes unstable and collapses.

During the collapse, the lepton content decreases due to net electron capture on nuclei and free protons. When the core density approaches 10^{12} g cm^{-3}, the neutrinos can no longer escape from the core on the dynamical time-scale. After neutrinos become trapped, the lepton number is frozen at a value of about 0.38-0.40, and the entropy also remains fixed. The core continues to collapse at a bounce density of a few times nuclear density. This bounce results in a shock which is largely dissipated by the energy required to dissociate massive nuclei in the still infalling matter of the original iron core. The larger lepton number Y_L of the core, the larger its mass and the smaller this shell. The final lepton number is then controlled by weak interactions, and is strongly dependent upon the number of protons, x_p. So the properties of nuclear matter determine largely the outcome of the collapse, in particular the resulting mass of the newly formed neutron star. Many questions are still open in this field.

Black holes

Einstein's general theory of relativity predicts the existence of black holes as astrophysical objects so dense that even light cannot escape from them. Whereas the solutions for rotating neutron stars can only be discussed within the framework of a numerical approach, black holes represent pure gravitational fields with a globally vanishing energy-momentum tensor, $T^{\alpha\beta} = 0$. Phenomenologically, the first type of black holes have measured masses ranging between 3–30 $M_\odot$ and are believed to form during supernova explosions. On the other hand, galaxy-mass black holes are found in nearby galaxies and active galactic nuclei. These are thought to have the mass of about a few million to 10 billion solar masses. The

masses of these supermassive black holes have been recently measured using various kinematic methods. X-ray observations of iron lines in the accretion disks may actually be showing the effects of such massive black holes as a well. Additionally, there is some evidence for intermediate-mass black holes, with masses of a few hundred to a few thousand $M_{\odot}$. These objects may be responsible for the emission of radiation with $L_{\mathrm{X}} \approx 10^{39-41}$ erg/s observed in nearby galaxies, the so called ultraluminous X-ray sources.

Candidates for stellar-mass black holes were identified mainly by their strong X-ray radiation and the presence of accretion disks of the right size and speed, without the irregular flare-ups that are expected from disks around other compact objects. And about 20 of them have been confirmed through dynamical studies.

1.4 The secondary star: a massive OB star

Massive early-type stars are the typical counterparts to HMXBs. Isolated OB stars, because of their fast and peculiar evolution, are very interesting laboratories to test theories of stellar and circumstellar structure and evolution.

While in the main sequence, they are perfect probes of the composition of their surroundings as they are very little evolved and their envelopes present the same composition as the local interstellar matter from which they formed. Because of this reason, they are often used as metallicity indicators. They also trace star-forming regions because do not grow old.

Many hot, luminous, OB-type stars, and their accompanying mass outflows, are highly structured and variable on a range of spatial and temporal scales. Their study allows to improve our knowledge on the underlying physical processes for such activity – magnetic fields, pulsation, rotation, radiative instabilities, binarity – with focus on implications for the structure and evolution of the central star, as well as any associated circumstellar envelope, disk, and mass outflow.

In particular, two extreme phenomena play a crucial role in the case of OB stars in HMXBs, since they are related to the mechanism that drives the accretion flow on to the compact object: stellar winds and the Be phenomenon.

1.4.1 Stellar winds

All hot stars are known to lose matter in the form of a stellar wind driven by radiation. Stellar winds are able to modify the ionizing radiation of hot stars dramatically and become directly observable in both spectral energy distributions and spectral lines as soon as the stars are above certain luminosity thresholds. The streaming matter from stellar winds contributes to the enrichment of the interstellar medium; in the case of binary systems, it can be partially accreted or produce shocks of colliding winds, resulting in X-ray emission in both cases. Nevertheless, due to their soft emission ($E \lesssim 2$ keV), these systems are not regarded as X-ray binaries.

Radiation-driven winds work on the principle that momentum contained in the stellar radiation field is transferred to gas particles in the wind via the scattering of photons. The main point is that momentum is a vector quantity and that the photons before scattering are all moving in one direction, i.e. away from the star, while they move in a random direction after the scattering. The result is that the associated radiative force is directed away from the star. The scattering process takes place via spectral lines of the gas particles in the outer atmosphere. Lucy & Solomon (1970) were among the first to realize that the scattering of photons over a few strong resonance lines would result in a strong enough force to drive a wind. An essential ingredient is that the wind in its way out reaches velocities which are about a 100 times larger than the typical thermal width of the spectral lines, so that due to the doppler shift of the lines many more photons can be "tapped" compared to the static case.

Winds of hot stars are characterized by two global parameters, the terminal velocity v_∞ and the rate of mass loss $\dot{M}$. The velocity v_∞ reached at very large distance from the star, where the radiative acceleration approaches zero because of the geometrical dilution of the photospheric radiation field, corresponds to the maximum velocity of the stellar wind. If we assume that winds are stationary and spherically symmetric, then the equation of continuity yields at any radial coordinate R in the wind

$$\dot{M} = 4\pi\rho(R)V(R). \tag{1.1}$$

$V(R)$ and $\rho(R)$ are the velocity field and density distribution, respectively, and can be regarded as local stellar wind parameters. A determination of global parameters from the observed spectra is only possible with realistic assumptions about the stratification of the local parameters. Global parameters, in fact, are not direct observables, but their determination relies on stellar atmospheres models. For a review of physical and observational properties of winds from hot stars, see Kaper (1998) and Kudritzki & Puls (2000).

1.4.2 The Be-phenomenon

Classical Be stars are OB-type, non supergiant, stars that exhibit hydrogen line emission over the photospheric spectrum. These are characterized by infrared excess, fast rotation and high mass-loss rates. Both emission lines and infrared excess are believed to originate in a high density circumstellar envelope around the equator.

The Be phenomenon is commonly found in O and B stars, with a 20% of known B stars being Be, and a considerable increase in this percentage if one considers young stellar clusters.

In concomitance with the Be phenomenon, Be stars can show variability on several timescales. Short term variability, from a few minutes to a few days, is shown in the shape of photospheric lines and may be explained by non-radial oscillations (see Hubert et al. 1997). Medium term variability, from months to years, is observed in the Hα line shell profile with a modulated variation of the relative intensity of the red and blue peaks. This kind of variations were satisfactory explained by Okazaki (2000) through its one-armed oscillation model. On the time scale of a few decades, substantial changes in photometry and spectroscopy can occur that may lead the star to pass through B to Be.

In order to explain the formation of the dense circumstellar envelope in Be stars, many explanations were proposed, namely the wind compressed disk model of Bjorkman & Cassinelli (1993); axi-symmetric radiative wind models by Stee & de Araujo (1994); non-radial pulsations (Owocki 1994). It is now widely accepted the the Be phenomenon is linked to fast rotation, which would be the main responsible for the formation of the outwarding equatorial disk (Porter & Rivinius 2003). Therefore many instabilities, as *e.g.* non-radial pulsations, begin to be ef-

fective for orbital ejection. Very interestingly, recent interferometric observations brought strong support to the idea that these stars are very fast rotators, showing for the first time the oblateness of a Be star, Archenar, (Domiciano de Souza et al. 2003), which suggests that the star is indeed rotating near the critical limit. For a recent study on how the surface velocity varies during the Main Sequence and the possible origin on Be stars, see Ekström et al. (2008).

1.5 High-mass X-ray binaries: observational properties

There are two main sub-groups of HMXBs, the supergiant counterparts (normally of luminosity class I or II), and the Be/X-ray (or BeX) binary systems (normally luminosity class III to V). Recently, a new class has been added by Negueruela et al. (2006), the Supergiant Fast X-ray transients (SFXTs), with peculiar X-ray properties. All sub-groups involve OB type stars and are commonly found in the galactic plane and the Magellanic Clouds, among their OB-type progenitor stars. They mainly differ in accretion modes with the supergiant systems accreting from a radially outflowing stellar wind, and the BeX binaries accreting directly from the circumstellar disc (possibly with some limited Roche lobe overflow on rare occasions). As a result the supergiants are *persistent* sources of X-rays (with the exception of the SFXTs, see below), while the BeX systems are very variable (often unobservable for months to years) and occasionally much brighter, characterizing themselves as *transient* systems.

In the present work, both X-ray and IR data were employed. While the nature of the compact object and its properties are largely determined from X-ray studies, longer-wavelength observations allow detailed studies of the properties of the mass donor. This is most straightforward for the intrinsically luminous early-type companions of HMXBs, which provides the potential for a full solution of the binary parameters for those systems containing X-ray pulsars. In the framework of HMXB evolution, it allows a comparison of the derived masses with those obtained for neutron stars in the much older binary radio pulsar systems. In the following sections, the main observational properties of HMXBs, as exhibited from X-ray and IR data, will be explored.

1.5.1 X-ray observations

Supergiant-XRBs

SGXBs are systems composed of an accreting compact object and a massive supergiant early-type star (OB). The X-ray emission is powered by accretion of material originating from the donor star through strong stellar wind or occasionally by Roche-lobe overflow. Up to recently SGXBs were believed to be very rare objects due to the evolutionary timescales involved; supergiant stars have a very short lifetime. This idea was supported by the fact that only a dozen of SGXBs have been discovered in almost 40 years of X-ray astronomy and it was largely believed that the dozen of known objects represented a substantial fraction of all SGXBs in our Galaxy. The *INTEGRAL* satellite is changing this classical picture on SGXBs. Since its launch in 2002, *INTEGRAL* in just a few years doubled the population of SGXBs. The majority of them are persistent X-ray sources which escaped previous detection because of their very strong absorbed nature, being the $N_{\rm H}$ typically greater than 10^{23} cm^{-2} (Walter et al. 2006; Nespoli et al. 2008b).

As the compact object always orbits within the stellar wind, these systems are persistent X-ray emitting objects and show high variations on short time scales. They have $P_{orb} \leq 10$ days and $e \leq 0.1$. According to their X-ray luminosity, they are divided into *high-luminosity* sources and *low-luminosity* sources.

The high-luminosity sources (10^{37}–10^{38} erg s^{-1}), and "standard" systems such as Cen X-3 and SMC X-1, are characterized by the occurrence of regular X-ray eclipses and double-wave ellipsoidal light variations produced by tidally deformed ("pear-shaped") giant or sub-giant companion stars with masses $> 10M_{\odot}$. However, the optical luminosities ($L_{opt} > 10^5 L_{\odot}$) and spectral types of the companions indicate original zero-age main-sequence (ZAMS) masses $\geq 20M_{\odot}$, corresponding to O-type progenitors. The companions have radii 10 – 30 $R_{\odot}$ and (almost) fill their critical Roche-lobes. The mass transfer process takes place in the form of Roche lobe overflow. Among the standard HMXBs, there are at least three systems that are thought to harbor black holes: Cyg X-1, LMC X-1 and LMC X-3.

The low-luminosity SGXBs ($\sim 10^{36}$ erg s^{-1}) show erratic flaring activity, with large luminosity changes on a timescale of tens of minutes. The X-ray luminosity

is consistent with the accretion process being driven by material captured from the stellar wind of the optical companion. Vela X-1 is an example of this kind of systems. For this class of HMXBs, the X-ray characteristics tend to be not very dramatic. Because of the predominantly circular orbits and the quite steady wind outflow, the X-ray emission tends to be a regular low-level effect, if considered on medium time scales.

Supergiant Fast X-ray transients

This new class of HMXBs, introduced by Negueruela et al. (2006), is characterized by the occurrence of X-ray outbursts of a very different nature from those seen in other X-ray binaries. These outbursts are very short (lasting from $\sim$3 to $\sim$8 hours) and display very sharp rises, reaching the peak of the flare in $\leq$1 h. The decay is generally characterized by a complex structure, with two or three further flares. The physical reason for fast outbursts is still unknown, although theoretical speculations have been made which would connect them to some form of discrete mass ejection from the supergiant donor (Golenetskii et al. 2003) or to wind clumping (in't Zand 2005; Walter & Zurita Heras 2007). Numerical simulations (Runacres & Owocki 2005) predict low density contrasts in the wind up to $\sim 10 R_\star$, when they become of the order of 10^{-18} – 10^{-13} g cm^{-3}.

Classical SGXBs are characterized by small orbital radii, with $R_{orb} = (1.5 - 2.5)\ R_\star$. Within the frame of wind clumping, the main difference between SFXTs and classical SGXBs could thus be their orbital radius. At very low orbital radius ($< 1.5 R_\star$) tidal accretion would take place through an accretion disk and the system would evolve to a common envelope stage. At low orbital radius ($\sim 2 R_\star$), the wind would be perturbed in any case and efficient wind accretion will lead to persistent X-ray emission. At larger orbital radius ($\sim 10 R_\star$) and if the wind is clumpy, the SFXT behavior is expected (see also Negueruela 2009; Blay et al. 2008).

Some of the known SFXTs are associated with O-type supergiants. Though no pulsations have been detected, they display spectra typical of accreting neutron stars. The other known sources are X-ray pulsars and are associated with luminous early B-type stars. This class differ from classical wind-fed SGXBs,

whose X-ray luminosity is variable but always detectable around $L_X \sim 10^{36}$ erg s^{-1}. Quiescent fluxes of SFXTs have been near the sensitivity limit of focusing observatories, with values or upper limits in the range of $\sim 10^{32}$ to 10^{33} erg s^{-1}. It is important to point out that without the identification of the optical/infrared counterpart with an OB supergiant, little can be said about the belonging of an object to the class of the SFXTs. In fact, the only X-ray behavior is not enough to unambiguously characterize the X-ray emitter, since short X-ray outbursts are typical of an extensive range of classes, including for instance flare stars, RS CVn binaries, or LMXBs showing superbursts.

Since the SFXTs are difficult to detect and their number is growing fast and steadily since the launch of *INTEGRAL*, they could actually represent a major class of X-ray binaries.

Be/XRBs

Another group of HMXBs consists of the moderately wide, eccentric binaries with $P_{orb} \simeq 20 - 100$ days and $e \simeq 0.3 - 0.5$. The orbital separation is too large to allow Roche-lobe overflow. They are in general transient systems. A new (sub-)group, proposed by Reig & Roche (1999), is constituted by persistent systems with $P_{orb} \simeq 30 - 250$ days and small eccentricities $e < 0.2$. Together these two groups form a separate sub-class of HMXBs: the Be-star X-ray binaries (see Figure 1.2), first recognized as a class by Maraschi et al. (1976). In the Be/X-ray binaries the companions are rapidly rotating OB-emission stars situated on, or close to, the main-sequence (luminosity class III-V).

The BeX binary systems represent until now the largest sub-class of HMXBs. Of the currently proposed HMXB pulsars, 57% are identified as BeX type. The Be-stars are deep inside their Roche-lobes, as is indicated by their generally long orbital periods and by the absence of X-ray eclipses and of ellipsoidal light variations. The X-ray emission from Be/XRBs tends to be extremely variable, ranging from complete absence to giant transient outbursts lasting weeks to months. During such an outburst episode one often observes orbital modulation of the X-ray emission, due to the motion of the neutron star in an eccentric orbit, see Figure 1.2.

The recurrent X-ray outbursts have been explained by Okazaki & Negueruela

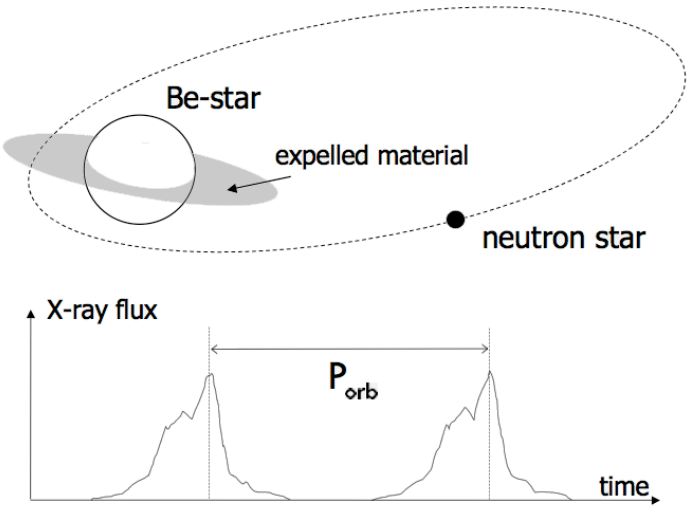

Figure 1.2: Schematic model of a Be-star X-ray binary system. The neutron star moves in an eccentric orbit around the Be-star which is not filling its Roche-lobe. However, near the periastron passage the neutron star accretes circumstellar matter, ejected from the rotating Be-star, resulting in an X-ray burst lasting several days.

(2001) in terms of the decretion disc model. The circumstellar discs of the primaries are truncated because of the tidal and resonant effect of the neutron star. The geometry of the systems and the value of viscosity determine the presence or absence of Type I X-ray outbursts. The interaction of a strongly disturbed disc with the neutron star originates Type II X-ray and optical outbursts.

Be/XRBs show hard X-ray spectra (1-20 keV) which, in combination with the regular X-ray pulsations, indicate that the compact object must be a strongly magnetized neutron star. Pulse periods range from a few seconds to $\sim 10^3$ seconds. During X-ray outbursts, spin-up phenomena have been observed in several systems (A 0535+26, 4U 0118-61). This is consistent with the formation of an accretion disc. During quiescence, a spin-down phase is expected, as the rotational period is largely greater at the beginning of an X-ray outburst than that measured at the end of the previous one.

Schematically, X-ray behavioral features of Be/XRB systems include:

- short (a few days) outbursts ($L_{\rm X} \sim 10^{36} - 10^{37}$ erg s^{-1}) occurring in series separated by the orbital period (Type I), generally (but not always) close to the time of periastron passage of the neutron star;
- giant (or Type II) outbursts ($L_{\rm X} \geq 10^{37}$ erg s^{-1}), which do not correlate clearly with orbital parameters and last several weeks.
- shifting outburst phases due to the rotation of density structures in the circumstellar disc (Wilson et al. 2002).

1.5.2 IR observations

Optical/IR observations reveal that many of the counterparts to HMXBs exhibit mass outflow to the extent of creating a circumstellar disc or spherical envelope of material around the mass donor. Free-free and bound-free IR emission from this disc show themselves as a significant excess over the normal stellar spectrum at all wavelengths greater than the V band. This IR signature, often quantified as a J-K color excess, is important for the following reasons:

- in order to detect sources which are obscured due to high interstellar extinction;
- in confirming the identity of a Be star in the absence of optical spectral information;
- in providing an estimate of the size of the circumstellar disc (this is often directly related to the magnitude of the X-ray emission);

One system that has been the subject of extensive IR observations over the years is X-Per. Detailed study by Telting et al. (1998) found that the density of the disc varies along with the brightness of X-Per, and that in optical high states the disc is among the densest of all Be stars, with $\rho_0 = (1.5 \pm 0.3) \times 10^{-10}$ g cm^{-3}. The disc density at the photosphere varies by a factor of at least 20 from optical high to low states.

With the recent advent of IR spectroscopy on large telescopes, the possibilities of obtaining spectra despite high levels of extinction have become a reality. This is a very powerful tool not only for exploring previously inaccessible objects – it has in fact allowed the first detailed investigations of X-ray binaries in the inner parts of the Galactic Plane and the Galactic Center – but also directly collecting information on the circumstellar environment. The project to which this work belongs, takes its place within this scenario of research. A good example of the strength of this tool may be seen in Clark et al. (1999b): we report in Fig. 1.3 their IR spectra of 5 HMXBs.

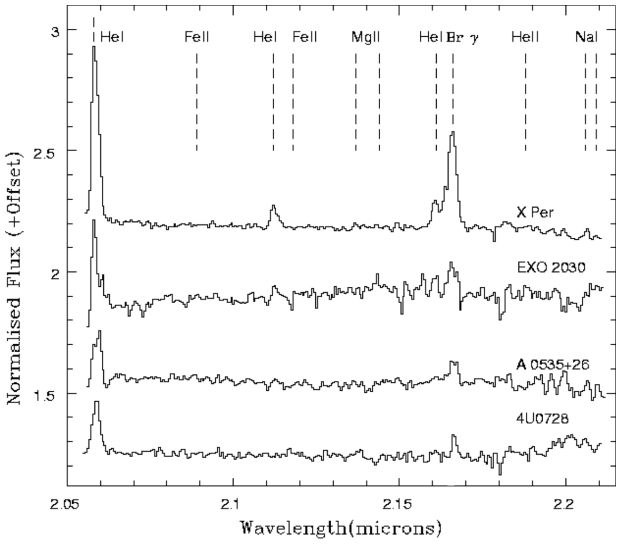

Figure 1.3: *K* band spectra of BeX binaries (Clark et al, 1999). The positions of prominent H, He and metallic transitions are marked.

Just as the optical spectrum is dominated by Balmer emission, we see the same effect from the Brackett series emission in the IR. In addition, emission lines from He and metallic transitions are also detected.

Part I

IR photometry and spectroscopy

We are all in the gutter, but some of us are looking at the stars.

Oscar Wilde

2

Search for IR counterparts to obscured HMXBs

2.1 Scientific objective

Up to now, the *INTEGRAL* survey of the Galactic Plane and central regions has revealed the existence of more than 200 sources (Bird et al. 2007; Bodaghee et al. 2007) in the energy range 20–100 keV, with a position accuracy of $2' - 3'$, depending on count rate, position in the FOV and exposure. A large fraction of the newly discovered sources are found to be heavily obscured, displaying much larger column densities ($N_H \gtrsim 10^{23}$ cm^{-2}) than would be expected along the line of sight (see Kuulkers 2005). These sources were missed by previous high-energy missions, whose onboard instruments were sensitive to a softer energy range. Moreover, optical counterparts to these obscured sources are poorly observable due to the high interstellar extinction, with A_V in excess of up to ~ 20 mag.

It is remarkable that the vast majority of HMXBs in the Norma and Scutum regions, whose optical/IR counterparts have been identified, are SGXBs. Conversely, no one Be/XRB has been found yet. This is in strong contrast with the rest of the Galactic Plane, where BeXRBs outnumber SGXBs by a factor of three to five. We propose that this anomaly is due to an observational effect, because of the transient nature of BeXRBs which precludes follow-up surveys in the X-ray

band.

In this chapter we present the photometric technique we developed in order to identify IR counterparts to obscured HMXBs in the Scutum and Norma galactic arms, looking for Be/XRBs. This technique was tested with known Be/XRBs, providing successful results. Eventually, we applied it to ten newly discovered *INTEGRAL* sources, selecting possible Be counterparts.

2.2 A new photometric technique

We selected suitable candidates by means of a photometric search for emission-line stars in the error boxes of the X-γ ray sources detected by the ISGRI instrument on board *INTEGRAL*.

Be stars are characterized by strong emission features, being He I 20 581 Å and Brγ 21 670 Å the most remarkable ones in the K band. This is clearly shown in Fig. 2.1, which report SOFI K_s spectra of four known classical Be stars and one supergiant B star with emission lines (first spectrum from the top). Data were collected during our spectroscopy observing campaign (see Chapter 3).

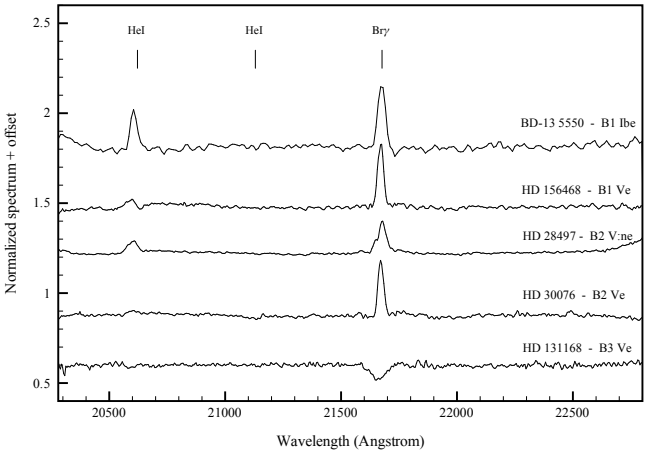

Figure 2.1: K_s-band spectra of classical Be-stars (first four spectra from the bottom) and one supergiant B star with emission lines (first spectrum from the top). The positions of identified spectral features are marked by solid lines.

In order to photometrically select emission-line stars we observed through two narrow band filters centered in the Brγ and He I lines in the K band, together with the H and K_s broad-band filters (see Table 2.1). In optical wavelengths, detection of emission-line stars by means of imaging photometry can be done with a filter centered in the Hα line and two other filters in the Paschen continuum. The sensibility of the method is improved if one of the continuum filters is centered in – or close to – the Hα line (Grebel et al. 1992; Keller et al. 1999; Pigulski et al. 2001, see, for an example, Fig. 2.2).

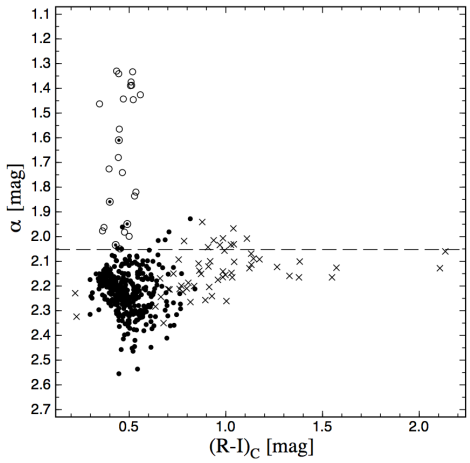

Figure 2.2: Color-color diagram for NGC663, from Pigulski et al. (2001). The α index is defined as the difference between the Hα magnitude and the R magnitude. The symbols denote: crosses, non-members; open circles, known cluster Be stars; encircled dots, newly discovered Be stars; filled circles, remaining stars.

The efficiency of this technique in selecting emission line objects and associations was also largely demonstrated by the recent results of IPHAS, the survey of the Northern Galactic Plane being carried out, in Hα, R and I filters (Drew et al. 2005; González-Solares et al. 2008).

We applied a similar technique in the infrared, building up (Brγ-K_s)–($H-K_s$) and (He I-K_s)–($H-K_s$) photometric diagrams, in which emission-line stars are expected to show up below the absorption-line stars sequence.The suitability of these techniques to identify emission lines from infrared data has been recently

demonstrated by Groh et al. (2006), who detected additional Wolf-Rayet stars in the starburst cluster Westerlund I (see Fig 2.3).

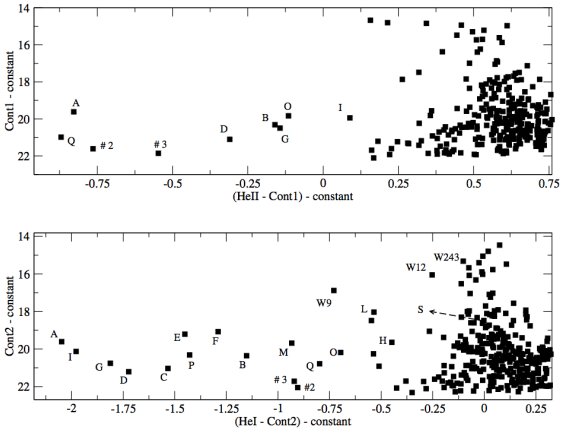

Figure 2.3: Line-continuum versus continuum diagram for the narrow-band filters used by Groh at al. (2007). Upper panel: filter centered at He II 1.0124 μm. Lower panel: filter centered at He I 1.0830 μm. New candidate WRs are identified by letters.

We applied the technique to field stars, and with this objective, for the first time. The most critical factors are, in our case, the large error circle of IBIS detection and the crowdedness of the Galactic Plane.

The described strategy would represent a very strong tool to detect counterparts to Be/XRBs, which constitute $\sim 80\%$ of all HMXBs. In the case of SGXBs, which are persistent X-ray emitters, dedicated observations with X-ray observatories with high spatial resolution, like XMM or Chandra, can produce very small error circles and facilitate the detection of the counterpart.

2.3 Observations

Data were obtained during one observing run in 2008, at the European Southern Observatory (ESO), in Chile. The employed instrument was SOFI (Moorwood et al. 1998c), on the 3.5m New Technology Telescope (NTT) at La Silla. The SOFI camera has a largest field of view of 4.92 arcmin, a pixel scale of 0.288 arcsec/pixel and covers the 0.9-2.5 micron wavelength range.

The optical layout is shown in Fig. 2.4.

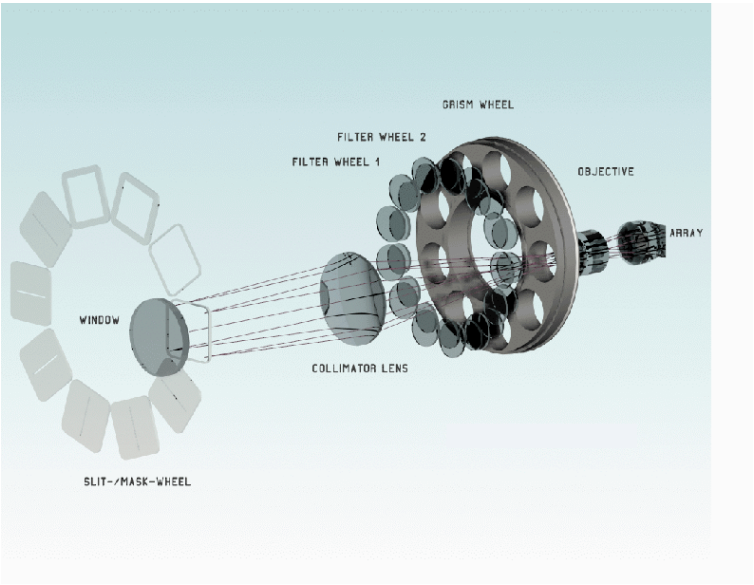

Figure 2.4: Optical layout of SOFI.

The filters employed in this work, together with their central wavelengths and widths at half maximum, are listed in Table 2.1

Table 2.1: The broad band and narrow band Sofi filters employed in this work.

Filter name	Central wavelength (μm)	Width (μm)	Peak transmission (%)
H	1.653	0.297	83
K_s	2.162	0.275	88
NB HeI	2.059	0.028	81
NB Brγ	2.167	0.028	71

Transmission curves for each filter, together with the atmospheric transmission, are shown in Fig. 2.5. The K short or K_s filter is different from both the standard K filter and the K' filter defined by Wainscoat & Cowie (1992). The

long wavelength edge of the K_s filter is similar to that of the K' filter, but the short wavelength edge is similar to that of the K filter. Thus, the K_s filter avoids both the atmospheric absorption feature at 1.9 μm and radiation from the ther-

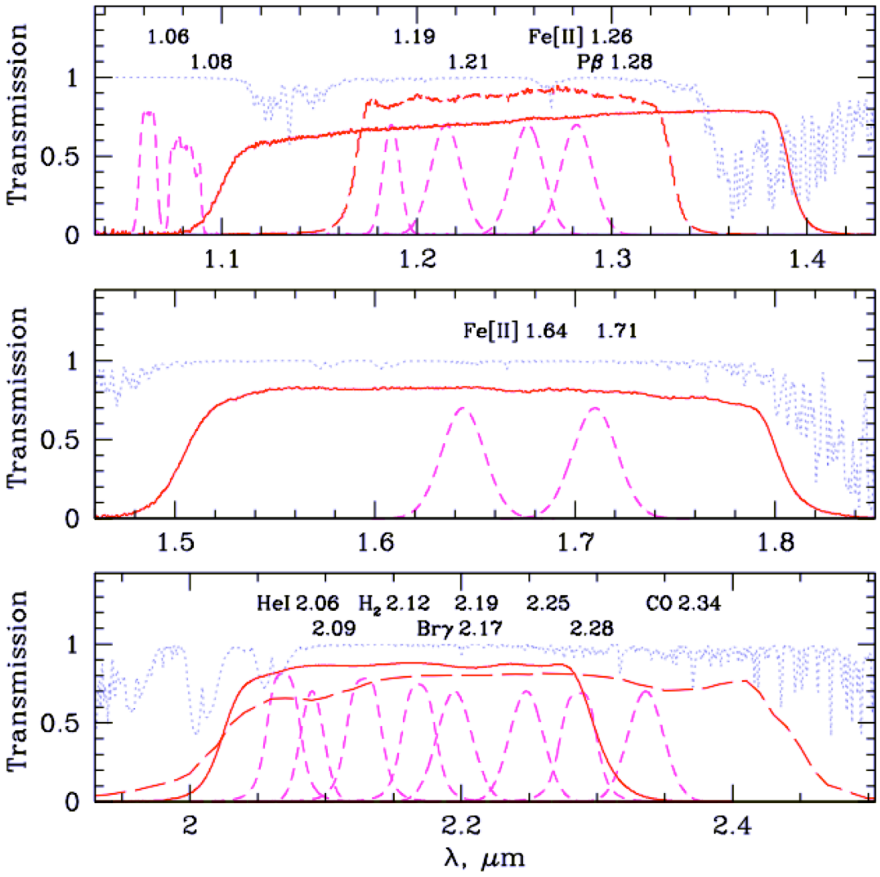

Figure 2.5: SOFI filters. The solid (red) lines indicate the currently available broad-band J, J_s, H and K_s filters. The short-dashed (magenta) lines are the available narrow-band filters. The long-dashed (red) lines show the soon to be commissioned J_s filter (top panel) and the typical broad K filter (Persson et al. 1998, AJ, 116, 2475; see their Table 10). The dotted (blue) line is the atmospheric transmission model for Mauna Kea, for airmass = 1 and water vapor column of 1mm (Lord, S.D. 1992, NASA Technical Memor. 103957; courtesy of Gemini Observatory).

mal background beyond 2.3 μm. The difference between K_s and K is given by $K - K_s = -0.005\ (J - K)$.

According to the position uncertainty of each field, in some cases a mosaic of 2×2 SOFI FOV images was taken. Exposure times were computed with the ESO exposure time calculator in order to obtain photometry with SNR $\sim$100 up to $\sim$15 mag in the broad band filters. Table 2.2 reports the log of observations: for each source, coordinates, uncertainty on the position determination, date of observation and exposure time in each filter are shown.

Table 2.2: Journal of observations. The references at the bottom of the table refer to the *INTEGRAL* discovery.

Field name	RA (J2000)	DEC (J2000)	Unc.	Date and time (UT)	Exposure time (s) H	Ks	He I	Brγ
IGR J17331–2406[1]	$17^h33^m08^s$	$-24°06'$	$2'$	2008-05-15T03:55	12	60	180	240
IGR J17407–2808[2]	$17^h40^m42^s$	$-28°08'$	$2.3'$	2008-05-15T04:33	12	60	180	240
IGR J17454–2703[3]	$17^h45^m24^s$	$-27°03'$	$1'$	2008-05-15T04:21	12	60	180	240
IGR J17507–2856[4]	$17^h50^m40^s$	$-26°44'$	$2.4'$	2008-05-14T05:43	12	60	180	240
IGR J17585–3057[5]	$17^h58^m33^s$	$-30°57'$	2–$3'$	2008-05-14T05:56	64	192	960	1920
IGR J17586-2129[4]	$17^h58^m34^s$	$-21°23'$	$0.6'$	2008-05-15T05:12	12	60	180	240
IGR J18159–3353[6]	$18^h15^m54^s$	$-33°53'$	$4'$	2008-05-15T08:53	64	192	960	1920
IGR J18175–1530[7]	$18^h17^m34^s$	$-15°30'$	$2.5'$	2008-05-15T07:11	64	192	960	1920
IGR J18193–2542[8]	$18^h19^m18^s$	$-25°42'$	$1.5'$	2008-05-15T04:59	12	60	180	240
IGR J18214–1318[8]	$18^h21^m20^s$	$-13°18'$	$0.9'$	2008-05-14T08:56	12	60	180	240
IGR J18307–1232[4]	$18^h30^m50^s$	$-12°32'$	$0.9'$	2008-05-15T08:02	12	60	180	240
IGR J18406–0539[9]	$18^h40^m55^s$	$-05°39'$	2–$3'$	2008-05-14T07:05	64	192	960	1920
IGR J18462–0223[10]	$18^h46^m54^s$	$-02°23'$	$2'$	2008-05-15T06:56	12	60	180	240
IGR J19048-1240[4]	$19^h04^m48^s$	$-12°40'$	$4.2'$	2008-05-15T09:43	64	192	960	1920

References:
[1] Lutovinov et al. (2004), [2] Kretschmar et al. (2004), [3] Kuulkers et al. (2007),
[4] Bird et al. (2007), [5] Krivonos et al. (2007), [6] Sguera et al. (2006), [7] Paizis et al. (2007),
[8] Bird et al. (2006), [9] Molkov et al. (2003), [10] Grebenev et al. (2007).

The reported exposure time is the net on-source time, excluding overheads. Photometric standard stars were observed in the H and K_s bands from the catalogue of Persson et al. (1998); typical integration times were of 30–50 s .

2.4 Data reduction

Data reduction was performed using the IRAF package. Pre-reduction required the following procedures:

1. correcting for inter-quadrant row cross talk
2. combining dithered frames to create a sky image and subtracting it to each image
3. performing flat field correction
4. aligning and combining the reduced images

Finally, on the reduced, co-alligned images, point-spread function (PSF) fitting photometry was performed. Through the final steps of aperture correction and photometric calibration, the obtained magnitudes were transformed to the standard system.

2.4.1 Inter-quadrant row cross-talk

The inter-quadrant row cross-talk is a feature affecting high SNR images taken with SOFI. It is apparent when part of the array is exposed to bright illumination and faint objects have to be detected on the same rows which are exposed to the bright illumination. A bright source imaged on the array produces "ghosts" that affects all the lines where the source is and all the corresponding lines in the other half of the detector.

The effect is a peculiarity of the instrument array and, though it is not completely understood, it is well described and can be easily corrected. The intensity of the ghost is in fact 1.4×10^{-5} times the integrated flux of the line. In order to remove it, we used an IRAF script, available from the instrument web-pages for downloading. This is an efficient and simple algorithm which removes the effect of row cross-talk without any degradation of image quality. The principles for the construction of the algorithm employed are illustrated below.

Model for row cross-talk

The row cross-talk is uniform within one row and does not depend on column index j. Let $I_{i,j}$ be the intensity of the pixel at row i and column j. Due to row cross-talk the observed intensity is modified as follows

$$I'_{i,j} = I_{i,j} + C_i + C_{i\pm512}. \tag{2.1}$$

The row cross-talk consists of two terms, namely the *intraquadrant row cross-talk* C_i and the *interquadrant row cross-talk* $C_{i\pm512}$. The plus sign applies for indices $i \leq 512$, the minus sign for $512 < i \leq 1024$. Both cross-talk terms depend linearly on the integrated intensity of row number i and row number $i \pm 512$:

$$C_i = \alpha \sum_{k=1}^{1024} I_{i,k}. \tag{2.2}$$

The intensity $I_{i,j}$ can be derived from the observed intensity $I'_{i,j}$ by subtracting the row cross-talk as follows

$$I_{i,j} = I'_{i,j} - C_i - C_{i\pm512}. \tag{2.3}$$

2.4.2 Sky subtraction

This is a critical operation, especially if dealing with very crowded images, like ours. For each field and filter, we took 3–6 images at different location. The more dithered frames we had, the better the results. The images were scaled to a common median, which to first approximation is the sky image. This was improved after some tests, by a 3σ rejection. The sky image was scaled to have the same median as the image from which it would be subtracted, and then the subtraction was carried out. This method reduces the negative traces of stellar images on the sky-subtracted data.

2.4.3 Flat fields

At the telescope, images of the dome flat field screen with the dome lamp on and off were taken. The simplest way of creating flat fields is to subtract the average of the lamp-off images to the average of the lamp-on ones. However, in this case

the image obtained would be affected by two issues: since the shade pattern of the array is a function of the overall flux, the shade pattern in the image with the lamp on is different from that in the image with the lamp off. Thus, the difference of the two will contain a residual shade pattern; secondly, the illumination of the dome panel is slightly different from that of the sky. Furthermore, it changes with time because of the aging of the lamps used to illuminate the screen. Both these effects are at the 1-2% level and both can be removed. To do that, a special observation template was used, which takes, in addition, a set of images with the mask wheel vignetting the array (see Fig. 2.6).

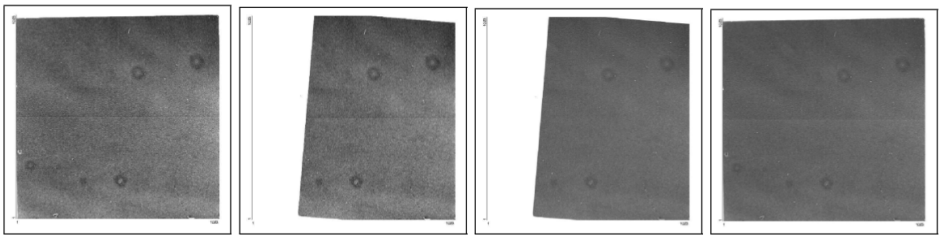

Figure 2.6: Examples of "Special Dome Flat" images. From left to right: lamp off, lamp off with mask, lamp on with mask, lamp on

The vignetted part of the array is relatively free of scattered light, so it can be used to estimate and remove the shade pattern.

2.4.4 Image alignment and combination

The whole set of dithered frames were aligned and combined using the IRAF tasks `imexam, imalign` and `imcombine`.

2.4.5 PSF-fitting photometry

All the fields analyzed in this work belong to the Galactic Plane. This required the use of PSF-fitting in order to obtain reliable photometry. In this section we will briefly introduce the steps we followed in our analysis.

IRAF `apphot` and `daophot` packages were used. When possible, automatic

procedures were developed. However, some operations required the visual inspection of each image, mainly to determine the typical parameters like FWHMs, standard deviation of the background, minimum and maximum good data value. Together with the characteristics of the detector (read-out noise, gain), these values were used as input for `daofind` in order to produce a list of coordinates for each object identified. The four images, one for each filter, were aligned and only objects for one of them (the K_s image, usually the best quality one) were detected. The same list of coordinates was then used as input for `phot`, once for each image. This allowed to obtain aperture photometry for the same objects in all the filters.

Candidate PSF stars were selected from the photometry catalogue produced by `phot` in an automatic way, using `pstselect`. A second run of `pstselect` on the candidate stars, in interactive mode, allowed a convenient selection of the brightest, least crowded stars. In some cases, due to the crowdedness of the fields, no more than three PSF stars could be found.

In order to construct the optimum PSF, an iterative procedure was developed. As a first step, the PSF model was computed using only an analytic function, chosen among various profiles as the one producing the smallest standard deviation for the model fit. The PSF model was constant over the image. The size of the PSF radius was then decreased in order to exclude possible contributions from objects different than the PSF stars. The PSF stars and their neighbors were fitted using `nstar`. Then the fitted PSF star neighbors were subtracted from the image with `substar`. An improved PSF was then built, increasing the PSF radius back to the original value (11 pixels were used), from the image with the neighbors subtracted. In this step, the analytic function and one look-up table containing the deviations of the true PSF from the analytic model PSF were used. Again, the PSF star and their neighbors were fitted and subtracted from the image. The result was inspected, and if good, we proceed by lowering again the PSF radius, building the final PSF profile on the image subtracted by the PSF neighbors. Finally, PSF-fitting was performed simultaneously on all the stars of the field, with `allstar`.

An example of the PSF profile for the IGR J18159–3353 field, through the

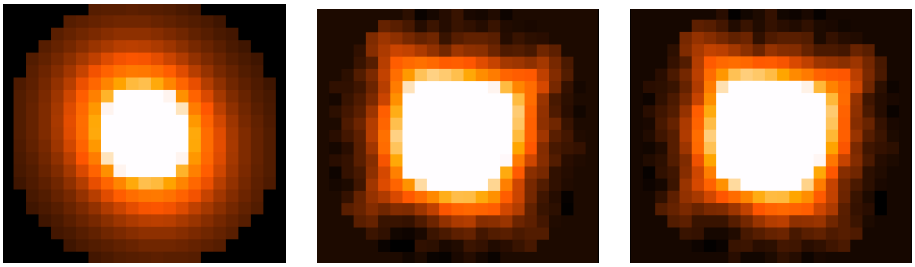

Figure 2.7: PSF profiles from the first approximation with an analytical function (left panel) to the optimum model (right panel). The second and the last models are usually very similar, like in this example.

three steps described above, is shown in Fig. 2.7. The function profile employed in this case is constituted by an elliptical gaussian core with Lorentzian wings (`penny2` function, see `daophot` manuals for more options). This was, on the average, the best fitting model for the SOFI images analyzed in this work. Its analytical form is given by the following equations:

$$z = \frac{x^2}{p_1} + \frac{y^2}{p_2} + p_5\ x\ y$$

$$e = \frac{x^2}{p_1^2} + \frac{y^2}{p_2^2} + x\ y\ p_4$$

$$\text{penny2} = A\ \Big(\frac{1-p_3}{1+z} + p_3\ \exp(-0.693\ e)\Big),$$

where p_n are the fitted parameters and A a normalization constant. Usually, as in this case, the second and last approximation only displayed slight differences.

An example of analyzed field and the corresponding residuals after PSF fitting is shown in Fig. 2.8. In general, small residuals are left after subtraction, and the final result is acceptable, considering the crowdedness of the field. Saturated stars cannot be well fitted and thus not well subtracted.

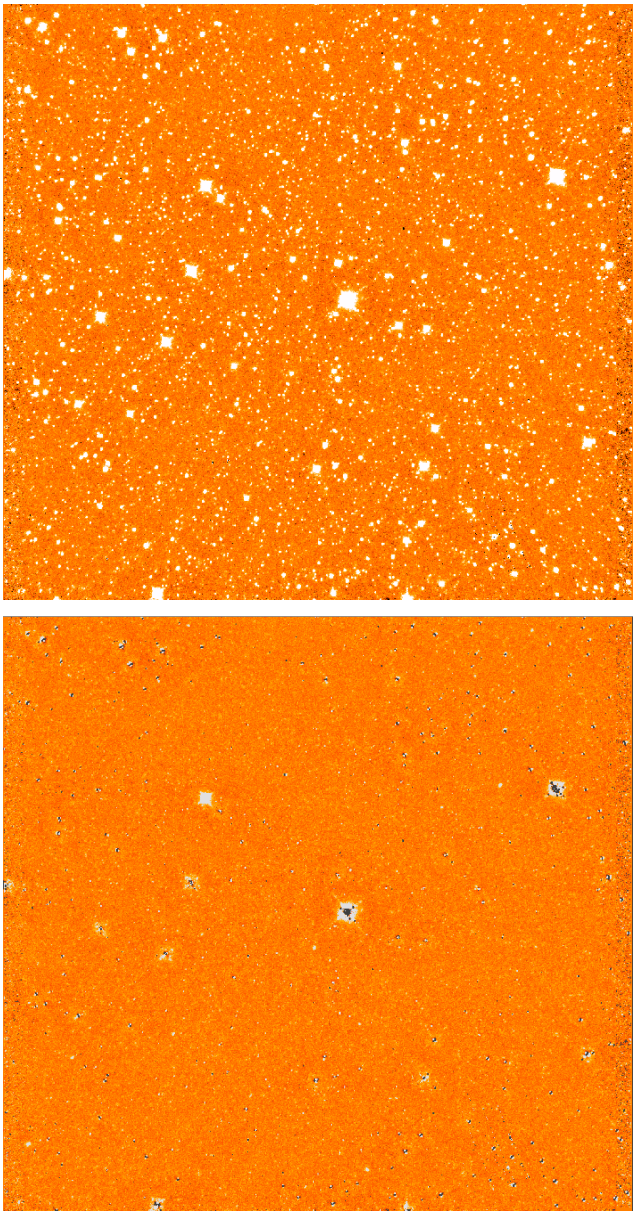

Figure 2.8: Example of PSF fitting for one of the fields studied in this work. Above, the pre-reduced image in the K_s filter. Below, residuals after PSF fitting and subtraction. The image refers to IGR J18159–3353 (one of the 2×2 mosaic frames).

2.4.6 Photometric calibration and aperture correction

The aperture correction was estimated as the difference between aperture photometry and the retrieved PSF photometry. For each field, this difference was computed on the brightest and well isolated stars (typically the PSF stars). According to the field, the difference varied between 0–0.1 mag both in K_s and in H. When necessary, PSF photometry was then corrected according to the obtained values.

Photometric calibrations were carried out in a two-step way. Firstly, for each night, filter and standard star, we obtained the *Bouguer's law* plotting the instrumental magnitudes vs. the corresponding value of airmass. Linear fit was performed in order to obtain a value for the extinction coefficients in K_s and in H. The highest accuracy was obtained for data from May 14, so that we employed the instrumental system defined by that night to calculate the extinction coefficients for both nights. The retrieved coefficients, k_H and k_{Ks}, are shown in Table 2.3.

Table 2.3: Retrieved extinction coefficients for the two observing nights.

	May 13	May 14
k_H	0.050 ± 0.002	0.062 ± 0.008
k_{Ks}	0.061 ± 0.002	0.051 ± 0.004

The second step consisted in solving the *standard transformation equations*, using the instrumental magnitudes corrected for the extinction. All the 2-night data for each filter were used together this time, providing excellent results.

The resulting transformation equations are the following:

$$\begin{aligned} K_{s(std)} - K_{s(ins)} &= 0.0024\ (H - K_s)_{std} + 18.86 \\ (H - K_s)_{std} &= 1.02\ (H - K_s)_{ins} + 0.59 \end{aligned}$$

Results for the linear fit solving the transformation equations are shown in Fig. 2.9.

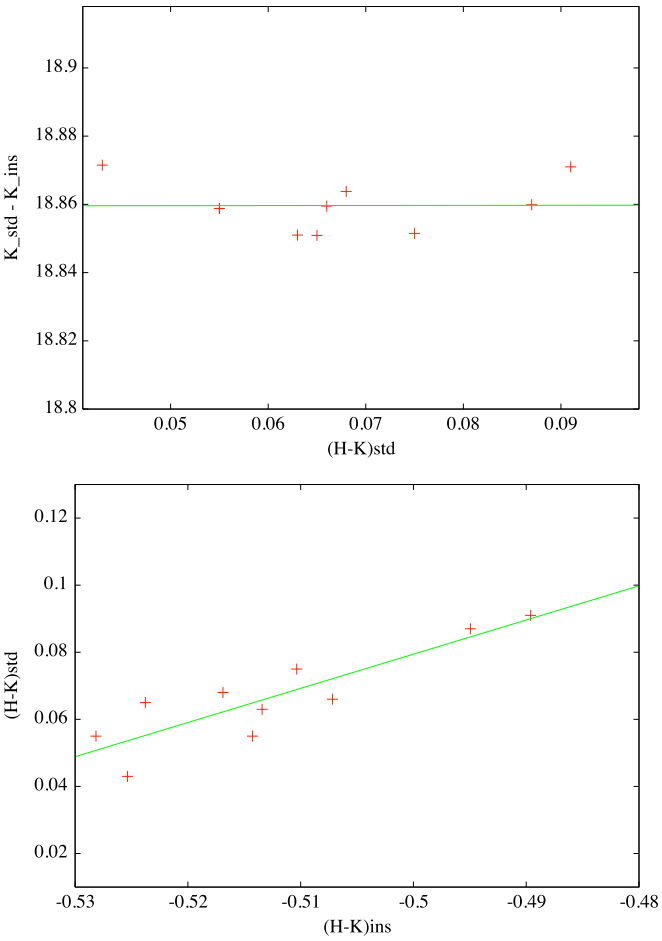

Figure 2.9: Linear fit solving the standard transformation equations. Error bars are within the marks.

The reduced chi square for the two linear fits is 3×10^{-4} for the first equation and 6×10^{-5} for the second one. The obtained accuracy of the transformation is 0.007 mag in K_s and 0.008 mag in H. These are calculated as the standard deviations of the residuals mean values. This contribution, quadratically summed

to the instrumental error of the PSF photometry, constitutes the final error on the calibrated photometry

2.5 Results

Candidate counterparts were selected from both color-color diagrams, (Br$\gamma - K_s$)–($H - K_s$) and (He I$-K_s$)–($H - K_s$). Brγ is the most prominent feature in Be stars in the K band, while He I 20 580 Å is found in early type Be stars, up to B2.5 (see, for instance Clark & Steele 2000). Since it was demonstrated that Be/XRBs have early counterparts, with spectral type up to B3 (Negueruela 1998), in our selection we considered both criteria as equivalent.

We select as candidates the objects that are below the sequence defined by the field stars in both photometric diagrams. This selection can be done statistically. To do so, the locus of the sequence is represented by a function obtained by a low order polynomial fit to all points in the photometric plane. The stars outside the sequence are selected by a n-sigma clipping criterion. The star selected in this way are removed from the whole sample, and the locus of the sequence is recalculated. This procedure is repeated until convergence (i.e. until no star is rejected by the n-sigma clipping criterion). All stars rejected in the above procedure do not belong to the stellar sequence of the photometric plane. Those of them which are placed below the sequence are candidate emission-line stars.

On the other hand, Be stars present moderate emission line strengths, when compared to other groups like YSO, CV, PN, and others. Therefore, stars below the photometric sequence with an important separation are not likely to be Be stars. These classes of stars can be also selected by their distance to the sequence in terms of sigma. In conclusion, Be star candidates are objects below the sequence locus, with separations between n-sigma and m-sigma.

The critical point is to select the right values of n and m for the sigma clipping. This should be done from the knowledge of the situation in the photometric diagrams of the different classes of emission-line objects. In our case, as we are proposing the use of photometric diagrams which have not been used before for

the selection of emission-line stars, we have no previous knowledge of the typical loci of the different stars. The arbitrary selection of values for n and m would lack of statistical and physical sense.

For this reason, we have choosen to select the Be star candidates just from visual inspection of the diagrams, by using the two following criteria:

- The points are below the photometric sequence, and clearly detached from it.
- The distance to the mean sequence is lower that 0.3 mag to avoid the very strong emitters which are unlikely to be Be stars.

Obviously, this selection criterion has some amount of subjectivity. But we are just trying to explore a new technique without any previous development. Once we can probe our technique is efficient to detect emission-line stars and study where these stars are placed in the photometric diagrams, we will easily implement statistic selection criteria as explained above.

We report in Table 2.4 the selected candidate counterparts for each field. The obtained color-color diagrams for each field are shown in Figs. 2.10–2.22. Candidate counterparts retrieved from any color-color diagram are marked in both diagrams with red points; the strongest candidates, i.e. those emerging from both diagrams, are shown with blue points. For the selected candidates, error bars are displayed. We obtained emission-line candidates from all the field analyzed in this work, except for IGR J17331–2406. The corresponding color-color diagrams are reported for the sake of completeness in Fig. 2.23.

The selected candidate counterparts will be observed in July 2010 during a spectroscopy campaign already awarded by ESO. Data will be analyzed and classified in the same manner as presented in the next chapter. This will constitute the final validation of the technique illustrated here.

For IGR J175866–2129, 2MASS J17583455-2123215 was recently proposed as counterpart by Tomsick et al. (2009), based on CHANDRA localization. No optical/IR spectra of this object are available. Since the X-ray spectrum of the

system is hard, they suggest it is a HMXB. The suggested counterpart is not among our candidates.

Table 2.4: Selected candidate counterparts, with corresponding coordinates and retrieved photometry. When available, in the first column, the corresponding 2MASS designation is reported. Stronger candidates, i.e. those emerging from both diagrams, are marked with (*).

2MASS object	RA (deg)	DEC (deg)	H (mag)	K_s (mag)
IGR J17407–2808				
2MASS J17403036–2807217$^{(*)}$	265.126	-28.124	10.24±0.03	9.58±0.04
2MASS J17404558–2806429$^{(*)}$	265.189	-28.112	10.22±0.05	10.15±0.06
2MASS J17405212–2808137	265.217	-28.137	11.37±0.04	11.20±0.04
2MASS J17403548–2810084	265.148	-28.169	10.61±0.05	10.41±0.04
2MASS J17405062–2809170	265.211	-28.155	11.99±0.02	11.77±0.03
2MASS J17404868–2807303	265.203	-28.125	10.40±0.04	10.10±0.04
2MASS J17403880–2807521	265.162	-28.131	12.14±0.03	11.83±0.03
2MASS J17403608–2806399	265.150	-28.111	10.26±0.03	9.93±0.03
2MASS J17404035–2807374	265.168	-28.127	9.66±0.01	9.15±0.01
2MASS J17403944–2807221	265.164	-28.123	8.63±0.02	8.05±0.04
2MASS J17404557–2807263	265.190	-28.124	11.56±0.07	10.9±0.1
2MASS J17403037–2806364	265.126	-28.110	12.32±0.06	11.99±0.04
—	265.179	-28.115	11.66±0.03	11.83±0.03
2MASS J17403210–2806365	265.133	-28.110	11.54±0.05	11.77±0.07
2MASS J17403050–2811115	265.127	-28.186	10.71±0.06	10.54±0.04
2MASS J17403752–2810580	265.156	-28.183	11.57±0.07	11.6±0.1
IGR J17454–2703				
2MASS J17451479–2705183$^{(*)}$	266.312	-27.091	9.93±0.05	9.69±0.03
2MASS J17451275–2700433$^{(*)}$	266349	-27.012	9.35±0.05	8.69±0.04
2MASS J17452423–2704309	266.351	-27.075	9.42±0.03	8.80±0.03
2MASS J17452219–2700485	266.342	-27.013	9.33±0.05	8.68±0.03
2MASS J17451312–2704425	266.305	-27.078	11.49±0.03	11.15±0.04
2MASS J17452805–2701332	266.367	-27.026	8.54±0.03	8.14±0.03
—	266.304	-27.057	10.98±0.02	10.53±0.04
2MASS J17451609–2703554	266.317	-27.065	8.81±0.03	8.15±0.03
2MASS J17451847–2702807	266.327	-27.036	9.31±0.02	8.60±0.03
2MASS J17451881–2704299	266.329	-27.075	9.22±0.02	8.40±0.02

Continued on Next Page...

Table 2.4 – Continued

2MASS object	RA (deg)	DEC (deg)	H (mag)	K_s (mag)
2MASS J17453482–2701416	266.395	-27.028	11.82±0.06	11.43±0.05
2MASS J17452723–2705224	266.363	-27.089	10.82±0.02	10.59±0.03
2MASS J17452398–2700538	266.350	-27.015	12.47±0.05	12.15±0.04
2MASS J17452128–2704125	266.339	-27.070	12.18±0.05	11.77±0.06
2MASS J17453298–2701550	266.387	-27.032	12.36±0.04	12.16±0.04
2MASS J17451826–2705155	266.326	-27.088	11.52±0.02	11.44±0.04
2MASS J17453460–2701261	266.394	-27.023	12.40±0.07	12.13±0.08
2MASS J17451714–2704331	266.321	-27.076	10.24±0.02	9.98±0.03
2MASS J17451348–2703568	266.306	-27.066	11.10±0.02	10.98±0.02
2MASS J17452856–2701171	266.397	-27.021	10.02±0.04	9.86±0.03
IGR J17507–2856				
2MASS J17503177–2857557(*)	267.633	-28.965	13.07 ± 0.07	12.34±0.06
2MASS J17505339–2856338(*)	267.723	-28.943	12.36±0.09	12.17±0.09
2MASS J17503610–2858431(*)	267.650	-28.979	9.76±0.07	8.33±0.07
2MASS J17504298–2858139	267.683	-28.971	10.59±0.05	9.86±0.03
2MASS J17504462–2858074	267.691	-28.97	12.33±0.06	11.70±0.04
2MASS J17503197–2858364	267.633	-28.977	12.02 ±0.09	11.01±0.07
2MASS J17504193–2855251	267.729	-28.983	10.55±0.09	9.99±0.06
2MASS J17505268–2859009	267.719	-28.983	12.36±0.10	12.17±0.10
IGR J17585–3057				
2MASS J17584038–3058446	269.668	-30.979	12.3±0.1	11.85±0.04
2MASS J17583570–3058214	269.649	-30.973	11.75±0.05	11.22±0.05
2MASS J17584243–3105527	269.677	-31.098	12.6±0.1	12.26±0.05
—	269.677	-31.011	12.40±0.07	11.94±0.05
2MASS J17584299–3059450	269.679	-30.996	12.10±0.07	11.58±0.04
2MASSJ17583584–3059084	269.649	-30.986	12.45±0.08	12.11±0.06
2MASS J17580987–3059295	269.541	-30.991	9.93±0.05	9.67±0.05
2MASS J17581935–3100102	269.581	-31.003	11.66±0.04	11.8±0.02
2MASS J17581805–3059260	269.575	-30.990	12.41±0.07	12.09±0.03
2MASS J17581721–3057460	269.572	-30.963	11.06±0.04	11.09±0.05
2MASS J17580982–3101485	269.540	-31.030	9.68±0.07	9.53±0.05
IGR J17586–2129				
2MASS J17583417–2128409(*)	269.642	-21478	10.23±0.06	9.22±0.04
2MASS J17585005–2123516(*)	269.708	-21.398	12.42±0.09	11.55±0.08
2MASS J17583428–2124204	269.643	-21.406	11.3±0.1	10.60±0.09

Continued on Next Page...

Table 2.4 – Continued

2MASS object	RA (deg)	DEC (deg)	H (mag)	K_s (mag)
2MASS J17583402–2121472	269.642	-21.363	12.61±0.06	11.94±0.03
2MASS J17583400–2124046	269.642	-21.401	11.56±0.03	11.04±0.03
2MASS J17585226–2124452	269.718	-21.412	12.12±0.05	11.05±0.03
—	269.712	-21.372	13.05±0.04	11.82±0.04
—	269.712	-21.405	12.96±0.05	11.76±0.03
2MASS J17581598–2125052	269.566	-21.418	11.25±0.15	10.03±0.04
2MASS J17582842–2124127	269.618	-21.403	8.81±0.03	9.71±0.04
IGR J18159–3353				
2MASS J18155120–3359003	273.963	-33.983	11.20±0.08	10.55±0.08
2MASS J18155364–3358596	273.957	-33.986	11.06±0.05	10.48±0.05
2MASS J18161193–3400384	274.050	-34.011	10.95±0.06	10.19±0.07
IGR J18175–1530				
2MASS J18171361–1537072(*)	274.307	-15.619	9.39±0.08	8.52±0.05
2MASS J18171363–1536307(*)	274.307	-15.608	11.18±0.07	9.97±0.04
2MASS J18173021–1536034(*)	274.376	-15.601	12.27±0.05	11.04±0.05
2MASS J18173011–1538088(*)	274.375	-15.636	12.38±0.04	11.62±0.04
2MASS J18171668–1531004	274.319	-15.517	12.74±0.09	11.95±0.04
2MASS J18171361–1532057	274.307	-15.535	12.2±0.1	11.58±0.03
2MASS J18171421–1533556	274.309	-15.565	11.97±0.07	10.43±0.07
2MASS J18171382–1534432	274.308	-15.579	12.04±0.09	11.07±0.05
—	274.307	-15.525	12.82±0.09	11.96±0.03
—	274.307	-15.587	12.54±0.07	11.81±0.06
2MASS J18171417–1534552	274.309	-15.582	12.62±0.08	11.26±0.07
2MASS J18173028–1535409	274.377	-15.595	11.40±0.06	10.28±0.04
2MASS J18171364–1535344	274.307	-15.593	11.52±0.05	10.65±0.04
IGR J18193–2542				
2MASS J18192899–2544090	274.871	-25.736	12.45±0.05	12.29±0.04
2MASS J18190771–2544469	274.782	-25.747	12.44±0.08	12.12±0.04
IGR J18214–1318				
—	275.330	-13.310	12.90±0.08	12.37±0.08
2MASS J18213778–1315082	275.407	-13.252	12.6±0.1	11.9±0.1
2MASS J18212903–1315070	275.371	-13.252	10.12±0.04	10.75±0.05
2MASS J18213468–1315587	275.395	-13.266	12.37±0.08	11.8±0.1
2MASS J18213438–1317445	275.393	-13.296	12.3±0.1	11.5±0.1

Continued on Next Page...

Table 2.4 – Continued

2MASS object	RA (deg)	DEC (deg)	H (mag)	K_s (mag)
2MASS J18211916–1318348	275.330	-13.310	12.4±0.1	11.9±0.1
IGR J18307–1232				
2MASS J18304334–1233504(*)	277.680	-12.564	12.33±0.05	11.47±0.02
2MASS J18304323–1236042(*)	277.680	-12.601	11.73±0.04	12.86±0.06
2MASS J18304337–1232429	277.681	-12.545	12.86±0.06	11.73±0.04
IGR J18406–0539				
2MASS J18405233–0543214	280.218	-05.723	11.31±0.08	10.1±0.1
2MASS J18404929–0543210	280.205	-05.722	11.51±0.08	10.4±0.1
IGR J19048–1240				
2MASS J19044599–1241202	286.191	–12.689	12.92±0.06	12.78±0.06

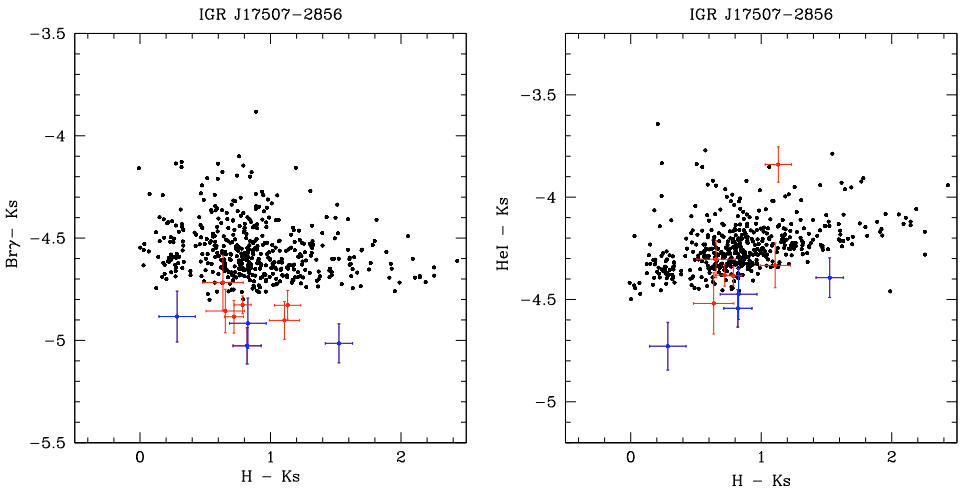

Figure 2.10: Color-color diagrams for IGR J17507–2856.

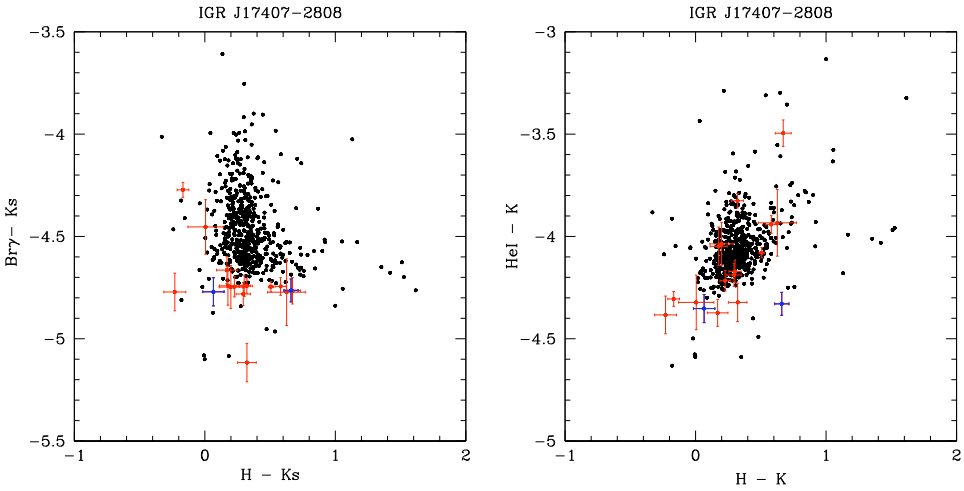

Figure 2.11: Color-color diagrams for IGR J17407–2808.

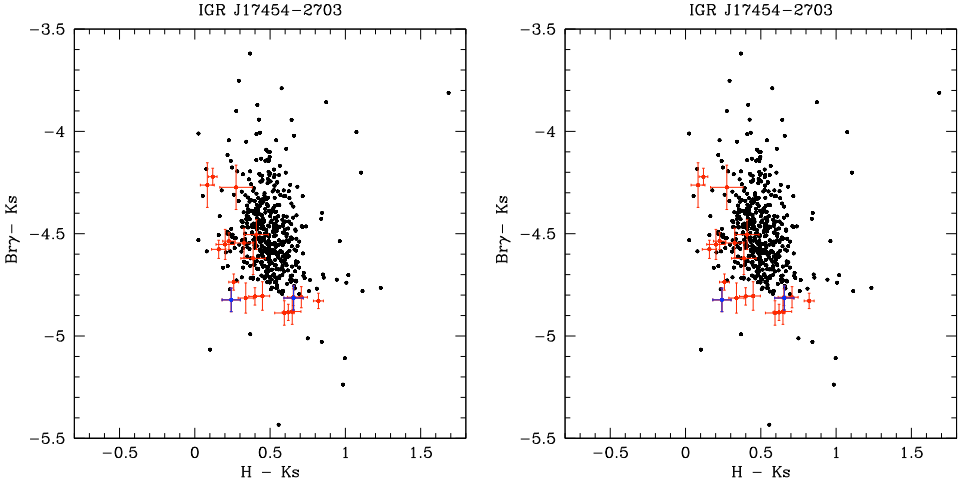

Figure 2.12: Color-color diagrams for IGR J17454–2703.

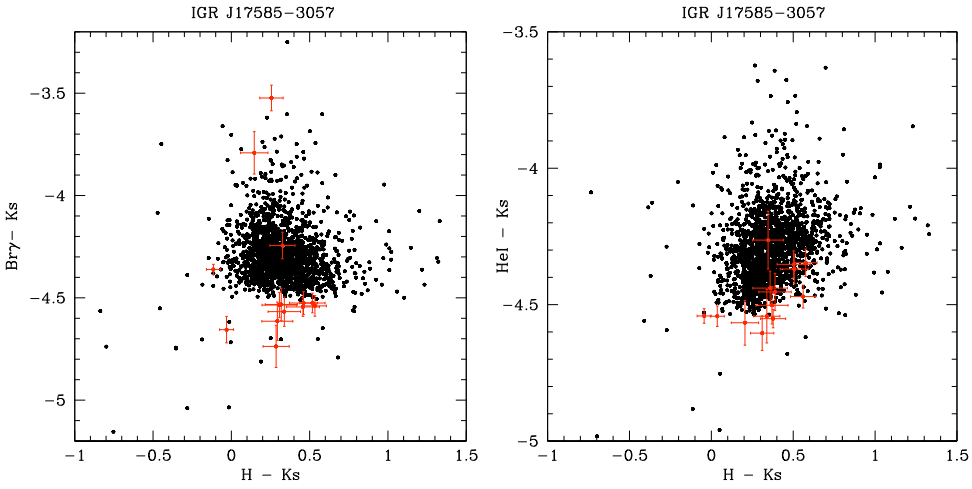

Figure 2.13: Color-color diagrams for IGR J17585–3057.

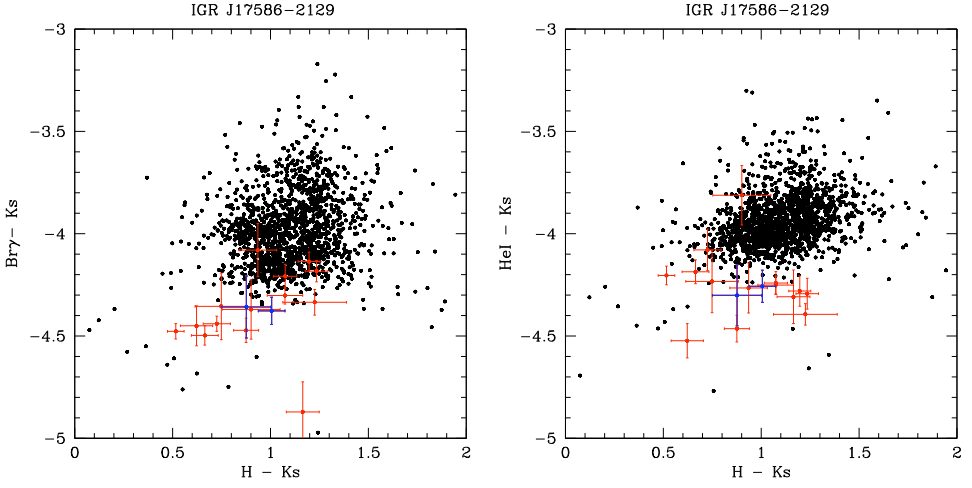

Figure 2.14: Color-color diagrams for IGR J17586–2129.

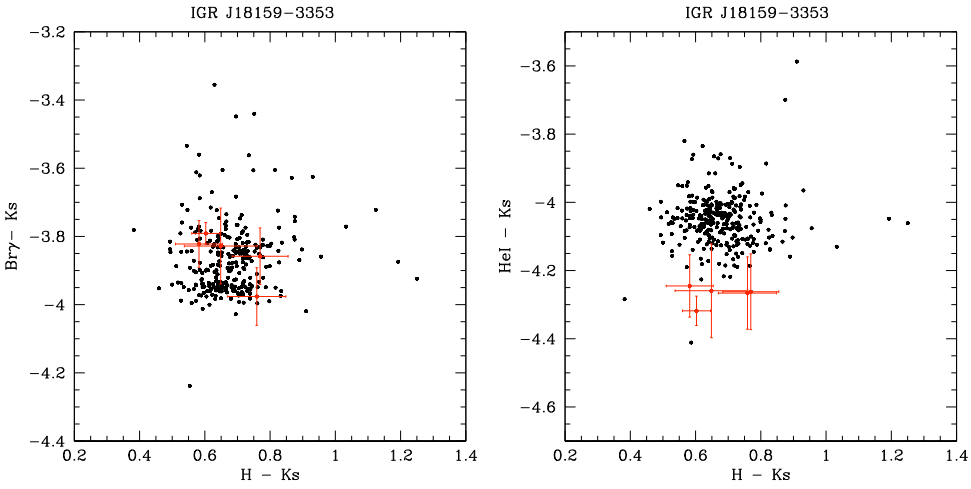

Figure 2.15: Color-color diagrams for IGR J18159–3353.

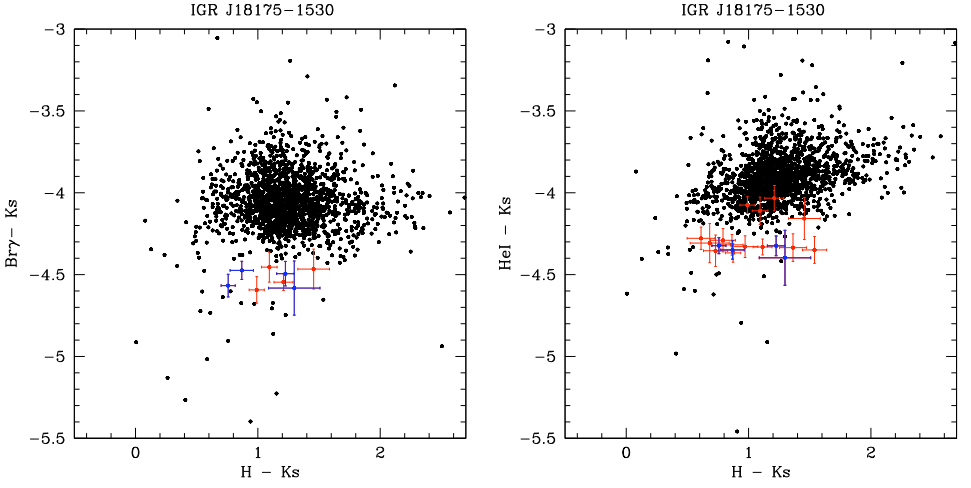

Figure 2.16: Color-color diagrams for IGR J18175–1530.

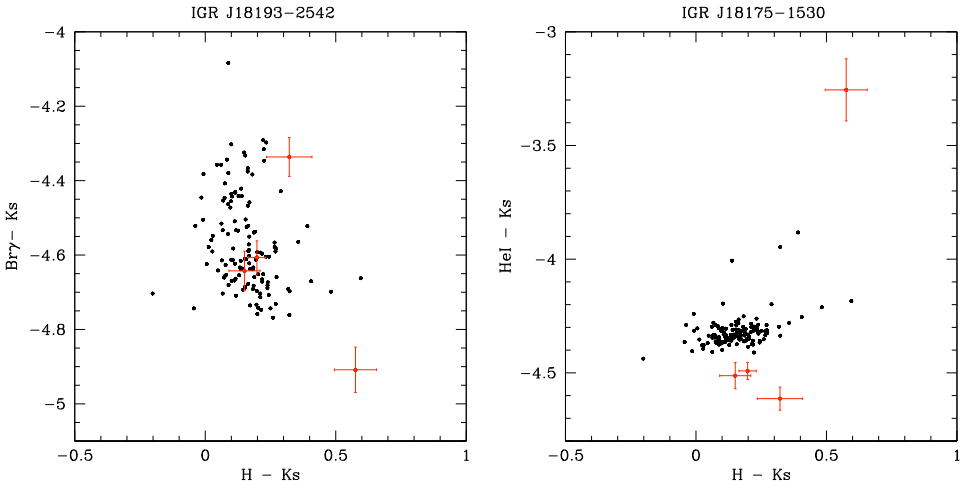

Figure 2.17: Color-color diagrams for IGR J18193–2542.

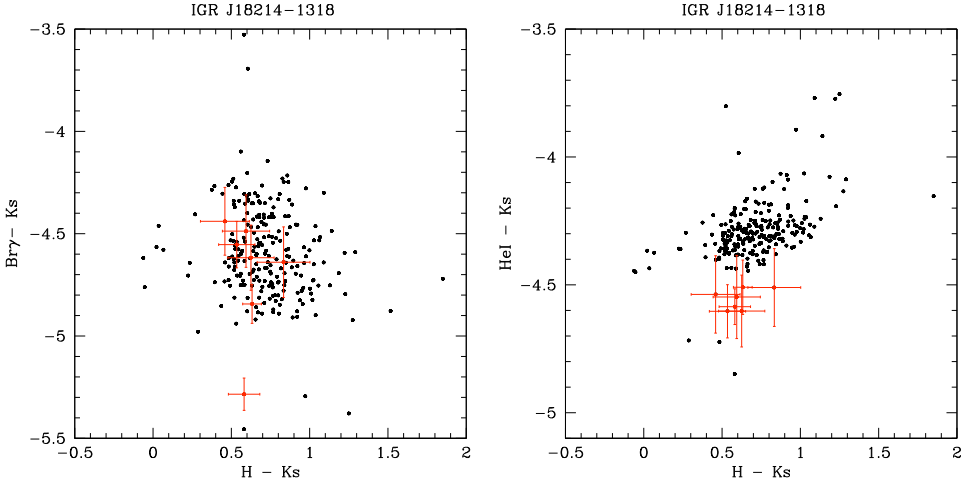

Figure 2.18: Color-color diagrams for IGR J18214–1318.

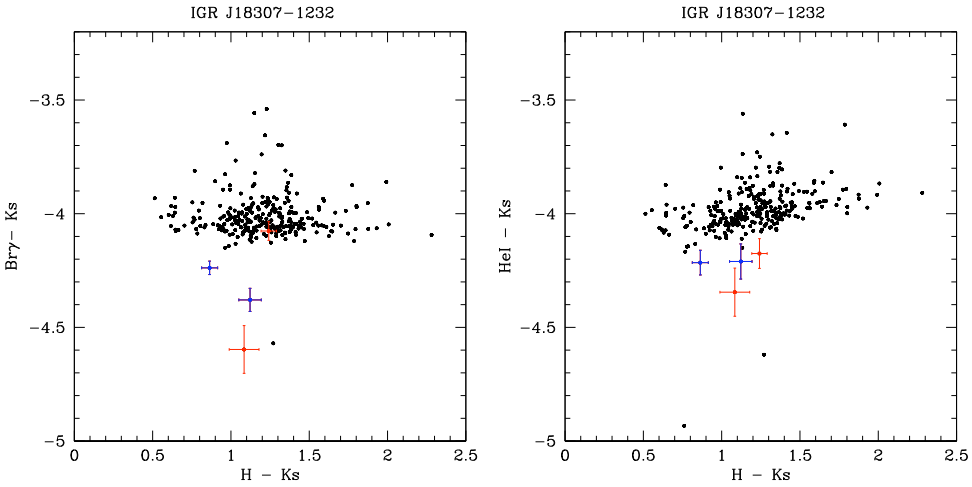

Figure 2.19: Color-color diagrams for IGR J18307–1232.

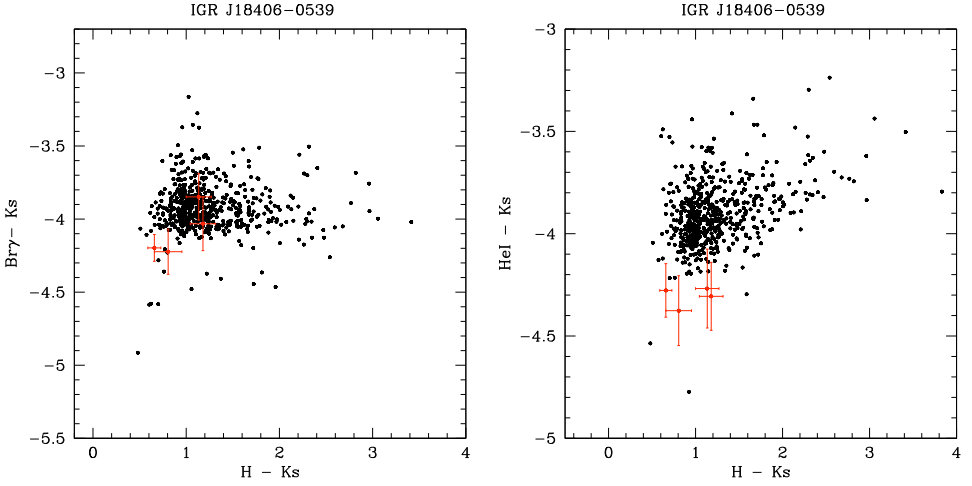

Figure 2.20: Color-color diagrams for IGR J18406–0539.

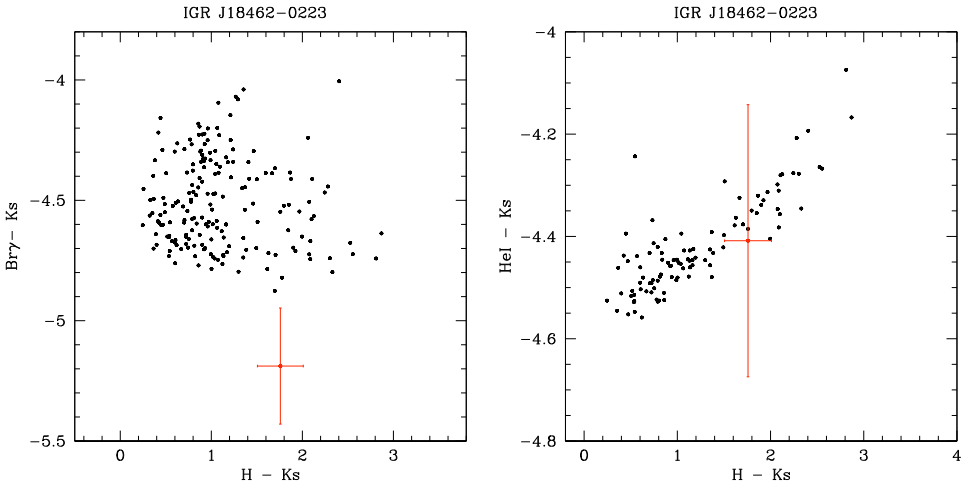

Figure 2.21: Color-color diagrams for IGR J18462–0223.

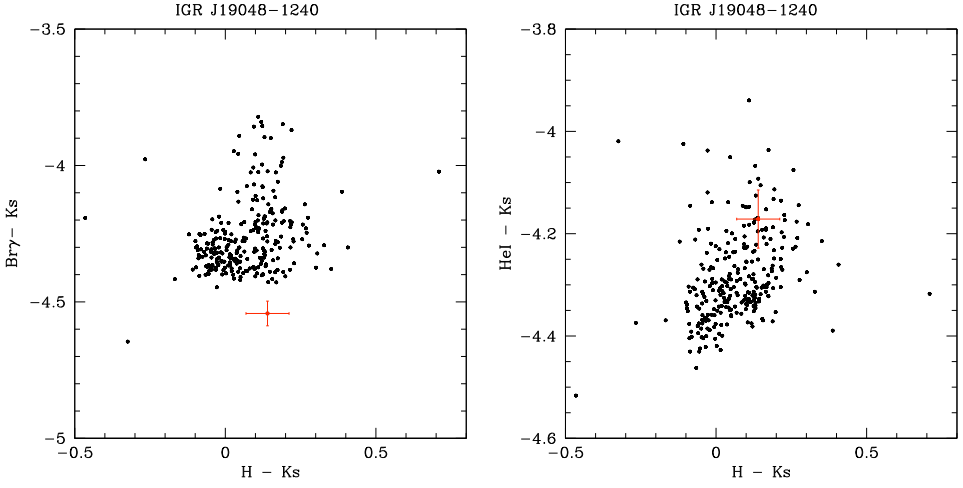

Figure 2.22: Color-color diagrams for IGR J19048–1240.

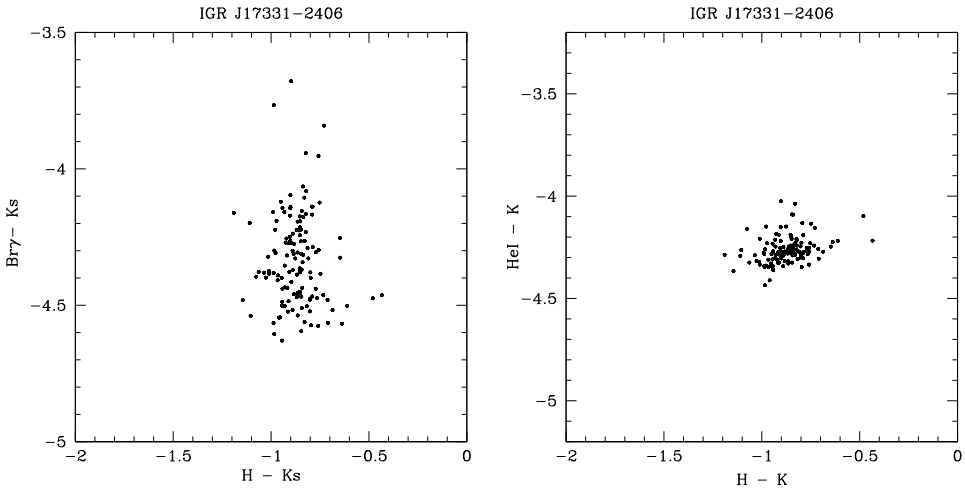

Figure 2.23: Color-color diagrams for IGR J17331–2406.

2.6 First tests

As a first test, we applied the described technique to a known Be/XRB, 1A 1118-615. A K_s spectrum of the IR counterpart, 2MASS J11205717–615502, was taken with SOFI during our observing campaign (for data reduction, see Chapter 3). This is presented in Fig. 2.24. The IR counterpart is a O 9.5 IVe star, and its spectrum clearly displays both He I 20 581 and Brγ in emission, being the last one the strongest feature.

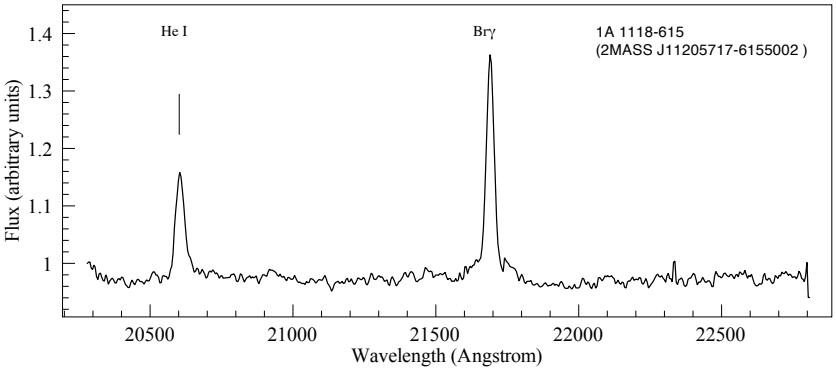

Figure 2.24: K_s spectrum of the known Be/XRB 1A 1118-615.

Both emissions are well traced in our color-color diagrams, reported in Fig. 2.25. From the (Brγ–K_s) color we identified six candidate counterparts, including the correct one; from the (HeI–K_s) only the correct counterpart is selected. In this case, our criterion based on both the narrow-band colors, would thus select the correct object. In this case, the (HeI–K_s) color seems to be more effective in selecting the correct object.

As a further test, we obtained K_s-band spectroscopy of the brightest candidate counterpart, among the two strongest candidates, to IGR J18307–1232, i.e. 2MASS J18304334–1233504. The employed instrument/telescope were NICS/TNG. Unfortunately, the telescope size prevented from observing the second selected object (K=12.86 mag). The obtained spectrum is shown in Fig. 2.26.

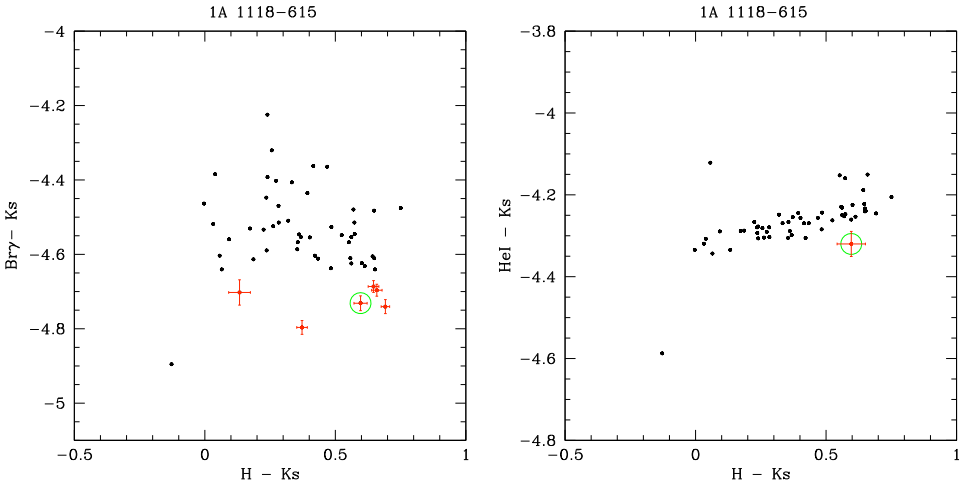

Figure 2.25: Color-color diagrams for the known Be/XRB 1A 1118-615.

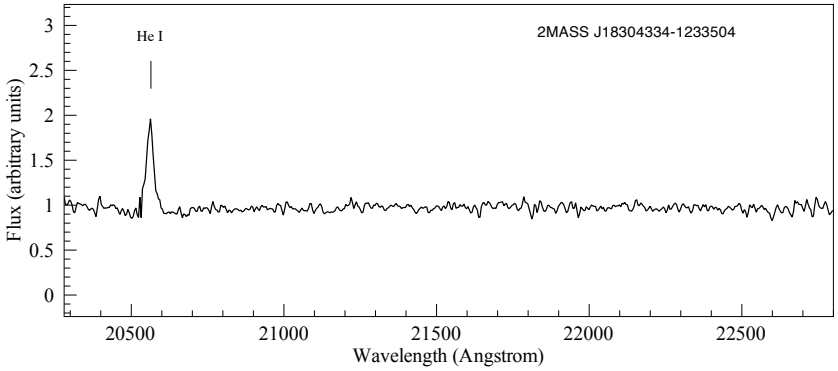

Figure 2.26: K_s spectrum of one candidate counterpart to IGR J18307–1232.

This displays He I 20 581 Å in quite strong emission, as expected from our color-color diagram. Instead, no Brγ emission is detected. No other spectral feature is recognizable. In fact, the retrieved spectrum does not present Brγ either in emission or in absorption: while the emission feature is a characteristic phenomenon of Be stars, in most stars this line is present in absorption. The selected candidate thus stands out in the (Brγ-K_s) – ($H - K_\mathrm{s}$) color-color diagram just because it does not have Brγ in absorption, as most field stars do.

Since He I emission is a typical feature of early-type companions in HMXBs, and Brγ emission, although typical, is not always present in this kind of objects, (see, for instance, Clark & Steele 2000), NICS data give support to this candidate as suitable counterpart, i.e. validate our detection technique.

However, a different candidate counterpart to this *INTEGRAL* source was recently proposed by Butler et al. (2009). The object, with $I = 16$ mag, is not present in the 2MASS catalogue due to its faintness, and for the same reason was not included in our photometry. Its optical spectrum is typical of either CVs or LMXBs, so that the possibility for the system to be a Be/XRB is consistently ruled out. These findings, although indicating a different star as the counterpart to IGR J18307–1232, do not weaken the general validation of our technique from NICS data.

And over all the sky — the sky!
far, far out of reach, studded,
breaking out, the eternal stars.

Walt Whitman

3

NIR spectral analysis and classification of HMXBs identified by *INTEGRAL*

3.1 Scientific objective

As we already discussed in the previous chapter, many of the new galactic X-ray sources discovered by *INTEGRAL* are found to be heavily obscured. Counterparts to these objects are hard to observe in the optical band due to the high interstellar extinction, with A_V in excess of up to ~ 20 mag.

In this context, the recent availability of infrared spectroscopy has emerged as a strong tool to characterize these systems and, together with high-energy data, reveal the HMXB sub-class they belong to. This results in the identification of the mass transfer process of the system, with information about the intrinsic physics of the X-ray binary. The need for low energy data is particularly urgent in the case of SFXTs, which show X-ray properties common to other objects (such as RS CVs binaries and Low Mass X-ray binaries) and thus crucially require the spectral classification of their counterpart in order to be properly discerned.

In this chapter we present spectral analysis and classification of seven HMXBs discovered (or re-discovered) by *INTEGRAL*. The selected IGR sources are the following: IGR J16207–5129, IGR J16465–4507, IGR J16479–4514, IGR J16493–

4348, AX J1841.0–0536 and IGR J19140+0951. We also included the well known system 4U 1907+09 since the spectral classification of its counterpart has been a matter of debate in the past, and no infrared spectra have been published up to now. The first four sources are located in the direction of the Norma-arm tangent region, the next one in the Scutum-arm tangent region and the last two in the Sagittarius arm tangent. Moreover, 5 reference spectra of isolated Be stars were taken during poor weather conditions. These would allow us, by comparison, to better classify the spectra if one of our candidates was a Be star. Eventually, none of them turned out to be a Be star, nevertheless we will report them for completeness in Sect. 3.4.2

In the next two sections we describe the observations and data reduction; in Section 3.4 we report the obtained spectra, analyze their features and propose a classification; we calculate the interstellar hydrogen column density and estimate the distance to each source; in section 3.5 we discuss our results, before concluding.

3.2 Observations

We selected proposed counterparts, choosing sources observed by the X-ray missions *XMM*, *Chandra* and *Swift*, which produce a very small error circle and facilitate the detection of the counterpart.

Data were obtained during several observing runs at the European Southern Observatory (ESO), in Chile. The employed instruments were, in visiting mode, SOFI (Moorwood et al. 1998c), on the 3.5m New Technology Telescope (NTT) at La Silla, in July 2006 and May 2005; and, in service mode, ISAAC (Moorwood et al. 1998a) on the 8.2m UT1 in Paranal, in April 2007.

Since all the spectra analyzed in this chapter except one were obtained with SOFI, only this instrument will be described here. For an overview on ISAAC, see Chapter 4. The SOFI spectrograph has a largest field of view of 4.92 arcmin, and it covers the 0.9-2.5 micron wavelength range with spectral resolution from 600 to 2200. There are three grisms available with SOFI: two low resolution grisms and a medium resolution grism. Of the two low resolution grisms, one covers

Table 3.1: The wavelength range, resolution and dispersion of the SOFI grisms employed in this work. The resolution is given for the 1 arc-second slit.

		Grisms specifications		
Grism name	Order sorting filter	Wavelength range (μm)	Resolving power	Dispersion (Å/pixel)
Red	GRF	1.53-2.52	588	10.22
3	K_s	2.00-2.30	1320	4.62

the region from 0.95 to 1.64 microns and the second covers the region from 1.53 to 2.52 microns. The medium resolution grism gives about twice the resolving power of the two low resolution grisms. It is used with the H and K_s filters as order sorting filters in the 3rd and 4th orders to cover respectively the H and K atmospheric transmission windows. The wavelength ranges, the resolving powers and the dispersions of the used grisms are given in Table 3.1. Table 3.2 reports the observation log, including, for each spectrum, the retrieved signal-to-noise ratio (S/N).

For SOFI observations, we used the long slit spectroscopy mode, at medium ($R = 1320$) and low ($R = 588$) resolution with a K_s and red grism respectively, and $1''$- width slit. ISAAC observation was performed at low resolution ($R = 500$) with the $1''$- width slit. The sky had thin cirri in 2006, while it was generally clear in 2007. Seeing averaged between $0.9''$ and $1.2''$, with the exception of the observation of IGR J16749–4514 which was performed with a seeing of $1.6''$.

3.3 Data reduction

Data reduction was performed using the IRAF package, following the standard procedure. A full reduction of IR spectroscopic data required the following operations, which will be described in more detail below:

1. correcting for the inter-quadrant row cross-talk;

2. combining like images and perform the sky subtraction;

3. creating a flat field and perform flat field correction;

4. extracting the spectra;

5. applying wavelength calibration;

6. applying terrestial atmospheric (telluric) correction.

3.3.1 Inter-quadrant row cross-talk

This feature affects both imaging and spectroscopy performed with SOFI and ISAAC. Unlike the imaging, when users can rotate the instrument to avoid it, the spectra are always aligned along the array columns, so a ghost of the upper half of the spectrum always appears in the lower one, and vice versa. In our case, since we are mainly looking for emission lines, the effect is particularly dangerous because ghosts of emission lines are emission line like and can be confusing. For instance, one has to account for this effect when faint lines have to be detected between bright OH lines, or when the continuum-to-line ratio is of interest.

Figs. 3.1 and 3.2 from Finger & Nicolini (1998) show the shading effect with a long slit oriented parallel to the rows of the detector. The slitwidth is in this case 2 arcseconds on the sky. The image shows the spectrum of ambient background radiation observed with the narrow-band CO filter and the red grism of SOFI. The dispersion of the grism is 10.22 Å/pixel. The peak flux in the center of the slit image is 1374 e^-/sec/pixel. The calculated photon flux for the given instrument setup is 1846 photons/sec/pixel. The rows in quadrants III and IV near row 798, which have increased intensity but do not receive any photons, are read out at the same time as the rows close to row 286, which are illuminated by the slit. The intensity of row 798 is 1.5% of the intensity of row 286.
The result of the correction algorithm (2.3) is demonstrated in Fig. 3.3 by comparison of the raw K_s-band spectrum with the modified K_s-band spectrum: one can clearly see that the row cross-talk can be well removed.

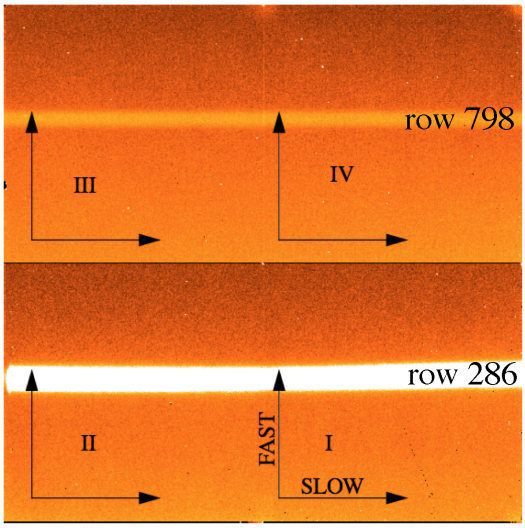

Figure 3.1: Shading effect with long slit oriented parallel to rows of the detector. Rows in quadrant III and IV, read out at the same time as row illuminated by the bright slit, show increased intensity.

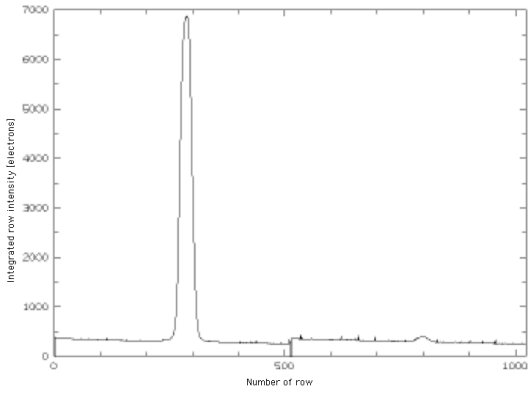

Figure 3.2: Average intensity of rows taken from image in Fig. 3.1 showing the shading effect.

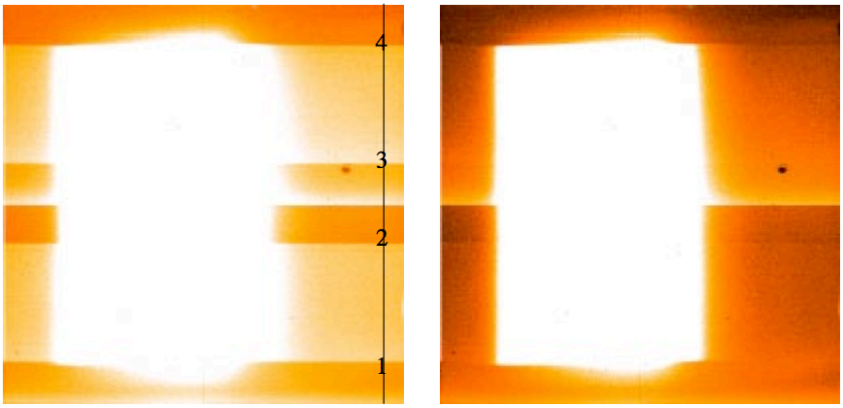

Figure 3.3: Comparison between a raw K_s-band spectrum (on the left) and the K_s-band spectrum (on the right) modified by the correction algorithm using equation (2.3).

3.3.2 Sky subtraction

Below about 2.3μm most the sky emission arises from molecules (primarily OH and O_2) excited by solar radiation during the day. These emission lines typically far exceed the counts in the target star, so they must be removed before the two-dimensional spectrum is summed along the cross-dispersed direction to obtain the one-dimensional spectrum. The strength of the sky emission is a function of airmass and atmospheric conditions, and significant variations occur over time-scales of approximately tens of minutes in clear weather.

We attained the best results by subtracting one slit position from another unique slit position, the preceding one or the following one during the execution (task `imarith` of IRAF). Obviously, one chooses to subtract the image with the target in a different position along the slit with respect to the image that one wants to correct. The advantage of this technique is that it takes into account sky variation on time-scale a few `DIT`[1] times, so that we could achieve a good quality subtraction even in case of thin cirrus and very low target signal, i.e. when the sky is variable and dominant on the object. In Fig. 3.4 one can appreciate the

[1]In the context of the ESO detectors control system, the DIT, or Detector Integration Time, is defined as the amount of time during which the signal is integrated onto the detector diodes. For SOFI, under the worst transparency conditions, we chose typical values of 30-35 s, while under the best conditions we chose $\sim$ 60s DITs. For ISAAC, the DIT was 60s.

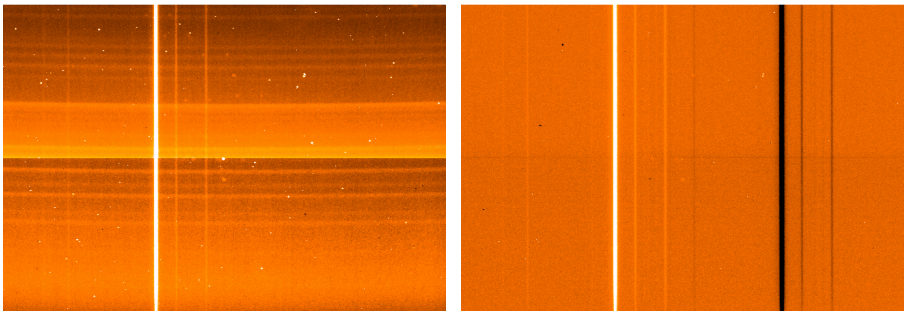

Figure 3.4: A single frame before (left panel) and after (right panel) sky subtraction. The "negative" spectra appearing in the final image are a secondary result of the subtraction, which doesn't affect data analysis.

effect of sky subtraction on a single frame of data.

3.3.3 Flat fields

A dome flat-field was create by obtaining, both at medium and low resolution, a set of alternated images of an illuminated/unilluminated panel inside the dome. The average of the unilluminated set of images was subtracted from the average of the illuminated ones (tasks `imcombine` and `imarith` of IRAF). The two-dimensional dome flat was then normalized to unit taking care of the large-scale variations, using the task `response` with a spline3 function of high order (45) to best follow the pixel variations; finally, the sky-subtracted, two-dimensional data were divided by the normalized dome flat field to remove pixel-to-pixel sensitivity variations in the array.

3.3.4 Extraction of the one dimensional spectra

The two-dimensional spectra were in this phase integrated along the cross-dispersed direction and displayed as counts versus pixel position along the dispersed direction. In the package `apextract`, we used the task `apsum` interactively in order to carefully inspect each image and identify the correct aperture.

The task `apsum` calls several other tasks (`apdefault`, `aptrace`, `apfind` and `apedit`). The steps that mark this phase are: selecting the object window by defining the aperture size one wants to use in the extraction of the spectrum;

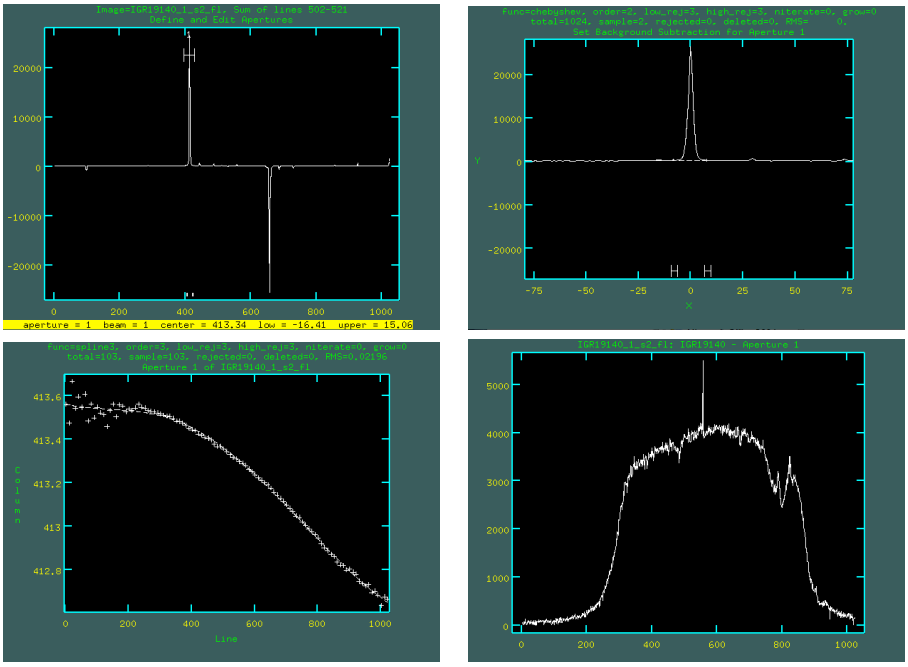

Figure 3.5: The different phases in the extraction of a one-dimensional spectrum, as performed using the task `apsum`. From top left: definition of the aperture size; definition of the background window; tracing the spectrum; the final extraction of the one-dimensional spectrum displayed as counts versus pixel position.

selecting the background window and fitting it; tracing the spectrum, i.e. fitting the center of the star profile along the image; extracting the one dimensional spectrum. This stages are graphically shown in Fig. 3.5.

Since the regions of the sky we observed, belonging to the Galactic Plane, are very crowded, in a few cases there was no chance of excluding other – even brighter – objects from the field of view. That resulted in the presence of more than one two-dimensional spectrum in the frames, but this inconvenience could be easily overcome in the extraction phase.

3.3.5 Wavelength calibration

After extracting the one-dimensional spectrum for the arcs – both at medium and low resolution – one is able to perform the wavelength calibration, which consists

of three steps. The first one was done interactively with the task `identify` which allows to get from an arc a dispersion solution (wavelength versus pixel), using the calibration arc spectra with identified lines reported in instrument manuals. The calibration arc spectra are shown in Figs. 3.6 and 3.7 for SOFI, and in Fig. 3.8 for ISAAC.

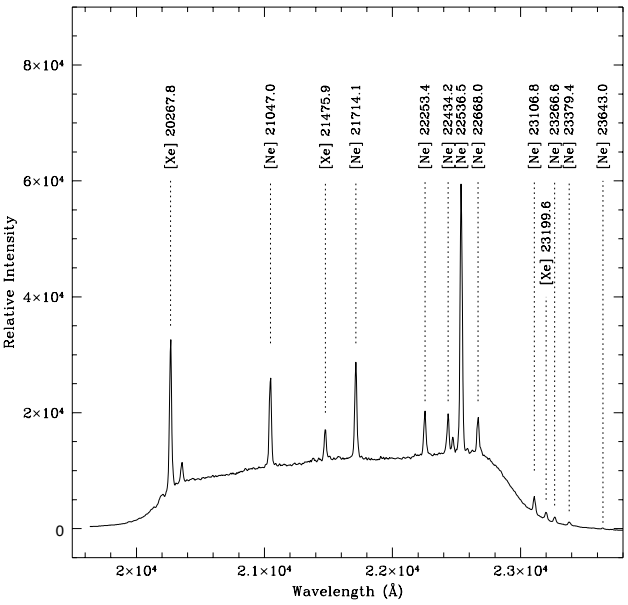

Figure 3.6: A Xenon and Neon arc spectrum taken with SOFI medium resolution grism at the K_s atmospheric window. The main lines are marked.

With `identify`, features in the input images are identified interactively and assigned user coordinates. A "coordinate function" mapping pixel coordinates to user coordinates may be determined from the identified features. We used a cubic fit to calibrate the dispersion both for the medium resolution and the red grism. The dispersion solution is the output from the task and it is stored in a text file.

The next step consists in assigning arc references to scientific objects; this step was performed with the task `refspectra` which writes this assignment in the header of the objects under the keywords `REFSPEC1` and `REFSPEC2`. The third step consists in linearizing the x-axis of the extracted spectra with the task

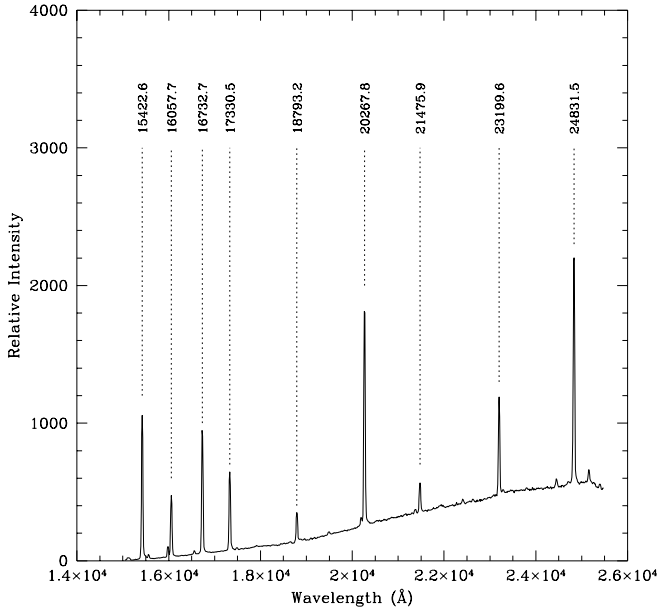

Figure 3.7: A Xenon arc spectrum taken with SOFI low resolution red grism. The main lines are marked.

`dispcor` using the reference found in the header and the corresponding solution from the database. The output of the task is a wavelength calibrated image, with x-scale in Angstrom.

After wavelength calibrating, and before performing the removal of telluric features, we graphically removed spurious features such as bad pixels or cosmic rays (task `splot`), we added up all the one-dimensional spectra for each observation (task `sarith`), cut the resulting spectrum in order to keep only the region where the transmission function of the K_s filter is nearly constant (task `scopy`), and finally we normalized the obtained spectrum (task `continuum`) by dividing it by a fitted polynomial continuum.

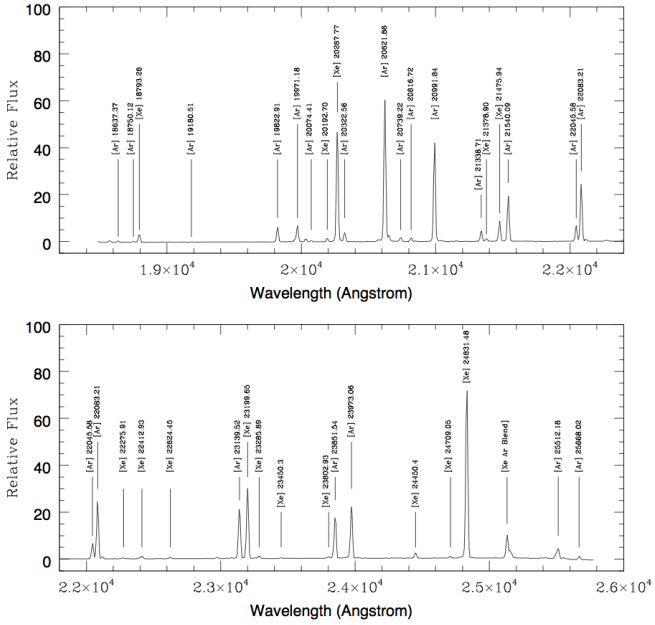

Figure 3.8: A Xenon/Argon arc spectrum taken with ISAAC low resolution grism. The main lines are marked.

3.3.6 Telluric absorption correction

The near-infrared spectrum of the atmosphere from 1 to 5 μm is dominated by telluric water and CO_2 absorption, between which the major observing windows in the wavelength region are defined. Broad molecular absorption bands of CO_2 are resolved at moderate spectral resolution into individual pressure-broadened rotovibrational transitions. These transitions vary in both time and observed elevation, making their removal problematic in ground-based spectroscopic studies. There is a tremendous impetus from astronomers to obtain highly accurate spectral profiles for lines existing in the near-infrared. For hot stars like the ones we were interested into, an important line for spectral classification – but also for the modeling of extended atmospheres and stellar winds – is the HeI transition at 2.058 μm (Clark & Steele 2000): this line is located near the short-wavelength edge of the K_s-band window, where CO_2 absorption bands dominate the spectrum. The challenge for observational astronomers is to obtain observations of

the 2.058 μm line profile with a high enough signal-to-noise ratio to be suitable for detailed modeling despite considerable telluric contamination.

In order to correct for telluric absorption, it is necessary to divide the object spectrum by the spectrum of what one can call a *telluric standard*. We adopted the procedure outlined by Hanson et al. (1996). At the telescope, we observed an A0-A3 III-V star immediately before or after each target and a G2-3 V star once per hour in order to obtain very small differences in airmass (differences between 0.01 and 0.04 airmasses were generally accomplished). The only non-telluric feature in the A star spectra is Brγ. A simple interpolation over this feature is not appropriate however, as there is also a telluric feature at this wavelength that would lead to spurious emission features contaminating the strength and profile of the Brγ emission lines we expected from the targets. Instead we used the G star observations divided by the solar spectrum to calculate the telluric features in the region of Brγ (between 21590 Å and 21739 Å).

In order to do that, we employed a high resolution (R = 40 000) K-band spectrum of the sun[2]. We degraded it to the resolution of SOFI/ISAAC spectra using the task `gauss` which performs a convolution with an elliptical – circular, in our case – Gaussian function; we also applied to the solar spectrum the same dispersion solution than SOFI/ISAAC data (task `dispcor`). In order to ensure that the A star, G star and solar spectra were all properly aligned in wavelength space, when necessary, appropriate offsets were applied. The ratio between the G star and the solar spectrum in the Brγ region was patched into the A star spectrum (tasks `scopy` and `scombine`), obtaining a specific telluric spectrum for each target. Fig. 3.9 shows an example of a telluric spectrum and the A and G star spectrum from which it was derived.

After constructing the specific telluric spectrum for each target, we applied the removal of telluric features by dividing the targets by the shifted and scaled telluric spectra.

In the case of low-resolution observations, the H-band spectra were corrected for telluric features by ratioing observed G type standards with the solar spec-

[2]NSO/Kitt Peak FTS data, that were produced by NSF/NOAO.

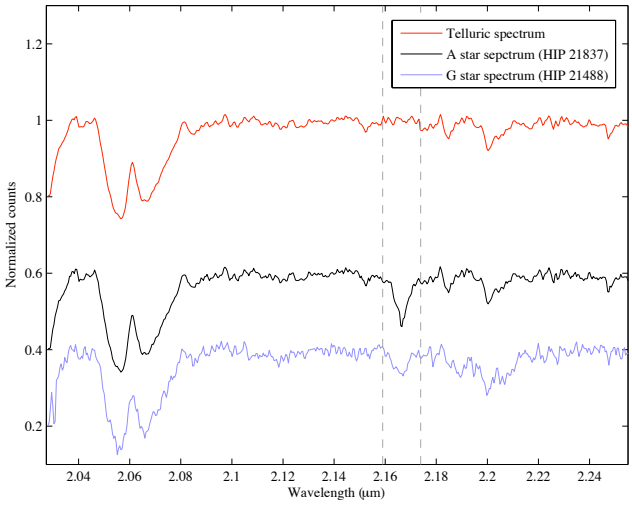

Figure 3.9: Construction of telluric spectrum from A and G star spectra. The region marked by dashed lines indicates where the ratio between the G star and solar spectrum was patched into the A star spectrum. The spectra have been normalized to 1 and displayed with an offset for clarity.

trum to remove features within their photosphere, and then ratioing the object spectrum with the modified standard spectrum.

The correction was done interactively with the task `telluric`, which is characterized by the parameters of the *shift* and the *scale*. The shifting takes into account possible small misalignments or errors in the dispersion zeropoints, while the intensity scaling allows for differences in the airmass and variations in the abundance of the telluric species. The intensity scale used Beer's law which is the approximation that the change in absorption with abundance is an exponential relation. The task determines the best values of the shift and scale parameters by cross-correlating the calibration and scientific spectra to find the parameters values that minimize the RMS of the output corrected spectrum, which is calculated as follows. Let $J'(x_i)$ be the calibration spectrum at a set of pixel x_i. An interpolation function is fit to this spectrum to give $J'(x)$. The shifted and scaled

calibration function is then:

$$I'(x_i) = I(x_i)\frac{< J' >}{J'(x_i)}, \tag{3.1}$$

where I' is the corrected spectrum, I is the input spectrum, and $< J' >$ is the mean of the shifted and scaled calibration spectrum to keep the output intensities comparable to the input spectrum. As the spectra were dispersion calibrated, the x values in equation 3.1 from the input spectrum were converted to matching pixels in the calibration spectrum using the dispersion function.

We first run the task automatically and then used the interactive mode in order to best adjust the values of the shifting and scaling parameters. Fig. 3.10 shows the effect of telluric absorption correction.

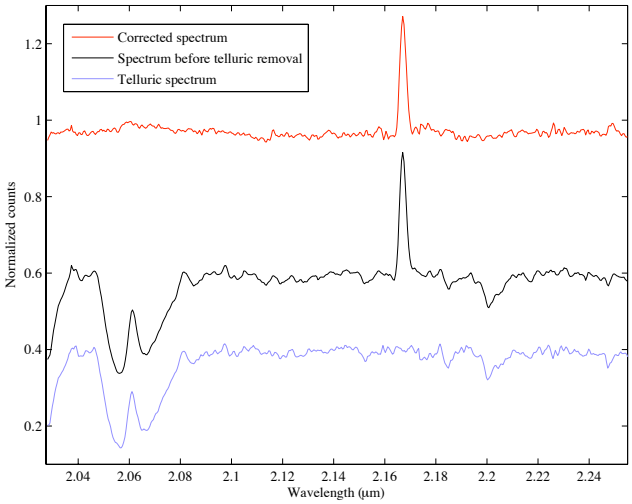

Figure 3.10: Effect of atmospheric absorption correction: example for the target HD 30076. The spectra have been normalized to 1 and displayed with an offset for clarity.

3.4 Results

In this section we present the results of spectral classification and analysis for each target. The field of NIR spectral classification is still very young and the level of required S/N and resolution to perform a quantitative profile analysis are very high ($R \sim 12\,000$ and S/N $\gtrsim 250$), especially for young massive stars, as shown by Hanson et al. (2005b). The difficulty of the analysis depends on the few lines available and the relatively large uncertainty in their strength, due to their intrinsic weakness; moreover, some significant spectral regions, specifically through the 20 580 He I and the Brγ features, pose systematic complications because of the strong telluric absorption.

Under this premise, our analysis will be qualitative, based on the comparison with available NIR spectral atlases (Hanson et al. 1996, 2005a). According to our estimation, this approach implies that the resulting spectral classification is provided with an uncertainty of no more than one luminosity subclass. The spectral type is precise up to one subtype.

Some of the identified features exhibit a 10-20 Å displacement with respect to the nominal values, consistent with the instrumental resolution. Greater displacements, up to a maximum of 29 Å, are found corresponding to lines characterized by a complex profile, such as Brγ, or placed in a region of strong telluric absorption, such as both H I 20 581 Å and Brγ.

In the next sub-section we will classify the spectra, showing the features we were able to identify, with the corresponding equivalent width. Although it was pointed out (Hanson et al. 1996) that equivalent widths may show variations between stars, we report them for completeness. The values we calculated are affected by an average 15% error. For each object, a figure displays the spectrum we obtained, together with some comparative spectra from the atlas of Hanson et al. (1996) in a separate box. At the end of this chapter, Table 3.3 summarizes the line identifications for all the observed targets.

3.4.1 Spectral analysis and classification

IGR J16207–5129

The source was discovered by IBIS/ISGRI in the first Galactic Plane Survey performed by *INTEGRAL* (Bird et al. 2004), which measured a flux of 3.8 ± 0.3 mCrab in the 20–40 keV range. Instead, only the upper limit of < 4 mCrab was obtained in the 40–100 keV band. Subsequent Chandra observations allowed the identification of the optical/infrared counterpart. This was associated with USNO-B1.0 0384-0560857 = 2MASS J16204627-5130060 by Tomsick et al. (2006). The power-law spectral fit provided $N_H = 3.7^{+1.4}_{-1.2} \times 10^{22}$ cm^{-2} and photon index equal to $0.5^{+0.6}_{-0.5}$, indicating an intrinsically hard source. The lower limit to the stellar temperature was estimated to > 18 000 K, revealing the presence of a very hot, massive star. From the fit of optical/IR spectral energy distributions, the distance was estimated to be between 3-10 kpc (3-9 kpc in the case of a supergiant classification). Subsequent optical spectroscopy from Masetti et al. (2006a) refined the distance estimate to 4.6 kpc. Negueruela & Schurch (2007), from optical observations, constrained the spectral type to earlier than B1.

Fig. 3.11 shows the K_s spectrum we obtained, with identified spectral features marked. The spectrum shows no metal lines (no N III or C IV), strong He I 20 581 Å emission, He I absorption at 21 126 Å and moderately strong Brγ absorption. The atomic transitions observed are the typical of OB star spectra. The He I 20 581 Å line is a prominent feature in supergiant stars, so that it is considered an important tracer of stars with extended atmospheres. It becomes weak or even disappears in main sequence stars and it is observed in emission in B type supergiants, whereas it is in absorption in O type supergiants (Hanson et al. 1996). The He I 21 126 Å line is present in late O – early B spectra.

For what was outlined above, and by visually comparing the relative strengths of the identified lines with those of Hanson et al. (1996, 2005a), we estimate the spectral type of the IGR J16207–5129 counterpart to be B1 Ia. This allows us to classify the system as a SGXRB, as also inferred by Negueruela & Schurch (2007).

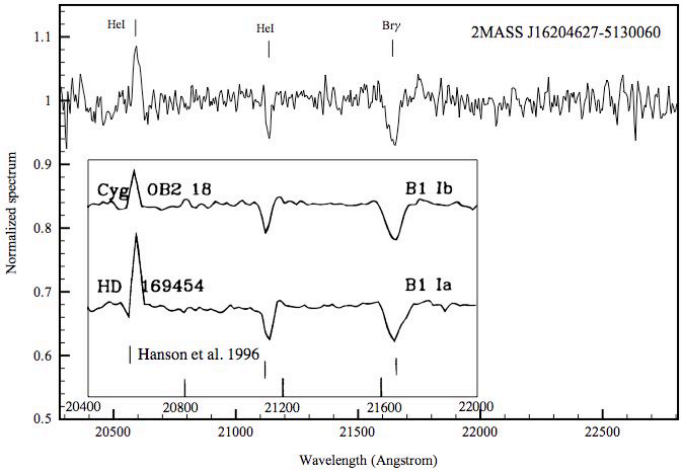

Figure 3.11: K_s spectrum for 2MASS 16204627–5130060, the infrared counterpart of IGR J16207-5129. The positions of identified spectral features are marked by solid lines.

IGR J16465-4507

The source was discovered by *INTEGRAL* during its only observed X-ray flare on 2004 September 6th-7th (Lutovinov et al. 2004). Using data of XMM/Newton, Lutovinov et al. (2005) found pulsations with period $P_s = 228$ s in the X-ray flux and high photoabsorption, with $N_H \sim 7 \times 10^{23}$ cm^{-2}. The single star falling in the XMM/Newton error circle was identified by Zurita & Walter (2004) as the counterpart to the X-ray source, and associated with 2MASS J16463526-4507045.

From an optical spectrum, Negueruela et al. (2006) classified the source as a B1 Ib supergiant, subsequently refining their classification to B0.5 Ib (Negueruela et al. 2007). They also estimated the distance of the source to 8 kpc.

Our IR data suggest a different spectral classification. Fig. 3.12 shows the K_s spectrum we obtained, with identified spectral features marked.

The spectrum shows He I 20 581 Å in quite strong absorption; a feature at 20 730 Å is possibly identifiable with a faint blend of the C IV transitions at 20 690, 20 780 and 20 830 Å, which appear in the atlas from Hanson et al. (1996) only in the very high S/N spectra. We observe He I 21 126 and Brγ, both in strong

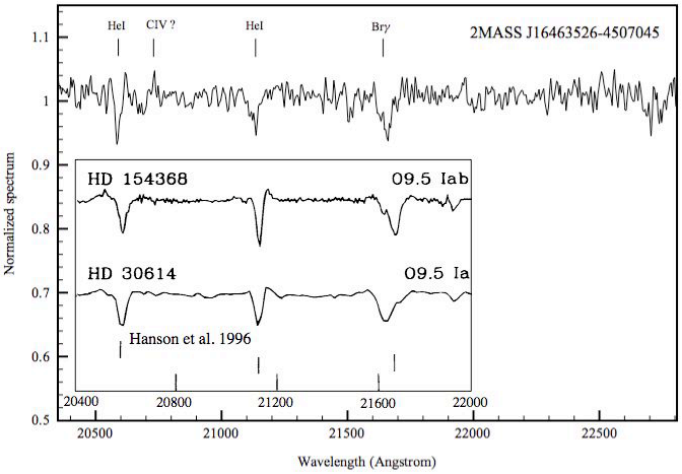

Figure 3.12: K_s spectrum for 2MASS J16463526-4507045, the infrared counterpart of IGR J16465-4507. The positions of identified spectral features are marked by solid lines.

absorption.

We agree with Negueruela et al. (2007) in the classification of the counterpart as an early supergiant. However, we suggest that the observed features point to an earlier type than B1: in fact, the He I 20 581 Å line is seen in emission in B1 supergiants, while it is in absorption in late-O supergiant. Visually comparing the relative strengths of the outlined features with those from the atlases of Hanson et al. (1996, 2005a), we refine the spectral classification of the source to O9.5 Ia. We thus confirm the supergiant nature of the companion, which, together with the X-ray behavior of the system, classifies it as an SFXT, as proposed by Negueruela et al. (2006).

IGR J16479–4514

The source was discovered by *INTEGRAL* (Molkov et al. 2003) during an outburst. The X-ray spectrum is fitted with a power law with a high-energy cut-off, with spectral index $\Gamma = 1.4$, and the column density is $N_H = 12 \times 10^{22}$ cm^{-2} (Lutovinov et al. 2005).

IGR J16479–4514 showed short outbursts with very fast rises, observed in 2003

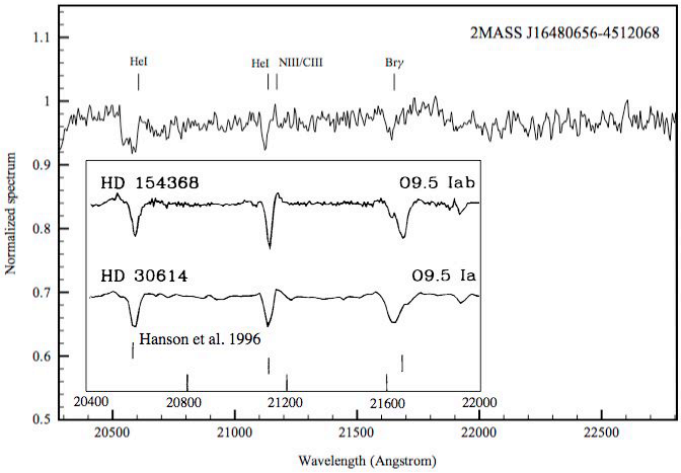

Figure 3.13: K_s spectrum for 2MASS J16480656-4512068, the infrared counterpart of IGR J16479–4514. The positions of identified spectral features are marked by solid lines.

by Sguera et al. (2005). Its X-ray behavior is thus typical of SFXTs (Negueruela et al. 2006), however the lack of an optical/infrared spectral classification prevented the possibility of enrolling it in this new class of objects. The counterpart to the source was identified by Kennea et al. (2005) through SWIFT observations.

Fig. 3.13 shows the K_s spectrum we obtained, with identified spectral features marked. The spectrum shows He I 20 581 Å in strong absorption, well recognizable although affected by a clear telluric residual. The difference we obtained in airmasses between the telluric standard star and the target was in this case very low, equal to 0.004: we thus suppose that the poor correction of telluric absorption is due to the passage of a cirrus during the observation of the telluric standard. We can also detect absorption at He I 21 126, a weak N III 21 155 Å emission (which, according to Hanson et al. (2005a), could alternatively be C III), and moderately strong Brγ absorption.

We conclude that the spectrum shows the typical features of a late O supergiant, especially the presence of He I 21 126 (typical of late-O and early-B stars) in combination with He I 20 581 Å, present in supergiant stars, and seen in absorp-

tion in late-O supergiants. Through the visual comparison with the atlases from Hanson et al. (1996, 2005a), we estimate the spectral type to be O9.5 Iab. This result, together with those from X-ray data, allows us to affirm that the object belongs to the new class of SFXTs.

IGR J16493–4348

This *INTEGRAL* source was discovered by Grebenev et al. (2005). RXTE observations by Markwardt et al. (2005) found that the mean spectrum is consistent with a heavily absorbed power law with $N_H \sim 10^{23}$ cm^{-2} and a photon index of 1.4. The retrieved flux was 1.0×10^{-11} erg cm^{-2} s^{-1} in the 2–10, 10–20 and 20–40 keV energy bands. Chandra imaging of the field of IGR J16493–4348 was performed for 4.1 ks by Kuiper et al. (2005). They detected a single point source within the $2'$ error circle of the *INTEGRAL* source at R.A. $=16^h49^m26.92^s$, Dec $=-43°49'8.96''$, with a $0.6''$ error in each coordinate. No spectrum could be extracted from these data and Kuiper et al. (2005) noted that previous measurements of IGR J16493–4348 by RXTE may be contaminated by another X-ray source, 1RXS J164913.6–435527, located $\sim 6.7'$ away. From *INTEGRAL* data, Hill et al. (2008) discarded the previously proposed association with the free radio pulsar PSR J1649–4349; the best fit of the X-ray spectrum was obtained with an absorbed cut-off power-law with $N_H = 5.4 \times 10^{22}$ and $\Gamma = 0.6$.

The infrared counterpart to the source was proposed by Kuiper et al. (2005), who reported a single 2MASS source, 2MASS J16492695–4349090, compatible with both the Chandra and Swift/XRT positions. Kuiper et al. (2005) observed the source in the K_s band and found a magnitude of 12, consistent with the 2MASS magnitude. No optical/IR spectrum of the counterpart are available, and the nature of the source, although with position and X-ray behavior pointing to a HMXB system, is not proved.

Fig. 3.14 shows the K_s spectrum we obtained, with identified spectral features marked. The spectrum shows He I 20 581 Å in strong emission, He I 21 126 Å in absorption and Brγ 21 661 Å in relatively strong absorption. We possibly identify also a N III/C III line in very faint emission. The atomic transitions detected are the typical ones of OB stars spectra. In particular, He I 20 581 Å is a prominent

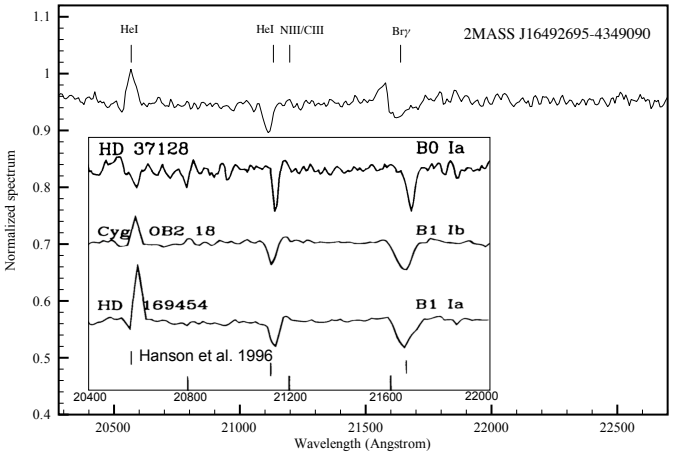

Figure 3.14: K_s spectrum for 2MASS J16492695–4349090, the infrared counterpart of IGR J16493–4348. The positions of identified spectral features are marked by solid lines.

feature in supergiant stars and it is observed in emission in B type supergiants. The He I 21 126 line is present in late O - early B spectra. By visually comparing the relative strength of the identified lines with those from the atlas of Hanson et al. (1996), we estimated the spectral type to B0.5 Ib, with an uncertainty of one subtype. Together with information provided by X-ray data (Hill et al. 2008), our results thus permit to classify the system as a neutron star SGXRB.

AX J1841.0–0536

AX J1841.0–0536 was discovered as a violently variable transient by ASCA in April 1994 (Bamba et al. 2001). The source showed multi-peaked flares with a sharp rise. Analysis of the ASCA data revealed that the source is a pulsar with $P_{spin} = 4.7$ s. The spectral fit provided a value of $N_H = 3.2 \times 10^{22}$ cm^{-2} (Bamba et al. 2003). A fast outburst observed by *INTEGRAL* was attributed by Halpern & Gotthelf (2004) to this source.

A Chandra observation of the field revealed the counterpart to be 2MASS 18410043-0535465, a reddened star with weak Hα in emission (Halpern et al.

2004), suggesting it was a Be star. Negueruela et al. (2006), from optical spectroscopy, proposed the star is instead a luminous B0-1 type, although with some uncertainty, classifying the system as an SFXT.

Fig. 3.15 shows the K_s spectrum we obtained, with identified spectral features marked.

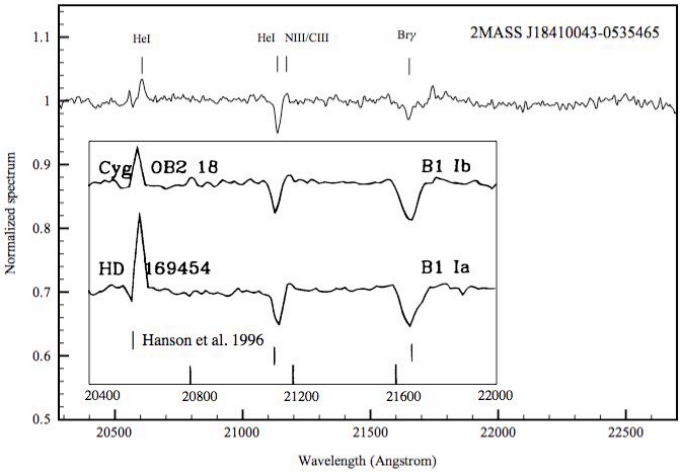

Figure 3.15: K_s spectrum for 2MASS 18410043-0535465, the infrared counterpart of AX J1841.0-0536. The positions of identified spectral features are marked by solid lines.

The spectrum shows He I 20 581 Å emission, accompanied by a spurious feature, possibly due to poor telluric component removal; we observe absorption at He I 21 126, a weak N III (C III) 21 155 Å emission; moreover, there is moderately strong Brγ absorption. The side features of the Brγ absorption profile are probably due to poor telluric correction, but they do not prevent us from measuring the equivalent width.

The observed transitions are typical of an early supergiant, and by comparison with the atlases from Hanson et al. (1996, 2005a), we can conclude that the star is of B1 Ib type. Together with X-ray properties, this NIR spectral classification allows us to confirm the nature of the system as an SFXT.

4U 1907+09

The wind-accreting system 4U 1907+09 (Giacconi et al. 1971) is a known HMXB consisting of a neutron star in an eccentric ($e = 0.28$) 8.3753 day orbit around its companion, which has been optically identified as a highly reddened star (Schwartz et al. 1980). The spectral classification of the counterpart to 4U 1907+09 has been matter of debate. The presence of X-ray flaring seen twice per neutron star orbit (Marshall & Ricketts 1980) had led some authors (e.g. Makishima et al. 1984; Cook & Page 1987; Iye 1986) to the hypothesis of a Be star companion. However, this classification would require a distance of <1.5 kpc, which is in contradiction with the significant interstellar extinction measured in optical observations by van Kerkwijk et al. (1989), who also classified the counterpart as a B supergiant. Using interstellar atomic lines of Na I and K I, Cox et al. (2005) set a lower limit of 5 kpc for the distance and proposed that the stellar companion is instead a O8-O9 Ia supergiant with an effective temperature of 30 500 K, a radius of 26 $R_\odot$, a luminosity of 5×10^5 $L_\odot$, and a mass loss rate of 7×10^{-6} $M_\odot$ yr^{-1}.

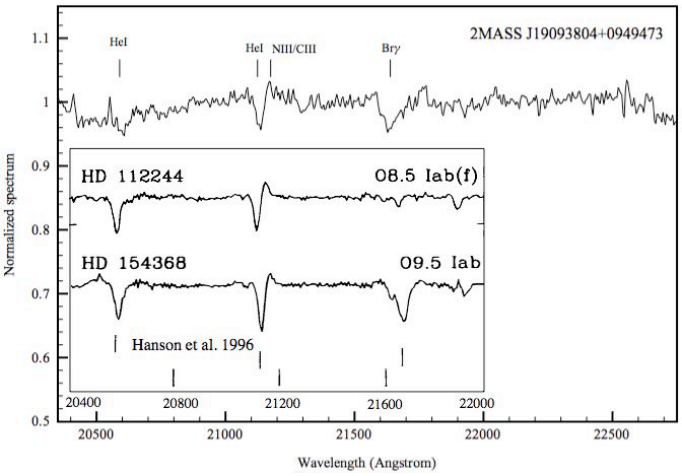

Figure 3.16: K_s spectrum for 2MASS J19093804+0949473, the infrared counterpart of 4U 1907+09. The positions of identified spectral features are marked by solid lines.

Similarly to other accreting neutron stars, the X-ray continuum of 4U 1907+09

can be described by a power-law spectrum with an exponential turnover at 13 keV. The spectrum is modified by strong photoelectric absorption with a column density $N_H = 1.5 - 5.7 \times 10^{22}$ cm^{-2} (e.g. Cook & Page 1987).

We show for the first time an infrared spectrum of the source, which permits us to confirm the spectral classification as estimated from optical data. Fig. 3.16 presents the K_s spectrum we obtained, with identified spectral features marked. The spectrum shows He I absorption both at 20 580 Å and at 21 126 Å, a weak N III (or C III) emission line at 21 155 Å and strong Brγ absorption (EW $<$ 4 Å), the typical features of an early supergiant. The presence of He I 20 580 in absorption strongly constrains the spectral type to a late O star. By visual comparison with the atlases from Hanson et al. (1996, 2005a), especially from the relative ratio between the He I and Brγ features, we conclude that the star is an O9.5 Iab. We thus confirm and refine the previous spectral classification.

IGR J19140+0951

The *INTEGRAL* discovery of this source was reported by Hannikainen et al. (2003). Observations with the Rossi X-Ray Timing Explorer (RXTE) revealed a rather hard spectrum, fitted with a power law of photon index 1.6 and an absorption column density of $N_H = 6 \times 10^{22}$ cm^{-2} (Swank & Markwardt 2003). Timing analysis of the RXTE All-Sky Monitor (ASM) data showed an X-ray period of 13.55 days (Corbet et al. 2004).

Hannikainen et al. (2004) presented high energy spectral analysis of the period of the discovery, concluding that the source manifests two distinct spectral behaviors, the first showing a thermal component in the soft X-ray and hard X-ray tail, the second being harder and possibly originating from thermal Comptonization. This second, low-luminosity, behavior was confirmed to be the preferred state of the source (Rodriguez et al. 2005).

The optical/infrared counterpart to IGR J19140+0951 was identified by in't Zand et al. (2006), from Chandra accurate position determination, as the heavily reddened 2MASS 19140422+0952577.

Fig. 3.17 shows the K_s spectrum we obtained, with identified spectral features

marked.

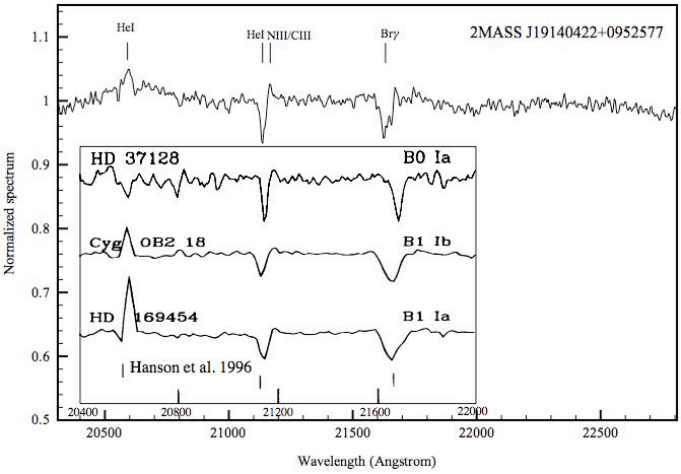

Figure 3.17: K_s spectrum for 2MASS J19140422+0952577, the infrared counterpart of IGR J19140+0591. The positions of identified spectral features are marked by solid lines.

The spectrum shows He I 20 581 Å emission, absorption at He I 21 126 Å, a weak N III (or C III) emission feature at 21 155 Å, and moderately strong Brγ absorption, typical features of an early supergiant. By visual comparison with the atlases from Hanson et al. (1996, 2005a), we can conclude that the star is a B0.5 Iab type. Together with X-ray properties, this allows us to confirm the nature of the system as an SGXRB.

Our preliminary results were published in Nespoli et al. (2007), and later confirmed by Hannikainen et al. (2007), who, from K- and H-band spectra, constrained the spectral type to a B0.5 supergiant. They also estimated the distance of the source as 5 kpc.

3.4.2 Reference spectra of Be stars

In this section we report on the spectra obtained from four isolated classical Be stars, and also included a supergiant B star showing emission lines. As mentioned before, these objects are well known and their study is not part of the scientific

objective of this project. They are almost all very bright objects, and data were taken in bad transparency conditions, in order to have reference spectra for the classification of the proposed IR counterparts to HMXBs in case a Be star was found. Fig. 3.18 illustrates the spectra and marks the identified spectral features.

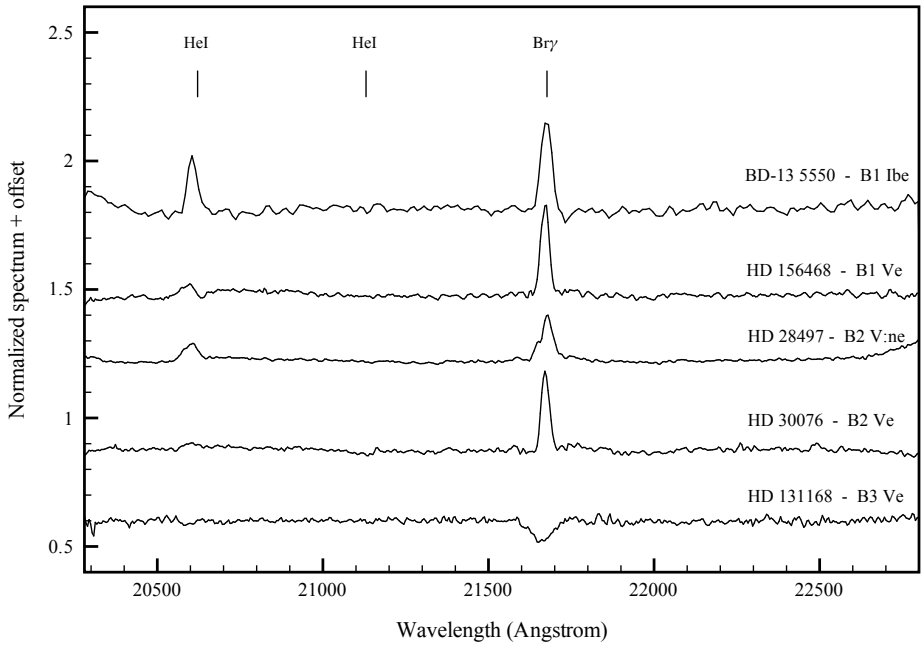

Figure 3.18: K_s-band spectrum for four classical Be-stars (first four spectra from the bottom) and one supergiant B star showing emission lines (first spectrum from the top). The positions of identified spectral features are marked by solid lines.

We will now analyze the variation of the observed features on the basis of both temperature and luminosity.

The spectra show hydrogen and helium lines, typical features of OB types. The 21 660 Brγ line is in emission in the earliest both supergiant and Be stars (first 4 spectra from the top in Fig. 3.18).

For Be stars, the known general trend of stronger Brγ emission at earlier spectral types was explained with simulations of the infrared spectrum of ψ Per (Marlborough et al. 1997). It was shown that the strenght of Brγ is very sensitive

to both changes in disc temperature and density (and the radial gradients of these parameters). For the near infrared hydrogen lines, a decrease in disc temperature in general leads to a decrease in the line emission. Firstly, the source function of the line, taken to be the Planck function, decreases with temperature. Also, the temperature dependent factors in the disc opacity term (Equation (5) in Marlborough et al. 1997) cause the opacity to increase with decreasing temperature for the majority of the disc. Therefore both effects combine to reduce the line emission from the disc as the temperature decreases. Since the disc temperature is likely to be a function of stellar temperature, a reduction in line emission from early to late stars is expected.

In HD 131168 we observe instead Brγ in absorption: the object could have been misclassified and correspond to a B star, or alternatively, since the Be phenomenon is known to be variable it may simply mean that this object have undergone a phase change from emission to non-emission.

The He I triplet at 21 126 Å is seen in the late-O and early-B stars. The individual features in this triplet are not detectable at our resolution, and the line is apreciable just in the only early B supergiant (BD 135550). The main He I singlet line at 20 581 Å, which is a strong transition, is very weak or absent in the main-sequence (dwarf and giant) stars, while it becomes prominent in emission or both in emission and in absorption in the supergiant stars and thus is an important tracer of stars with extended atmospheres. The line is also known to vary with respect to the spectral type, being confined to stars earlier than B2.5. In fact the two requirements for this line to be produced in emission are a large ionizing flux and a dense circumstellar environment, characteristic of the earliest types.

3.4.3 Reddening and distance estimation

From the identified spectral types, we obtained the intrinsic colors $(J-K)_0$ from Wegner (1994); we then calculated, from 2MASS photometry, the instrumental colors $(J-K)_{2MASS}$, properly transformed through the formula from Carpenter

(2001) [3] to the Bessell & Brett (1988) homogenized photometric system in order to estimate the infrared color excess $E(J-K)$. Assuming the mean extinction law ($R_V = 3.1$), from $A_V/E(J-K) = 5.82 \pm 0.10$ (Rieke & Lebofsky 1985), we obtained the total measured visual extinction A_V and the corresponding hydrogen column density value from $N_H/A_V = 1.79 \pm 0.03 \times 10^{21}$ atoms cm^{-2} mag (Predehl & Schmitt 1995). We were thus able to compare the retrieved interstellar value of N_H with the one provided by X-ray data. In our calculation, we estimated errors through error propagation. Errors in the final values of N_H are mainly due to errors in the infrared colors and the transformation between the two photometric systems.

We also estimated the distance of the seven sources, applying the relation $M_K = K + 5 - 5 \log d - A_K$. For each source, M_V was obtained from our proposed spectral type (Wegner 2006), the intrinsic color index $(K-V)_0$ from Wegner (1994) was used in order to calculate M_K, and the 2MASS K magnitude was employed. We derived A_K from the relation $A_\lambda/E(J-K) = 2.4(\lambda)^{-1.75}$, for $\lambda = 2.2$ μm (Draine 1989).

The results of our calculations are given in Table 3.4, together with some crucial quantities used in the calculations or displayed for comparison.

The distance estimation is mainly affected by the uncertainty in the value of the absolute magnitude M_V, which is due to two contributions, the errors given in the tabulated values of M_V and the uncertainty in the spectral classification, from which the absolute magnitude is determined. The largest role is played by the errors in the mean tabulated values themselves (see Wegner 2006 for more details). The retrieved values for d must thus be assumed with prudence.

3.5 Discussion

Using near-infrared spectroscopy of seven high-energy sources, IGR J16207–5129, IGR J16465–4507, IGR J16479–4514, IGR J16493–348, AX J1841.0–0536, 4U 1907+097 and IGR J19140+0951, we classified their counterparts through comparison with published atlases. We found that all the observed systems have a

[3] In its updated version at http://www.astro.caltech.edu/~jmc/2mass/v3/transformations/

supergiant companion. Our results, combined with information from X-ray data, allow for the first time to firmly include one source, IGR J16479–4514, in the newly discovered class of the SFXTs. Moreover, we can confirm with infrared data the identification of IGR J16465–4507 and AX J1841.0–0536 as SFXTs, as recently proposed by Negueruela et al. (2007) from optical spectra.

From our spectral classification, we estimated the distance of the seven sources. The retrieved values are consistent with the location of the sources in the Norma (IGR J16207–5129, IGR J16465–4507, IGR J16479–4514, IGR J16493–4348), Scutum (AX J1841.0–0536) and Sagittarius arm (4U 1907+097 and IGR J19140+0951) regions respectively. This determination, although affected by some uncertainty, can be considered an *a posteriori* confirmation of the proposed spectral classification.

This work allowed us to calculate the extinction from IR data for the seven systems. Recently, it has been pointed out (see Kuulkers 2005; Chaty 2007) that *INTEGRAL* is revealing two new classes of supergiant HMXBs, the highly obscured HMXBs and the SFXTs. The first ones are characterized by strong intrinsic absorption, the second by strong and short X-ray outbursts. High, variable, hydrogen column densities have in some cases been measured for SFXTs (e.g. IGR J11215–5952: Smith et al. 2006a; IGR J17391–3021: Smith et al. 2006b), suggesting a possible intrinsic absorption for this class as well, and marking a potential overlap between the two new classes. The origin and position (around the compact object only, or enveloping the entire system) of the absorbing material are still a matter of debate, and only multiwavelength studies are able to address the problem, distinguishing between the absorption in X-ray and in the IR/optical bands. We calculated the effective interstellar extinction A_V and converted it into hydrogen column density N_H. Our results can be compared with the values obtained from X-ray data. If the two retrieved values are compatible within the corresponding errors, we face two possible scenarios: either the source of absorption is just the interstellar medium or there is a contribution from an extensive envelope around the whole binary system, if the extinction shows an excess of some orders of magnitude with respect to the estimated IS value. Conversely, if the reddening (measured from the IR colors) is low for the measured

N_H from X-rays, this reveals the presence of an additional source of extinction, which only affects the compact object in which the X-ray emission originates, and that can be regarded as the presence of absorbing material around it.

In our case, the comparison reveals that for four systems, IGR J16465–4507, IGR J16479–4514, AX J1841.0–0536 and IGR J19140+0951, the extinction measured at high energy shows an excess of one or two orders of magnitude with respect to that obtained from IR data, probing that the material absorbing the X-rays is concentrated around the neutron star. Our result is consistent with the detection of the Fe fluorescence line at 6.4 KeV in the X-ray spectra of all the four sources (Walter et al. 2006; Bamba et al. 2001; Rodriguez et al. 2005), which is considered a signature of a dense spherical envelope around the compact object.

Usually, the so called highly absorbed IGR sources are identified from their measured N_H being $\gtrsim 10^{23}$ cm^{-2}, i.e. one to two orders of magnitude higher than the assumed Galactic value of $\sim 10^{22}$ cm^{-2} (Kuulkers 2005). The comparison of X-ray data, which are sensitive to the absorption from the environment of the compact object, with infrared data, which are in general only absorbed by the interstellar medium, can be a strong and alternative criterion to recognize this class of highly absorbed sources. In particular, all the three identified SFXTs show strong intrinsic absorption from circumstellar material, reported as well for other members of this new class (e.g. Negueruela et al. 2006; Pellizza et al. 2006), and so emerging as a common feature of the group. This scenario is relevant to discussions about the physical mechanism, still unknown, which powers the fast outbursts that these sources undergo. Together with their X-ray fast transient nature, the high intrinsic absorption can be regarded as one of the reasons why this class has remained undiscovered until only recently.

A more complete, multiwavelength investigation is necessary to reveal the nature of these systems, especially if it is able to find and physically describe correlations between their X-ray behavior and IR properties. In the case of SFXTs this is possibly the only way to explore the physical mechanism driving the fast outbursts.

3.6 Conclusions

From near-infrared spectroscopy of the seven high-energy sources, we have found that:

- the proposed optical counterparts were confirmed and the spectral classification of the sources provided; all the sources were classified as HMXBs;
- one source, IGR J16479–4514, was added to the SFXTs and the confirmation of IGR J16465–4507 and AX J1841.0–0536 as members of the class was proven with infrared data;
- the comparison between N_H obtained from X-ray data and interstellar extinction from our data showed for four systems (IGR J16465–4507, IGR J16479–4514, AX J1841.0–0536 and IGR J19140+0951) the presence of an absorbing envelope, strictly confined around the compact object;
- all the three identified SFXTs are intrinsically absorbed, suggesting that this might be a characteristic of the class;
- the distance estimation, compatible with the location of the sources in the respective galactic arms, is a possible confirmation of the spectral classification provided here.

Results from this study were partly published in Nespoli et al. (2008b).

Table 3.2: Journal of observations for the spectra analyzed in this work. We report in the fourth column the net accumulated exposure time. Column five gives the obtained signal-to-noise ratio. The references listed in the last column relate to the identification of the optical/infrared counterpart. The first lines refer to SOFI/NTT spectra; the last line refers to the ISAAC/UT1 spectrum.

Source	K mag	Start time (UT)	Exp. (s)	S/N	R ($\lambda/\Delta\lambda$)	IR counterpart	Reference
IGR J16207–5129	9.1	2006-07-14 23:19	600	100	1320	2MASS J16204627-5130060	Tomsick et al. (2006)
IGR J16465–4507	9.8	2007-05-26 05:03	240	100	1320	2MASS J16463526-4507045	Zurita & Walter (2004)
IGR J16479–4514	9.8	2007-05-26 05:11	240	100	1320	2MASS J16480656-4512068	Kennea et al. (2005)
AX J1841.0–0536	8.9	2006-07-14 03:57	600	180	1320	2MASS J18410043-0535465	Halpern et al. (2004)
4U 1907+097	8.8	2006-07-15 07:37	600	130	1320	2MASS J19093804+0949473	Schwartz et al. (1980)
IGR J19140+0951	7.1	2006-07-14 04:46	360	130	1320	2MASS J19140422+0952577	in't Zand et al. (2004)
BD–13 5550	10.8	2006-07-15 08:44	600	120	588	–	–
HD 28497	6.6	2006-07-15 10:09	80	250	1320	–	–
HD 30076	5.5	2006-07-15 10:23	80	180	1320	–	–
HD 131168	11.7	2006-07-15 01:01	180	150	1320	–	–
HD 156468	6.8	2006-07-15 01:23	120	230	1320	–	–
IGR J16493–4348	11.9	2007-04-05 09:38	360	150	500	2MASS J16492695-4349090	Kuiper et al. (2005)

Table 3.3: K_s-band line identifications and spectral classification of the seven objects analyzed in this work: for each target spectrum, the observed wavelength, the corresponding EW and our proposed classification are reported. Positive EWs refer to features in absorption.

	He I ($2s^1S$ - $2p^1P^0$) 20 581 Å		C IV ($3p^2P^0$ - $3d^2D$) 20 690, 20 780, 20 830 Å		He I ($3p^3P^0$ - $4s^3S$), 21 120 Å + HeI ($3p^1P^0$ - $4s^1S$), 21 130 Å		N III (C III) 21 155 Å		Brγ 21 661 Å		Spectral
Object	Wavelength [Å]	EW [Å]	Wavelength [Å]	EW [Å]	Wavelength [Å]	EW [Å]	Wavelength [Å]	EW [Å]	Wavelength [Å]	EW [Å]	classification
IGR J16207–5129	20 595	-2.90	–	–	21 134	1.23	–	–	21 642	3.52	B1 Ia
IGR J16465–4507	20 589	2.72	20 730	-0.42	21 128	2.31	–	–	21 654	3.25	O9.5 Ia*
IGR J16479–4514	20 570	3.10	–	–	21 123	1.23	21 162	-0.39	21 640	1.39	O9.5 Iab*
IGR J16493–4348	20 571	-4.02	–	–	21 112	1.90	21 149	-0.20	21 655	2.68	B0.5 Ib
AX J1841.0–0536	20 599	-0.94	–	–	21 135	1.64	21 171	-0.23	21 652	1.89	B1 Ib*
4U 1907+09	20 602	1.12	–	–	21 130	1.84	21 170	-0.25	21 641	3.19	O9.5 Iab
IGR J19140+0951	20 591	-1.38	–	–	21 136	1.56	21 167	-0.33	21 632	1.86	B0.5 Iab

* Systems classified through this work as new or confirmed SFXTs.

Table 3.4: Summary of the spectral analysis and extinction calculations for the seven objects studied in this work. For each observed source in the first column, the obtained spectral classification, intrinsic infrared colors, 2MASS photometry, calculated infrared excess, hydrogen column density obtained from X-ray published measurements, effective interstellar column density obtained from our work and distance estimation are reported. See text for corresponding references.

Source	Spectral type	$(J-K)_0$ [mag]	$(J-K)_{2MASS}$ [mag]	$E(J-K)$ [mag]	N_H from X-ray data [10^{22} cm^{-2}]	Interstellar N_H [10^{22} cm^{-2}]	Distance [kpc]
IGR J16207–5129	B1 Ia	-0.12	1.31	1.43	$3.7^{+1.4}_{-1.2}$	1.53 ± 1.02	6.1 (-3.5, +8.9)
IGR J16465–4507	O9.5 Ia	-0.15	0.69	0.84	72 ± 6	0.87 ± 0.56	9.5 (-5.7, +14.1)
IGR J16479–4514	O9.5 Iab	-0.14	3.19	3.33	12 ± 4	3.47 ± 2.16	2.8 (-1.7, +4.9)
IGR J16493–4348	B0.5 Ib	-0.12	2.66	2.81	5.4	2.92 ± 1.96	15.3 (-9.0, +11.0)
AX J1841.0–0536	B1 Ib	-0.13	0.80	0.93	3.2	0.97 ± 0.64	3.2 (-1.5, +2.0)
4U 1907+097	O9.5 Iab	-0.14	1.22	1.36	1.7 – 5.7	1.42 ± 0.90	3.0 (-1.9, +5.1)
IGR J19140+0951	B0.5 Iab	-0.12	1.50	1.62	$\sim 6^a$	1.68 ± 1.5	1.1 (-0.8, +2.3)

[a] A maximum value of $10.1 \pm 0.2 \times 10^{22}$ cm^{-2} was reported by Rodriguez et al. 2005.

There's real poetry in the real world. Science is the poetry of reality.

Richard Dawkins

4

K-band spectroscopy of two INTEGRAL sources reveals two new SyXBs

4.1 Symbiotic X-ray binaries

Low-mass X-ray Binaries (LMXBs) are interacting systems constituted by an accreting compact object and a low-mass (typically ≤ 1 $M_{\odot}$) main-sequence or slightly evolved late-type star. Recently, a new sub-class of LMXBs is emerging, in which the secondary is an M-type giant. This rare class of systems was named Symbiotic X-ray Binaries (SyXBs) after Masetti et al. (2006b) by analogy with symbiotic binaries, in which a white dwarf accretes matter from an M giant companion, either from the wind of the M star or via Roche-lobe overflow. At present, only six X-ray sources are known to belong to this subclass: GX 1+4 (Davidsen et al. 1977; Chakrabarty & Roche 1997), 4U 1700+24 (García et al. 1983; Masetti et al. 2002), 4U 1954+319 (Masetti et al. 2006b; Mattana et al. 2006), Scutum X-1 (Kaplan et al. 2007), IGR J16194-2810 (Masetti et al. 2007) and 1RXS J180431.1-273932 (Nucita et al. 2007). See Masetti et al. (2007), Table 3, for a summary of the main properties of the first 5 SyXBs; see Nucita et al. (2007) for the last discovered one.

The increasing number of systems with an evolved giant donor makes this subclass an emerging evolutionary channel of X-ray Binaries. Moreover, they have

been proposed as the probable progenitors of most wide-orbit LMXBs (Chakrabarty & Roche 1997).

4.2 IGR J16358-4726 and IGR J16393-4643

During our campaign of spectroscopic observations of IR counterparts to HMXBs (see Chapter 3), we took data of IGR J16358-4726 and IGR J16393-4643, two supposed HMXBs.

IGR J16358-4726 was discovered by Revnivtsev et al. (2003), then serendipitously observed by Chandra that located the source at RA = $16^h35^m53.8^s$, DEC = -47°25′41.1″, with an accuracy of 0.6″ (Kouveliotou et al. 2003). This allowed them to suggest an infrared counterpart, 2MASS J16355369-4725398. Subsequent astrometry performed by Chaty et al. (2008), although stating that the 2MASS object is 1.2″ from the Chandra detection, resulted in substantiating it as the actual counterpart, mainly because of its brightness (J = 15.41 mag, H = 13.44 mag, K = 12.59 mag).

The X-ray source was identified as a transient, and its spectrum fitted with a power law with spectral index $\Gamma \sim 0.5$, hydrogen column density $N_{\rm H} \sim 3.3 \times 10^{23}$ cm^{-2} and a FeKα fluorescence line at 6.4 keV (Patel et al. 2007). Periodic variations of 5880 ± 50 s were found by Patel et al. (2004), then confirmed by several authors (Lutovinov et al. 2005; Mereghetti et al. 2006). From accurate spectral and timing analysis of multi-satellite data, Patel et al. (2007) argued the neutron star nature of the source, estimating the magnetic field between 10^{13} and 10^{15} G if the retrieved spin up was due to disk accretion, and thus proposed that the object might be a magnetar. The source is thought to be located in the Norma Galactic arm, at a distance of 5–6 kpc or 12–13 kpc, depending on which crossing of the arm with the line of sight is chosen (Lutovinov et al. 2005). From NIR spectroscopy, Chaty et al. (2008) suggested that the system is a HMXB, showing that the counterpart might be a sgB[e] star since the detection of H Brackett series, He I and He II absorption lines and the presence of a forbidden [FeII] line at 2.22 μm. This result was then corroborated by Rahoui et al. (2008) through SED fitting.

IGR J16393-4643 was first discovered by the *ASCA* satellite (Sugizaki et al. 2001) and listed as AX J16390.4-4642. It was later detected by *INTEGRAL* during the first Galactic Plane Scan (Malizia et al. 2004).

Subsequent observations with *XMM-Newton*/EPIC derived an improved position (RA = $16^h39^m05.4^s$, DEC = $-46°42'12''$) that allowed Bodaghee et al. (2006) to identify 2MASS J16390535-4642137 as the most probable counterpart to the source. The X-ray spectrum was fitted with a highly absorbed ($N_{\rm H} = 2.5 \times 10^{23}$ cm^{-2}) power law ($\Gamma = 0.8 \pm 0.2$); together with the discovery of a pulse period of 912.0 ± 0.1 s, this led to conclude that the source is an X-ray pulsar (Bodaghee et al. 2006). Thompson et al. (2006, hereafter T06) used *RXTE* data to carry out pulse timing analysis in order to determine the orbital parameters of the system. They obtained three mathematical solutions, among which the most plausible one indicated, with an orbital period of 3.7 days and a mass function of 6.5 ± 1 $M_\odot$, that the system would be a HMXB. The other two solutions foresaw the following parameters: an orbital period of 50.2 days together with a mass function of 0.092 $M_\odot$ and an orbital period of 8.1 days with a mass function of 221 $M_\odot$; both of them were rejected by the authors because they are statistically and physically weaker. Chaty et al. (2008) obtained accurate astrometry and photometry of the field of IGR J16393-4643, finding three more candidate counterparts, although their lower NIR brightness seemed to favor the 2MASS object. They also performed SED fitting of optical to MIR observation, inferring a BIV-V spectral type for the companion.

In this chapter we present K-band spectroscopy of the proposed counterparts to the two X-ray systems. In the case of IGR J16393-4643, ours is the first available IR spectrum; in the case of IGR J16358-4726, ours is the first IR spectrum beyond 2.3 μm, covering a range that is crucial, as our analysis will show, for the spectral classification of the star. We will show the need for a new classification of the counterparts, which implies a new classification of the systems as SyXBs, if the proposed counterparts are the actual ones.

4.3 Observations and data reduction

The two proposed counterparts to the X-ray sources were observed in service mode on 2007 April 5 with the ISAAC spectrograph (Moorwood et al. 1998b) on UT1 at ESO/Paranal observatory. The optical layout of ISAAC is shown in Fig. 4.1. At the top and bottom are two cameras which are optimized for the 1–2.5 μm and 2–5 μm ranges and used to either re-image the telescope focal plane or the intermediate spectrum produced by the grating spectrometer. Data were taken in the Short Wavelength - Low Resolution mode, with a pixel scale of 0.147″/pixel and a resolution of 500.

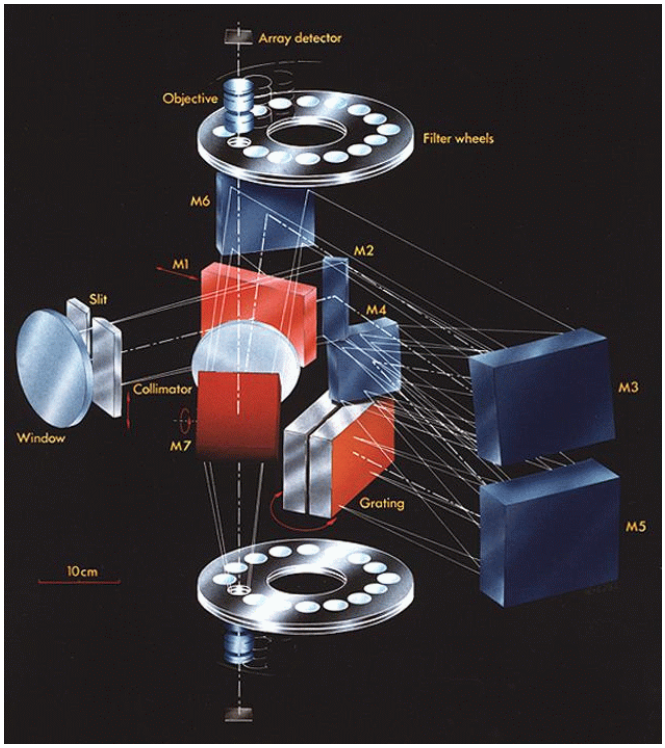

Figure 4.1: ISAAC optical layout.

The sky was clear during the observations, the seeing was $\leq$ 1.4″ and the

targets were observed at airmass 1.08 and 1.09 respectively. Table 4.1 reports the observation log, including the retrieved signal-to-noise ratio (S/N). Typical on-source integration times for standard stars were between 6 and 10 seconds.

Table 4.1: ISAAC/VLT journal of observations. We report in the fourth column the net accumulated exposure time. Column five gives the obtained signal-to-noise ratio. The references listed below the table relate to the identification of the optical/infrared counterpart.

Source	K mag	Start time (UT)	Exp. time (s)	S/N	IR Counterpart
IGR J16358-4726	12.6	2007-04-05 08:26	480	120	2MASS J16355369-4725398[1]
IGR J16393-4643	12.8	2007-04-05 08:56	1280	160	2MASS J16390535-4642137[2]

References:
[1] Kouveliotou et al. (2003), [2] Bodaghee et al. (2006)

Data reduction was performed using the IRAF package, following the standard procedure for IR spectra (see also Chapter 3). We first corrected for the inter-quadrant row cross-talk, then applied sky subtraction; we employed dome flat-fields, extracted and rectified the one dimensional spectra. Wavelength calibration was accomplished using Xenon and Argon lamp spectra. Spurious features, such as cosmic rays or bad pixels, were removed by interpolation, when necessary. The reduced spectra were normalized by dividing them by a fitted polynomial continuum. Standard telluric stars were observed at very small differences in airmass (differences of 0.008 and 0.007 airmasses were accomplished for IGR J16358-4726 and IGR J16393-4643 respectively). Correction of telluric absorption lines was performed as described in Cap. 3.

4.4 Results

4.4.1 Spectral classification

In this section we present the results of spectral analysis and classification for the two targets, based on the comparison with available NIR spectral atlases. The spectra are shown in Figs. 4.2 and 4.3, while their most remarkable features are reported in Table 4.2. The two spectra are in fact very similar, being their most prominent features the series of strong CO absorption bands between 2.29 and

2.40 μm, which are characteristic of late-type stars.

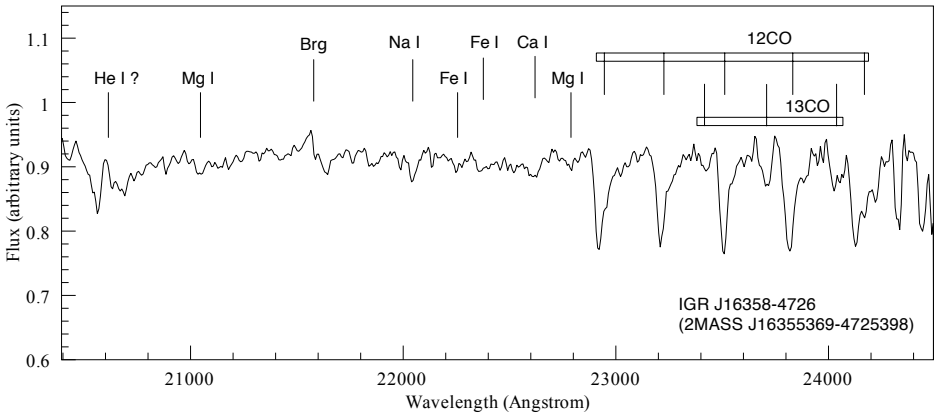

Figure 4.2: K-band spectrum of 2MASS J16355369-4725398, the infrared counterpart to IGR J16358-4726. The positions of identified spectral features are marked by solid lines.

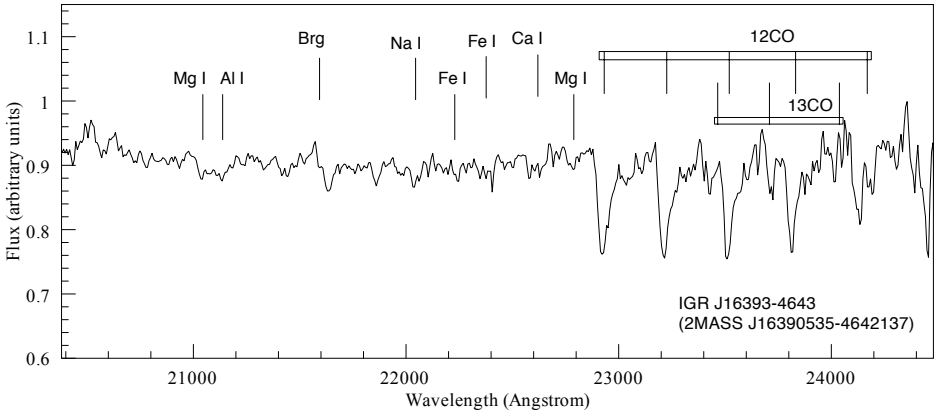

Figure 4.3: K-band spectrum of 2MASS J16390535-4642137, the infrared counterpart to IGR J16393-4643. The positions of identified spectral features are marked by solid lines.

Several metallic lines are clearly recognizable as well, although at our resolution they are generally blended. Although weaker than the CO bands, they appear significative within the retrieved errors. We also tentatively propose the

presence of He I 20 581 Å and Brγ in faint emission in both spectra; since they are not a proper spectral feature of late-type stars, these lines might be the signature of an accretion disk around the compact object. However, they are very weak, and we cannot discard they might be a residual artifact from the telluric lines removal procedure, which in this region is very critical. This interpretation would be supported by the P-Cygni like profile of the Brγ line, identical in the two spectra. In any case, emission features typical of HMXBs seem not to be present in nearly any of the optical spectra of SyXBs (e.g. Masetti et al. 2006b, 2007). The reason of this is the high total luminosity of such evolved giant companions, that would overwhelm the light derived from the reprocessing of X-ray irradiation.

Table 4.2: K-band line identifications for IGR J16358-4724, denoted by (I), and IGR J16393-4643 (II).

Feature	Transition	Wavel. (Å)	EW_I (Å)	EW_{II} (Å)
He I	$2s^1S - 2p^1P^o$	20 581	-1.8±0.4	–
Mg I	$4f^3F_{2,3,4} - 7g^3G^o_{3,4,5}$	21 066	0.8±0.2	1.6±0.3
Al I	$4p^2P^o_{1/2} - 5s^2S_{1/2}$	21 099	–	1.8±0.3
Brγ	$4^2F^o - 7^2G$	21 661	-2.8±0.2	-0.9±0.2
Na I	$4s^2S_{1/2} - 4p^2P^o_{1/2}$	22 100	1.9±0.4	2.0±0.8
Fe I	$x^5F^o_3 - e^5D_2$	22 263	1.6±0.2	0.8±0.2
Fe I	$x^5F^o_4 - e^5D_3$	22 387	1.2±0.4	1.1±0.4
Ca I	$4d^3D_{3,2,1} - 4f^3F^o_{4,3,2}$	22 636	1.4±0.4	1.1±0.4
Mg I	$4d^3D_{3,2,1} - 6f^3F^o_{2,3,4}$	22 800	2.7±0.5	1.6±0.4
^{12}CO	(2, 0) bandhead	22 900	9.9±0.3	11.9±0.4
^{12}CO	(3, 1) bandhead	23 226	13.0±0.6	12.9±0.6
^{13}CO	(2, 0) bandhead	23 448	2.5±0.4	2.5±0.8
^{12}CO	(4, 2) bandhead	23 524	7.8±0.4	9.8±0.3
^{13}CO	(3, 1) bandhead	23 739	4.2±0.2	4.5±0.8
^{12}CO	(5, 3) bandhead	23 829	12.8±0.6	8.05±0.7
^{13}CO	(4, 2) bandhead	24 037	3.6±0.5	1.98±0.3
^{12}CO	(6, 4) bandhead	24 156	10.1±0.8	7.0±0.4

Our ISAAC spectra clearly point to a late-type nature of both objects, and exclude that the systems are HMXBs with OB companions. From the identified

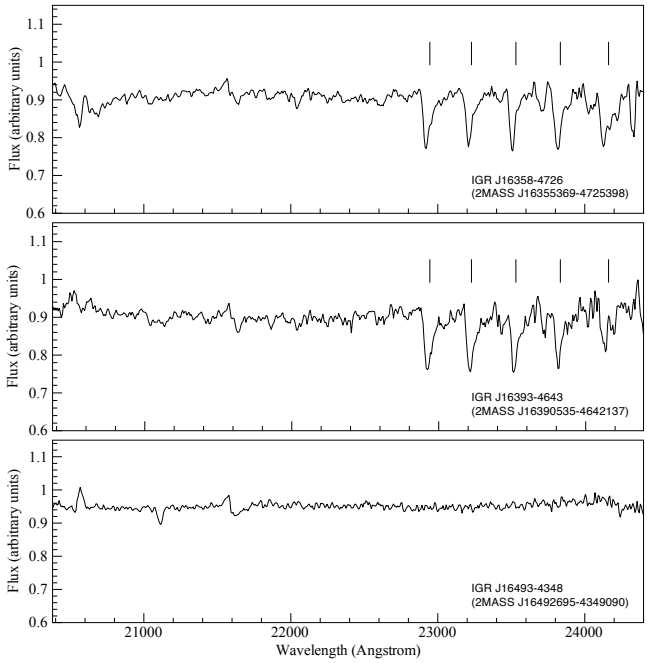

Figure 4.4: Comparison among the obtained K-band spectra of IGR J16358-4726 (upper panel), IGR J16393-4643 (medium panel) and IGR J16493-4348 (bottom panel). The three targets were observed in the same night under the same telescope/instrument configuration. Data reduction was performed in the same way. ^{12}CO absorption bands ($\lambda \geq 22\,900$ $\AA$) are marked in the two first panels from the top. These deep absorption features, typical of late-type stars, are completely absent in the spectrum of IGR J16493-4348, that was in fact classified as SGXB (Nespoli at al. 2010b).

spectral lines, our conclusion is that both stars are of K or M spectral type (see, for instance, Kleinmann & Hall 1986; Förster Schreiber 2000; Ivanov et al. 2004, for a comparison with atlases of cold stars). The forbidden [Fe II] transition at 22 200 Å detected in IGR J16358-4726 by Chaty et al. (2008) is not present in our spectrum. The faintness and very high absorption of the low-resolution spectrum from Chaty et al. (2008) might have led to that spurious detection. The general morphology of the spectra and the comparison between the relative strength of CO 22 900 Å and both Na I and Ca I lines, which are luminosity indicators (Ramírez et al. 1997), reveal that both stars are giants. In particular, from the empirical

relation EW(CO) vs. $T_{\rm eff}$ those authors found, our EW(^{12}CO(2, 0)) points to a K giant classification for both objects, with retrieved nominal values of $T_{\rm eff} \sim 4400$ K for IGR J16358-4726 and $T_{\rm eff} \sim 4250$ K for IGR J16393-4643.

We believe that the level of precision reachable in our spectral classification cannot be higher than this, because the strongest $T_{\rm eff}$ indicators in the NIR domain are found in the J and H bands (Wright et al. 2008). Unfortunately, we have no spectra in these ranges.

In order to corroborate the accuracy of our analysis and to avoid any possible mistaking of CO absorption bands with telluric components, we show in Fig. 4.4 a comparison of the spectra from the two sources described in this work with the spectrum of IGR J16493-4348, a Supergiant X-ray binary we observed in the same night and conditions than the previous ones. We classified the counterpart to IGR J16493-4348 as a B0.5Ib star (Nespoli et al. 2008a, see Chapter 3) and, as one can see, the telluric corrected spectrum of the source shows no trace of the deep absorption features that characterize the spectra which are the subject of this work.

4.4.2 SED fitting

In Figs. 4.5 and 4.6 we present the spectral energy distribution of IGR J16358-4724 and IGR J16393-4643 respectively, in the $\log(\lambda F_\lambda(\lambda)/\lambda_K F_\lambda(K))$ – $\log\ \lambda$ plane, using photometry given by Chaty et al. (2008) and Rahoui et al. (2008). This includes $RIJHK$ plus GLIMPSE 3.6 μm and 4.5 μm bands for both sources; for IGR J16393-4643 also V photometry was available. We built SEDs corresponding to different spectral types, according to intrinsic colors given by Pickles (1998) for optical/NIR bands and by Koornneef (1983) for MIR. In the figures, data are marked by crosses, and fitted SEDs by lines. Photometric data and spectral type distributions are normalized in the K band. The aim of the figures is to illustrate that very different choices of spectral type and reddening produce reasonable fits to the data. In our calculation, we employed the mean extinction law, $R_V = 3.1$ (Rieke & Lebofsky 1985).

We chose to plot a blue supergiant and two red giants as representative examples. We found that, even with slight differences, every spectral type can be fitted to the data by choosing the appropriate value for the extinction. In the case of

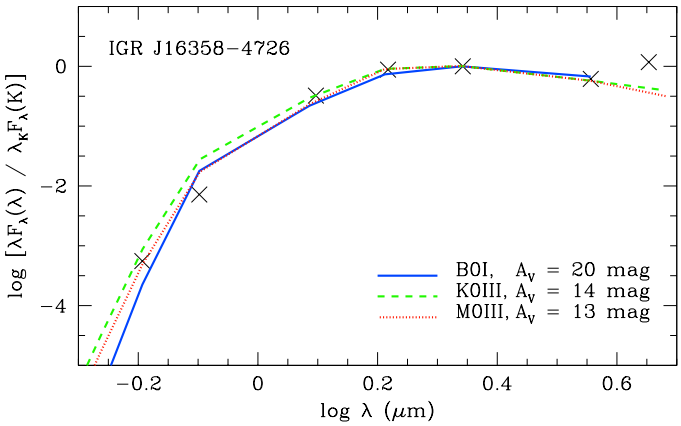

Figure 4.5: Spectral energy distribution of IGR J16358-4724 (crosses) and SED fitting using intrinsic colors for three different spectral types (lines). The errors for the photometric data are within the size of the marks.

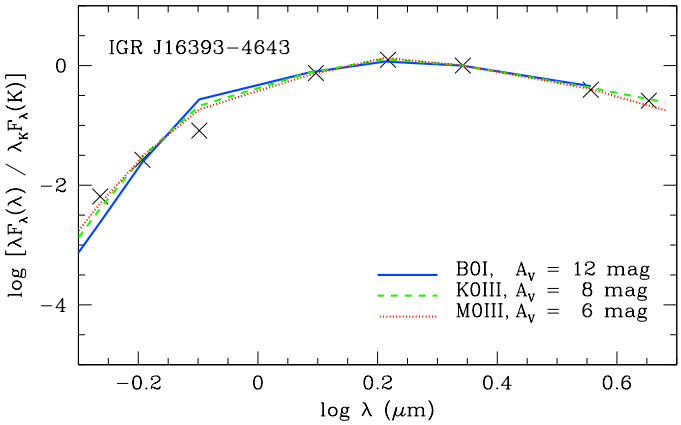

Figure 4.6: Spectral energy distribution of IGR J16393-4643 (crosses) and SED fitting using intrinsic colors for three different spectral types (lines). The errors for the photometric data are within the size of the marks.

IGR J16358-4726, we obtained best fits choosing $A_V = 20$ mag for a B0I type, $A_V = 14$ mag for a K0III type and $A_V = 13$ mag for a M0III type. Analogous results were obtained for IGR J16393-4643, with $A_V = 12$ for a B0I, $A_V = 8$ for a K0III and $A_V = 6$ for a M0III.

The reason why very different spectral types are able to reasonably fit the data must be found in the degeneracy between the direction of the reddening vector and the effective temperature variation in the spectral range we employed, which makes almost every spectral type possible if the opportune extinction value is chosen. Consequently, the results provided by SED fitting do not allow the improvement of the spectral classification. They provide a valuable tool, however, to calculate the interstellar extinction for any assumed spectral type.

In the case of IGR J16393-4643, the low values retrieved for the extinction are in contrast with the high hydrogen column density measured in the X-ray range, namely $N_{\rm H} = 2.5 \times 10^{23}$ cm^{-2}. This could be an indication that the star is not the actual counterpart to the system; another explanation could be the presence of an additional source of extinction intrinsic to the system, which only affects the compact object where the X-ray emission originates. Huge absorption, with $N_{\rm H} \sim 10^{23}$ cm^{-2}, has been observed in other SyXBs, (see, for instance, Mattana et al. 2006).

For the aforementioned spectral types and corresponding extinction value, we calculated the distance from the relation $M_K = K + 5 - 5 \log d - A_K$. In each case, absolute magnitudes and intrinsic color indexes were obtained from Pickles (1998). The estimated distance values were, for IGR J16358-4726: 36.6 kpc (if B0I), 1.4 kpc (if K0III) and 20.1 kpc (if M0III); for IGR J16393-4643: 24.1 kpc (if B0I), 1.0 kpc (if K0III), 13.9 kpc (if M0III). For both sources, a type B0I counterpart would thus result in an unrealistically large value of the distance; the same occurs, for IGR J16358-4726 only, in the case of a M0III companion.

The remaining estimates are compatible with both the classical (four arms, Vallée 2008) and the recently proposed (two main arms, Churchwell et al. 2009) spiral structure models of our Galaxy. A K0I companion would locate both sources in the Sagittarius/Carina inner arm according with the classical model, or the

Sagittarius minor arm, according to the recently proposed one. Finally, a M0III companion for IGR J16393-4643 would imply that the source is placed in the tangential region of the Norma arm with both models.

The error estimation on the distance is mainly affected by the error on the mean absolute magnitude assigned to the spectral type, which can be very large, and can reach more than 50% when propagated to the distance calculation. Moreover, since the retrieved extinction value for each type would also apply to a wide range of subtypes, the consequent distance value range would largely extend. Retrieved distance estimates are thus to be taken with prudence.

4.5 Discussion

From the spectral classification of the proposed counterparts as cold giants or supergiants and from the X-ray features of the systems illustrated in Sect. 4.2, we propose that both of them belong to the class of SyXBs, in which the companion to the neutron star is an evolved late-type star. In the discussion that follows we use the terms giant and supergiant in its physical sense, i.e., related to the mass, internal structure and evolutionary status of the star and not to the luminosity class. As discussed above, a precise determination of the spectral type and luminosity class is difficult from our K-band spectra.

A red giant is the late evolutionary stage of either a low mass star (0.8 to 2.3 $M_{\odot}$) or an intermediate-mass star (2.3 to 10 $M_{\odot}$). The red giant phase includes the shell hydrogen-burning phase (first giant branch), the core helium-burning phase (horizontal branch or "red clump" for low-mass stars, "blue loop" for intermediate-mass stars), and the shell helium-burning phase (asymptotic giant branch). See, for instance, Iben (1974) and Iben & Renzini (1983). Red supergiants are short-lived stages in the late evolution of moderately massive stars (10 to 25 $M_{\odot}$, e.g. Massey et al. 2009; Figer et al. 2006)

In the case of IGR J16358-4724, we classified the proposed counterpart as a K-M giant/supergiant. The evidence that the system houses a neutron star is

strongly supported by the detection of X-ray pulsations (Patel et al. 2004) together with the description of the X-ray energy spectrum by an absorbed power law model plus a high energy cut-off and an Fe line (Patel et al. 2007), which are typical features of neutron stars in galactic X-ray binaries. The designation of 2MASS J16355369-4725398 as counterpart was as well doubly validated in the literature (see Kouveliotou et al. 2003; Chaty et al. 2008). Previous NIR spectroscopy from Chaty et al. (2008) led to a proposal of classification as sgB[e], but, as the authors warned, their NIR spectrum was very faint and extremely absorbed. Moreover, ending at 2.3 μm, it missed the last and most significant portion of the K band, where the presence of CO bands clearly reveals the K-M spectral type of the star. We propose that these factors could lead to a misclassification of the system.

In the case of IGR J16393-4643, our spectrum reveals a K-M giant/supergiant as well. The presence of a pulsar in the binary system is validated both by the spectral shape of the X-ray emission (Bodaghee et al. 2006) and by the finding of pulsations (T06). The optical counterpart we considered is, because of its magnitude, the most probable one among the four objects falling in the error circle of the X-ray detection.

According to T06, IGR J16393-4643 has an orbital period of 3.7 days and a mass function of 6.5 $M_\odot$ (orbital solution 1 in T06). It seems unlikely that an intermediate-mass red giant can fit in such a narrow orbit. To check this, we will use the physical parameters of a 7 $M_\odot$ star along its evolutionary track given by Schaller et al. (1992).

The size of the Roche lobe of a star in a binary system is usually characterized by the *Roche lobe radius* R_L, defined as the radius of a sphere which has the same volume as the Roche lobe. To calculate the Roche lobe radius, we used the Eggleton (1983) approximation:

$$\frac{R_L}{a} = \frac{0.49\ q^{2/3}}{0.6\ q^{2/3} + \ \ln\ (1 + q^{1/3})}\ , \tag{4.1}$$

where a is the semimajor axis and q is the mass ratio of the binary components

($q = M_c/M_X$). We used the common approximation for the mass of a neutron star, $M_X = 1.4\ M_\odot$.

To obtain the Roche lobe radius for solution 1 of T06, we first calculated the semimajor axis of the orbit from the third Kepler law:

$$M_X + M_c = \frac{4\pi^2}{G}\frac{a^3}{p^2}\ , \tag{4.2}$$

where G is the gravitational constant, that we wrote as $G = 2945.02\ R_\odot^3\ M_\odot^{-1}\ \mathrm{d}^{-2}$, a is the semimajor axis and $p = 3.7$ d is the orbital period. With the above parameters, we obtained a Roche lobe radius of $R_L = 10.68\ R_\odot$. According to Schaller et al. (1992) the radius of a 7 $M_\odot$ star at the beginning of the giant branch is 86.5 $R_\odot$. The minimum radius reached during its later evolution, at the core He-burning phase is 50 $R_\odot$. The only evolutionary phase in which a 7 $M_\odot$ star can fit in a 10.68 $R_\odot$ Roche lobe is during the main sequence, with temperatures higher than 15 000 K. This corresponds to a B-type spectrum, which is completely discarded by our spectral classification. This result shows that the system IGR J16393-4643, with the binary orbit proposed by T06, cannot harbor a late-type giant star of $\sim$7 $M_\odot$.

Among the orbital solutions calculated by T06, the above discussion thus excludes solution 1. Our conclusion may be supported by the non-detection of any orbital period of the order of a few days, as solution 1 estimates, by Bodaghee et al. (2006) from ISGRI light curves. We also exclude solution 3 because of, as the authors point out, its statistical weakness and physically unrealistic constraints; although statistically less favored than the first one, solution 2 appears to be the only acceptable one. With a mass function of 0.092 $M_\odot$ and an orbital period of 50.2 days, it is indeed compatible with our spectral classification, as we show hereafter.

In order to constrain the mass of the companion, we calculated, for increasing values of mass, the corresponding radius at the beginning of the giant branch, and compared it with the maximum permitted one, i.e. the Roche lobe radius.

Again, we first calculated the major axis of the orbit from the third Kepler

Table 4.3: Results from the analysis of the orbital parameters of IGR J16393-4643 for different values of mass of the companion star M_c. Tabulated values for $T_{\rm eff}$ and L are taken from Schaller et al. 1992, for a star at the beginning of the giant branch. For each case, the last column shows the corresponding spectral type. Up to $M_c = 5\ M_\odot$, a red giant is able to fit in the orbit foreseen by solution 2 of T06. Results for $M_c = 5 M_\odot$ are shown for completeness.

M_c $(M_\odot)$	a $(R_\odot)$	R_L $(R_\odot)$	log $T_{\rm eff}$	$\log(L/L_\odot)$	R_c $(R_\odot)$	i $(^\circ)$	Sp. t.
1	76.5	26.8	3.72	0.33	1.75	54.0	G5 III
2	85.9	35.2	3.71	1.23	5.19	30.7	G5 III
3	93.6	41.7	3.70	1.95	12.46	23.8	G8 III
4	100.3	47.3	3.68	2.46	24.35	20.3	K0 III
5	106.1	52.1	3.67	2.85	40.93	18.1	K1 III
7	116.2	60.5	3.64	3.39	86.5	15.4	K3 III

law (4.2), using $p = 50.2$ d from solution 2 as the orbital period. Taking the common approximation $M_X = 1.4\ M_\odot$, we solved equation 4.2 with respect to a for different values of M_c, and employed the retrieved value in equation 4.1 to obtain the corresponding Roche lobe radius. We then considered a red giant at the beginning of the giant branch, took tabulated values of $T_{\rm eff}$ and L from Schaller et al. (1992), and solved the black-body equation, $L = 4\pi R^2 \sigma T_{\rm eff}^4$, to obtain the stellar radius. For each value of mass, starting with $M_c = 1\ M_\odot$, we compared the retrieved radius with the Roche lobe radius of the system. Results from this analysis are reported in Table 4.3, where we also show, for each case, the corresponding spectral type, obtained from temperature and luminosity, and the inclination i of the system as calculated from the mass function of solution 2.

We stress that the parameters R_c and i in Table 4.3 correspond to the beginning of the first giant branch ascent. In consequence, they only represent a lower limit to the radius and upper limit to the inclination angle for stars of the given mass.

Up to $M_c = 5\ M_\odot$, a red giant is able to fit in the orbit foreseen by solution

2 of T06, while for higher values the stellar radius would exceed the Roche lobe radius of the system. We thus set an upper limit of 5 $M_{\odot}$ to the mass of the companion star. This mass limit excludes the possibility that the companion is a supergiant since the lower limit for the mass of a red supergiant is 10 $M_{\odot}$ as discussed above.

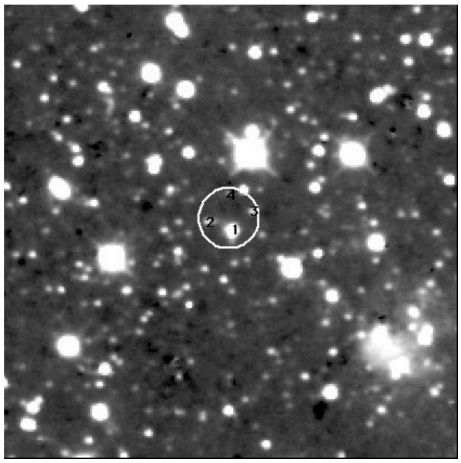

Figure 4.7: Possible counterparts to IGR J16393-4643 within the error circle of *XMM*/Newton. SOFI/NTT K-band image from Chaty et al. (2008). The counterpart we adopted in this work is number 1.

An alternative explanation is that 2MASS J16390535-4642137 is not the actual optical/infrared counterpart to IGR J16393-4643. A spectroscopic study of the other three stars (see Fig. 4.7, from Chaty et al. 2008) found in the error box of the X-ray source is needed in order to confirm or exclude this case. If one of those targets were an OB supergiant, this would then support the classification of the system as a HMXB, and would make the orbital solution 1 from T06 acceptable.

For the sake of comparison, we collect in Table 4.4 the main properties of the two systems studied, thus extending Table 3 by Masetti et al. (2007).

The mass accretion rate was calculated from the X-ray luminosity, as

$$\dot{M} = \frac{L_{\rm X} R}{GM} \ , \tag{4.3}$$

Table 4.4: Synoptic table reporting the main known parameters for IGR J16358-4724 and IGR J16393-4643. The X-ray luminosity is given in the 2–10 keV band. The mass accretion rate $\dot{M}$ was estimated assuming typical parameters for a neutron star, i.e. $R_{\rm X} = 10$ km and $M_{\rm X} = 1.4\ M_{\odot}$.

Parameter	IGR J16358-4724	IGR J16393-4643
Spectral type of the secondary	K-M III [1]	K-M III [1]
V-band magnitude	> 23.67 [2]	21.53 [2]
A_V (mag)	12–13 [1]	4–6 [1]
Distance (kpc)	5–6 ; 12–13 [3]	~ 10 [4]
X-ray spectrum	[5]	[4]
$L_{\rm X}$ (erg s^{-1})	3×10^{32} – 2×20^{36} [5]	2×10^{34} [4,1]
$L_{\rm X}/L_{secondary}$	–	–
$\dot{M}$ (g s^{-1})	1.6×10^{12} – 1.1×10^{16} [1]	1.1×10^{14} [1]
P_{spin} (s)	5850 [6]	~ 912 [4,7]
$\dot{P}_{spin}/P_{spin}$ (s^{-1})	3.1×10^{-8} [5]	1.0×10^{-11} ? [7,1]
$P_{\rm orb}$ (d)	–	50.2 ? [7,1]

References:
[1] this work; [2] Chaty et al. (2008); [3] Lutovinov et al. (2005);
[4] Bodaghee at al. (2006); [5] Patel at al. (2007); [6] Patel et al. (2004);
[7] Thompson et al. (2006).

where $R \sim 10$ km is the radius of the neutron star, and $M \sim 1.4 M_{\odot}$ its mass. For IGR J16393-4643, $L_{\rm X}$ was obtained from the X-ray 2–10 keV flux given by Bodaghee et al. (2006), and assuming a distance of 1.4 kpc, according to our estimate in the most probable case of a K0III counterpart.

Although the class of SyXBs is not well characterized yet, we note that the known properties of these two systems are homogeneous with the other six members. We confirm the peculiarity of the class with respect to the spin, which displays periodicities spanning a wide range, from hundreds of seconds to hours (see Masetti et al. 2007, and references therein).

4.6 Conclusions

We used infrared medium-resolution spectroscopy to classify the proposed counterparts to IGR J16358-4724 and IGR J16393-4643. The results we obtained for IGR J16393-4643 are valid if the candidate counterpart is confirmed by excluding as possible companion one of the other three sources found in the error circle of the *XMM-Newton* position. Future spectroscopic studies of these faint sources will be able to confirm without any doubt the classification of the system. By this work, we have found that:

- both objects show the typical features of cold giant or supergiant stars. Our classification constrains the spectral type to K-M.

- previous classification of the systems as HMXBs is dismissed.

- spectral classifications of the counterparts as late type giant stars, together with X-ray behavior characteristic of neutron stars known from previous works, allowed us to include both systems in SyXB class, increasing the number of this recently discovered group from six to eight members.

- among the orbital solutions for IGR J16393-4643 proposed by Thompson et al. (2006) from pulse timing analysis, only one, with a mass function of 0.092 $M_{\odot}$ and orbital period of 50.2 days, is compatible with our spectral classification.

- an upper limit to the mass of the companion star in IGR J16393-4643 was set to 5 $M_{\odot}$.

We emphasized the failure of SED fitting techniques alone with the aim of spectral classification in the K-band, due to the degeneracy between the direction of the reddening vector and the effective temperature variation. Moreover, our data clearly stress the importance to obtain K-band spectroscopy beyond 2.3 μm, where CO absorption features are located. With spectra limited before this range, which can be featureless in particular at low resolution and S/N, classification can be misleading.

5

Conclusions and future projects

5.1 Main results

- We elaborated a photometric technique in the IR in order to select Be counterparts to obscured X-ray sources discovered by *INTEGRAL*.

- For each field, a number of 1–3 strong candidate counterparts, i.e. objects selected from both (Brγ-K_s) – ($H-K_s$) and (He I-K_s) – ($H-K_s$) color-color diagrams, were found.

- First tests validated the proposed technique.

- From IR spectroscopy of seven proposed counterparts to high-energy sources – IGR J16207–5129, IGR J16465–4507, IGR J16479–4514, IGR J16493–4348, AX J1841.0–0536 and IGR J19140+0951 and 4U 1907+09 –, we classified all of them as HMXBs,by identifying three of them as SFXTs and four of them SGXBs.

- We found that all the three SFXTs are intrinsically absorbed, suggesting that this might be a characteristic of the entire class.

- For the seven objects analyzed, we estimated the distance to values compatible with the location of the sources in the respective galactic arms.

- From K-band spectroscopy of two *INTEGRAL* objects, IGR J16358–4724 and IGR J16393–4643, we proposed to classify both of them as two new

SyXBs, dismissing previous classification as HMXBs.

- We compared the previously proposed orbital solutions for IGR J16393–4643 with our findings and concluded that only one of them is compatible with our classification.

- We set an upper limit of 5 $M_{\odot}$ to the mass of the companion star to IGR J16393–4643.

5.2 Future work

As a future project, we plan to observe the photometrically selected emission-line objects with intermediate resolution spectroscopy in the K band. Observing time for these objects has already been awarded by ESO for 2010. This will be the immediate exploitation of the technique developed with this work and will provide its final validation.

The characterization of the systems with identified counterparts will make use of both infrared and high-energy observations. This project will signicantly contribute to map the distribution of HMXRBs in the inner parts of our galaxy, and to trace the star formation regions at opposite sides of the Milky Way.

Part II

X-ray analysis

Science is a way of trying not to fool yourself. The first principle is that you must not fool yourself, and you are the easiest person to fool.

Richard Feynman

6

X-ray analysis techniques

In the last quarter of a century, thanks to the large amount of new information available from X-ray observatories, a unified characterization of the spectral evolution of LMXBs, both containing a neutron star and a black hole, was made possible (Homan & Belloni 2005; Dunn et al. 2010; Belloni 2010). In this chapter we describe the main tools employed in the X-ray analysis of LMXBs and black hole binaries, since most of previous work was performed for these systems. In the next chapter the same techniques will be applied to study HMXBs.

Two different techniques of analysis are mainly in use to characterize the observed X-ray emission from X-ray binaries, namely broad-band spectral and timing analysis. They both approach source emission changes appearing on seconds to minutes time scales. Average energy spectra over a few days are also used sometimes.

Variations in broad-band ($\Delta E/E > 0.1$, usually continuum-dominated) X-ray spectral shape are diagnosed by two complementary methods: *multi-band photometry* and *spectral fitting*, while temporal variability of the X-ray emission is assessed typically by flux time-series through the methods of *Fourier power spectral analysis*. All the three procedures were employed in this work, so we describe them in this section, before entering the specifics of our analysis in the following sections.

6.1 Spectral analysis

6.1.1 Multy-band photometry

In analogy with optical photometry, one can quantify broad-band X-ray spectral shape by defining X-ray colors. An X-ray color, also named "hardness", is the ratio between the photon counts in two broad bands. Since the $\sim$ 2–30 keV X-ray continuum spectra of virtually all HMXBs can be characterized by a power law (i.e. a straight line in log-log plots), a color thus corresponds to a rough measure of spectral slope. The low-energy region of the spectrum is called the "soft" part, while the high-energy region is called the "hard" part. A *color-color diagram* (CD) is the plot of one color vs. another calculated in a different energy band. The higher energy range color, corresponding to harder X-ray emission, is called hard color, while the lower energy range is the soft color. There is not in the literature a unique definition for the energy bands to choose, which can vary according to the category of the studied source (if black hole or neutron star), the author, and the sensitivity of the detector employed, although their meaning is uniquely identified. A *hardness-intensity diagram* (HID) is instead the plot of a color vs. the count-rate in some broad spectral range. These kind of diagrams are model-independent and reflect the intrinsic properties of the system. In the study of LMXBs, they have become an essential tool of analysis by introducing the notion of spectral states. A state is defined by the sudden appearance of a spectral or timing component associated with a particular and well-recognizable position in the CD/HID (see Sect. 6.4). The curve length along a traced one-dimensional track on the CD/HID is conventionally indicated with the symbol S, S_z and S_a for Z and atoll sources, respectively. Examples of CDs/HID for neutron stars are provided in Fig. 6.1

6.1.2 Spectral fitting

X-ray spectral variations can be described in a more detailed way in terms of a combination of one or more physically motivated mathematical functions, or models, fitted to the observed spectra. The analysis of the behavior of model parameters while the source emission evolves along the CD/HID describing a pattern, together with the identification of parameters correlations, is a strong

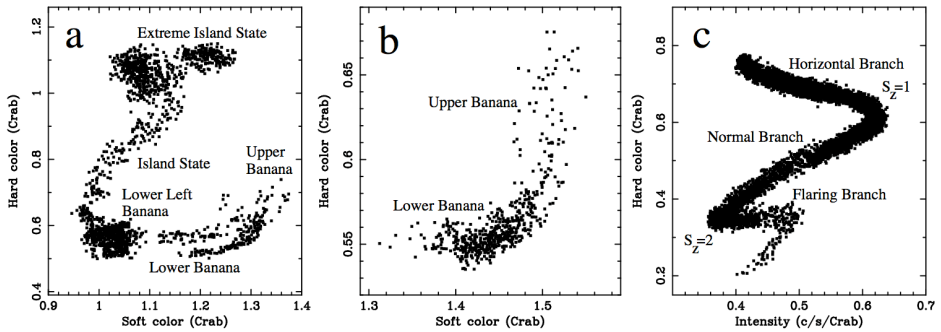

Figure 6.1: Typical spectral branches for neutron stars LMXBs from RXTE data. *(a)* CD of the atoll source 4U 1608-52, *(b)* CD of the GX atoll source GX 9+1, and *(c)* HID of the Z source GX 340+1. Diagrams from van Straaten et al. (2003), van der Klis (2006), Jonker et al. (2000) respectively.

tool to characterize the source states and to individuate state transitions (see Sect. 6.4).

Both methods have in fact limitations, in the first case due to unavoidable detector dependence, in the second case because of the presence of many parameters and because the correct models are in fact not known and in many cases the data can be satisfactorily described by different models. Thus experience and combinations of both methods are absolutely necessary.

6.2 Timing analysis

Observations of X-ray binaries show considerable variability on a wide range of time scales in all wavelengths and down to less than a millisecond in X-rays. The main tool used for studying the timing properties of an X-ray source is the Fourier power spectrum, or a Power Spectral Density (PSD), of the count-rate time series, in which data are transformed from the time to the frequency domain. This technique is particularly needed when the counting noise dominates the time series and it is only possible to study the averaged properties of the timing phenomena. A number of variability components, or power-spectral components, together make up the power spectrum. An aperiodic component by definition covers sev-

eral frequency resolution elements. Broad features are called *noise* and narrow features are called *quasi-periodic oscillations* (QPOs). With the aim of providing a unified description of the aperiodic variability, timing components are usually fitted with Lorentzian functions ($L_{\rm i}$). For an extensive overview of how Fourier techniques are used in X-ray variability studies, we refer to van der Klis (1989).

As can be seen in Figs. 6.3 and 6.4, the power spectrum consists of a superposition of different components. Unfortunately, there is no physical model able to describe all these components consistently, as the real processes behind the X-ray variability are still poorly understood.

6.3 This work

While there have been numerous studies on the application of CD/HID and spectral analysis techniques to LMXBs, very little work of this kind has been done on high-mass X-ray binaries. Belloni & Hasinger (1990) performed an aperiodic variability study on a sample of 14 X-ray binaries, among which 12 were HMXBs: ten of them were SGXRBs; the only BeXRBs were EXO 2030+375 and V 0332+53. Data from EXO 2030+375 only covered a part of the decay of the 1985 outburst; data from V 0332+53 did not correspond to a major outburst. After the discovery of aperiodic variability in V 0332+53 (Stella et al. 1985), timing analysis on accreting pulsars have concentrated on the detection of QPOs (see, for instance, Angelini et al. 1989; Jernigan et al. 2000; Qu et al. 2005). The only study of aperiodic variability on Be/XRBs was recently accomplished by Reig (2008), who characterized the spectral/timing behavior of four systems through CD/HID and timing from RXTE data, constructing time-averaged energy and PSD.

This work is intended to provide for the first time a systematic study of four Be/XRBs during giant outburst, using the three techniques introduced before, namely CD/HID, spectral fitting and timing, simultaneously, and using the retrieved results and correlations to try to define and characterize spectral states for this class of systems.

We have used the same data set as Reig (2008). However, while Reig (2008)

divided the outburst into several (between 7–9) intervals and extracted averaged power spectra for each interval, in this work we obtained energy spectra and PSD for each RXTE observation interval. In Reig (2008) each observation interval had a duration of a few days to weeks. In this work, each observation interval is a few thousand seconds long. This order of magnitude increase in time resolution allows us to:

1. Track much faster changes, likely to be associated with accretion;

2. Search for correlations between the spectral and timing parameters.

6.4 Spectral states

Although this work is addressed to the investigation and characterization of possible spectral states in HMXBs, for the sake of comparison we give in this section an overview of the present definitions of states for LMXBs, both those containing neutron stars and black holes.

6.4.1 Neutron star LMXBs states

Hasinger & van der Klis (1989) classified the neutron star LMXBs based on the correlated variations of X-ray spectral and rapid aperiodic variability properties. They distinguished two sub-classes, the *Z sources* and the *atoll sources*, whose names were inspired by the shapes of the tracks that they trace out in an X-ray CD on time scales of hours to days. The Z sources are the brightest of these two classes and are believed to accrete at near-Eddington luminosities (0.5 $L_{\rm Edd}$ – 1.0 $L_{\rm Edd}$; van der Klis 2006), while the atoll sources cover a much wider range in luminosities. Generally, the atoll sources tend to have harder spectra and to show larger amplitude variability.

It has been observed that in these sources X-ray luminosity $L_{\rm X}$ tends to correlate with state only within a source, not across sources, while X-ray spectral shape, i.e. the position of the source in the CD/HID, correlates with timing characteristics much better than $L_{\rm X}$ (see, for instance, van der Klis 2000). For each

type of source, several spectral/timing states are identified, which are thought to arise from qualitatively different inner flow configurations (e.g. differences in mass accretion rate $\dot{M}$, presence or absence of a corona, structure of accretion disk, jets). Nevertheless, at the time of writing, differences between Z and atoll sources still need an explanation, as well as those among states of each class.

Z sources

They are characterized by three-branched tracks in their CDs (see Fig. 6.1, panel c, and Fig. 6.2 as examples) and HIDs, which in some cases resemble the character "Z" (Cyg-like sources). In other cases they have a more "ν"-like shape (Sco-like sources), but are referred to as Z tracks nevertheless. From top to bottom, the three branches of the Z track are described as the horizontal branch (HB), normal branch (NB; "normal" because it was supposed that this state was more common than the HB state), and flaring branch (FB; named "flaring" after the flaring shown by Sco X-1 when moving up this branch).

Despite the various differences existing among the Z sources, it has often been assumed that in all of them the mass accretion rate increases monotonically from the HB, via the NB, to the FB. If this is the correct interpretation, it would imply that X-ray luminosity does not track $\dot{M}$.

Motion along the branches of the Z usually takes place on timescales of hours to days. On longer timescales it has been observed that the entire Z track changes its location in the CD and HID, or even changes its morphology ("secular motion"), as is best observed in Cyg X-2 (Kuulkers et al. 1996; Wijnands et al. 1997).

The power spectra of the Z sources show several types of QPOs and noise components (see fig. 6.2; for reviews, see van der Klis 2006). Their presence and properties are strongly correlated with the position of the source along the Z track (Hasinger & van der Klis 1989). Three types of low-frequency (<100 Hz) QPOs are seen in the Z sources: the horizontal branch (HBOs), normal branch (NBOs), and flaring branch oscillations (FBOs). Their names derive from the branches on which they were originally found. The HBO is found on the HB and NB with a frequency (15–60 Hz) that gradually increases along the HB toward the NB. The NBO and FBO are most likely part of one single phenomenon. They are found on the NB and FB (near the NB/ FB vertex) but not on the HB. On the NB the QPO has a frequency of $\sim$ 5–7 Hz, which (only in the Sco-like sources) rapidly

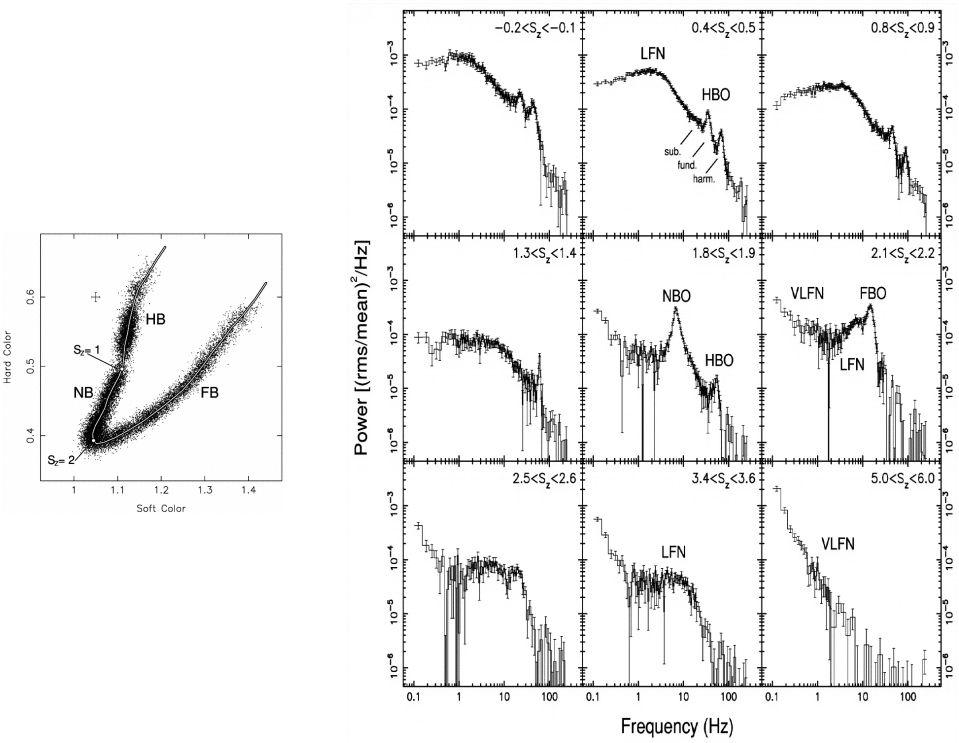

Figure 6.2: *Left:* Example of CD for a typical Z source (Sco-type) with S_z parameterization shown. *Right:* For nine different S_z selections, representative power-spectra for the same Z source, with power-spectral components marked. Adapted from Homan et al. 2002.

increases to ∼20 Hz when the source moves across the NB/FB vertex (Priedhorsky et al. 1986; Dieters & van der Klis 2000; Casella et al. 2006). Twin kHz QPOs have been found in all Z sources. They are often observed simultaneously, with a frequency difference of ∼300 Hz, and have frequencies between 215 and 1130 Hz, which increase from the HB to the NB (in Sco X-1 also onto the FB; van der Klis et al. 1996).

Two types of noise are seen in the Z sources. These are the very low frequency noise (VLFN) and the low-frequency noise (LFN). The VLFN, which is found at frequencies below 1 Hz, is generally described by a power law and is found on all

branches, whereas the LFN, which is a peaked or flat-topped noise component (with cutoff frequencies of 2–10 Hz), is only observed on the HB and NB.

Atoll sources

At high X-ray luminosity, atoll sources follow a well defined curved *banana branch* in the CD/HID (see Fig. 6.1, panel a), along which sources move back and forth with no hysteresis on time scales of hours to a day, showing sometimes secular motion than does not affect the variability. The banana branch is further subdivided into the *upper banana* (UB), dominated by the VLFN, the *lower banana* (LB), dominated by 10-Hz band-limited noise components (BLN), and the *lower left banana* (LLB), where twin kHz QPOs are observed. At the lower luminosity and generally corresponding to harder emission, the source trace the so-called *island state* (IS), whose power spectra are characterized by broad features and a dominant BLN component which becomes stronger and lower in characteristic frequency as the flux decreases and the spectrum gets harder above 6 keV. The hardest, lowest luminosity state is the *extreme island state* (EIS), characterized by strong, low-frequency flat-topped noise. The topology of this state has been a matter of some debate as similarities between this branch and the Z-source HB were claimed by a number of authors (Gierliński & Done 2002; Muno et al. 2002); nevertheless, studies by Barret & Olive (2002); van Straaten et al. (2003); Reig et al. (2004) later pointed out that differences in the luminosity associated with the spectral transitions, in spectral shape and mainly in timing features testify a different nature of the two classes.

In Fig. 6.3, a schematic CD/HID and representative power spectra for the EIS, IS, LLB, LB and the UB states are shown.

6.4.2 Black-holes states

The X-ray spectral properties of black holes LMXBs can be classified into two main components, a hard and a soft one. When a hard, non-thermal, power-law component with photon index in the range 1.5–2 dominates the energy spectrum, the source is in its *Low/hard State* (LS); when a soft, thermal, black-body like component with temperature $kT \lesssim 1$ keV dominates, then the source is in its *High/soft State* (HS). In between the low and the high states, the *intermediate*

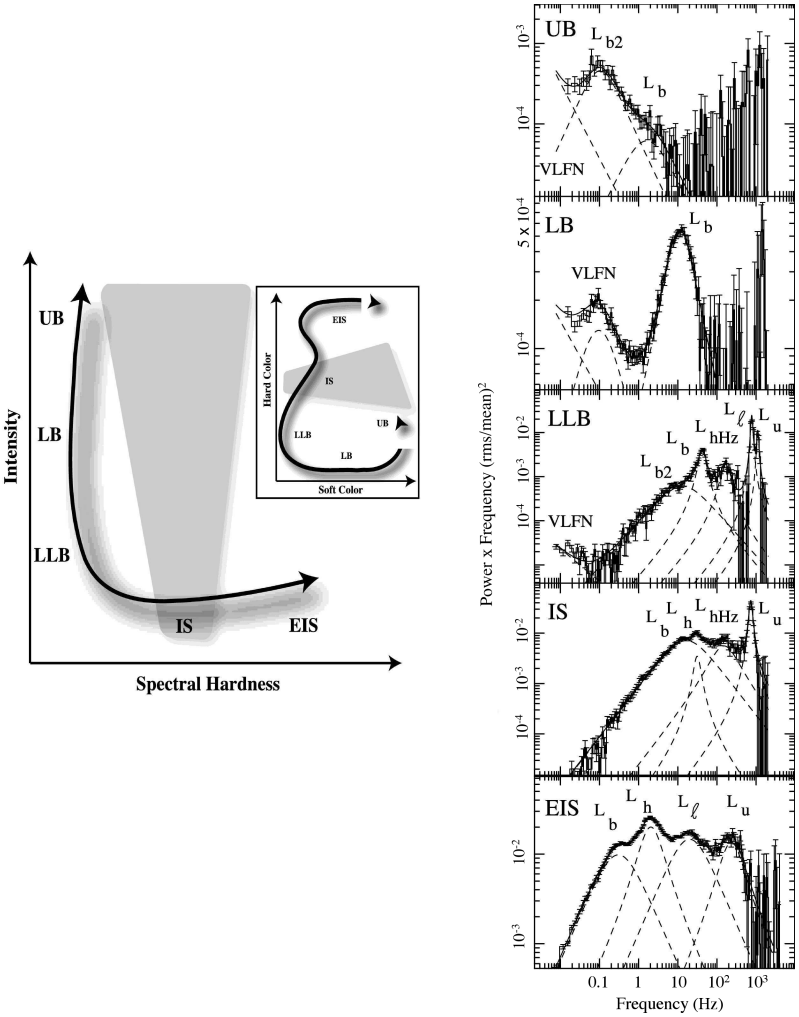

Figure 6.3: *Left:* Schematic HID and CD for a typical atoll source. The solid line shows the track the source follows during the outburst. Note that some sources show transitions among all states, while others are only observed in some of them. *Right:* Representative power-spectra for atoll sources states, with power-spectral components marked. Adapted from Klein-Wolt & van der Klis 2007.

state, or *very-high state* (VHS), is defined, which links both extremes and where complex behavior, including sometimes large flares in intensity, occurs. This intermediate state can be usefully subdivided into the Soft Intermediate State (SIMS) and the Hard Intermediate State (HIMS) based mainly on the aperiodic variability (see, e.g., a discussion in Belloni et al. 2005). In Fig. 6.4 a schematical view of a HID that typical black hole candidates tend to trace out during an outburst is shown (left panel), together with representative power spectra for the high state, soft and hard intermediate states and low state.

In both LS and HIMS, the power spectrum is dominated by a strong broad-band noise (up to 60% fractional rms) and sometimes QPOs. The SIMS shows power spectra without the broad-band noise component, dominated instead by a weak power law, on top of which several QPOs are present. The HS power spectra are similar to those of the SIMS, although the variability might be weaker and generally no QPOs are present. In all these cases, the broad and peaked features are found at low characteristic frequency (< 100 Hz), however, sometimes weak high frequency QPOs (100–450 Hz) are also found in the HIMS and SIMS. For a general description of how the power spectral components vary as a function of source state we refer to the reviews by Homan & Belloni (2005) and van der Klis (2006).

The behavior of black holes and neutron stars in their different states show similarities. Based on the spectral and timing characteristics, van der Klis (1994) suggested that the black holes LS is similar to the neutron star atoll EIS/IS, and that some of the softer black holes and neutron star states might also be identified with one another. Moreover, some frequency-frequency correlations found among the power spectral components (the so-called WK and PBK relations, see Wijnands & van der Klis 1999; Psaltis et al. 1999), are analogous for black holes and atoll neutron stars, suggesting they result from the same physical process.

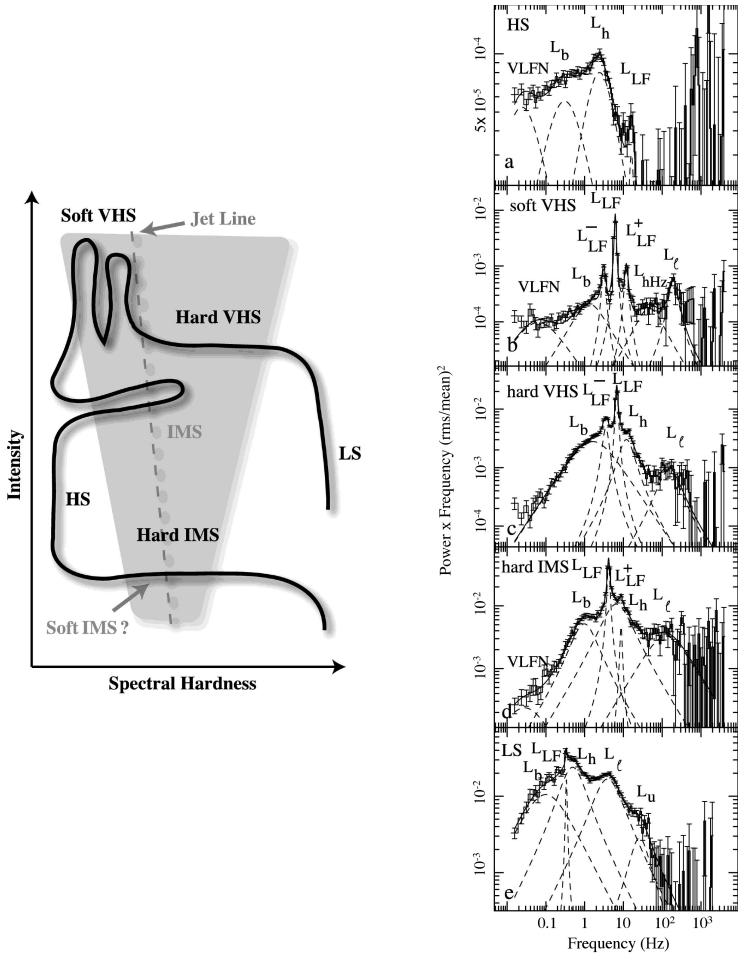

Figure 6.4: *Left:* Schematic HID for a typical black hole source outburst. The solid line shows the track the source follows during the outburst. *Right:* Representative power-spectra for black hole states, with power-spectral components marked. Adapted from Klein-Wolt & van der Klis 2007.

Puedo escribir los versos más tristes esta noche; escribir, por ejemplo: "La noche está estrellada, y tiritan, azules, los astros, a lo lejos"

Pablo Neruda

7

X-ray spectral and timing analysis of Be/XRBs during giant outbursts

7.1 Scientific objective

With the work presented in this chapter we investigated the spectral and timing variability of four accreting X-ray pulsars with Be-type companions during major outbursts. By major outbursts we mean type II outbursts in which the X-ray luminosity reaches Eddington values, similarly to X-ray outbursts from transient LMXBs and black-hole binaries. Based on the spectral and timing properties, on the position of the sources in the color-color diagram along the outburst, and the correlations between all these features, we aim to define and characterize possible "source states" as in Low Mass X-ray Binaries (LMXBs) and Black Holes.

The systems analyzed in our work, Be/XRBs, display two kind of variability in X-ray intensity, being one of them strictly periodic and the other one aperiodic. The X-ray periods range from a fraction of a second to several months, and can be separated into coherent modulation due to the rotation of the neutron star (*spin* or pulse period) and modulation due to the *orbital motion* on the neutron star around the Be star companion.

As the neutron star rotates, the polar hotspots, i.e. the regions where gas accreted from the stellar companion is channeled by the neutron star's magnetic

field, move in and out of view if the magnetic axis is tilted with respect to the spin axis. This results in X-ray pulsations. The pulse periods lie in the range $10^{-1} - 10^{3}$ s.

The orbit of the neutron star around the Be star and the transfer of mass from the massive companion together with the strong gravitational potential of the compact object originate high-energy radiation which in many cases is modulated. In fact, in some cases the only estimate of the orbital period of the system comes from the periodic modulation of the X-ray emission (e.g type I outbursts), which covers the range of $10 - 10^{2}$ days. The X-ray periodic variability is not the subject of this work.

Instead, we focused on rapid aperiodic variability, as this is one of the phenomena that are firmly grounded in the unique physics of the process of accretion onto a compact object. During the accretion, large amounts of gravitational energy ($\sim 10^{38}$ erg s^{-1}, or 10^{5} L$_{\odot}$) are released in a small volume ($\lesssim 10^{4}$ km^{3}), which leads to high temperatures ($T \sim 10^{7}$ K) and results in the emission of high-energy photons. The accreting matter moves through the small emitting volume under influence of a large gravitational force which produces strong accelerations. The resulting high velocity ($\sim 0.1c$) lead to short characteristic time scale (the dynamical time scale, $\tau = \sqrt{r^3/GM}$ is about 0.1 ms). Therefore, one may expect to observe rapidly variable X-rays in these systems.

As the X-ray spectrum and the rapid X-ray variability arise through processes in the same physical region, their properties may be expected to be coupled. The monitoring and analysis of these properties in X-ray pulsars are the subject of this chapter.

7.2 The sources

During type II outbursts, Be/XRBs display 2–3 orders of magnitude variations in X-ray intensity. It is believed that a temporary accretion disk is formed around the neutron star during these major outbursts (although no Roche lobe overflow occurs): these two features (transient nature and accretion disc) appear as a possible analogy domain with LMXBs, for which a well established description in terms of source states has been provided.

7.2.1 KS 1947+300

The Be/X-ray binary KS 1947+300 was first detected in the X-ray band on June 8, 1989 by the TTM coded mask X-ray spectrograph on the Kvant module of the Mir space station (Borozdin et al. 1990) with a peak flux of 70 mCrab. About 35 days later the flux was at the limit of sensitivity of the instrument with a 3σ upper limit of 10 mCrab. X-ray pulsations with a pulse period of 18.7 s were found in the X-ray flux of GRO J1948+32 in April 1994 by the all-sky monitor BATSE aboard *CGRO* (Chakrabarty et al. 1995). The source reached a peak pulse flux of 50 mCrab in the energy range 20–75 keV. About 25 days later the flux decayed below the detection threshold of BATSE. Due to the very large error box of GRO J1948+32, no connection with this source and KS 1947+300 was realized at first. The source remained in quiescence until the beginning of 2001 (Galloway et al. 2004). In this occasion the source reached a maximum flux of 120 mCrab, the largest in its history. This outburst is the subject of the present work.

Prior to this major outburst, weak emission ($\sim$ 20 mCrab) and X-ray pulsations (18.7579$\pm$0.0005 s) from KS 1947+300 had been detected in November 2000 (Levine & Corbet 2000; Swank & Morgan 2000). The coincidence in the value of the pulse period and the location of KS 1947+300 inside the GRO J1948+32 error box suggested that the two sources were in fact the same object. Pulse timing analysis allowed to solve for the orbital parameters, resulting in orbital period $P_{\rm orb} = 40.415 \pm 0.010$ d, eccentricity $e = 0.033 \pm 0.013$ and projected semi-major axis $a_{\rm X} \sin i = 137 \pm 3$ lt-s (Galloway et al. 2004). A broad-band spectral study of KS 1947+300 using BeppoSAX observations (Naik et al. 2006) showed that the energy spectrum in the 0.1–100 keV energy band has three components: a Comptonized component, a $\sim$0.6 keV blackbody component, and a narrow, weak iron emission line at 6.7 keV with a low column density of material in the line of sight.

The optical counterpart to KS 1947+300 was correctly identified soon after the Kvant detection (Goranskii et al. 1991; Grankin et al. 1991), but its identification as a Be/X-ray binary was suggested later by Negueruela et al. (2003). KS 1947+300 is associated with a moderately reddened V=14.2 B0Ve star located

at ∼10 kpc.

7.2.2 EXO 2030+375

EXO 2030+375 is a 42s transient accreting X-ray pulsar discovered with EXOSAT during a giant outburst in 1985 (Parmar et al. 1989). Extensively observed since its detection in the X/γ-ray band, this system is the prototype for X-ray variability in Be/XRBs. A normal outburst has been detected for nearly every periastron passage since 1991 (Wilson et al. 2002, 2005). For these normal outbursts, the intensity and the global spin-up rate appeared to be tied to the K-band intensity of the Be star. In June 2006 EXO 2030+375 underwent its first giant outburst since its discovery (Corbet & Levine 2006; Krimm et al. 2006; McCollough et al. 2006). In this work we analyze data from this latest event.

In this system, the pulsar ($P_{\rm spin} = 41.7$ s) orbits a B0 Ve star (Motch & Janot-Pacheco 1987; Reig & Coe 1998) in a moderately eccentric ($e = 0.4$) orbit every 46 days (Wilson et al. 2005). The system is located at about 7.1 kpc (Wilson et al. 2002). Like other HMXBs, the continuum spectral shape in the range 1–30 keV can be modeled with a power law with an exponential cutoff (Reynolds et al. 1993). The inclusion of a blackbody component has been reported to give good fits at very high ($L_{\rm X} \sim 10^{38}$ erg s^{-1}) luminosity (Sun et al. 1994) and relatively low ($L_{\rm X} \sim 10^{36}$ erg s^{-1}) luminosity (Reig & Coe 1999). A cyclotron resonant scattering feature (CRSF) at $\sim$ 11 keV was identified by Wilson et al. (2008) during the brightest phase of the 2006 outburst.

7.2.3 4U 0115+63

This source is one of the most active and extensively studied Be/X-ray transients as it was one of the first to be discovered. It was detected by the UHURU observatory (Giacconi et al. 1972). Rappaport et al. (1978) determined the binary main parameters based on the known pulsation period of ∼3.6 s (Cominsky et al. 1978): orbital period of 24.3 days, orbital eccentricity $e = 0.34$, and projected semimajor axis $a_{\rm X} \sin i \sim 140$ light seconds. During RXTE's lifetime, three major outbursts have been detected, in 1999, 2000 and 2004. Here we analyse observations from the 2004 event. The optical counterpart to the X-ray source is the star V635 Cas (Hutchings & Crampton 1981). Optical observations performed by Negueruela &

Okazaki (2001) allowed its spectral classification to B0.2Ve, and distance estimation to 7–8 kpc.

The X-ray spectrum shows up to five CRSFs, with the fundamental at ∼12 keV (Wheaton et al. 1979), and four harmonics, making this pulsar the neutron star with the highest number of cyclotron lines (Heindl et al. 2004). During the 1999 and 2004 outbursts, mHz QPOs were detected (Heindl et al. 1999; Coburn et al. 2004).

7.2.4 V 0332+53

The transient X-ray pulsar V0332+53 was discovered by the Vela 5B observatory in 1973 (Terrell & Priedhorsky 1984) during an outburst when its intensity reached ∼ 1.4 Crab in the 3–12 keV energy band. The outburst lasted about three months before the source became undetectable again.

Through observations of three small outbursts in 1983–1984, the pulsars and orbital parameters were determined with the *EXOSAT* observatory: the pulse period was determined to be 4.4 s, the orbital period 34.25 days, eccentricity 0.31, and the projected semimajor axis $a_{\rm X}{\rm sin}i \sim 48$ lt-s (Stella et al. 1985). Later, when the source was observed by the *Ginga* observatory, a cyclotron resonance at $E_{\rm c} = 28.5 \pm 0.5$ keV was detected in its spectrum. This energy corresponds to a magnetic field on the neutron star surface of $\sim 3 \times 10^{12}$ G (Makishima et al. 1990). Later Mihara et al. (1998) reported measurements of two different values of the resonance energy for different levels of the source intensity. During the subsequent major outburst in 2004–2005, two harmonics were observed as well (Coburn et al. 2005). Data from this latest outburst are analyzed in this work.

The optical counterpart to the system, BQ Cam, was classified as O8-9Ve by Negueruela et al. (1999), who also estimated the distance to ∼ 7 kpc.

We provide in Table 7.1 the duration and peak intensity of each individual outburst studied in this work, together with some basic information about the systems.

Table 7.1: Relevant optical/X-ray information on the systems and on the outbursts analyzed in this work.

Source name	Spectral type	$P_{\rm spin}$ (s)	$P_{\rm orb}$ (d)	e	Distance (kpc)	Outburst duration (d)	$L_{\rm X,peak}$ 3–30 kev (erg s^{-1})
KS 1947+300	B0V	18.7	40.4	0.03	10.0	165	7.1×10^{37}
EXO 2030+375	B0.5III-V	41.8	46.0	0.41	7.1	155	1.5×10^{38}
4U 0115+63	B0.2V	3.6	24.3	0.34	8.1	55	1.4×10^{38}
V 0332+53	O8-9V	4.4	34.2	0.30	7.0	105	3.4×10^{38}

7.3 The instrument

We employed archive data by the Proportional Counter Array (PCA) onboard the Rossi X-ray Timing Explorer (RXTE, Bradt et al. 1993). The satellite was launched on December 30, 1995 and at the time of writing it is still operating. It orbits at 580 km around Earth, with an inclination of 22°, completing a circle around our planet every 100 minutes. Its primary objective is the study of phenomena associated to galactic stellar systems containing compact objects, both from the timing and the broad band spectral point of view. This is accomplished with three instruments: the All-Sky Monitor (ASM), the PCA, and the High Energy Timing Experiment (HEXTE). Fig. 7.1 shows a schematic view of the satellite and its instruments.

The objective of the ASM is the continuous sky monitoring in order to reveal transient sources. It is composed by three screening shadow cameras operating in the 1.3–12 keV band, that rotate by 6° every 90s, thus covering the 80% of the sky in 90 minutes. The high pointing velocity allows RXTE to observe X-ray sources with very low dead-times. The PCA is the main instrument onboard RXTE. It is a pointed instrument, co-aligned with the HEXTE and having the same collimated field of view of $\sim 1°$. It consists of five Proportional Counter Units (PCUs) with a total collecting area of ~ 6250 cm^2, operates in the 2–60 keV range and has a nominal energy resolution of 18% at 6 keV. The HEXTE is constituted by 2 clusters of 4 NaI/CsI scintillation counters, with a total collecting area of 2×800 cm^2, sensitive in the 15–250 keV band with a nominal energy resolution of 15% at 60 keV. Both instruments have a maximum time resolution of $\sim 1\mu$s. Thanks to

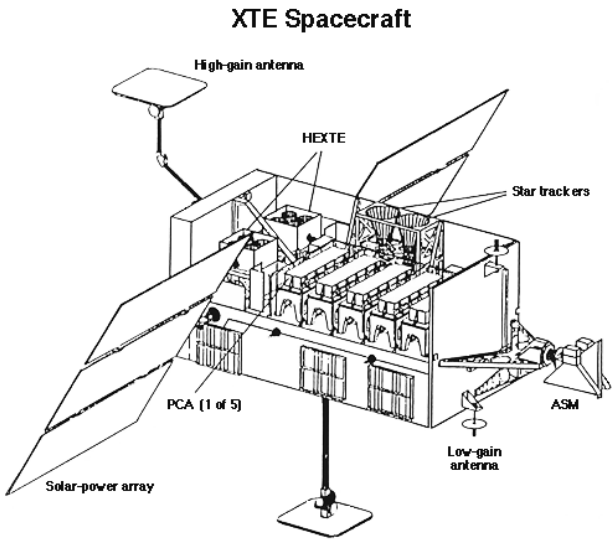

Figure 7.1: Diagram of the RXTE spacecraft, with instruments labeled

this very high temporal resolution, a very accurate analysis of aperiodic variations in X-ray sources became possible. With the exception of regions near the center of the Galaxy, the source density on the sky is low enough to provide sufficient positional resolution and avoid source confusion.

Multiple combinations of modes and configurations for PCA data are possible, nevertheless there are only two basic formats for science data: *science array* and *science event*. The science array format is used for data binned at regular intervals by the spacecraft electronics. An example is the Standard 2 configuration, which contains 129–channel spectra accumulated every 16 seconds. Given its high spectral resolution, this configuration was employed in this work for spectral analysis. The science event format is used for unbinned data, i.e. for individual events. An example is the Good Xenon configuration which contains time-stamped events with 256-channel resolution, PCU ID and anode ID. This kind of mode, with the highest temporal resolution, was employed for timing analysis.

7.4 Observations, data reduction and analysis

Table 7.2: Journal of RXTE observations.

Source	N. of observations	Proposal ID	MJD range	On-source time (ks)
KS 1947+300	33	50425	51874.1502–51968.5641	81.9
	53	60402	51970.2075–52878.0486	50.1
EXO 2030+375	84	91089	53914.8867–53998.6609	83.5
	48	92067	53999.5903–54046.9378	56.6
4U 0115+63	19	90089	53254.0689–53280.6947	58.8
	10	90014	53282.5716–53297.5954	37.6
V 0332+53	28	90089	53340.2869–53365.9140	82.2
	7	90427	53367.2273–53376.6352	13.1
	38	90014	53378.4241–53430.5380	79.2

The data analyzed in this work correspond to epochs in which the sources went through a type II outburst. Table 7.2 gives the observations log.

The PCA is the most appropriate instrument onboard RXTE to perform the type of analysis that we wish to carry out. It provides time resolution down to 1 μs and has a large collecting area. In addition, it is sensitive to X-rays below ~ 30 keV where most of the analysis in LMXBs and BHs, with which our study intends to compare, has been done.

Due to the aging of the detectors, each PCU provides at present a different performance. Only data from PCU2, the most convenient unit since its good operational status and its constant enabling, were employed for color and spectral analysis. All the PCU that were on were used for timing.

Due to the low-Earth orbit, observations consist of a number of contiguous data intervals (typically 1h long) interspersed with observational gaps produced by Earth occultations of the target and passages through the South Atlantic Anomaly, where the high flux of energetic particles make the instruments unusable. We will refer to each of these intervals as "pointings".

7.4.1 Spectral analysis

Using Heasarc FTOOLS version 6.6.3, a spectrum was produced for each observation, after filtering out unsuitable data according to the recommended criteria[1]. For extracting spectra, Standard 2 mode data were used, which have a time resolution of 16s and cover the 2–60 keV range with 129 channels. All spectra were background-subtracted and, when necessary, dead-time corrected. By dead time we mean any process by which the detection of an event subsequently changes the sensitivity of the detectors. For each observation, the spectrum was fitted in the 3–50 keV range, using XSPEC version 12.4 (Arnaud 1996). This energy range, extending to high energies, is accessible thanks to the high luminosity of the systems studied, showing high S/N in the DB ($> 90\%$ of the observations). For the sake of completeness we have also obtained spectra in the same range for the HB, although the S/N is considerably lower above 30 keV. Nevertheless, the best-fit values of the spectral parameters are not affected by whether we use 3–30 keV or 3–50 keV. In Fig. 7.2 we show a plot of an unsubtracted source (black points) and background (red points) together: it corresponds to the faintest of the four systems, KS 1947+300, at $L_{\rm X} \sim 40\%$ of the peak luminosity. Although the contribution of the background strongly increases above 25 keV, the unsubtracted spectrum still lies on top of it.

During the fitting, a systematic error of 0.6% was added to the spectra, which is a common practice. The lack of adequate theoretical continuum models for accreting neutron stars imposes the use of empirical models to describe the observations. In order to consistently compare fitting results from the four sources, we tried to employ the same (or very similar, if leading to better fit) spectral components. We used a model composed by a combination of photoelectric absorption (PHABS in XSPEC), a power law with high-energy exponential cutoff (CUTOFFPL or POWERLAW × HIGHECUT, according to the case) and a gaussian line profile (GAUSS) at ~ 6.5 keV to account for Fe Kα fluorescence. Three sources, EXO 2030+375, 4U 0115+63 and V 0332+53, are known to be characterized by cyclotron absorption, which we accounted for with the dedicated GABS or

[1]Among which, elevation from the Earth greater than 10° and pointing offset lower than 0.02°; see PCA digest at http://heasarc.gsfc.nasa.gov/docs/xte/pca_news.html or, e.g., van Straaten et al. (2003)

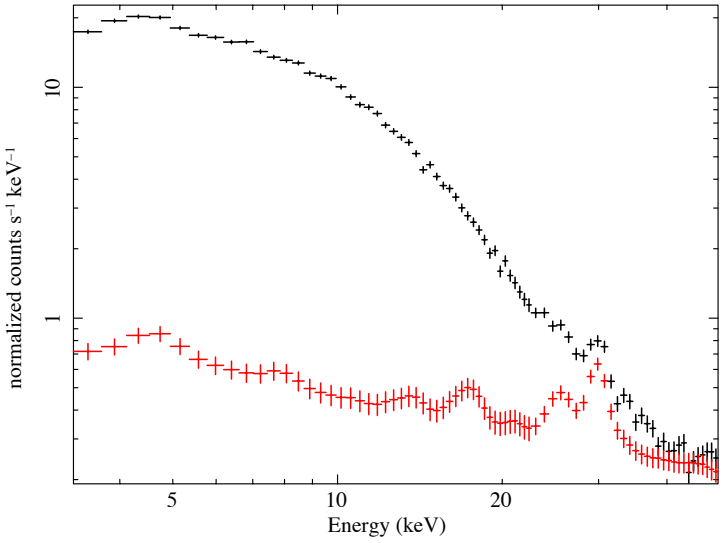

Figure 7.2: Plot of an unsubtracted source, KS 1947+300 (black points), together with the corresponding background (red points). In the range we considered, 3–50 keV, the source spectrum always lies on top of the background.

CYCLABS XSPEC components, both gaussian optical depth profiles. In general, the value of the hydrogen column density N_H cannot be well constrained by the PCA, whose energy threshold for the fit is 3 keV. When known from previous works with higher sensitive instruments below 3 keV, it was fixed to the known value. Fixing the absorption makes the fitting procedure more stable, mainly during error calculation.

In Fig. 7.3 we give an example of unfolded spectrum, for the observation 90014-02-01-01 of 4U 0115+63. The retrieved reduced chi-square for this fit was $\chi^2_{\rm red} = 1.06$.

Integrated fluxes were calculated through XSPEC in the 3–30 keV using the best-fit model.

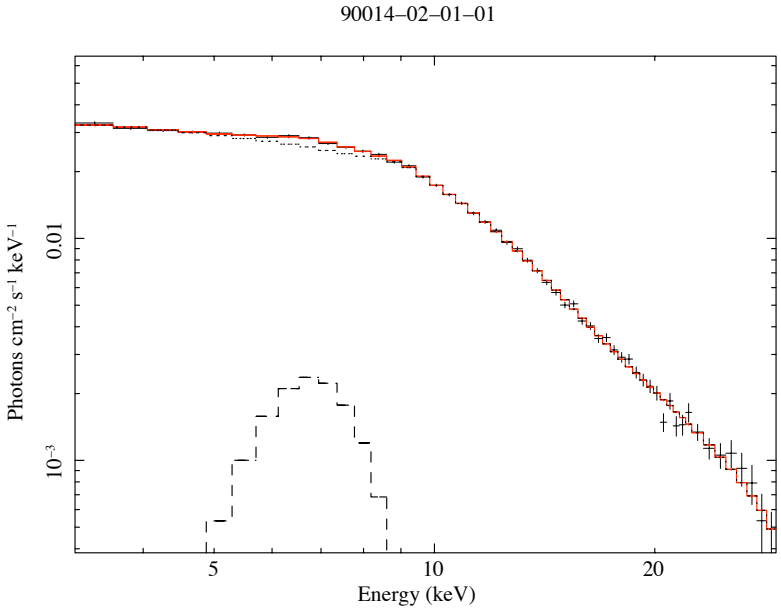

Figure 7.3: Example of the unfolded spectrum of 4U 0115+63, described by a model constituted by photoelectric absorption, power law with high-energy cutoff (dotted line), gaussian line (dashed line) and cyclotron absorption. In this kind of representation, only the additive components are shown. Data points are marked by black crosses, the resulting fitting model is marked by a red line.

CD and HID were directly obtained from count rate in the following energy bands:

- soft color (SC): 7–10 keV / 4–7 keV

- hard color (HC): 15–30 keV / 10–15 keV

Standard 2 mode data were used to obtain the lightcurves from which the colors are calculated. The average value of count rate for each observation was employed in order to have colors with the same sampling than the energy spectra (one point per observation).

7.4.2 Timing analysis

Power spectral density (PSD) was computed using mainly Good Xenon or Event mode data. According to archive availability, in some cases also Binned and Single Bit mode were used.

We first extracted, for each observation, a light curve in the energy range 2–20 keV (channels 0–49) with a time resolution of 2^{-8} s. The light curve was then divided into 256-s segments and a Fast Fourier Transform was computed for each segment. The final PSD was computed as the average of all the power spectra obtained for each segment. The final power spectra were logarithmically rebinned in frequency and corrected for dead time effects according to the prescription given in Nowak et al. (1999).

Power spectra were normalized such that the integral over the PSD is equal to the squared fractional rms amplitude, according to the so-called *rms-normalization* (Belloni & Hasinger 1990; Miyamoto et al. 1991).

In order to have a unified phenomenological description of the timing features within a source and among the four different sources, we fitted noise and QPOs with a function consisting of one or multiple Lorentzians, each denoted as L_i, where i determines the type of component. The characteristic frequency $\nu_{\max}$ of L_i is denoted ν_i. This is the frequency where the component contributes most of its variance per logarithmic frequency interval and is defined (Belloni et al. 2002) as

$$\nu_{\max} = \sqrt{\nu_0^2 + (FWHM/2)^2} = \nu_0\sqrt{1 + 1/4Q^2} \ , \tag{7.1}$$

where ν_0 is the centroid frequency and $FWHM$ the full width at half maximum of the Lorentzian component. Note that $\nu_{\max} \neq \nu_0$. The broader the noise component, the larger the difference between $\nu_{\max}$ and ν_0.

The quality factor Q is defined as $Q = \nu_0/FWHM$, and is used as a measure of the coherence of the variability feature.

Our choice of this over other models (such as a combination of power law and Gaussian functions) was motivated by the fact that the multi-Lorentzian model gives the possibility to identify and follow the characteristics of power spectral components as they evolve in time and as a function of spectral state using only one type of function (i.e., a Lorentzian function). This also allowed us to compare

the characteristics of different components. The peaks derived from the neutron stars pulsations were fitted to Lorentzian functions with frequency fixed at the expected value according to the spin period and width equal to 0.001 Hz (approximately, the inverse of the timing resolution of the PSD). The results from the use of Lorentzians are best visualized using the $\nu \times P_\nu$ representation, where each power is multiplied by the corresponding frequency. In this representation, the maximum power is attained at $\nu = \nu_{\max}$.

We show an example of fitted PSD in the $\nu \times P_\nu$ representation in Fig. 7.4. The spectrum is from observation 90089-01-04-02 of 4U 0115+63; each fitting component is represented by a colored line, while the whole resulting fit is shown as black solid line. The retrieved reduced chi-square for the fit was $\chi^2_{\rm red} = 1.2$.

7.5 Results

Here we present, for each system, the results of our analysis. For representative energy spectra and PSD, see the next section, where a comprehensive discussion is given.

7.5.1 KS 1947+300

The total duration of the outburst was $\sim$ 165 days. The peak X-ray luminosity, found at MJD = 51950, is $L_{\rm X} = 7.1 \times 10^{37}$ erg s^{-1}, assuming a distance of 10 kpc.

Spectral analysis

In Fig. 7.5 we show the behavior of the 3–30 keV flux during the outburst. We note that the outburst is well sampled, from its very beginning until its final decay. It is asymmetrical, characterized by a steeper rise and a slower decay. It took $\sim$70 days to rise from quiescence to maximun flux and about 120 days to return to quiescence.

In Fig. 7.6 we display the corresponding HIDs and colors trends. While Fig. 7.5 was obtained after the spectral fitting, which is a necessary step in order to calculate the flux from the source, Fig. 7.6 was directly retrieved from count rate.

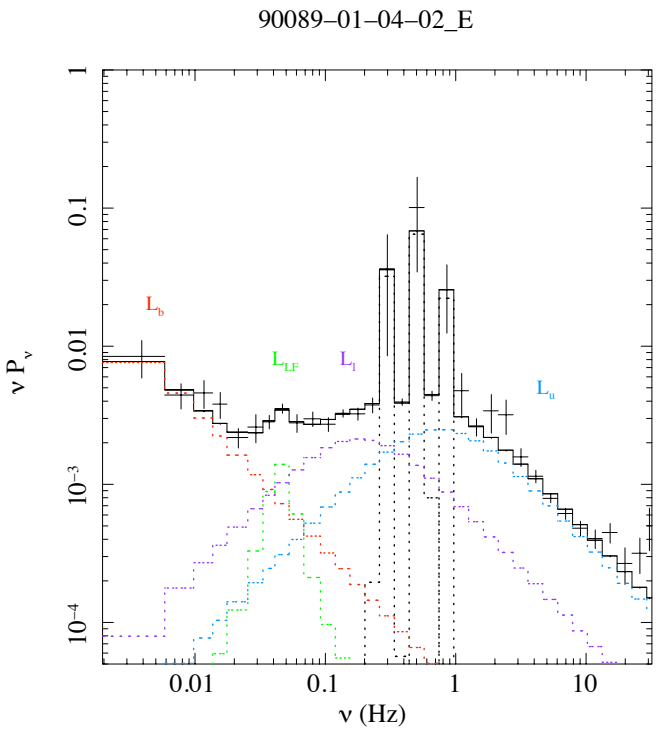

Figure 7.4: Example of fitted PSD for 4U 0115+63, in the $\nu \times \mathrm{P}_\nu$ representation. Data points are marked by crosses; each Lorentzian component is represented by a colored line, with its name labelled. Note the difference between broad noise (L_b, L_l, L_u) and peaked noise (L_LF) components. The three very peaked features at 0.1–1 Hz are the signature of the neutron star spin, with the fundamental and its two harmonics; they are fitted with fixed width Lorentzians (black dotted lines).

A clear pattern is recognizable in the HID/CD of the source, graphically marked by different colors: in correspondence to low intensity observations, the source draws an horizontal branch (HB, red points); it includes pointings both at the beginning and in the last part of the outburst, representing a start and an end point of the journey the source makes through the diagram. The remaining observations, covering the central, prolonged phase of the outburst, trace instead a diagonal branch (DB, black points), extending to a wider range in intensity than the HB. We defined the two branches according to this plot, and maintained the same color convention for subsequent diagrams with the aim of characterizing the

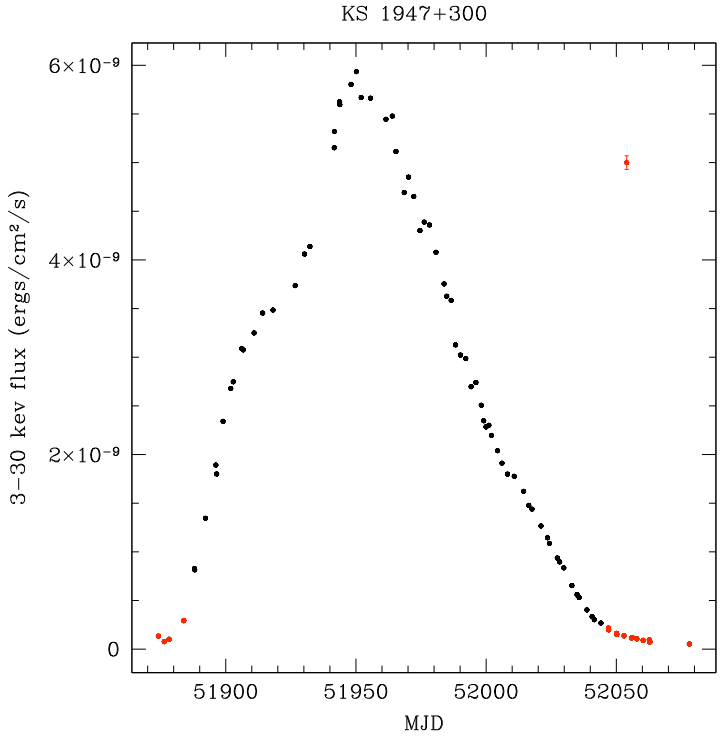

Figure 7.5: Integrated 3–30 keV flux for KS 1947+300. Red points represent observations at the beginning and at the end of the ourburst, defining the HB. Black points represent the central phase of the outburst, the DB (see Fig. 7.5). Typical error bars for red points are shown; for black points, error bars are of the same order of the marks.

two different branches.

The CD reflects what emerges from the HID, displaying the same two branches, although with large dispersion for the HB. Since it is constituted by low flux observations, this branch is affected by larger uncertainty. CD is not displayed here.

The two color vs. time diagrams show an inverse behavior one respect to the other in the DB; the HC correlates in fact with flux, reaching a maximum value in correspondence of the peak of the outburst; the SC follows an inverse path, anti-correlating with flux. In the HB, both colors behave the same, with a rise at

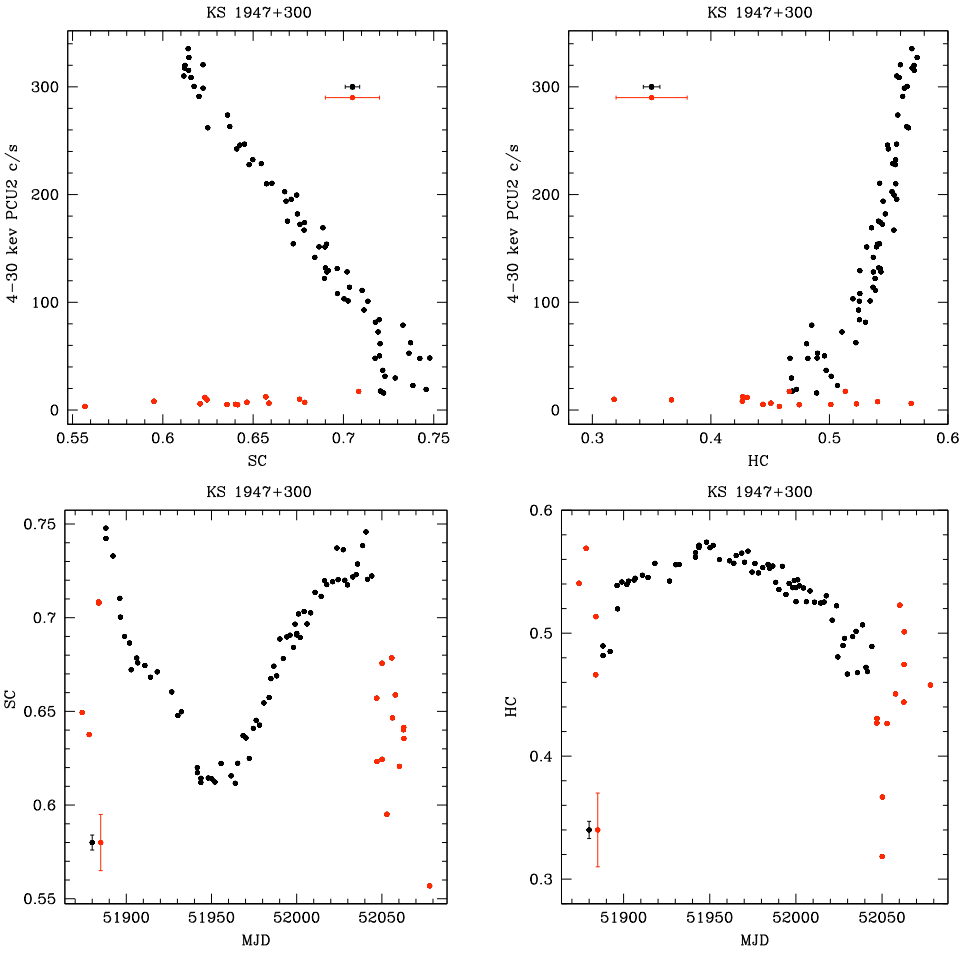

Figure 7.6: HIDs and colors behavior during KS 1947+300 outburst. Typical error bars are shown.

the beginning of the outburst, and a decay at the end.

Energy spectra were fitted by a model constituted by photoelectric absorption, a power law with high-energy cutoff and an iron fluorescence line. The photoabsorption was fixed at 4.5×10^{-21} cm^{-2} according to what Naik et al. (2006) found from *BeppoSAX* data. Leaving this parameter free did not result in consistent

fitted values along the outburst, so that we preferred to constrain it to the *BeppoSAX* value.

In Fig. 7.7 we display the behavior of the spectral parameters of the power law component, i.e. the spectral index Γ and the cutoff energy.

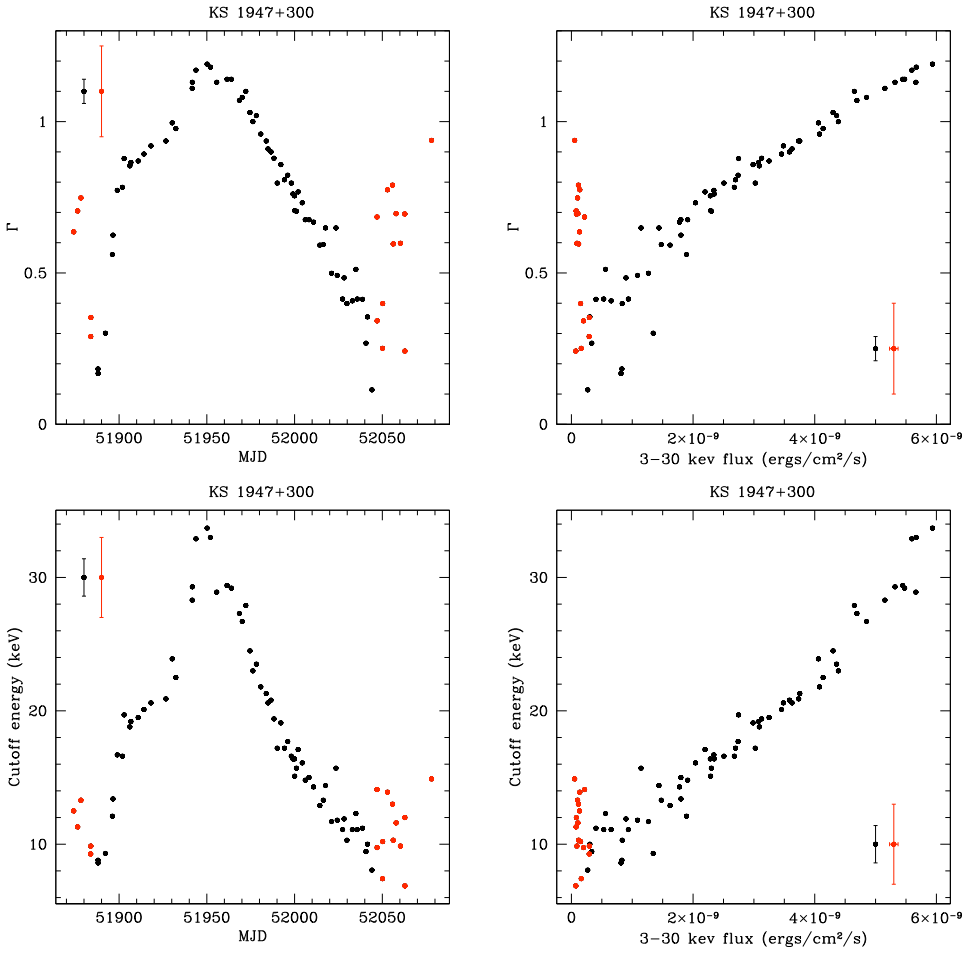

Figure 7.7: High-energy cutoff power law behavior during KS 1947+300 outburst.

Their trend with time (left side) and flux (right side) is shown. The spectral

index clearly correlates with flux in the DB, while anti-correlates with it in the HB. A similar trend is sketched by the cutoff energy. We show in Fig. 7.8 a tentative correlation between the two power law parameters.

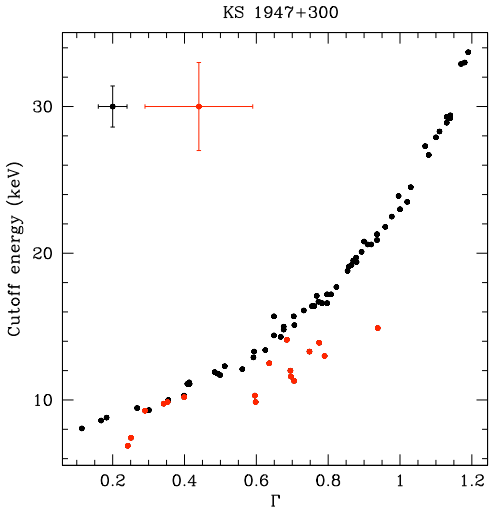

Figure 7.8: Relation between the spectral index and the cutoff energy.

In Fig. 7.9 the behavior of the Fe line with time and flux is presented. This component is needed to obtain best fit for all observations, except for the very last ones of the decay phase (until MJD = 52050). For the line energy, although showing a larger range of variability along the HB than in the DB, no clear trend during the outburst can be identified. The line width (σ) was almost constant during the outburst, and was eventually fixed at 0.5 keV in all the fits. The normalization is correlated with flux. The EW of the line is anti-correlated with flux at low luminosity, up to $L_{\rm X} = 3.4 \times 10^{37}$ ergs cm^{-1} (or flux = $2{\times}10^{9}$ ergs cm^{-2} s^{-1}), when it reaches an almost constant value of about 0.05 keV. This is due to an almost 1:1 relation between the normalization of the component and the total flux at high luminosity.

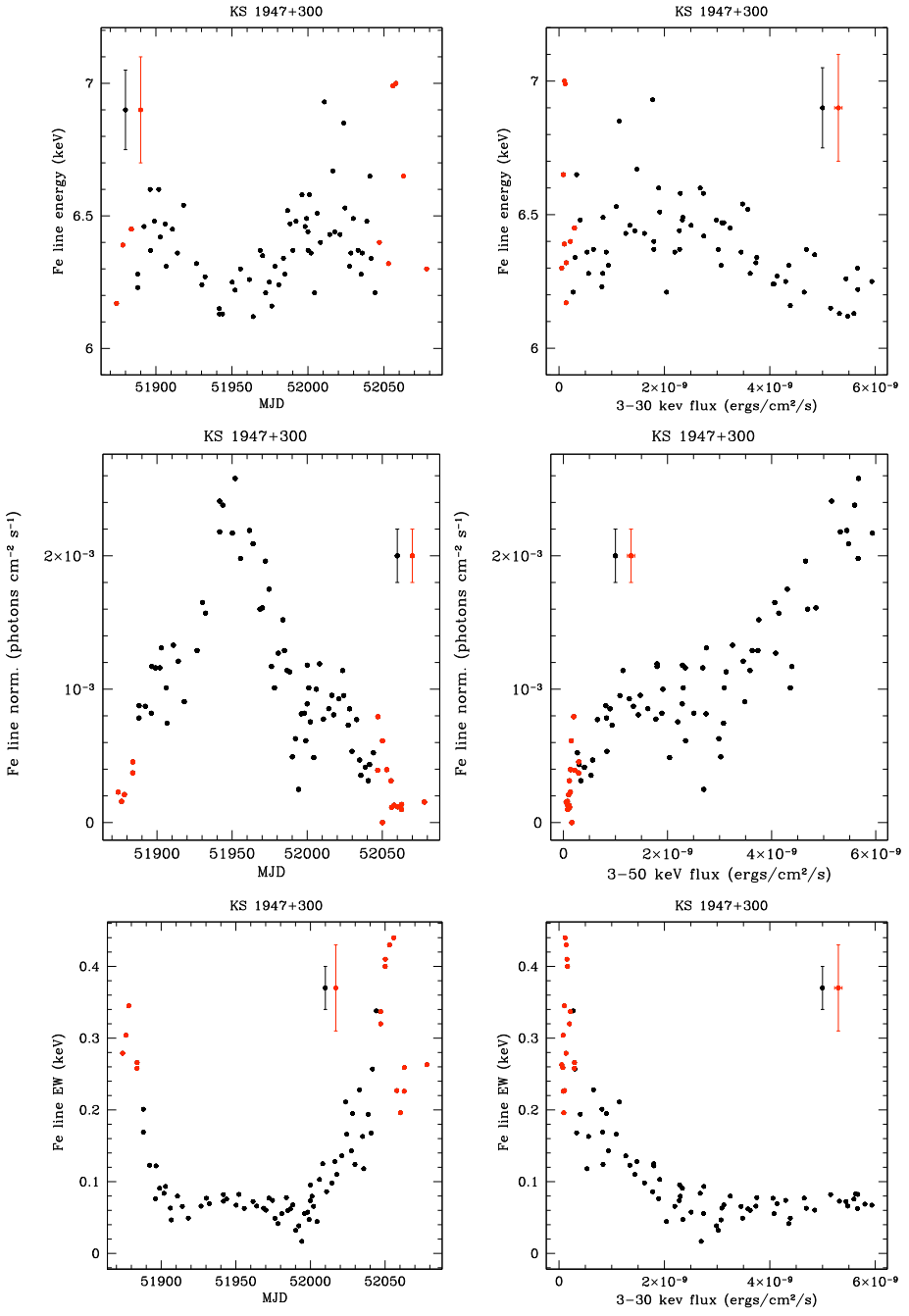

Figure 7.9: Fe fluorescence line during KS 1947+300 outburst.

Timing analysis

The power spectra were fitted with the sum of, at most, three zero-centered Lorentzians. The low-frequency noise is accounted for by $L_{\rm b}$, whose characteristic frequency varies along the outburst between 0.001–0.06 Hz. This component appears only during the brightest phase of the outburst, disappearing after that. Due to the very low characteristic frequency of this component (often peaks outside the available frequency range), this is generally poorly constrained. $L_{\rm l}$ describes the noise below 1 Hz, with a characteristic frequency varying between 0.01–0.35 Hz. When $L_{\rm u}$ is not present, it also describes the noise up to 10 Hz. This component is the only one which is constantly present along the outburst. With the highest fractional rms (up to 65 %), it is the best constrained component. $L_{\rm u}$ accounts instead for the high-frequency noise, with $\nu_{\rm u} \sim 0.7$–6.9 Hz. It appears close to the beginning of the outburst, but after the HB, and remains detectable up to the bright phase. Its rms varies between 4%–14%.

We show in Fig. 7.10 the evolution of $\nu_{\rm l}$ and the corresponding rms during the outburst. The characteristic frequency of the $L_{\rm l}$ component displays a clear relation with flux in the HB, while it remains fairly constant during the DB. During the HB as the flux increases the $L_{\rm l}$ characteristic frequency increases. At Lx $> 1.6 \times 10^{37}$ erg/s (or flux $> 1.3 \times 10^{-9}$ ergs cm^{-2} s^{-1}) the frequency saturates and remains unchanged within the errors at 0.2 Hz. The rms exhibits the highest values during the HB, decreasing and settling down to $\sim 20\%$ during the DB. The amplitude of the variation shown in the HB is considerable (25–65 %).

In Fig. 7.11 we show the possibly correlated behavior of the characteristic frequency of the two timing components, $\nu_{\rm l}$ and $\nu_{\rm u}$. In Fig. 7.12 we present the relation between $\nu_{\rm l}$ and spectral parameters, namely the spectral index and the cut-off energy. Weak associations could be established with the spectral parameters, although two distinct trends can be identified in correspondence of the two spectral branches. This is a confirmation of the correlation with flux.

Also from timing analysis, the two branches are clearly distinguishable, being the HB the state associated to lower characteristic frequencies of the Lorentzian components and strongest rms.

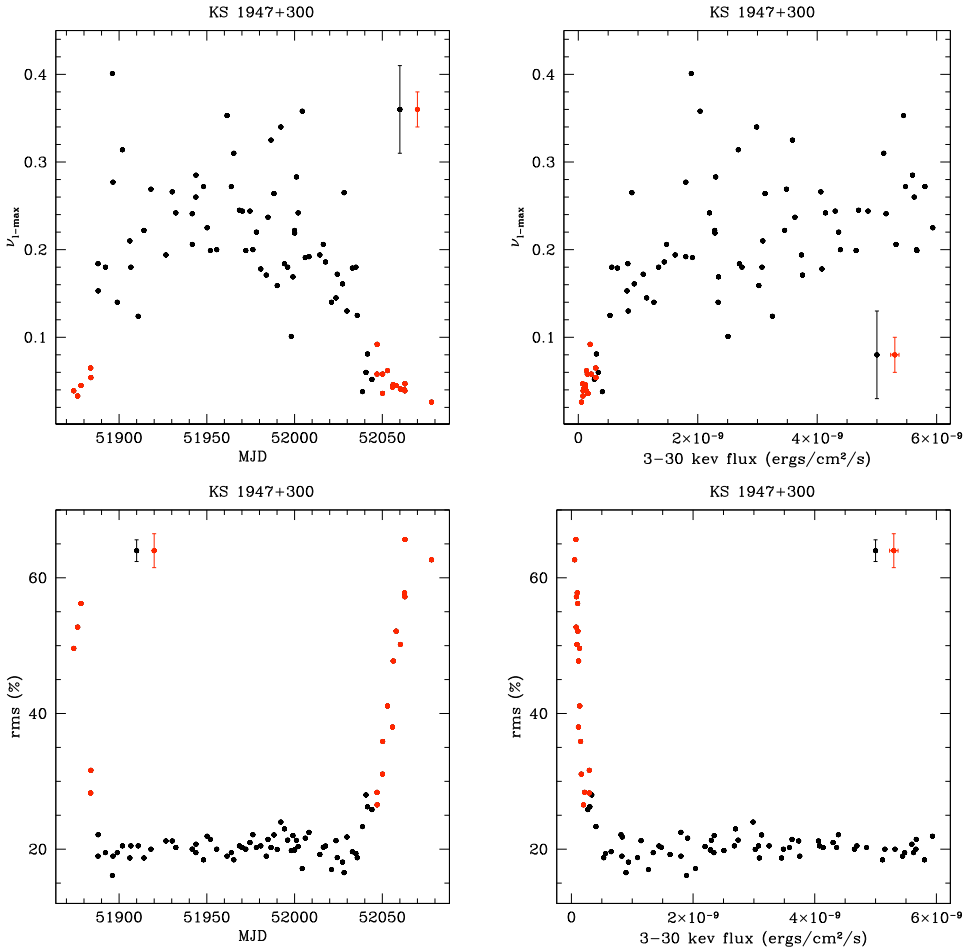

Figure 7.10: Characteristic (maximum) frequency ν_1 and corresponding rms during KS 1947+300 outburst.

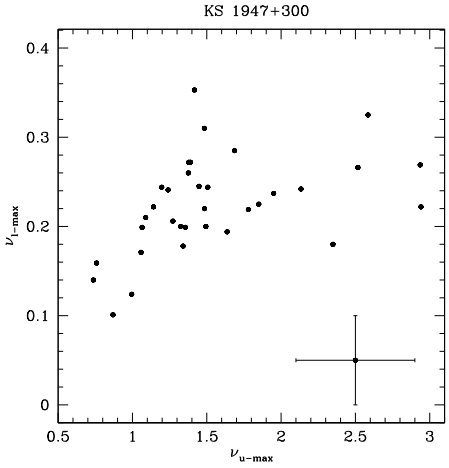

Figure 7.11: Relation between ν_{l} and ν_{u}.

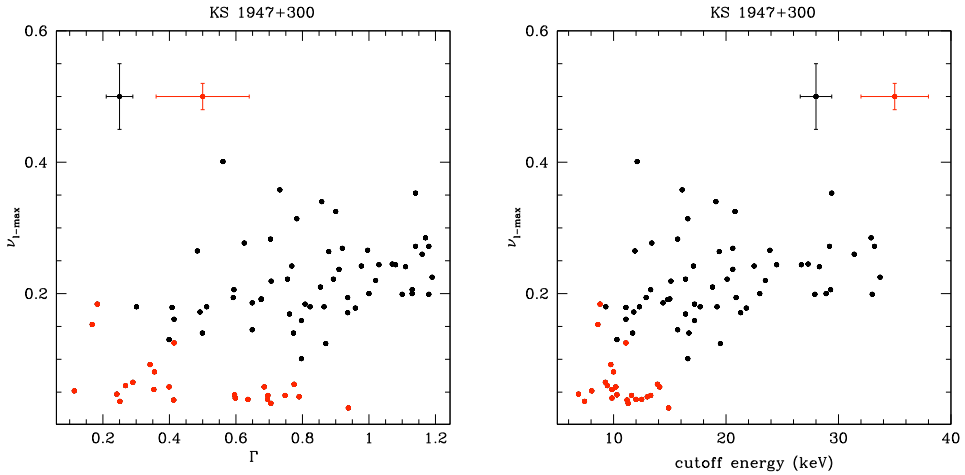

Figure 7.12: Relation between ν_l and spectral parameters.

7.5.2 EXO 2030+375

The total duration of the outburst was $\sim$ 155 days, the peak intensity was a factor of 4 larger than KS 1947+300. A peak X-ray luminosity of $L_{\rm X} = 1.5 \times 10^{38}$ erg s^{-1} is obtained at MJD = 53965, assuming a distance of 7.1 kpc. Spectral analysis of RXTE data from the 2004 outburst of EXO 2030+375 was also performed by Wilson et al. (2008): in this work, we extend their study to a low luminosity range.

Spectral analysis

This source is known to be characterized by a weak cyclotron resonance scattering feature at $\sim$10 keV (Wilson & Finger 2006; Klochkov et al. 2007). In our spectra its presence was consistently found only in correspondence to the brightest, central part of the outburst, while including it in spectra of observation taken at MJD $>$ 53 993 did not result in a better fit. No harmonics were found. To account for this feature, we employed the GABS component in XSPEC, a gaussian absorption line described by the following profile:

$$I(E) = \exp(-(\tau/\sqrt{2\pi}\ \sigma)\exp(-0.5((E - E_{\rm c})/\sigma)^2)) \quad ,$$

where $E_{\rm c}$ is the line energy in keV, σ is the line width in keV, and τ is the optical depth at the line center.

In Fig. 7.13 we show the trend followed by the 3–30 keV flux during the outburst. In this case the outburst is not as well sampled as for KS 1947+300, missing the very first phase of its rising phase. This is reflected in the HIDs (Fig. 7.14), where the HB, clearly recognizable in this source as well, is made up only by observations covering the last part of the outburst. In Fig. 7.14 we also present the behavior of the two colors along the outburst.

A trend very similar to that of KS 1947+300 is shown: two branches are recognizable in the CD as well, although with larger dispersion than in the HID; the HC correlates with flux, displaying a peak in correspondence with the peak of the outburst, while an opposite behavior characterizes the SC. This is true for the DB, while in the HB the two colors seem both to decrease with time (and thus

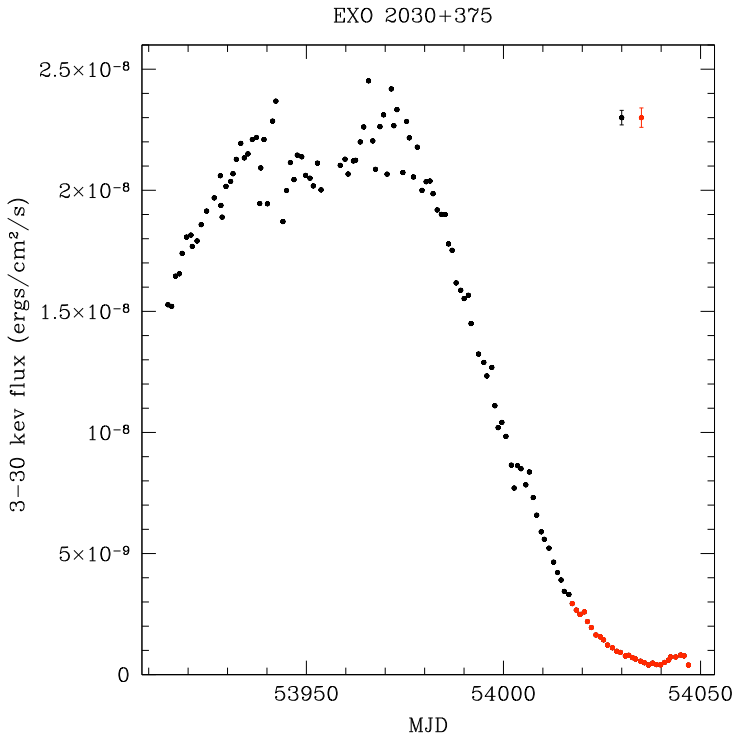

Figure 7.13: Integrated 3–30 keV flux for EXO 2030+375.

intensity).

Energy spectra were fitted by a model constituted by photoelectric absorption, a power law with high-energy cutoff and, in the brightest part of the outburst, a cyclotron line. The photoabsorption was left free to vary, since previous works did not provide a well constrained value for this parameter. The retrieved values along the outbursts were 1–3 $\times 10^{22}$ cm^{-2}, compatible with previous results (Reynolds et al. 1993; Sun et al. 1994; Klochkov et al. 2007; Wilson et al. 2008).

In Fig. 7.15 we show the behavior of the two spectral parameters relative to the power law component, i.e. the spectral index Γ and the cutoff energy. On the left side, their trend with time is shown, while on the right side their evolution

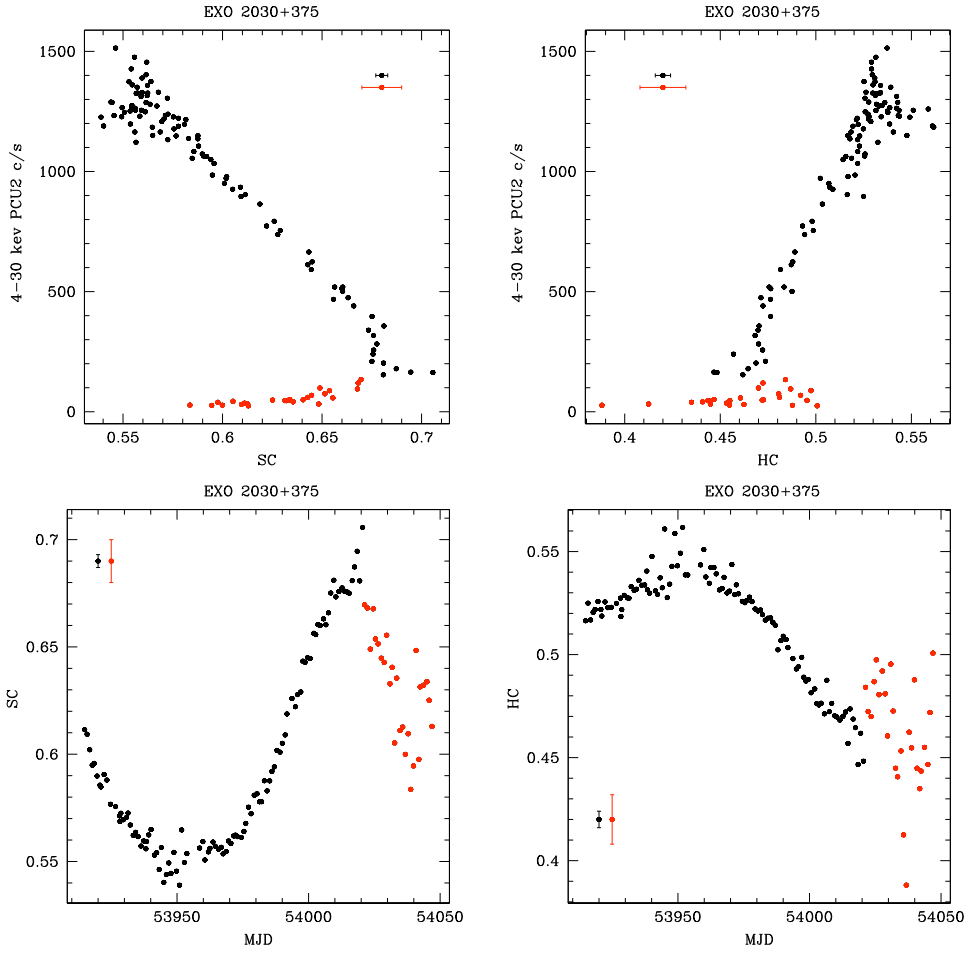

Figure 7.14: HIDs and colors behavior during EXO 2030+375 outburst.

with flux is presented. Again, strong similarities with KS 1947+300 can be established, as the spectral index correlates with flux in the DB, while anti-correlates with it in the HB. An analogous trend is sketched by the cutoff energy, pointing to a physical consistence of this phenological model, since the same physical process must be involved in order to produce both features.

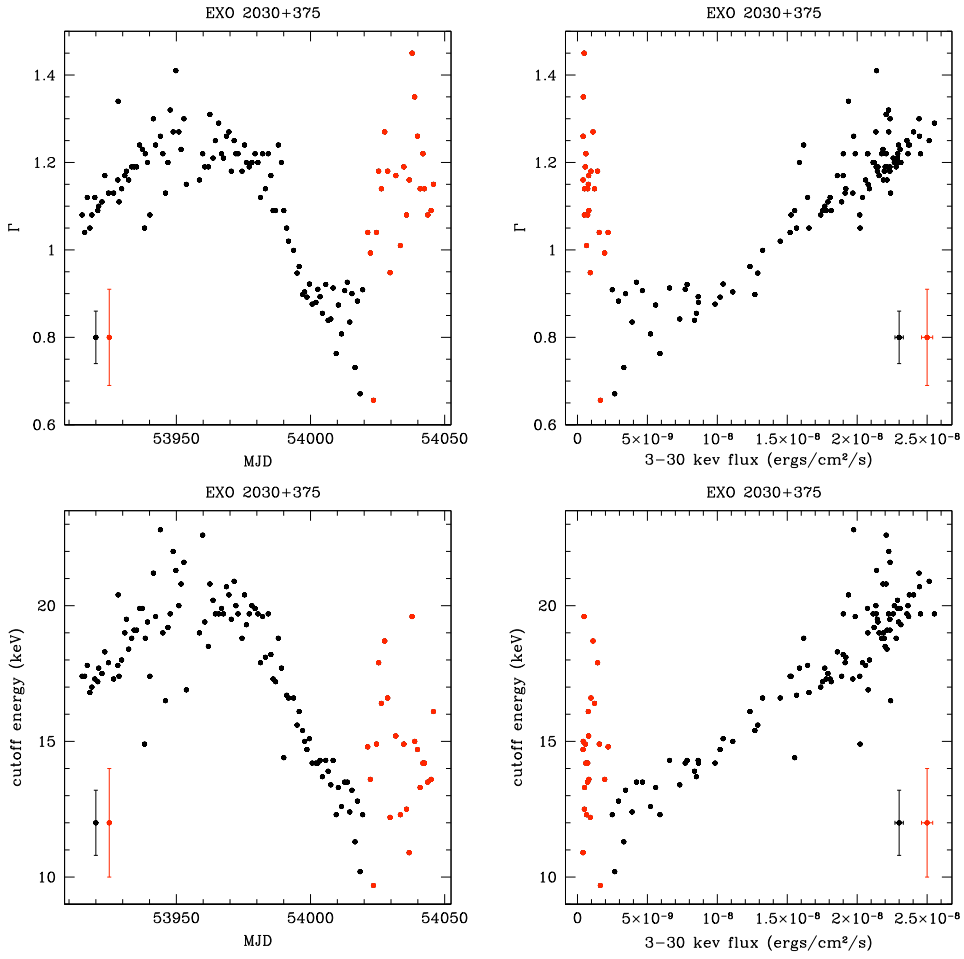

Figure 7.15: High-energy cutoff power law behavior during EXO 2030+375 outburst.

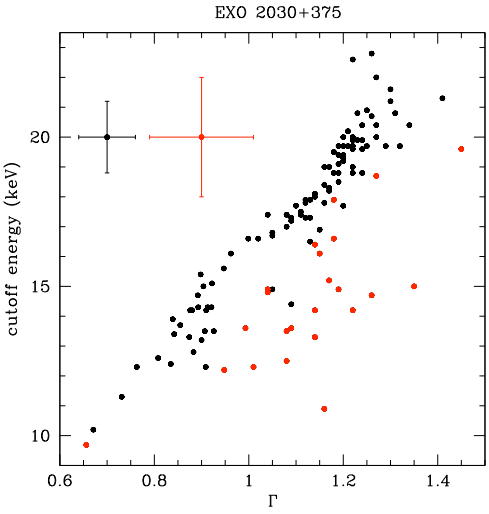

Figure 7.16: Relation between the spectral index and the cutoff energy.

We clarify this in Fig. 7.16, where a clear correlation can be seen during all the outburst, although different slopes mark the two branches.

In Fig. 7.17 the behavior of the Fe line energy with respect to time and flux is shown. The width of the component was fixed at 0.5 keV. No clear trend during the outburst can be identified in this case for the line energy and EW and the large dispersion shown in the HB may be due to the lower statistics of low flux observations. The component is very faint during the HB, so that also its central energy was fixed at 6.4 keV, while the normalization was left free to vary. The corresponding pointings are only shown in the plots of the normalization. The strength of this component is strongly correlated with flux. The equivalent width weakly correlates with flux.

The CRSF was found not to vary during the outburst, within the errors. Fitting its three parameters with a constant, gave the following results:

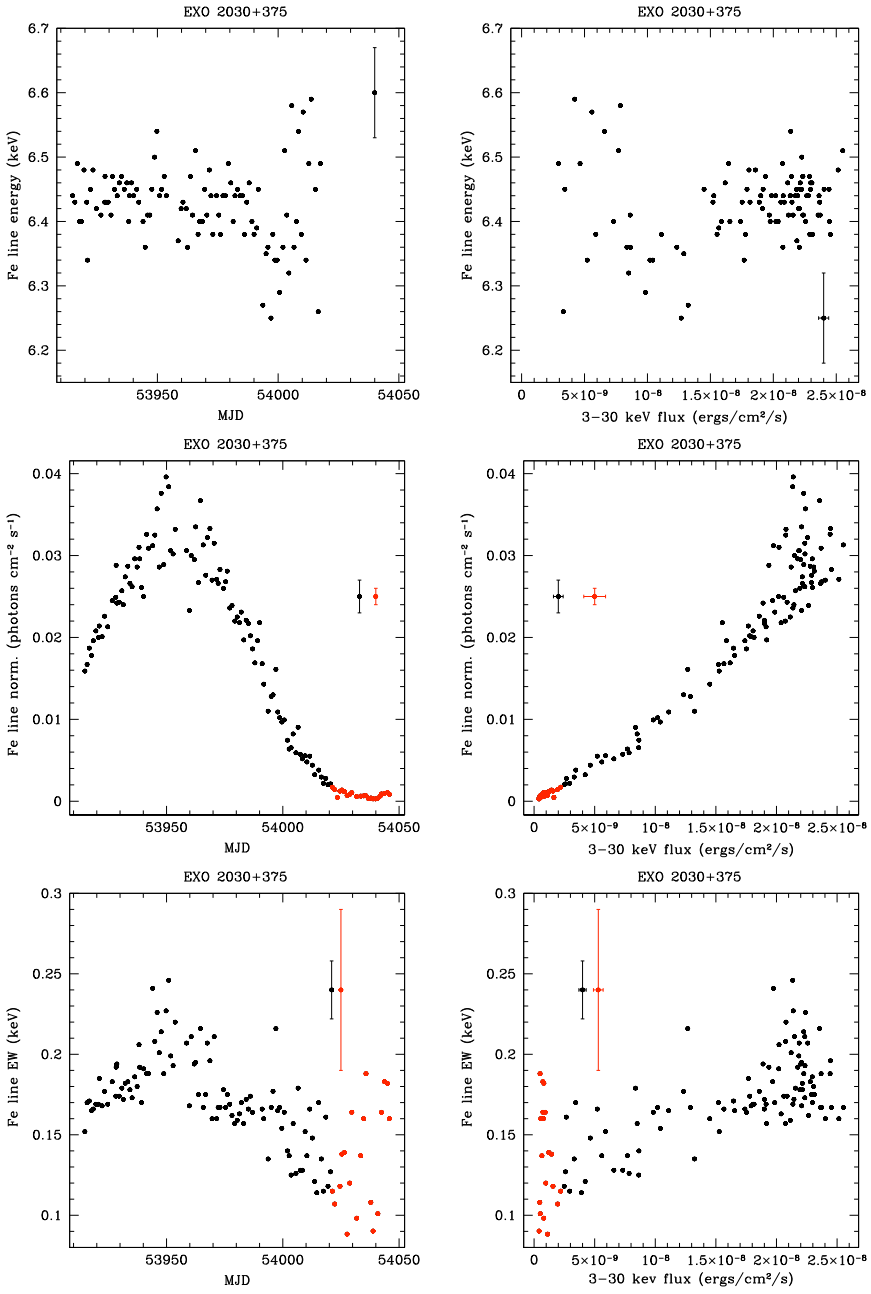

Figure 7.17: Fluerescence Fe line during EXO 2030+375 outburst.

$$E_{\rm c} = 9.62 \pm 0.04 \quad (\text{rms of residuals} = 0.63)$$
$$\tau = 1.36 \pm 0.03 \quad (\text{rms of residuals} = 0.29)$$
$$\text{width} = 4.03 \pm 0.06 \quad (\text{rms of residuals} = 0.55)$$

All the three parameters of the feature are thus consistent with a constant.

Timing analysis

The power spectra were at first fitted with the sum of, at most, four Lorentzians. The low-frequency component provided very poor constraints; with the presence of an additional component compared with KS 1947+300, this resulted in a high degree of freedom that could limit the possibility of good constraints for all the fitted components. We chose not to account for the low-frequency noise, excluding the first three channels in frequency at the moment of fitting. We thus employed a maximum number of three Lorentzians in this case.

$L_{\rm l}$ describes the noise below 5 Hz and is constantly present along the outburst. Its characteristic frequency varies in the range 0.02–0.5 Hz.

As for KS 1947+300, this components exhibits the highest fractional rms (16–40 %), being the best constrained component. $L_{\rm u}$ accounts instead for the high-frequency noise, with characteristic frequency ∼1–5 Hz. This component is present in the brightest phase of the outburst, from the beginning of our data sample, until MJD = 53981. During the whole DB, another, higher-frequency, component is detectable, $L_{\rm u'}$, with $\nu_{\rm u'} \sim 0.2$–10 Hz.

We show in Figs. 7.18 and 7.19 the evolution of the characteristic frequency and the rms of the $L_{\rm l}$ and $L_{\rm u}$ components along the outburst.

Like for KS 1947+300, $\nu_{\rm l}$ roughly correlates with flux, with lower values at the beginning and at the end of the outburst and higher values at its peak. The rms seems to show in general lower values in correspondence of the HB, but this relation is not straightforward. If this was the case, the source would show an opposite trend to KS 1947+300. The characteristic frequency of the $L_{\rm u}$ component, $\nu_{\rm u}$, shows a less marked correlation with flux, while the corresponding rms

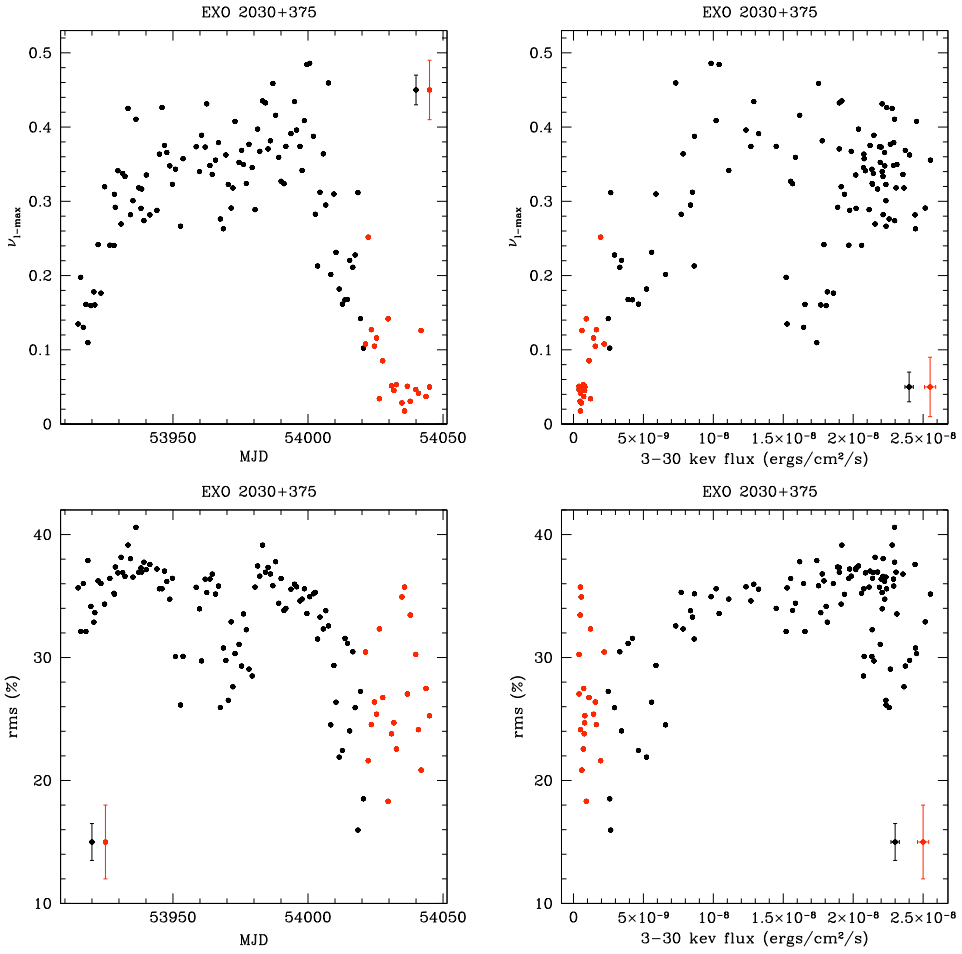

Figure 7.18: Characteristic (maximum) frequency and rms for the L_1 component during EXO 2030+375 outburst.

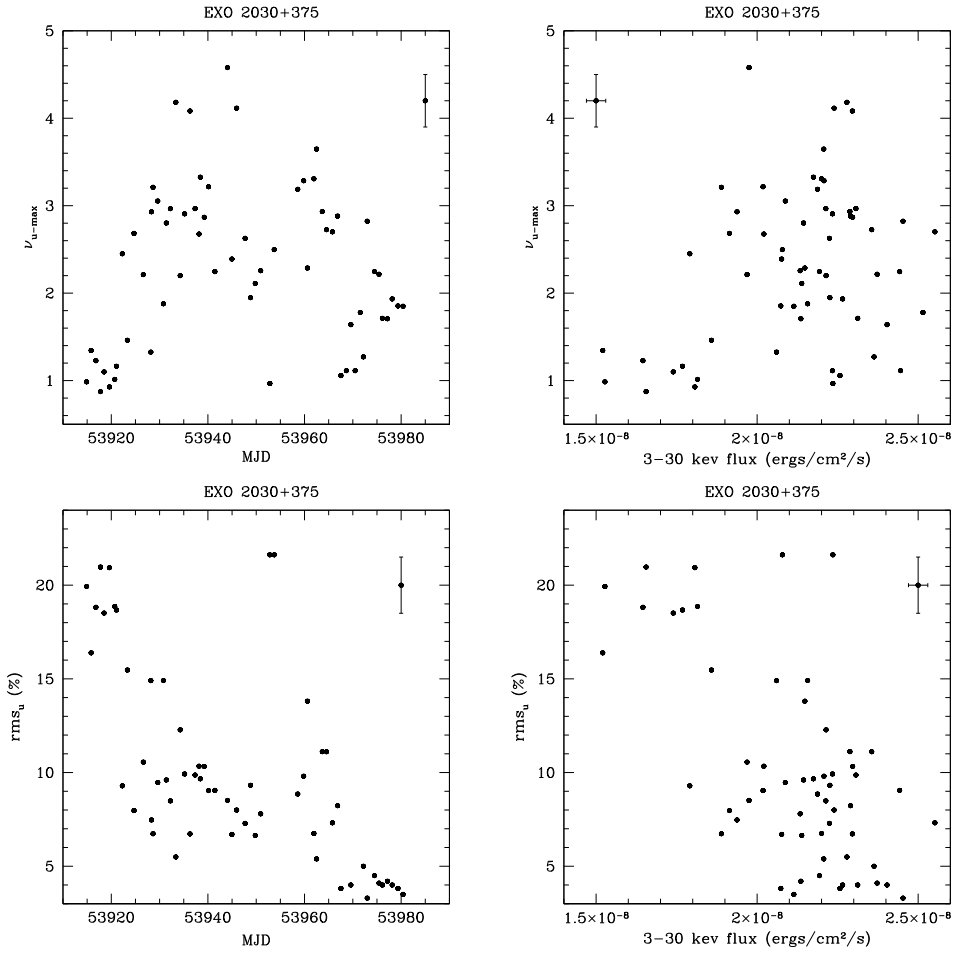

Figure 7.19: Characteristic (maximum) frequency and rms for the $L_{\rm u}$ component during EXO 2030+375 outburst.

anti-correlates.

For the best constrained component, $L_{\rm l}$, the HB is associated to lower frequency, as in KS 1947+300. The rms variation is instead similar in the two branches.

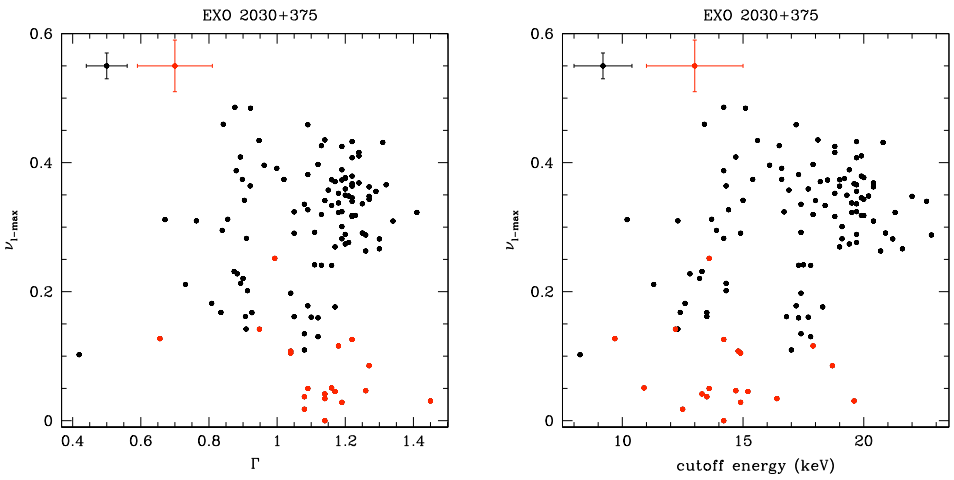

Figure 7.20: Characteristic (maximum) frequency ν_1 vs. spectral parameters during EXO 2030+375 outburst.

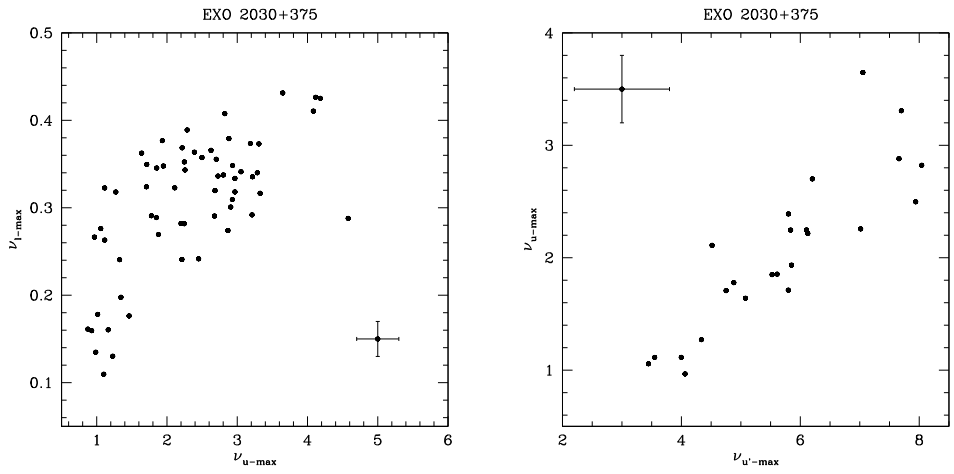

Figure 7.21: Correlation between the characteristic frequencies of the three timing components.

In Fig. 7.20 the relation between the characteristic frequency $\nu_{\rm l}$ and the spectral parameters (spectral index, cutoff) is shown. No clear correlations can be established in this case.

In Fig. 7.21 we show correlations between the characteristic frequencies of the three timing components, $\nu_{\rm l}$, $\nu_{\rm u}$ and $\nu_{\rm u'}$.

7.5.3 4U 0115+63

The total duration of the outburst was ∼55 days, the shortest among the sources analyzed in this work. The rise covered by RXTE data was shorter than the decay (∼6 days vs. ∼35 days). The brightest phase of the outburst displays a double-peak profile and lasted for ∼9 days. The maximum X-ray luminosity was reached at MJD ∼ 53262 and amounted to 1.4×10^{38} erg s^{-1}.

Spectral analysis

The retrieved 3–30 keV flux is shown in Fig. 7.22.

The energy spectrum is known to be complicated by a fundamental and up to four harmonics CRSFs. In the energy range considered in this work, namely 3–30 keV, not only the fundamental at 11 keV but also the first harmonic of the cyclotron line distort the spectral continuum. We obtained the best fit by using in this case the CYCLABS component in XSPEC (Mihara et al. 1990), described by the following profile:

$$I(E) = \left[- \tau_{\rm f} \frac{(\sigma_{\rm f} E/E_{\rm c})^2}{(E-E_{\rm c})^2 + \sigma_{\rm f}^2} + \tau_{\rm 2h} \frac{(\sigma_{\rm 2h} E/2E_{\rm c})^2}{(E-2E_{\rm c})^2 + \sigma_{\rm 2h}^2} \right] \quad ,$$

where $\tau_{\rm f}$ is the optical depth of the fundamental; $E_{\rm c}$ is the cyclotron energy in keV; $\sigma_{\rm f}$ is the width of the fundamental in keV; $\tau_{\rm 2h}$ is the optical depth of the first harmonic; $\sigma_{\rm 2h}$ is the width of the first harmonic. This component, analogous in profile to the GABS component, simultaneously accounts for the fundamental and its first harmonic. The central energy of the first harmonic is not a free parameter, being fixed, in this model, to the double of the fundamental.

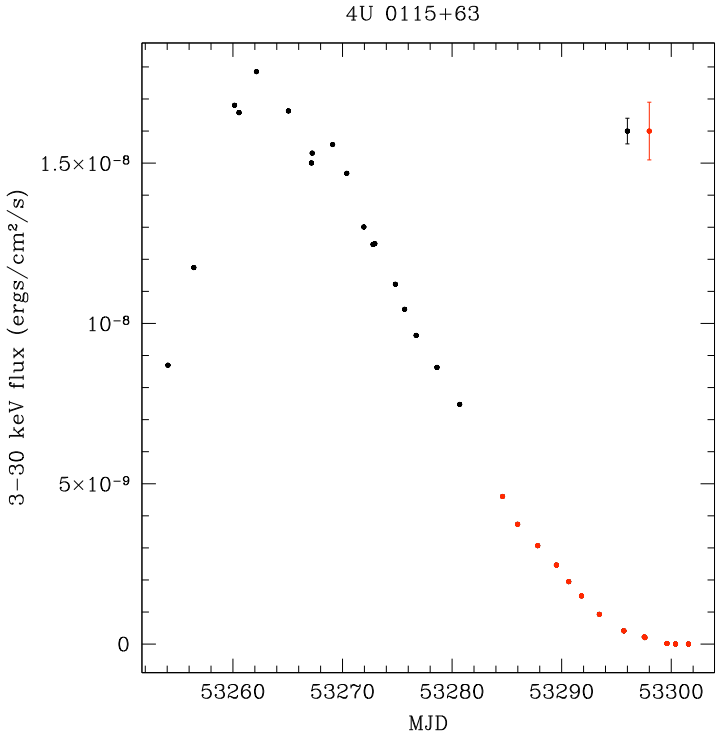

Figure 7.22: Integrated 3–30 keV flux for 4U 0115+63.

In Fig. 7.23 we show the HID, CD and colors trends during the outburst. The SC and HC follow a trend similar to that of KS 1947+300 and EXO 2030+375: in the DB, the HC correlates with flux and the SC anti-correlates with it; in the HB both colors anti-correlate with flux. For this source as well, we identified two spectral branches in the HID/CD. Moreover, we found that the system exhibits hysteresis both in the HID and in the CD. It means that points corresponding to observations of the rising phase of the outburst (black points) are shifted in color compared with those of the decay phase (green points), despite that the flux is similar. For similar values of flux, during the decay the emission is softer than during the rise. This effect was also present in EXO 2030+375, although not as significant as for this source.

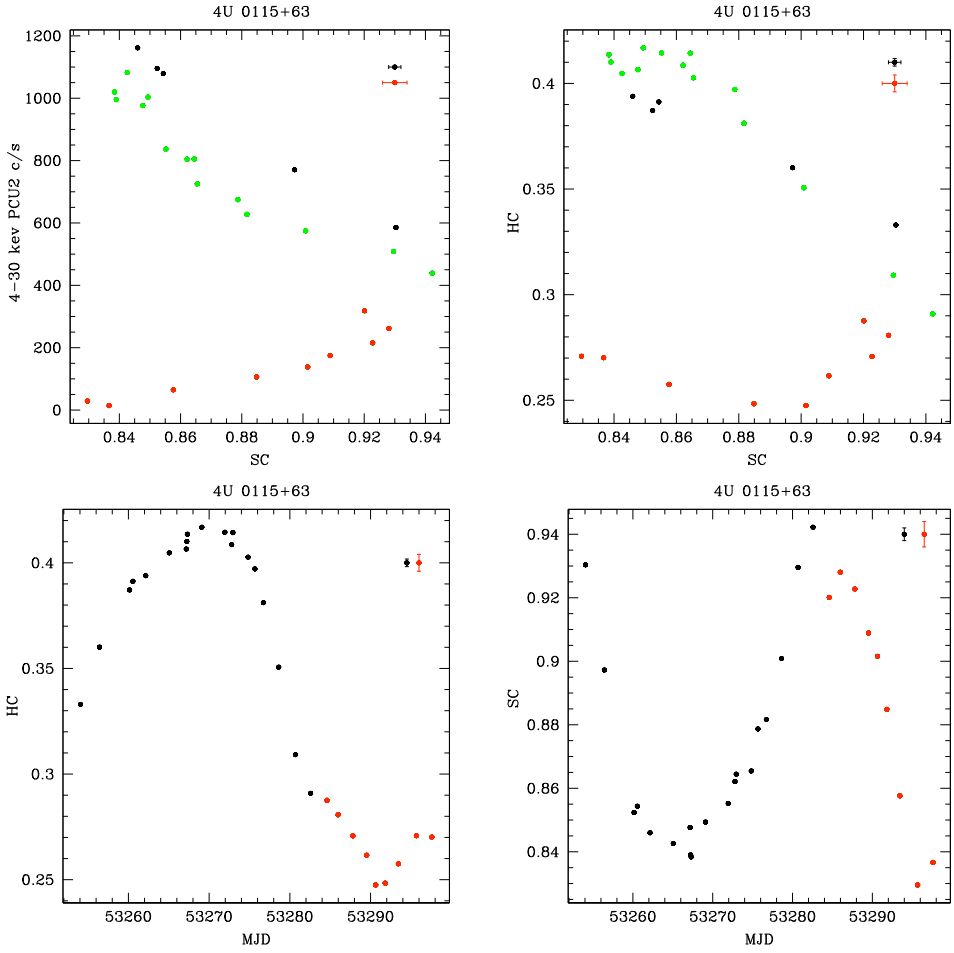

Figure 7.23: HID, CD and colors behavior during 4U 0115+63 outburst. Green points correspond to the decay phase, before the HB. Black error bars apply to both black and green points.

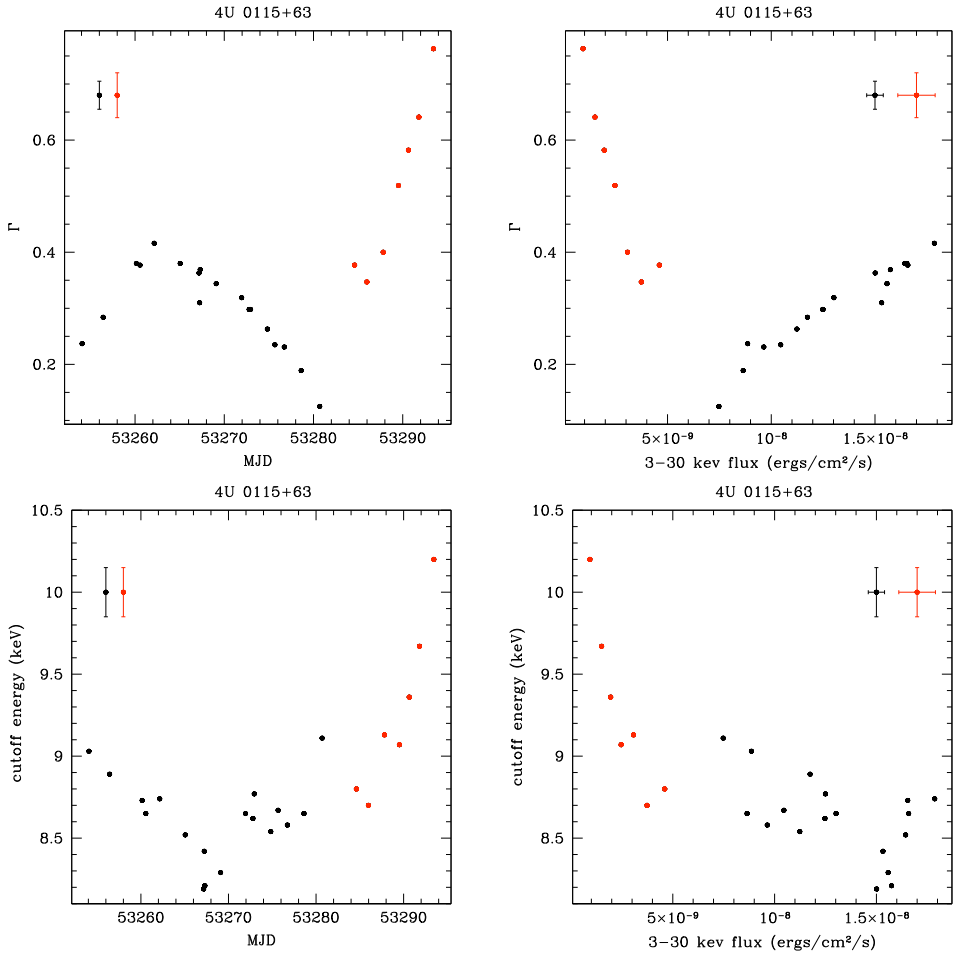

Figure 7.24: High-energy cutoff power law behavior during 4U 0115+63 outburst.

Energy spectra were fitted by a model constituted by photoelectric absorption, a power law with high-energy cutoff and a cyclotron absorption feature with two harmonics. The photoabsorption was left free to vary along the outburst, with a retrieved value of 0.9–1.5 $\times 10^{22}$ cm^{-2}, consistent with recent results by Ferrigno et al. (2009). It was eventually fixed at 0.9 $\times 10^{22}$ cm^{-2} for all the observations.

In Fig. 7.24 we show the behavior of the two spectral parameters of the power

law component, i.e. the spectral index Γ and the cutoff energy. On the left side, their trend with time is shown, while on the right side their evolution with flux is reported. Again, for the spectral index we found correlation with flux in the DB and anti-correlation in the HB, like in the previously analyzed systems. The cutoff anti-correlates with flux in both states. We illustrate the relation between the two parameters in Fig. 7.25.

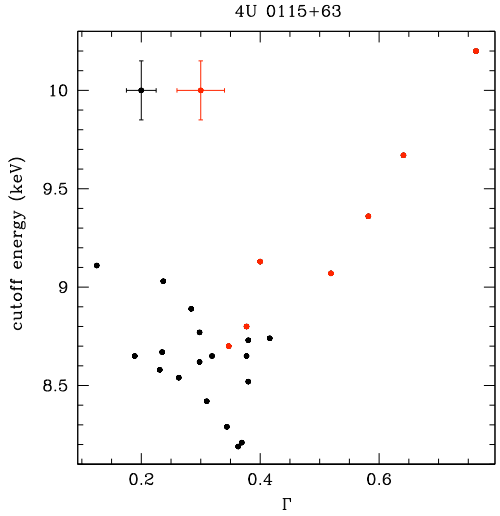

Figure 7.25: Relation between the spectral index and the cutoff energy.

In Fig. 7.26 the behavior of the Fe line with time (left panel) and flux (right panel) is displayed. During the fit, the width of the line was fixed at 0.5 keV. The normalization of the component correlates with flux. With an average value of 0.1±0.05, the equivalent width of the line is constant along the outburst.

We show in Fig. 7.27 the trend followed by the parameters characterizing the cyclotron feature (first harmonic). The fundamental energy varies along the outburst mainly between 10.5 and 17.5 keV, confirming results by Tsygankov et al. (2007). Its average optical depth varies between 0.2–0.5, while the line width varies between 2–11 keV. In 4U 0115+63 the CRSF firmly marks the two source states. In the DB, the central energy varies by ∼10% and it shows the

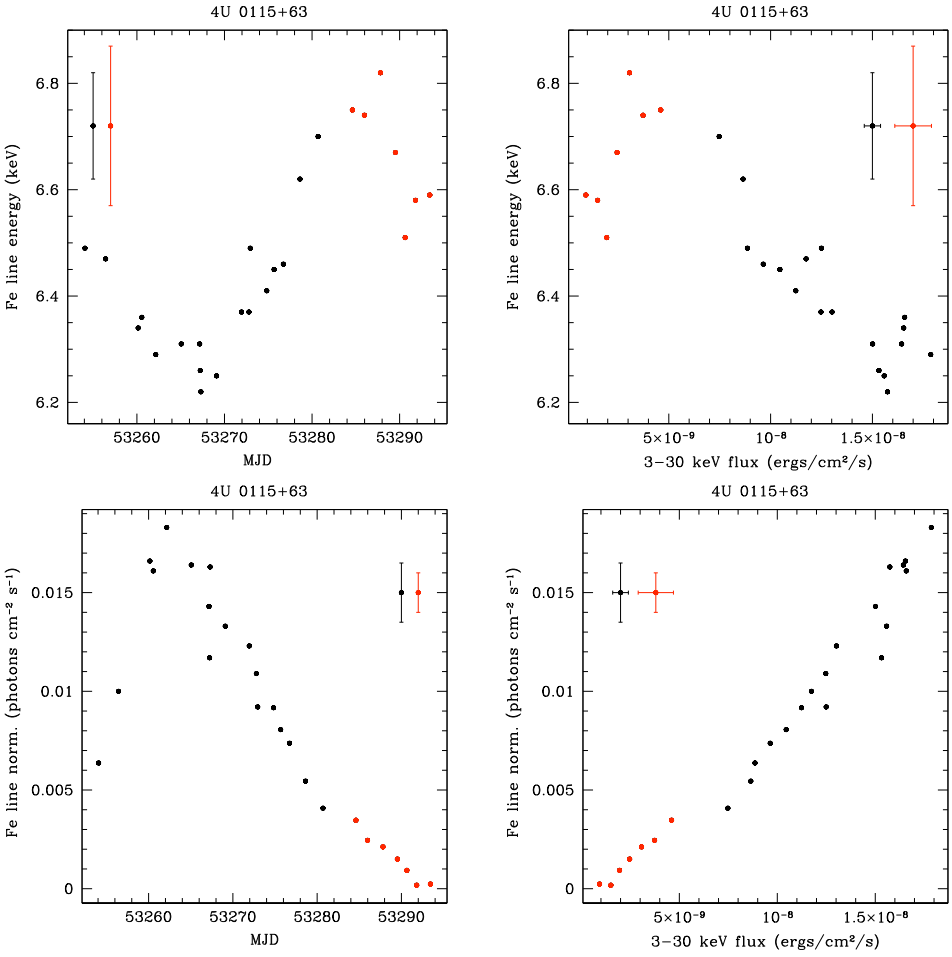

Figure 7.26: Fe fluorescence line during 4U 0115+63 outburst.

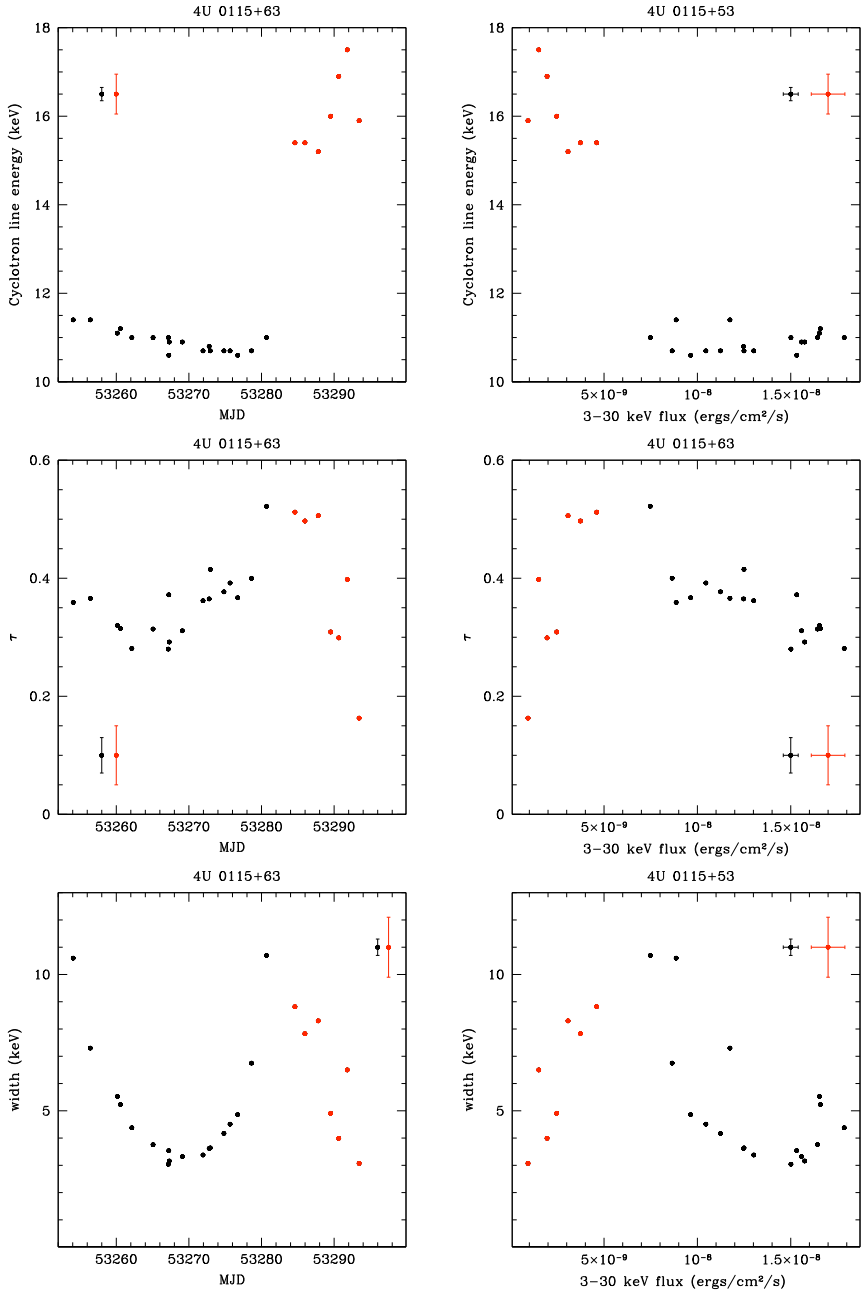

Figure 7.27: Cyclotron line parameters during 4U 0115+63 outburst.

lower values; in the HB, it varies with time by 17%, from lower to higher values. In the HB the highest values are retrieved. Anti-correlation with flux is shown in the HB, while no change is observed in the DB. The optical depth also shows the largest variation during the HB; it correlates with flux during the HB and anti-correlates during the DB. The same behavior is followed by the line width. A first harmonic is needed in order to obtain acceptable fits.

Timing analysis

The power spectra were fitted with the sum of, at most, four Lorentzians. The low-frequency noise is accounted for by $L_{\rm b}$, whose fitted characteristic frequency is always < 0.02 Hz. This component is present along the whole outburst, with the exception of the first two observations (corresponding to a X-ray luminosity of 7–9 $\times$ 10^{37} erg s^{-1}), where its inclusion did not lead to a better fit. Like for the other sources, due to the very low characteristic frequency of this component, this is generally poorly constrained. $L_{\rm l}$ describes the noise below 1 Hz and, like in the other systems, is constantly present along the outburst. Its characteristic frequency displays a variation between 0.1–1.2 Hz. $L_{\rm u}$ accounts for the high-frequency noise, with $\nu_{\rm u} \sim 0.7$–2.1 Hz. It appears very close to the beginning of the outburst (MJD = 53267.2) and remains detectable only in the few observations of the very bright phase (MJD = 53278.6), in correspondence of the DB.

In addition to the aforementioned broad noise components, a peaked noise component is also present, $L_{\rm LF}$. We will refer to this as a QPO, although the Q value is not always larger than 2. In fact, at the very beginning of the outburst, this is a zero-centered broad component ($Q = 0$), which evolves into a QPO after the first 4 observations (MJD = 53262.1). Its characteristic frequency varies between 0.03–0.16 Hz. We found evidence for this component in the entire DB and in only two observations of the HB.

We show in Fig. 7.28 the evolution of $\nu_{\rm l}$ and the corresponding rms during the outburst. The characteristic frequency of the $L_{\rm l}$ component displays a rather clear correlation with flux, with lower values at the end of the outburst and higher values at its peak; the rms varies between 10%–31%, showing the strongest variability in the HB. While it is constant on average in the DB, it exhibits a pro-

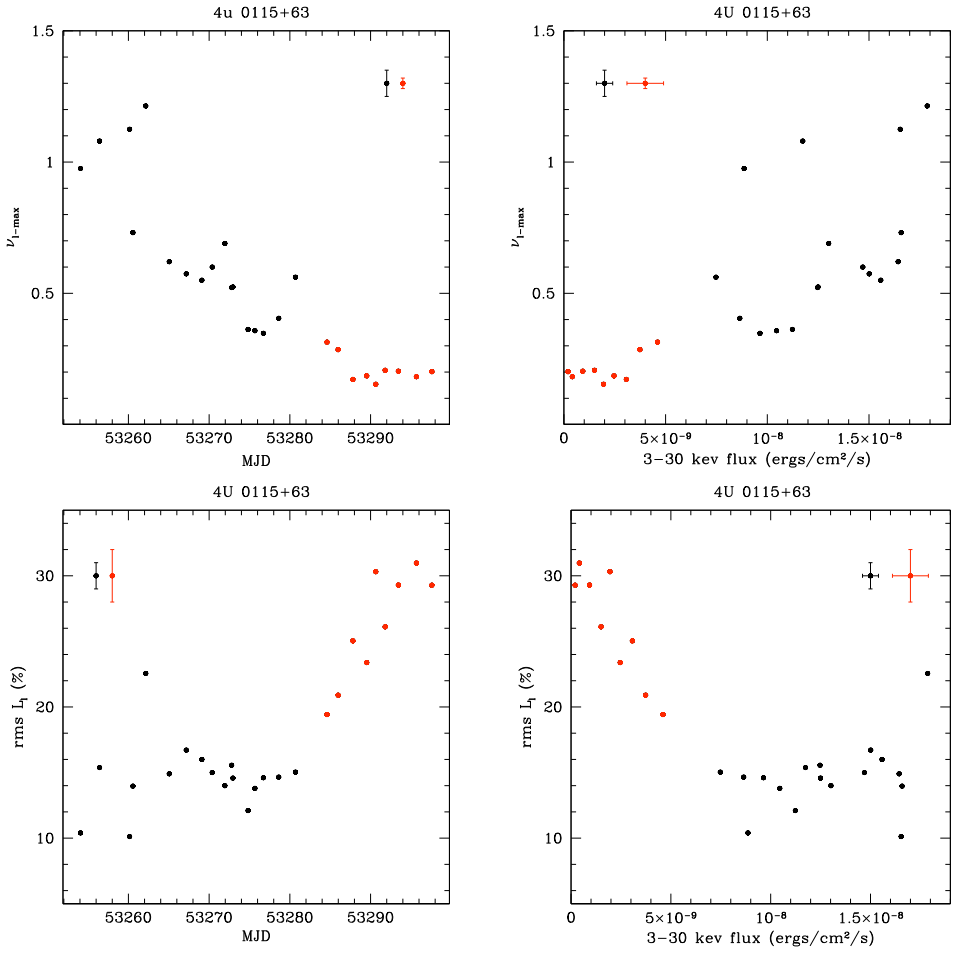

Figure 7.28: Characteristic (maximum) frequency and rms for the L_l component during 4U 0115+63 outburst.

nounced anti-correlation with flux during the HB: the strongest power for this component is given at the very end of the outburst, like for KS 1947+300. For both parameters we found evidence of two distinct trends during the two branches.

In Fig. 7.29 we show the evolution of $\nu_{\rm LF}$ and the corresponding rms. No clear trend can be invoked in this case.

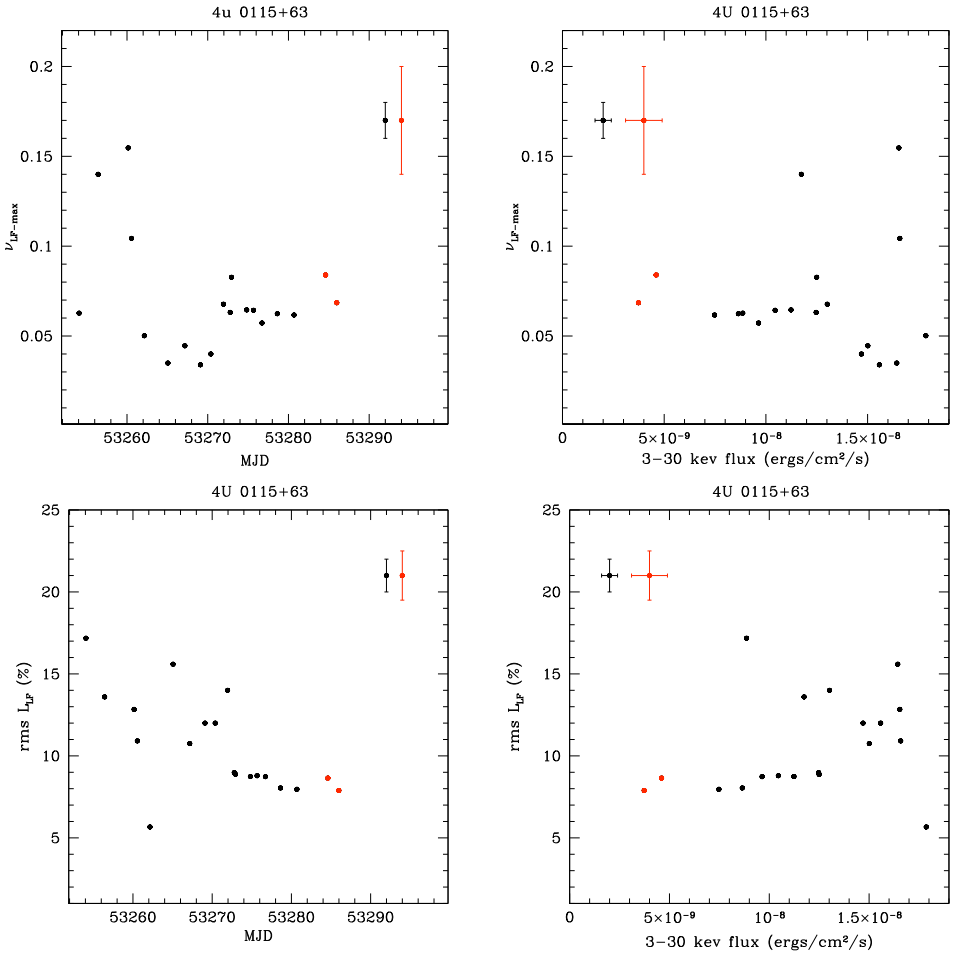

Figure 7.29: Characteristic (maximum) frequency and rms for the $L_{\rm LF}$ component during 4U 0115+63 outburst.

In Fig. 7.30 we show the relation between spectral and timing fit parameters. No correlations are found. Also, in this case no marked distinction emerges between the DB and the HB, with the exception of the plot of ν_1 vs. the central energy of the cyclotron absorption line: here the two branches are distinguishable, with low values of ν_1 associated to large values of the cyclotron energy and vice versa.

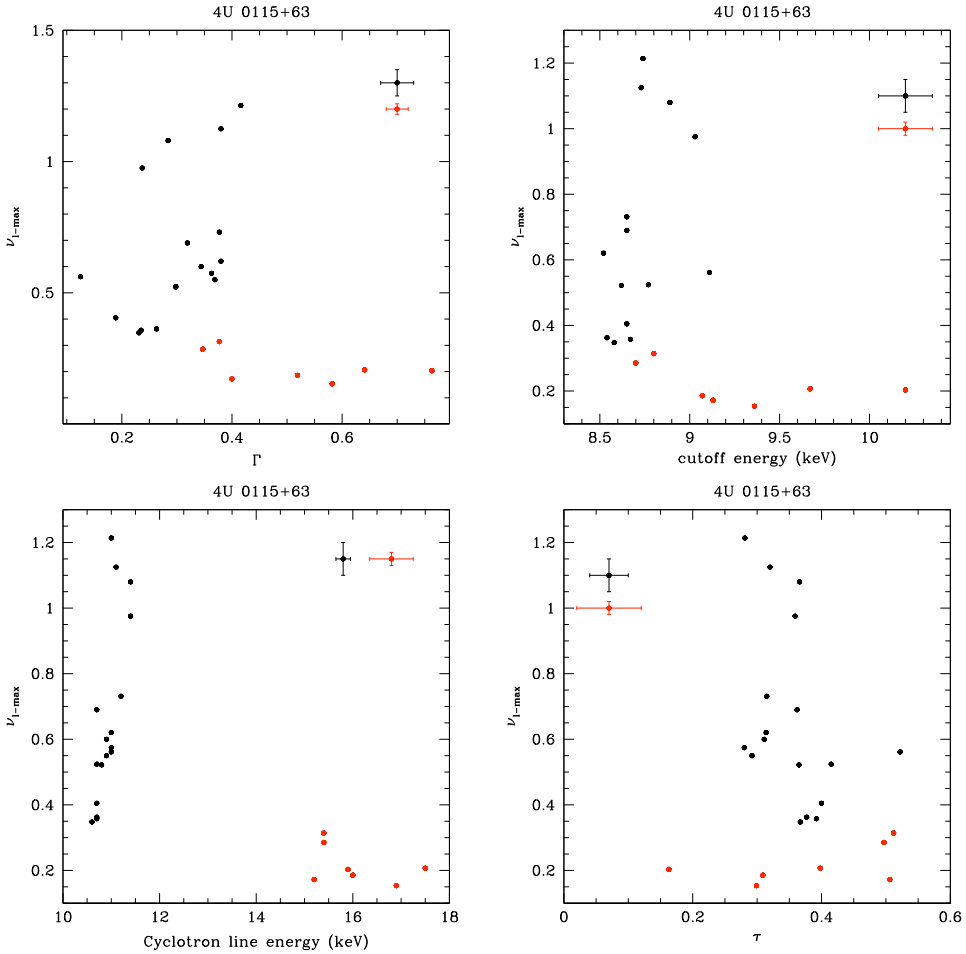

Figure 7.30: Timing vs. spectral fit parameters during 4U 0115+63 outburst.

7.5.4 V 0332+53

This system showed the brightest outburst of the four sources studied, whose total duration was $\sim$ 105 days. As in 4U 0115+63, the decay was slower than the rise, but with a longer tail than that shown by 4U 0115+63 at the end of the outburst. A maximum X-ray luminosity of 3.4×10^{38} erg s^{-1} was measured at MJD $\sim$ 53364

Spectral analysis

The 3–30 keV flux as a function of time is shown in Fig. 7.31.

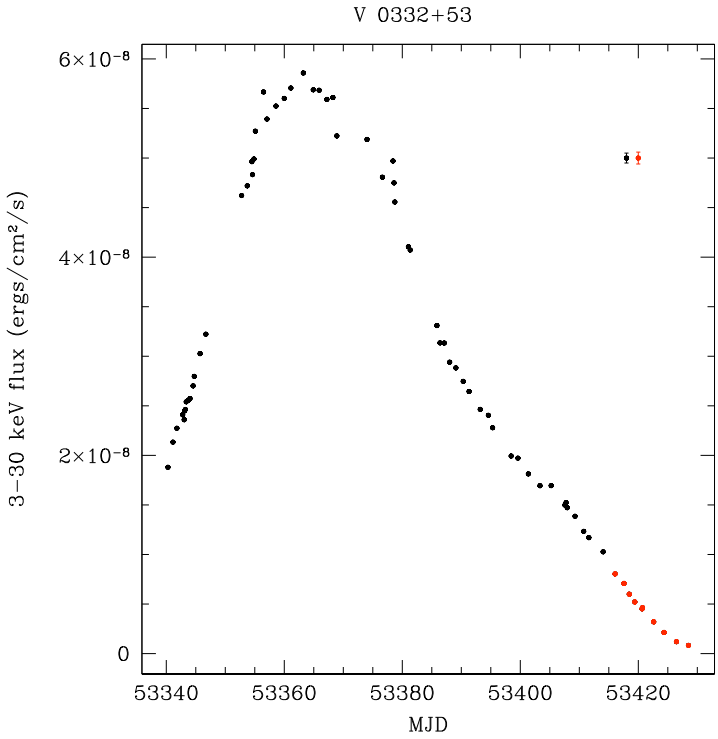

Figure 7.31: Integrated 3–30 keV flux for V 0332+53.

In Fig. 7.32 we show the HID, CD and colors trends during the outburst.

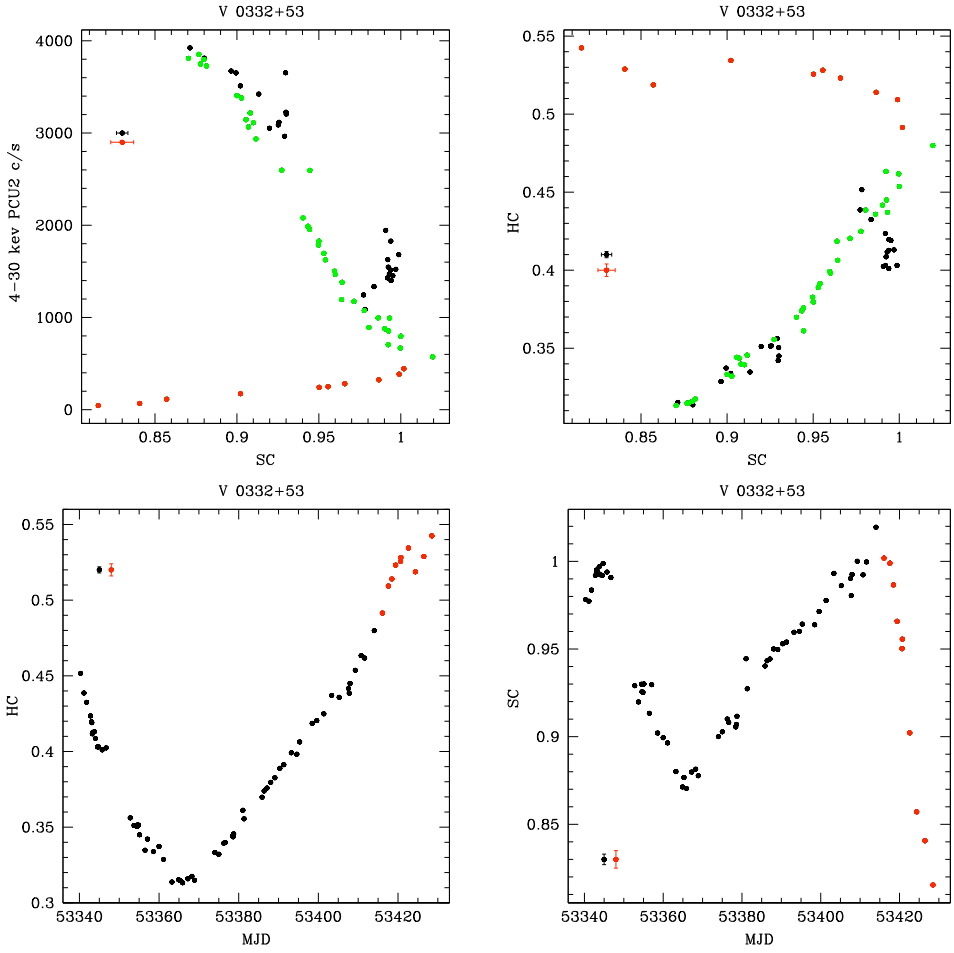

Figure 7.32: HID, CD and colors behavior during V 0332+53 outburst. Green points correspond to the decay phase, before the HB. Black error bars apply to both black and green data points.

The two branches are clearly distinguishable. The evolution of the X-ray colors as the outburst evolves, particularly the HC, is different for this source compared with the other three systems analyzed in this work. As also pointed out by Reig (2008), in the DB both the SC and the HC in V 0332+53 decrease as the flux increases and vice versa. In the HB, the HC keeps increasing in anti-correlation with flux, still in contrast to what is observed in 4U 0115+63, KS 1947+300 and EXO 2030+375; the SC decreases in the DB with flux, in the same way as in the other three system. This different behavior implies that the motion in the diagonal branch, as the intensity increases, is from the bottom right part of the CD to top left part in 4U 0115+63, KS 1947+300 and EXO 2030+375, while from bottom left to top right in V 0332+53. Another crucial difference is that the HB is harder than the DB in V 0332+53, while it is softer in the other three systems.

V 0332+53 displays hysteresis in the same way than 4U 0115+63, which means that the decay phase of the outburst corresponds to a softer emission than the rise. In Fig. 7.32 data points belonging to the rise are black, while those belonging to the decay are marked in green. The effect is more evident in the HID than in the CD. For V 0332+53, the better statistics allows to better appreciate this phenomenon than for 4U 0115+63.

Good spectral fit was obtained with two different models. We will present both and discuss similarities and differences.

- Model I

The first fit was performed with the usual components, photoelectric absorption, power law with exponential high-energy cutoff, iron gaussian line, and cyclotron line. The photoabsorption was fixed to 1.5×10^{22} cm^{-2} (Pottschmidt et al. 2005). The cyclotron line, with the fundamental ($E_c \sim 28$ keV) and its first harmonic, were accounted for with the CYCLABS model (see previous section). The harmonic, since it peaks outside the PCA spectral range, is not well constrained by our best fit. Results are shown only for the fundamental.

In Fig. 7.33 we display the behavior of the cutoff power-law parameters, the spectral index Γ, and the high-energy cutoff, with time and flux. No cutoff was needed during the HB. Both parameters, generally constant at high luminosity,

start anti-correlating with flux at $L_X \sim 1.6 \times 10^{38}$ erg s^{-1} (last half of the decay phase in the DB and whole HB, if present). For the spectral index plots, we used the same convention as in Fig. 7.32 to indicate pointings corresponding to the rise/decay (black/green) phase of the outburst. Hysteresis is not evident in the spectral index, according to this model.

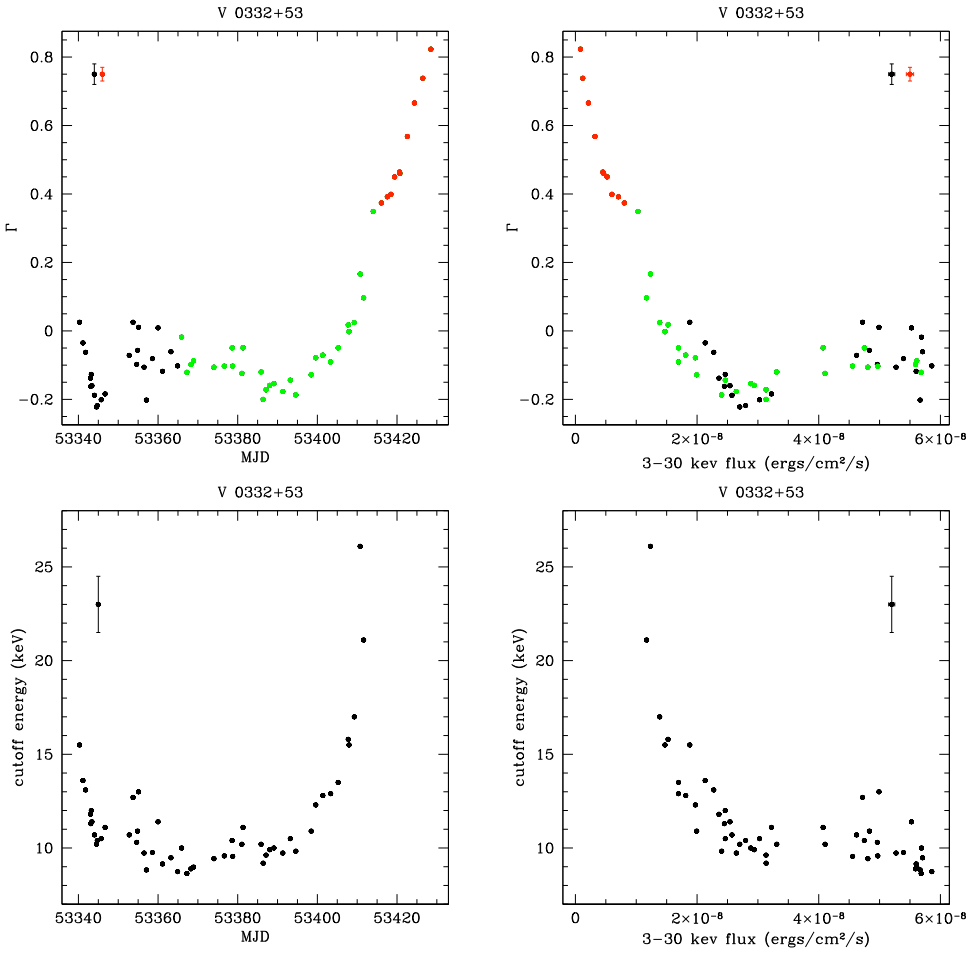

Figure 7.33: High-energy cutoff power law during V 0332+53 outburst according to Model I. Black error bars are also valid for green points.

We illustrate the relation between the two parameters in Fig. 7.34.

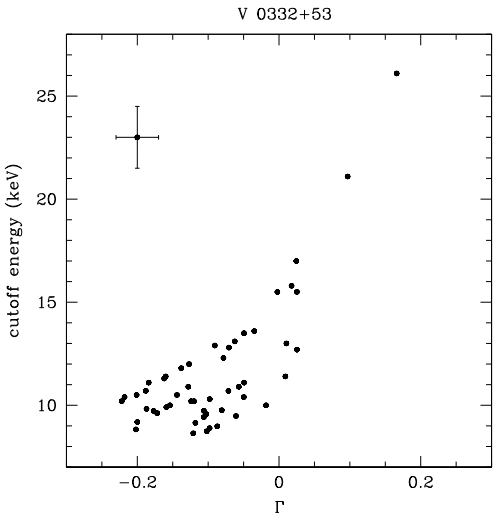

Figure 7.34: Relation between the spectral index and the cutoff energy (Model I).

In Fig. 7.35 the behavior of the Fe line with time (left panel) and flux (right panel) is presented. Also for this system, the line width was fixed at 0.5 keV. The line energy shows very little variation during the outburst, with an average value of ~ 6.5 keV. In the HB, this feature is very weak and its energy was fixed at 6.4 keV in the last observations. The corresponding pointings are not shown in the plot of the line energy. Like in the other systems studied in this work, the normalization correlates with flux. Since the relation is almost 1:1, the EW is generally constant.

We show in Fig. 7.36 the trend followed by the parameters characterizing the cyclotron feature (first harmonic). The fundamental energy varies along the outburst between 23 and 28 keV, confirming results by Tsygankov et al. (2009). Its optical depth varies between 1.4 and 3, while the width varies between 3.5–9.3 keV. The central energy shows a strong anti-correlation with flux, as also pointed out by Tsygankov et al. (2009). This behavior is common to the two branches.

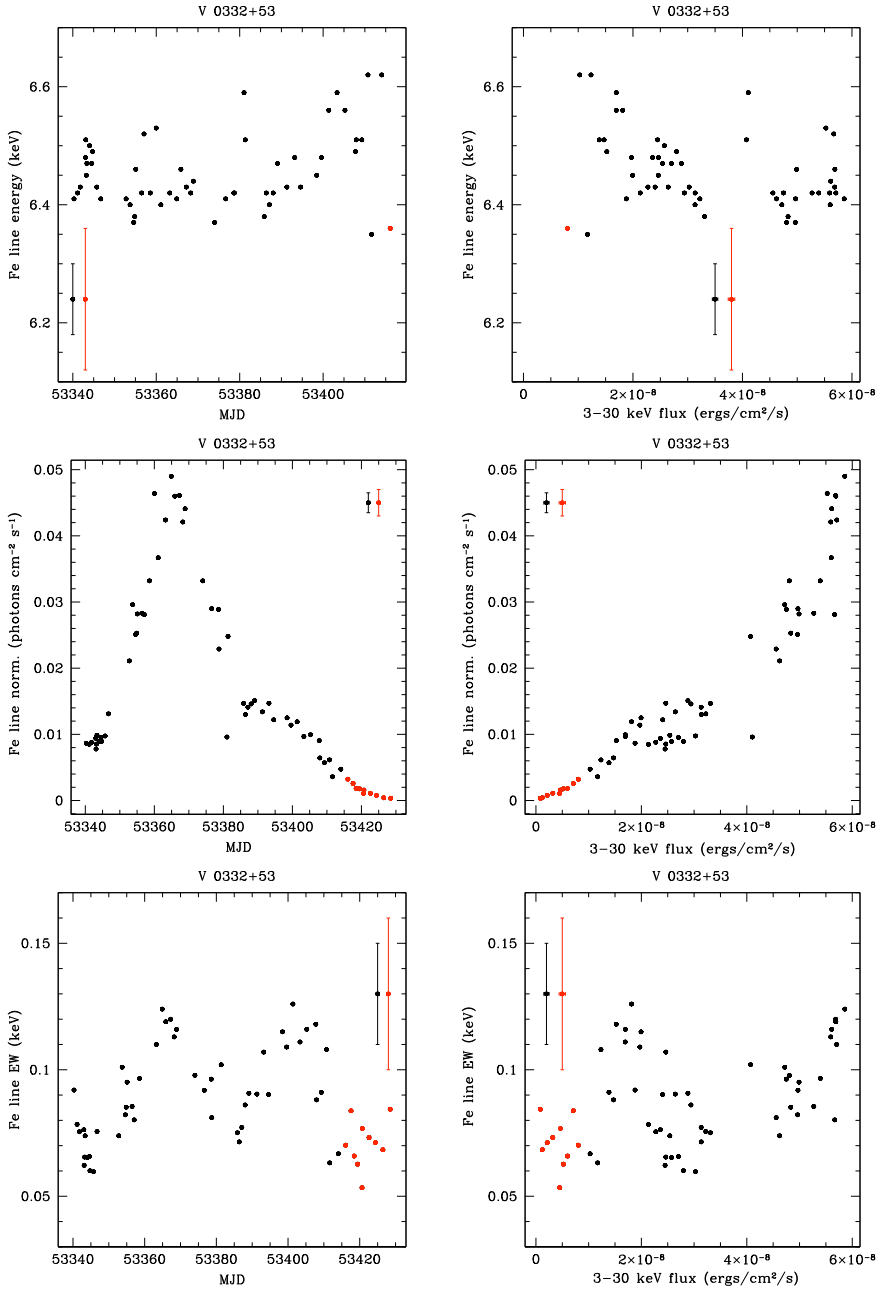

Figure 7.35: Fe fluorescence line during V 0332+53 outburst according to Model I.

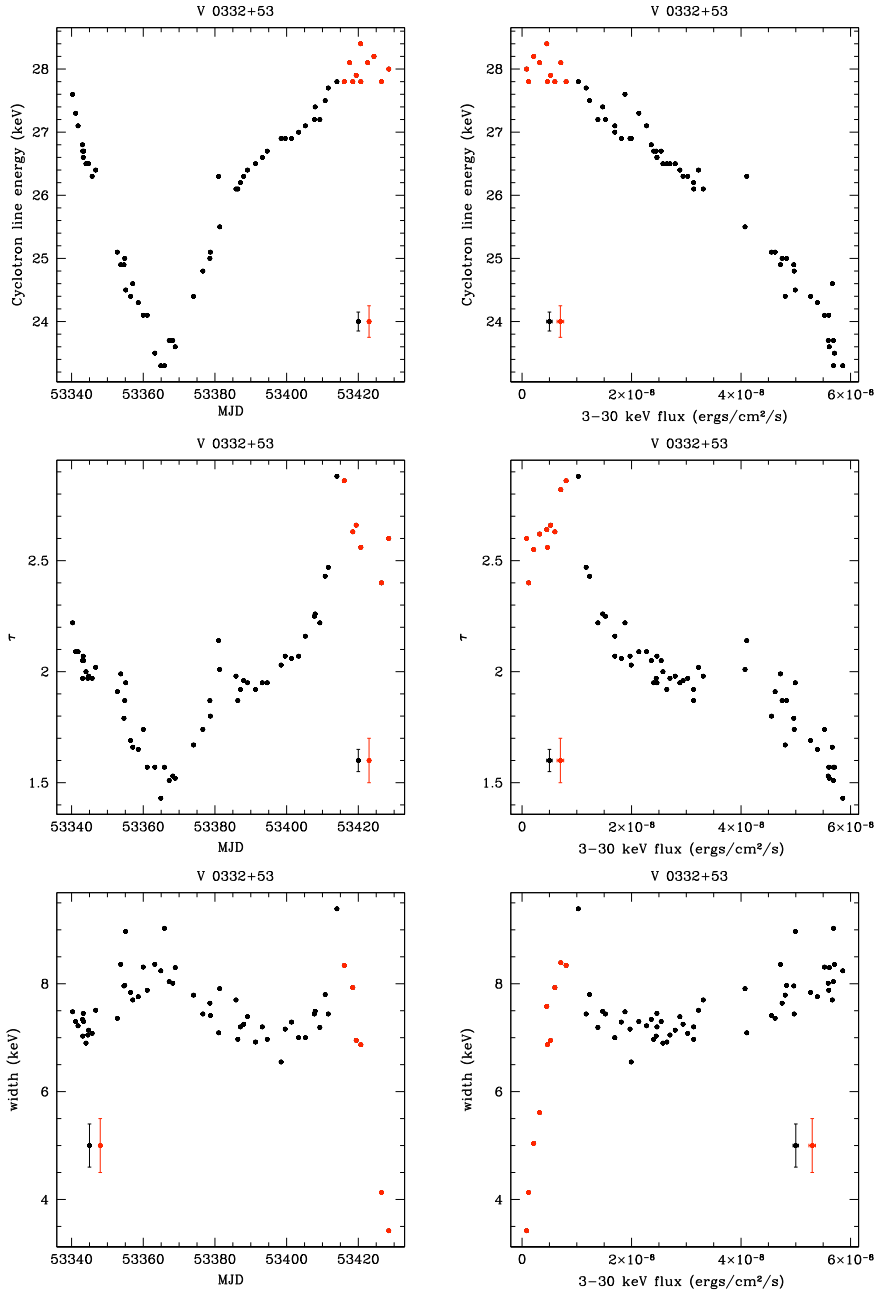

Figure 7.36: Cyclotron line parameters during V 0332+53 outburst according to Model I.

The optical depth and the line width correlate with flux in the HB and anti-correlate with it in the DB, similarly to what we observed for 4U 0115+63.

- Model II

As a test, a good fit was also obtained without exponential cutoff. The remaining components were the same as Model I. Again, the photoabsorption was fixed to 1.5×10^{22} cm^{-2}. The cyclotron line (fundamental and first harmonic) was accounted for with the CYCLABS model. Also in this case, results are shown only for the fundamental. The spectral range we employed in this case was limited between 3–30 keV, in order to use best signal-to-noise data.

In Fig. 7.37 we display the behavior of the spectral index Γ, with time and flux. With this model, the trend of the spectral index is clearly different in the two branches. It anti-correlates with flux in the HB and correlates with it in the DB, displaying a behavior common to all the systems analyzed in this work. Hysteresis is evident, using this model, in the spectral index trend, which is generally softer during the decay of the outburst, in accordance with the HID (see Fig.7.32).

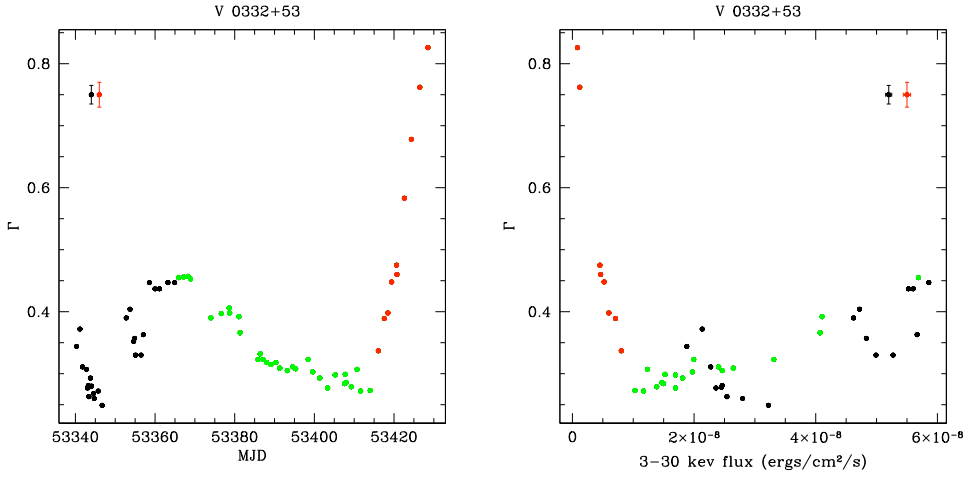

Figure 7.37: Spectral index behavior during V 0332+53 outburst according to Model II. Black error bars are also valid for green points.

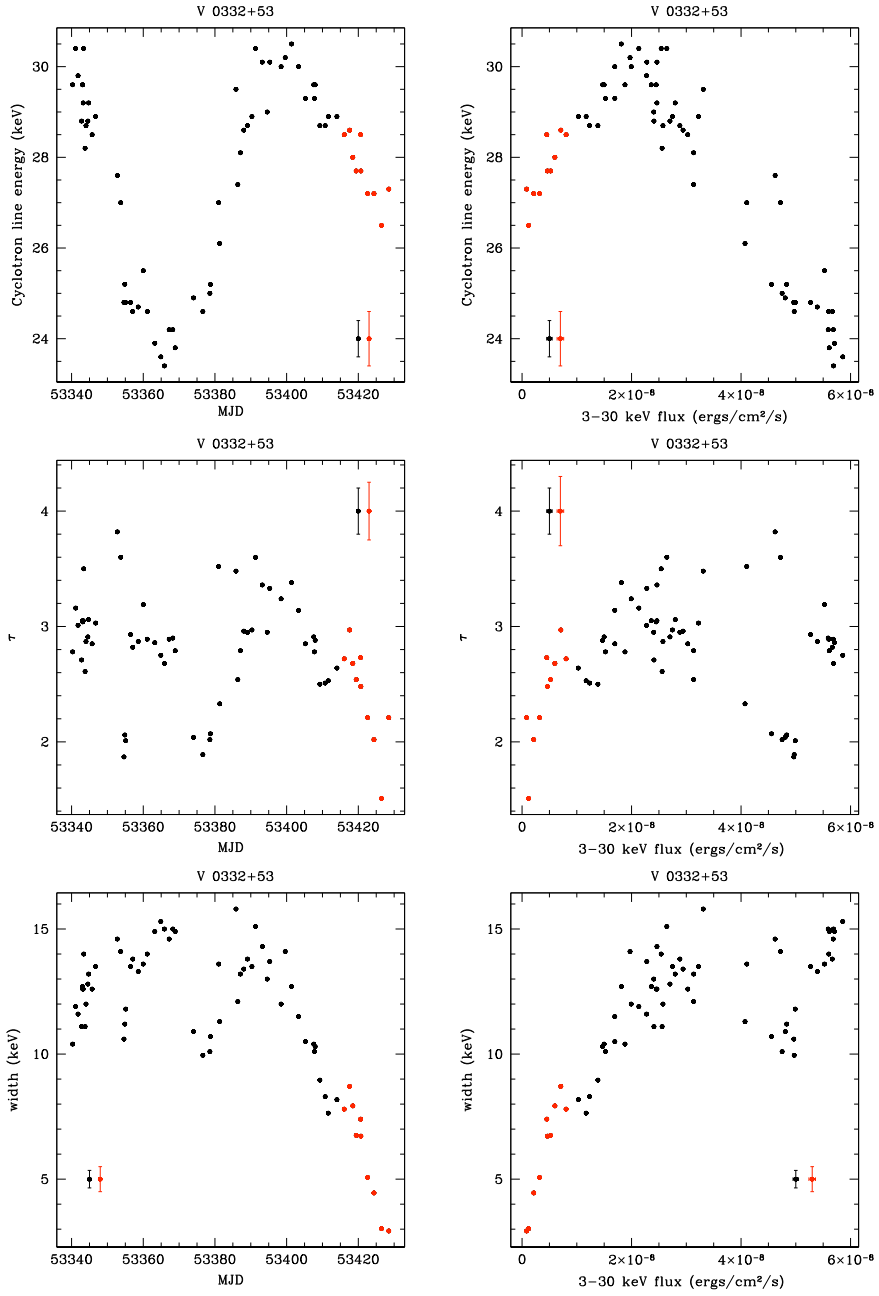

Figure 7.38: Cyclotron line parameters during V 0332+53 outburst according to Model II..

The main difference in comparison with Model I is found with respect to the central energy of the CRSF. This is displayed in Fig. 7.38, together with the other parameters of the feature.

The fundamental energy varies along the outburst between 23.5 and 30.5 keV. The optical depth varies between 1 and 4, while the width varies between 3–16 keV. All the three parameters reach slightly higher values than with Model I. As a general trend, in the DB the central energy shows a strong anti-correlation with flux, like with Model I. The final phase of the DB marks a change in this trend, as this starts displaying a correlation with flux as the emission gets fainter; the same effect is also displayed by the optical depth. In the DB, τ does not show any specific behavior, while in the HB it correlates with flux. The line width on average correlates with flux along the whole outburst.

The two main spectral features, the power law and the cyclotron line, both follow different trends with the two models. With Model I, the range of variation of the spectral index is higher, and also covers negative values. At low luminosities, with both models Γ anti-correlates with flux, but with a substantial difference: with Model II the HB marks the turning point, while with Model I the anti-correlation starts in the middle of the decay phase of the DB. Moreover, no hysteresis is found with Model I, while general softer spectral indexes are retrieved for the decay than for the rise of the outburst with Model II. This is indeed expected from the HID.

However, the most remarkable divergence between the two models is represented by the cyclotron feature. With Model I, the central energy of the line shows a variation of 19% in the DB and is roughly constant in the HB. In this case, during the whole outburst the central energy anti-correlates with flux. According to Model II, the line energy varies instead in anti-correlation with flux at high luminosity, and in correlation at low luminosity. This could be explained if the accretion took place within two different regimes (super-Eddington and sub-Eddington limits, see also Staubert et al. 2007, and Sect. 7.6.2). Although not well constrained due to its central energy, which peaks at $\sim$ 50 keV, a first harmonic is needed to obtain good fits.

Timing analysis

The power spectra were fitted with the sum of up to four Lorentzians. The low-frequency noise is accounted for by $L_{\rm b}$, whose fitted characteristic frequency is always < 0.02 Hz. This component is present along the whole outburst, with the exception of the first $\sim$10 day observations of the decay phase (53374.0 $<$ MJD $<$ 53385.8). Like for the other sources, due to the very low characteristic frequency of this component, this is generally poorly constrained. $L_{\rm l}$ describes the noise below 1 Hz and is constantly present along the outburst. Its characteristic frequency varies between 0.09–1.94 Hz.

In addition to the broad noise components, two peaked noise components are also present, $L_{\rm LF}$ and $L_{\rm s}$. As for 4U 0115+63, we will refer to these as QPOs, although the Q value is not always larger than 2. $L_{\rm LF}$, with a characteristic frequency variable between 0.01–0.09 Hz, is observable along the whole outburst. $L_{\rm s}$ has a characteristic frequency coinciding with the frequency of the fundamental peak (0.23 Hz) of the pulse period and remains roughly constant throughout the outburst. It is not present during the HB and in the last 5 observations of the DB. In contrast with 4U 0115+63, when present, both components are peaked since the beginning until the end of the outburst, not constituting the evolutionary stage from a broad component.

We show in Fig. 7.39 the evolution of $\nu_{\rm l}$ and the corresponding rms during the outburst. Like for 4U 0115+63, the characteristic frequency of the $L_{\rm l}$ component correlates with flux, with lower values at the beginning and at the end of the outburst and higher values at its peak; the rms, instead, during the DB anti-correlates with flux: the strongest power for this component is given at the end of the DB, then it starts decreasing. For both parameters we found evidence of two distinct trends during the two branches. The characteristic frequency $\nu_{\rm l}$ is almost constant in the HB and shows the lower values; the corresponding rms shows the higher values in the HB, when it starts decreasing, in correlation with flux.

In Fig. 7.40, the evolution of $\nu_{\rm LF}$ and the corresponding rms during the outburst is presented.

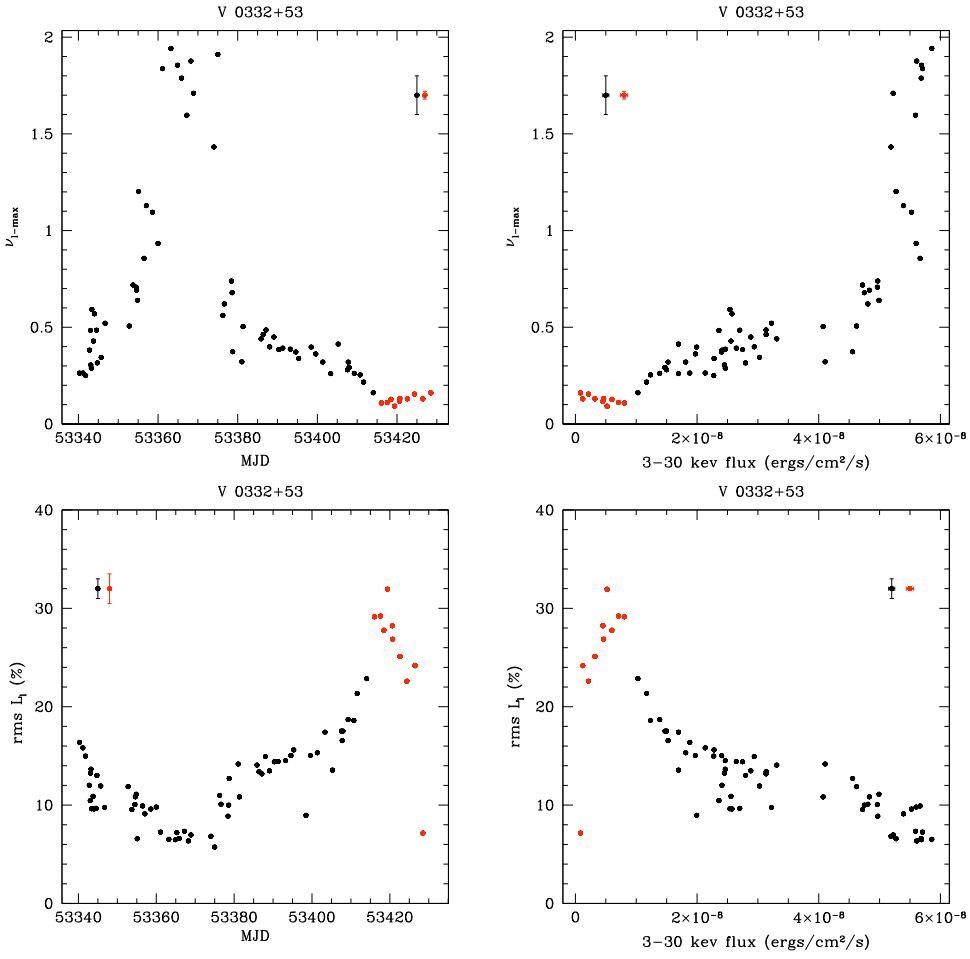

Figure 7.39: Characteristic (maximum) frequency and rms for the L_1 component during V 0332+53 outburst.

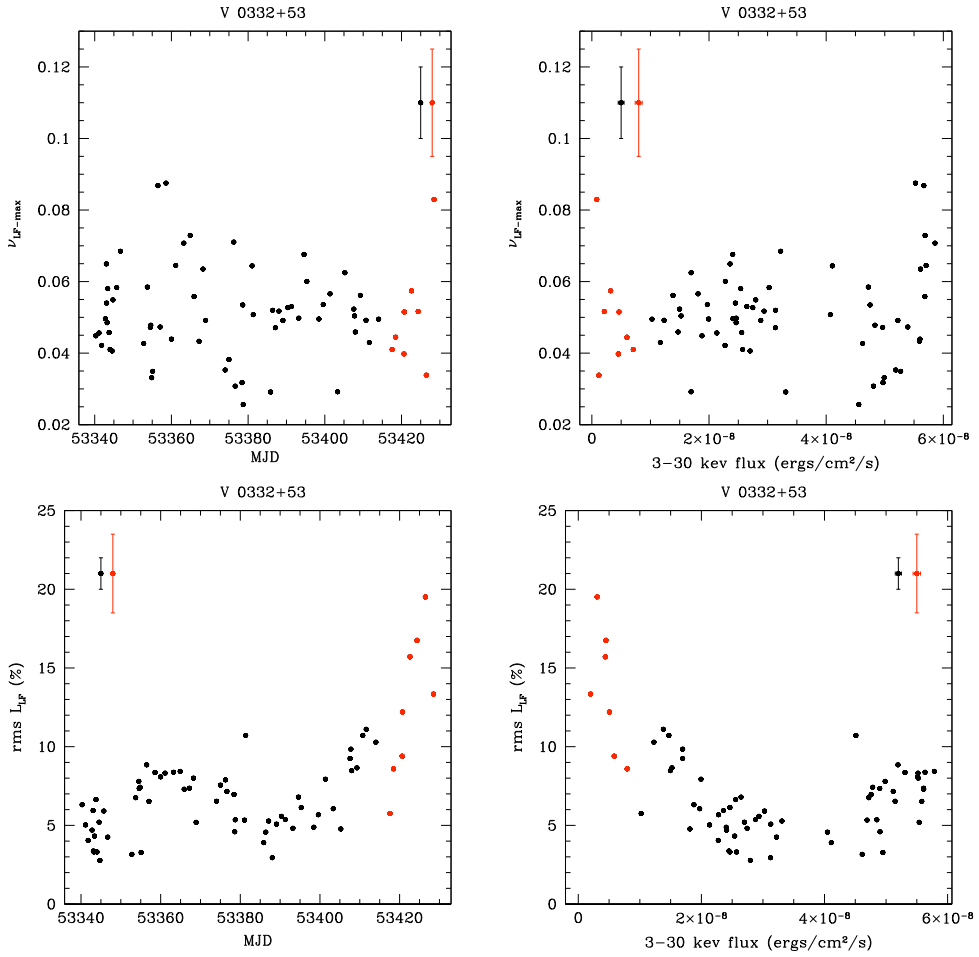

Figure 7.40: Characteristic frequency and rms for the $L_{\rm LF}$ component during V 0332+53 outburst.

While no clear correlations can be established for the characteristic frequency, the rms shows anti-correlation with flux along the whole outburst.

In Figs. 7.41 and 7.42 we show the relation between spectral and timing fit parameters, with the two spectral models respectively. The same trend observed

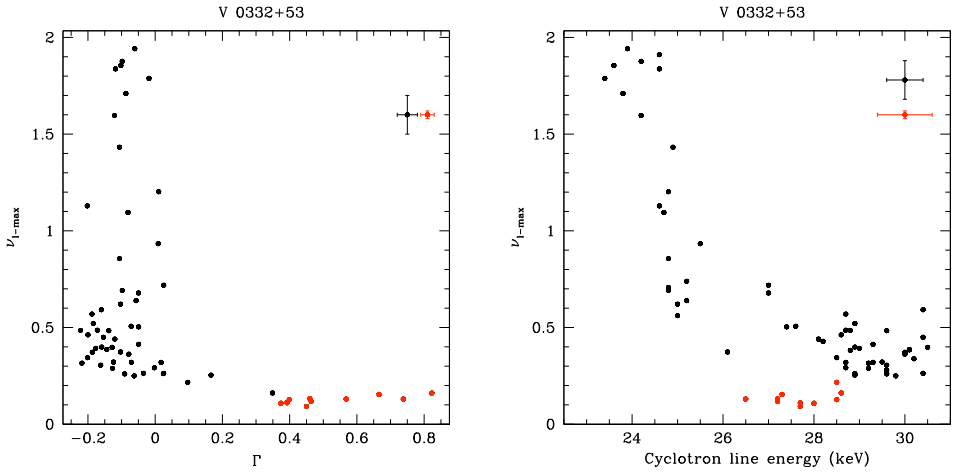

Figure 7.41: Timing vs. spectral fit parameters during V 0332+53 outburst using spectral Model I.

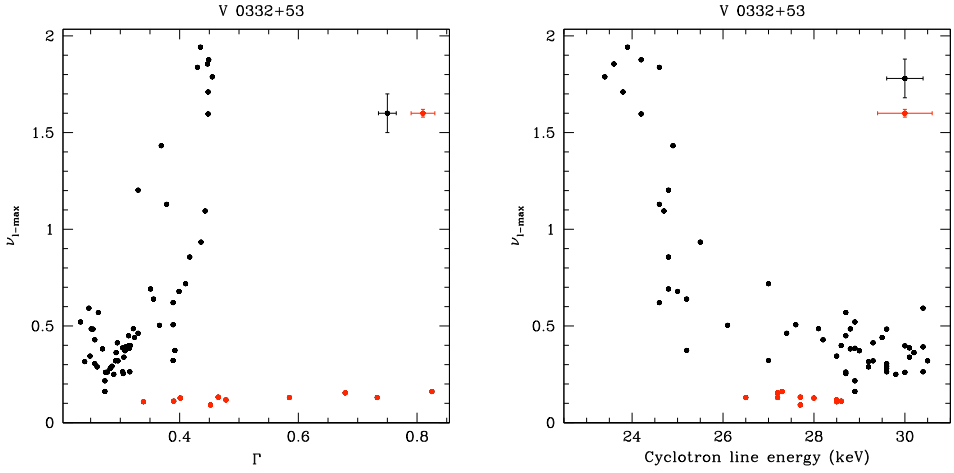

Figure 7.42: The same as Fig. 7.41, with spectral Model II.

for ν_1 vs. the cyclotron line energy in 4U 0115+63 is displayed here in all the three cases (ν_1 vs. Γ, the cyclotron energy, τ). To lower values of the spectral parameter correspond a high range of retrieved ν_1 and vice versa.

7.6 Discussion

7.6.1 Source states in HMXBs

In the previous section several common behaviors among the four systems arose and two distinct source states became evident. Here we try to describe more systematically what emerges from our work by comparing the results from the four systems. Our final goal is to provide a characterization of source states in HMXBs, from color, spectral and timing point of view.

Color features

In all the four systems studied in this work, two distinct branches or spectral states can be distinguished in the HID/CD. We shall refer to them as the diagonal branch (DB) and horizontal branch (HB) according to the shape they trace in the HID/CD. The diagonal branch corresponds to high-intensity flux and the horizontal branch to low-intensity flux. The DB is where the sources spend most of the time during the outbursts (70%-80% of the total duration). Typical timescales are months in the DB and weeks in the HB.

From our data set, the horizontal branch contains points both from the very beginning and from the end of the outburst only for KS 1947+300, while for the other three systems, since the PCA monitoring began when the outbursts were already in progress, only observations from the end of the outbursts are included. From KS 1947+300 data, it is reasonable to assume that the general property of the HB is to describe low-flux observations, regardless of whether they belong to the beginning or the end of the outburst, marking the HB the start and the end point of the source in its journey through the CD/HID while the outburst proceeds.

The transition between states takes place at $L_{\rm X}$ $\sim$10% of the peak value in KS 1947+300, EXO 2030+375 and V 0332+53. For 4U 0115+63, this change is observed at a higher ratio, $L_{\rm X} = 25\%$ of the peak value.

The two branches are recognizable in both CD and HID, as often is observed for LMXBs states, although the HID gives a clearer pattern than the CD for KS 1947+300 and EXO 2030+375. These two systems have, on average, a softer

spectrum in the HB than 4U 0115+63 and V 0332+53. This translates into larger uncertainties in the X-ray colors (especially the hard color) for KS 1947+300 and EXO 2030+375 in the HB. However, when the hard color is replaced by intensity, in the HID, the HB is well depicted in all the four systems.

The soft color shows the same pattern in all the four systems, anti-correlating with flux during the DB and correlating in the HB. The hard color distinguishes V 0332+53 from the other three sources. In fact, while we observe a general correlation between the hard color and flux in KS 1947+300, EXO 2030+375 and 4U 0115+63, the trend sketched by V 0332+53 is of anti-correlation, with the hard color decreasing in the first part of the outburst until the outburst peak, and subsequently increasing until the end. As pointed out in Sect. 7.5.4, this implies that the motion in the diagonal branch, as the intensity increases, is from the bottom right part of the CD to top left part in 4U 0115+63, KS 1947+300 and EXO 2030+375, while from bottom left to top right in V 0332+53. Another crucial difference is that the HB is harder than the DB in V 0332+53, while it is softer in 4U 0115+63, KS 1947+300 and EXO 2030+375. In this sense, in the last three systems, the horizontal branch represents a low-soft branch (in terms of hard color), a state that is not seen in LMXBs or in black-hole binaries, where low-intensity states correspond to hard spectra.

4U 0115+63 and V 0332+53 display hysteresis both in the HID and in the CD (see Figs. 7.23 and 7.32). This means that points corresponding to observations of the rising phase of the outburst are shifted in color in comparison with those of the decay phase, despite that the flux is similar. For similar values of flux, during the decay the emission is softer than during the rise.

Spectral features

Also, according to the spectral parameters retrieved from best fits, the two branches are always distinguishable. We present in Table 7.3 the range of variability of the spectral parameters and of the X-ray luminosity in the two branches. See Appendix A for the full retrieved set of spectral fit parameters.

For each system, in Figs. 7.43, 7.44, 7.45 and 7.46 typical energy spectra cor-

Table 7.3: Average main spectral parameters and L_X during the outburst for the four systems analyzed in this work. For each source, we defined a lower and and upper DB (l. DB and u. DB respectively, in the table) according to luminosity ranges indicated in the last line. For V 0332+53, only the "standard" fit with Model I is shown. The retrieved χ^2_{red} was between 0.6–1.9.

Parameter	Branch	KS 1947+300	EXO 2030+375	4U 0115+63	V 0332+53 (I)
Γ	u. DB	1.0±0.1	1.18±0.08	0.37±0.03	-0.10±0.06
	l. DB	0.5±0.2	0.85±0.11	0.24±0.06	-0.07±0.13
	HB	0.6±0.2	1.15±0.12	0.52±0.15	0.53±0.16
Cutoff	u. DB	23.4±5.4	18.9±1.6	8.5±0.2	14.5±3.5
energy (keV)	l. DB	12.4±2.6	13.5±1.7	8.7±0.2	9.7±8.7
	HB	11.3±2.3	14.6±2.3	9.3±0.5	–
Cyclotron line	u. DB	–	9.60±0.04	11.0±0.2(*)	24.9±1.0(*)
energy (keV)	l. DB	–	–	10.7±0.1	27.0±0.4(*)
	HB	–	–	16.0±0.9	28±0.2(*)
τ	u. DB	–	1.36±0.03	0.32±0.05	1.8±0.2
	l. DB	–	–	0.40±0.05	2.1±0.2
	HB	–	–	0.4±0.1	2.6±0.1
Cyclotron line	u. DB	–	4.03±0.06	4.0±0.9	7.8±0.5
width (keV)	l. DB	–	–	5.2±2.5	7.3±0.5
	HB	–	–	6.2±2.2	6.4±1.8
L_X	u. DB	2.7–7.1	8.0–15.4	11.5–13.7	16.9–33.9
(10^{37} erg s^{-1})	l. DB	0.3–2.8	1.5–7.8	5.7–10.0	6.4–16.4
	HB	0.1–0.3	0.2–1.3	0.7–3.5	0.4–4.7

(*) Besides the fundamental, in these systems also the first harmonic is needed in order to fit the energy spectra

responding to different X-ray luminosity are shown[2]. The additive model components are shown (power law and iron fluorescence line) with dashed lines, while the resulting model is marked by a solid line. Below each panel, the corresponding residuals after fitting are displayed.

[2]The complete set of fitted energy spectra and PSD is available at the following URL: http://www.uv.es/∼nese/spectra.pdf

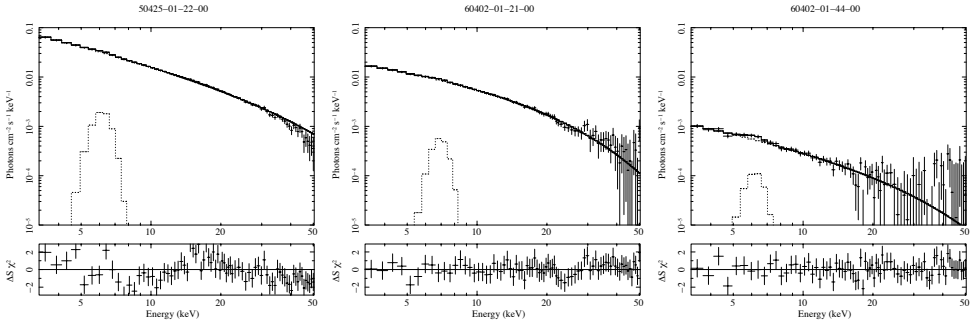

Figure 7.43: Typical energy spectra for KS 1947+300 in the DB at high luminosity ($L_{\rm X} = 6.7{\times}10^{37}$ erg s^{-1}, $\Gamma = 1.2$, left panel), DB at low luminosity ($L_{\rm X} = 2.1{\times}10^{37}$ erg s^{-1}, $\Gamma = 0.6$, middle panel) and in the HB ($L_{\rm X} = 1.1 \times 10^{36}$ erg s^{-1}, $\Gamma = 0.7$, right panel).

In all the four systems, the spectral index Γ shows a marked relation with flux, correlating in general with it during the DB and anti-correlating during the HB. On average, HB represents a softer state than the DB; this is in agreement to what we found from color analysis. It is also true that the HB shows the larger range of spectral index values, but the softest spectra are always found there. Instead, the DB covers a narrower range of spectral index values, generally harder. This is particularly true for EXO 2030+375, 4U 0115+63 and V 0332+53. For KS 1947+300, the spectral index range and the retrieved values are similar in the two branches. A high-energy cutoff was included in the spectral fit of all the four systems (with Model I for V 0332+53). Only for KS 1947+300 higher values are obtained in the DB, while for the other two systems in the HB, so that no general trend can be outlined here.

The iron fluorescence line is a necessary parameter to fit spectra from all the four systems during the DB. However, the strength of this feature decreases largely during the HB. In fact, no such component is required in some spectra of the HB. On average, the central energy of the line is constant throughout the outburst in all systems; its intensity, computed as normalization, correlates with continuum 3–30 keV flux. The line EW shows a weak correlation with flux in

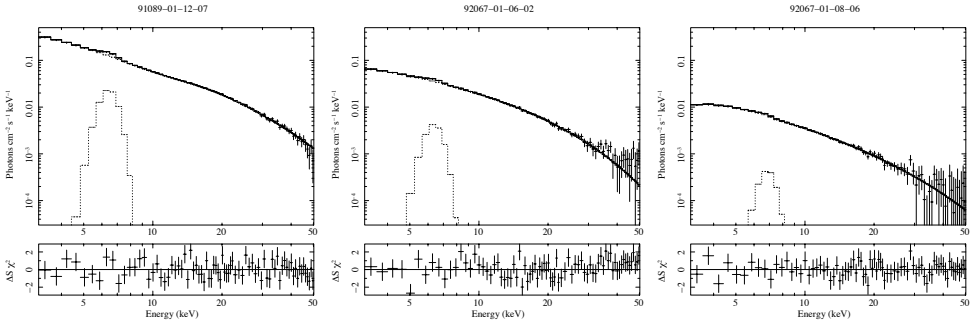

Figure 7.44: Typical energy spectra for EXO 2030+375 in the DB at high luminosity ($L_{\rm X} = 1.3 \times 10^{38}$ erg s^{-1}, $\Gamma = 1.3$, left panel), DB at low luminosity ($L_{\rm X} = 3.6 \times 10^{37}$ erg s^{-1}, $\Gamma = 0.7$, middle panel) and in the HB ($L_{\rm X} = 6.7 \times 10^{36}$ erg s^{-1}, $\Gamma = 1.2$, right panel).

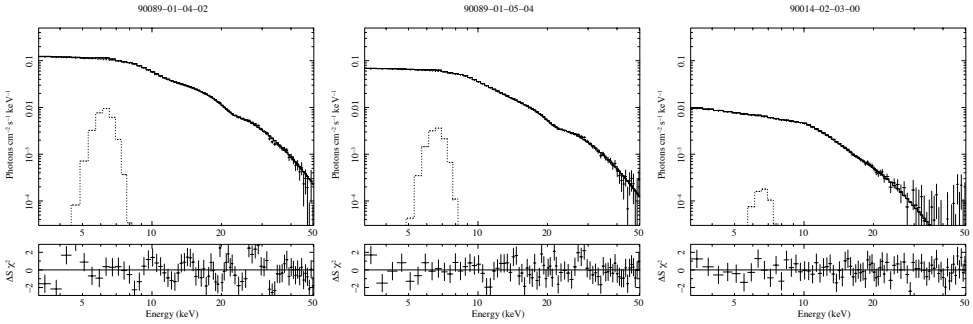

Figure 7.45: Typical energy spectra for 4U 0115+63 in the DB at high luminosity ($L_{\rm X} = 1.9 \times 10^{38}$ erg s^{-1}, $\Gamma = 0.3$, left panel), DB at low luminosity ($L_{\rm X} = 7.4 \times 10^{37}$ erg s^{-1}, $\Gamma = 0.2$, middle panel) and in the HB ($L_{\rm X} = 7.1 \times 10^{36}$ erg s^{-1}, $\Gamma = 0.8$, right panel). Note the two distortions at ∼11 keV and ∼22 keV introduced by the fundamental and first harmonic of the CRSF.

EXO 2030+375 and V 0332+53 (with Model II only). It anti-correlates with flux in KS 1947+300 at low luminosity. It is constant in 4U 0115+63 and V 0332+53 using Model I.

Three systems – EXO 2030+375, 4U 0115+63 and V 0332+53 – among the four analyzed in this work show evidence of a cyclotron resonant scattering feature at

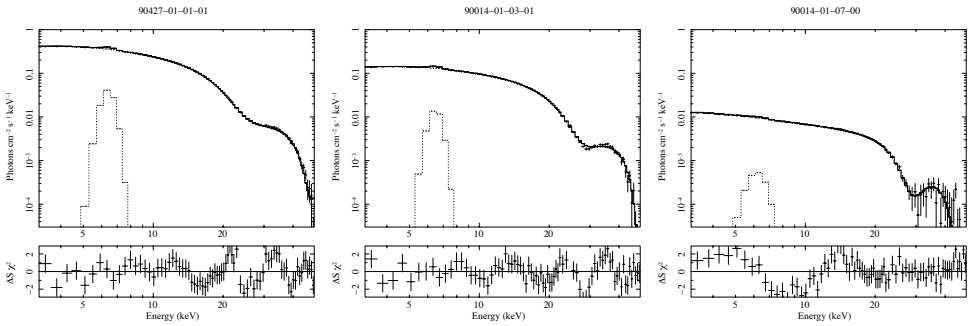

Figure 7.46: Typical energy spectra for V 0332+53 in the DB at high luminosity ($L_{\rm X} = 3.3{\times}10^{38}$ erg s^{-1}, $\Gamma = 0.4$, left panel), DB at low luminosity ($L_{\rm X} = 1.4{\times}10^{38}$ erg s^{-1}, $\Gamma = 0.3$, middle panel) and in the HB ($L_{\rm X} = 7.1 \times 10^{36}$ erg s^{-1}, $\Gamma = 0.7$, right panel).

∼10 keV, ∼11 keV and ∼30 keV respectively. However, EXO 2030+375 spectra need this feature only in the bright phase of the outburst; for this source, the central energy of the line shows no large variability, less than 10% in the major part of the observations. A fit to a constant gives a rms of residuals of 0.63 for the central energy, 0.29 for the optical depth and 0.55 for the line width, i.e. consistent with no change for all the three parameters of the component. No harmonic is required for this system. In 4U 0115+63 and V 0332+53 the central energy of the line is higher in the HB than in the DB, which means that it is anti-correlated with flux, with higher values observed at lower flux. On average, the same behavior is shown by the optical depth. Both systems need, besides the fundamental, the first harmonic in order to obtain a good fit.

Timing features

After fitting the peaks of the pulse components with fixed Lorentzians for each source, the power-spectra of Be/X-ray binaries are characterized by band-limited noise (BLN). All the spectra analyzed in this work were conveniently fitted with the sum of a small number of Lorentzians. Ignoring the peaks of the pulse components, for each system, 2–4 Lorentzian profiles are needed to obtain acceptable fits. Considering all the systems, we identified six different types of noise components, four of which are band-limited ($L_{\rm b}$, $L_{\rm l}$, $L_{\rm u}$, $L_{\rm u'}$) and two are QPOs ($L_{\rm LF}$

and $L_{\rm s}$). The results of the power spectral fitting are given in Table 7.4. In the vast majority of the cases, the resulting chi^2_{red} was lower than 2. In a few cases ($< 5\%$), additional subtle but statistical significant substructures are seen in the PSD. These features are hard to identify with a specific component as they do not follow any trend with luminosity or position in the HID. Adding more components (Lorentzians) to better fit the PSD does not provide any gain as they do not affect the fitting parameters of the other components.

For more details, and to follow each parameter across the whole set of observations, we refer to Appendix A. Typical power spectral densities are shown in Figs. 7.47, 7.48, 7.49 and 7.50.

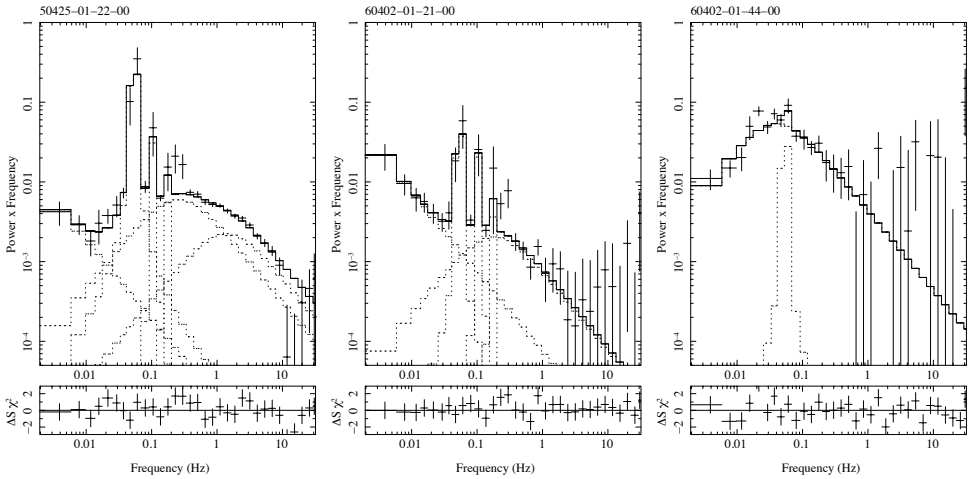

Figure 7.47: Typical PSD for KS 1947+300. In the left panel, corresponding to a high-luminosity observation in the DB ($L_{\rm X} = 6.7 \times 10^{37}$ erg s^{-1}, $\Gamma = 1.2$), from low to high frequency, the $L_{\rm b}$, $L_{\rm l}$ and $L_{\rm u}$ components are evident; in the middle panel, corresponding to a low-luminosity in the DB ($L_{\rm X} = 2.1 \times 10^{37}$ erg s^{-1}, $\Gamma = 0.6$), the $L_{\rm b}$ and $L_{\rm l}$ components are shown; in the right panel, corresponding to a HB observation ($L_{\rm X} = 1.1 \times 10^{36}$ erg s^{-1}, $\Gamma = 0.7$), only the $L_{\rm l}$ is present. In each PSD, the peaked profiles correspond to the NS pulse frequency (see Sect. 7.4.2).

The components we identified are the same as defined by Reig (2008). The best characterized component, and the only one found in all the systems and along the whole outburst, is $L_{\rm l}$. This is a broad component whose characteristic frequency shifts to low values in the HB; at the same time, in the HB its rms reaches the highest value (with the exception of EXO 2030+375, where the rms is

Table 7.4: Range of variability of the timing features during the outburst for the four systems analyzed in this work. For each spectral branch and for each component, the corresponding characteristic frequency and rms are shown.

Feature		Branch	KS 1947+300	EXO 2030+375	4U 0115+63	V 0332+53
$\mathbf{L_b}$	ν (Hz)	u. DB	< 0.01	–	< 0.01	< 0.02
		l. DB	< 0.01	–	< 0.01	< 0.01
		HB	–	–	< 0.01	< 0.03
	rms (%)	u. DB	14±5	–	25±21	55±101
		l. DB	19±12	–	21±19	78±117
		HB	–	–	41±40	56±49
$\mathbf{L_l}$	ν (Hz)	u. DB	0.23±0.05	0.32±0.08	0.8±0.2	0.93±0.54
		l. DB	0.18±0.08	0.30±0.06	0.6±0.2	0.35±0.10
		HB	0.05±0.01	0.08±0.06	0.21±0.05	0.13±0.02
	rms (%)	u. DB	20±1	35±3	15±3	10±3
		l. DB	22±9	30±6	13.6±1.7	15±3
		HB	44±13	27±5	26±4	25±7
$\mathbf{L_u}$	ν (Hz)	u.DB	1.6±0.6	2.3±0.9	1.0±0.3	–
		l. DB	–	–	1.8±0.3	–
		HB	–	–	–	–
	rms (%)	u. DB	11±2	10±5	10.7±1.6	–
		l. DB	–	–	6.1±1.6	–
		HB	–	–	–	–
$\mathbf{L_{u'}}$	ν (Hz)	u. DB	–	4.9±1.6	–	–
		l. DB	–	2.6±1.3	–	–
		HB	–	–	–	–
	rms (%)	u. DB	–	7±3	–	–
		l. DB	–	13±5	–	–
		HB	–	–	–	–
$\mathbf{L_{LF}}$	ν (Hz)	u. DB	–	–	0.07±0.04	0.05±0.02
		l. DB	–	–	0.07±0.02	0.051±0.008
		HB	–	–	0.08±0.01	0.05±0.01
	rms (%)	u. DB	–	–	12±3	6±2
		l. DB	–	–	10±3	6±2
		HB	–	–	8.2±0.5	12±4
$\mathbf{L_s}$	ν (Hz)	u. DB	–	–	–	0.25±0.01
		l. DB	–	–	–	0.23±0.02
		HB	–	–	–	–
	rms (%)	u. DB	–	–	–	6.4±1.4
		l. DB	–	–	–	6±3
		HB	–	–	–	–
L_X		u. DB	2.7–7.1	8.0–15.4	11.5–13.7	16.9–33.9
(10^{37} erg s^{-1})		l. DB	0.3–2.8	1.5–7.8	5.7–10.0	6.4–16.4
		HB	0.1–0.3	0.2–1.3	0.7–3.5	0.4–4.7

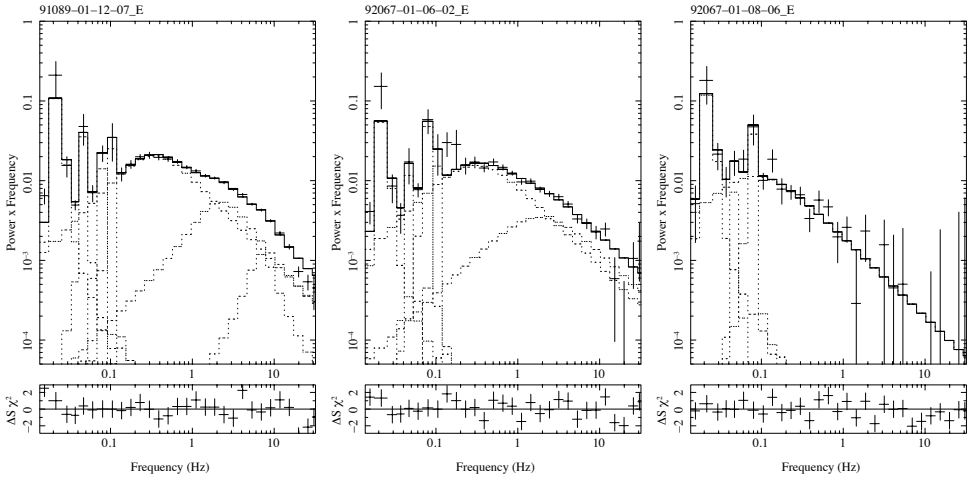

Figure 7.48: Typical PSD for EXO 2030+375. In the left panel, corresponding to a high-luminosity observation in the DB ($L_{\rm X} = 1.3 \times 10^{38}$ erg s^{-1}, $\Gamma = 1.3$), from low to high frequency, the $L_{\rm l}$, $L_{\rm u}$ and $L_{\rm u'}$ components are evident; in the middle panel, corresponding to a low-luminosity in the DB ($L_{\rm X} = 3.6 \times 10^{37}$ erg s^{-1}, $\Gamma = 0.7$), the $L_{\rm l}$ and $L_{\rm u'}$ components are shown; in the right panel, corresponding to a HB observation ($L_{\rm X} = 6.7 \times 10^{36}$ erg s^{-1}, $\Gamma = 1.2$), only the $L_{\rm l}$ is present.

similar in the two branches). The range of frequency covered by this component is ~ 0.1–2 Hz. In all the systems, $\nu_{\rm l}$ correlates with flux. The rms shows different trends according to the source. In V 0332+53 and during the HB of KS 1947+300 and 4U 0115+63, this is the only component fitting the high-frequency domain of the power spectrum.

$L_{\rm b}$ is a broad component fitting the noise below 0.1 Hz. It is not always well constrained due to its very low frequency, placed often outside the available range at our resolution. It was excluded by the power spectral fit of EXO 2030+375 by ignoring the first three channels due to the high degree of freedom that it introduced. It is present in the DB of the other three systems, and in the HB of 4U 0115+63 and V 0332+53; in KS 1947+300, only three spectra of the HB need this feature. The covered range of frequency is the same in the two branches, while the rms displays the higher values in the DB.

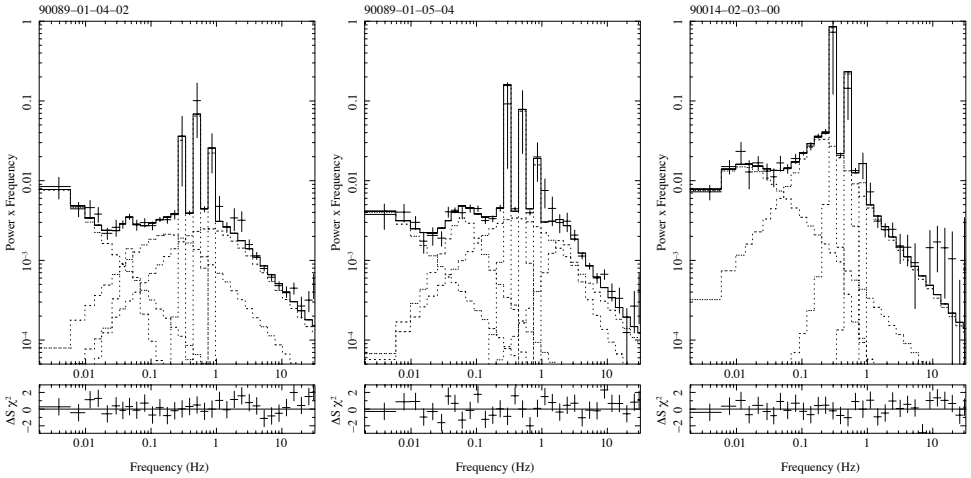

Figure 7.49: Typical PSD for 4U 0115+63. In the left (DB, $L_{\rm X} = 1.9 \times 10^{38}$ erg s^{-1}, $\Gamma = 0.3$), and in the middle panel (DB, $L_{\rm X} = 7.4 \times 10^{37}$ erg s^{-1}, $\Gamma = 0.2$) from low to high frequency, the $L_{\rm b}$, $L_{\rm LF}$, $L_{\rm l}$ and $L_{\rm u}$ components are evident; in the right panel, corresponding to a HB observation ($L_{\rm X} = 7.1 \times 10^{36}$ erg s^{-1}, $\Gamma = 0.8$), only the $L_{\rm b}$ and $L_{\rm l}$ are present.

$L_{\rm u}$ describes the high-frequency noise, covering a broad range of frequency, above 1–5 Hz. It is associated to high-luminosity observations, since it is only found in the DB. Its presence is consistently needed for three of the four systems, KS 1947+300, EXO 2030+375 and 4U 0115+63. In EXO 2030+375, its characteristic frequency shows a weak correlation with flux, while the corresponding rms anti-correlates with it.

In the power spectra of EXO 2030+375 another high-frequency component was identified, $L_{\rm u'}$, whose characteristic frequency varies between 0.2–10.2 Hz. Like $L_{\rm u}$, it is only found the DB. Its characteristic frequency weakly correlates with flux.

Two narrow components, which we will refer to as QPOs, are found in the faster pulsars, 4U 0115+63 and V 0332+53. $L_{\rm LF}$, with a characteristic frequency between 0.02–0.15 Hz, is common among the two sources. In V 0332+53, whose observations provide a better statistics, the rms clearly anti-correlates with flux.

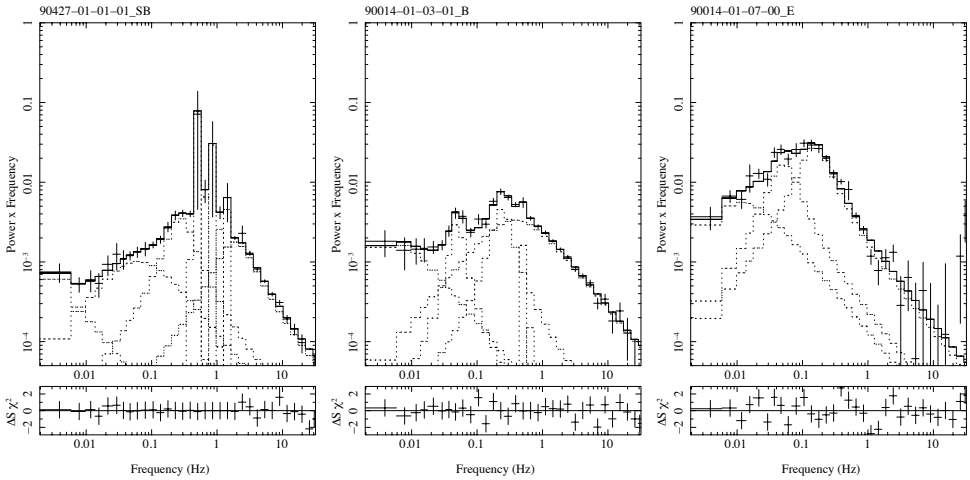

Figure 7.50: Typical PSD for V 0332+53. In the left (DB, $L_{\rm X} = 3.3 \times 10^{38}$ erg s^{-1}, $\Gamma = 0.4$), and in the middle panel (DB, $L_{\rm X} = 1.4 \times 10^{38}$ erg s^{-1}, $\Gamma = 0.3$) from low to high frequency, the $L_{\rm b}$, $L_{\rm LF}$, $L_{\rm s}$ and $L_{\rm l}$ components are evident; in the right panel, corresponding to a HB observation ($L_{\rm X} = 7.1 \times 10^{36}$ erg s^{-1}, $\Gamma = 0.7$), the $L_{\rm b}$, $L_{\rm LF}$ and $L_{\rm l}$ are present.

$L_{\rm s}$ is only found in V 0332+53; its characteristic frequency range, between 0.2–0.3 Hz, roughly corresponds to the frequency of the fundamental pulse peak (0.23 Hz). This component is only present in the DB.

7.6.2 Physical interpretation

With this work we identified two source states during Be/XRB giant outbursts. According to spectral analysis, the power law is a component always present during the outbursts of the four systems, as typically shown in X-ray pulsar spectra. In the physical scenario adopted for these accreting systems (see Davidson & Ostriker 1973; Becker & Wolff 2007), this feature is a signature of the bulk Comptonization process occurring in the accretion column. Within this picture, for strong magnetic fields ($B \sim 10^{11-12}$ G) of the compact object, the plasma is threaded at several hundreds NS radii and then channelled along the magnetic field lines onto the magnetic poles, forming one or two accretion columns. The system is powered by the conversion of gravitational potential energy into kinetic

energy, which is eventually emitted in the form of X-rays as the plasma decelerates, possibly through a radiative shock, and settles onto the stellar surface. Most of the photons are produced in a dense "thermal mound" at the base of the column, just above the stellar surface. These relatively low-energy photons are upscattered in the shock and eventually diffuse through the walls of the column, carrying away the kinetic energy of the gas. This Fermi mechanism characteristically produces a power-law continuum at high energies.

The inclusion of an exponential high-energy cutoff is a necessary step in both states for all the four systems analyzed here. This is usually interpreted as a trace of thermal Comptonization. A good fit was also obtained for V 0332+53 without this feature: this may be explained in connection with the cyclotron central energy of this system, which covers the characteristic values of the cutoff energy. As shown by Makishima et al. (1990), the CRSF may be, in fact, responsible for the formation of the cutoff.

A Fe fluorescence line is present in the DB of all the sources, while it is not necessary in half of the EXO 2030+375 HB. The Kα iron line from X-ray pulsar is ascribed to emission from less ionized iron in relatively cool matter. Iron in the circumstellar matter absorbs X-rays from the central source and produces the fluorescence line. This feature is not well constrained by RXTE data because of the poor spectral resolution at low energy. We found a well marked correlation of its intensity with flux, in all systems/states. As the 3–30 keV flux increases, so does the line intensity. A fit to a straight line gives a slope of $\sim$1. As a result, the EW remains fairly constant.

A unique spectral characteristic of many HMXBs is the presence of CRSFs, which provide a tool for direct measurement of the magnetic-field strengths of accreting pulsars. The fundamental line appears at $E_{\rm cyc} = 11.6\ B_{12} \times (1+z)^{-1}$ keV, where B_{12} is the magnetic field strength in units of 10^{12} G and z is the gravitational redshift in the line-forming region (Wasserman & Shapiro 1983). We found evidence from CRSFs in the three higher-luminosity systems, EXO 2030+375, 4U 0115+63 and V 0332+53, confirming previous works. This feature is present in both states of 4U 0115+63 and V 0332+53, while it is not found in the HB

of EXO 2030+375. According to our results, its presence seems to be associated to high luminosity systems. Also, while the X-ray spectra of 4U 0115+63 and V 0332+53 require the inclusion of the first harmonic of the cyclotron line, no such component is detected in EXO 2030+375. It is known since GINGA observations of 4U 0115+63 (Mihara et al. 1998) that the energies of cyclotron absorption features vary with X-ray luminosity. Such variations are interpreted in terms of the height of the line-forming region above the neutron star surface. Both positive and negative correlation between the cyclotron line energy and X-ray luminosity were observed in X-ray pulsars (see, for instance, Mihara et al. 1998; Tsygankov et al. 2006; Staubert et al. 2007), with a prevalent anti-correlation in high-luminosity pulsars and correlation in low-luminosity ones. This can been explained, according to Staubert et al. (2007), by considering if the accretion regime takes place in the super-Eddington or sub-Eddington limit. In this view, in the radiation-dominated super-Eddington regime, the height of the accretion column increases with luminosity (Burnard et al. 1991). Since the magnetic field value decreases with the height above the NS surface, this explains the observed anti-correlation between the CRSF energy in spectra of bright X-ray pulsars with luminosity. In the sub-Eddington accretion regime, Staubert et al. (2007) suggested that the fractional change in cyclotron line energy is directly proportional to the fractional change in luminosity.

For V 0332+53, we obtained two different trends of the CRSFs depending on the spectral model employed. The inclusion of a high-energy exponential cutoff led to results similar to Tsygankov et al. (2009), with a correlated behavior of the central energy of the cyclotron line with flux during the whole outburst. In the absence of a cutoff, things change and we observe correlation of $E_{\rm c}$ with flux at low luminosity (HB) and anti-correlation at high luminosity (DB). In this case, the CRSF displays within the same system both prevalent behaviors seen in X-ray pulsars, correlation and anti-correlation, according to the luminosity regime (sub-Eddington or super-Eddington) in which accretion takes place. Here we derive the critical luminosity which sets the sub-/super-Eddington accretion for V 0332+53 and compare it to our retrieved values.

The critical luminosity is given by the local Eddington luminosity $L_{\rm E}$ (Nelson

et al. 1993)

$$L_{\rm E} = \frac{2\pi GMcm_{\rm p}}{\sigma_{\rm T}}\left(\frac{\sigma_{\rm T}}{\sigma_{\rm m}}\right)\theta_{\rm c}^2 \simeq 10^{36}{\rm erg/s}\left(\frac{\sigma_{\rm T}}{\sigma_{\rm m}}\right)\left(\frac{\theta_{\rm c}}{0.1}\right)^2, \tag{7.2}$$

where M is the mass of the neutron star, $\sigma_{\rm m}$ is the photon-electron scattering cross-section in the magnetic field, $\sigma_{\rm T}$ is the Thomson cross-section, and $\theta_{\rm c}$ is the half-opening angle of the polar cap magnetic field lines. We note that this limit cannot be judged by the observed luminosity alone: decisive is the local accretion rate which depends on the accretion area and the photon-electron scattering cross-section, which in turn depends on the strength and structure of the magnetic field. For photon energies below the cyclotron line (∼30 keV) as the one expected from the polar caps (∼0.5–2 keV) , i.e. $E \ll E_{\rm c}$, $\sigma_{\rm T}/\sigma_{\rm m} \sim (E/E_{\rm c})^{-2}$ (Harding & Lai 2006). Thus, at low energies, $\sigma_{\rm m}/\sigma_{\rm T} \ll 1$ and for $\theta_{\rm c} < 0.1$, the critical luminosity is $L_{\rm E} \lesssim 5 \times 10^{37}$ erg s^{-1}, consistent with the turning point between the DB and the HB in V 0332+53. Therefore, within the aforementioned limit, we can confidently affirm that in the case of V 0332+53 accretion takes place at sub-Eddington luminosity regime in the HB and at super-Eddington luminosity regime in the DB, which explains the twofold behavior seen in the CRSFs with Model II.

The evident contrast between findings with the two models are still an open matter of debate and will be investigated in a further study.

The X-ray colors give an immediate picture of the state evolution and allow easy comparison among the four sources. In fact, the two branches are defined from HID/CD, although good correspondences with spectral/timing parameters are found. It is remarkable that the SC evolves exactly in the same manner in all the systems analyzed in this work. This finds correspondence in the spectral index trend, which is the same for all the systems. In the SC vs. time diagram, the sources move smoothly along the sketched pattern in both states, but a discontinuity shows up at the moment of the transition between them (see Fig.7.51 for a summary). Unlike the turning point during the DB, in correspondence with the outburst peak, this second discontinuity is not associated to any change in the source flux. In fact, the SC, which anti-correlates with flux in all the DB,

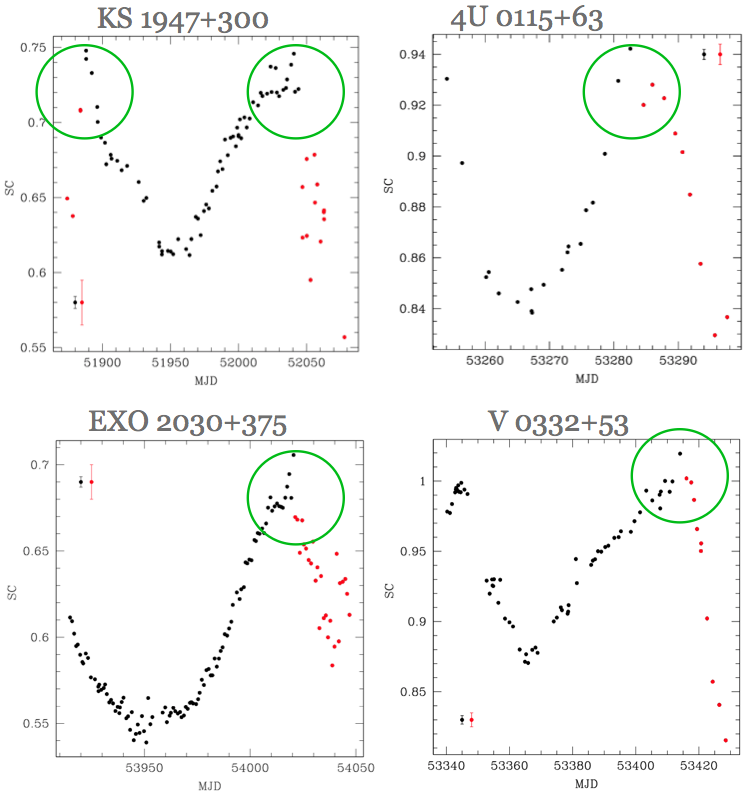

Figure 7.51: Soft color vs. time, for the four systems analyzed in this work. The turning point that marks the transition between the two states is shown with a green circle.

suddenly starts to correlate with it. This turning point in the SC defines the HB. One could fairly ask the reason why this turning point occurs, making the sources softer as the X-ray luminosity decreases. We try to provide a phenomenological explanation to this.

The decrease of the SC during the HB, indicates that the spectrum becomes softer as the source progresses in this state. In other words, extra emission at low energies is produced. We assume that during the DB the X-ray emission comes from the standing shock above the NS surface in the accretion column, as a results of Comptonization of low-energy photons coming from the thermal

mound by high-energy electrons from the accretion flow. With luminosities close to the Eddington limit, the accreted matter is halted at a certain distance from the NS surface due to the pressure exerted by the radiation. At some point the mass accretion rate is low enough that we start to see the spectrum resulting from the reprocessing of blackbody radiation injected into the accretion column from the thermal mound, that is, emission from the polar cap itself. We are entering the HB. Becker & Wolff (2007) computed for the first time the theoretical spectrum emerging from a pulsar accretion column that includes an explicit treatment of the energization occurring in the shock (see Fig. 7.52).

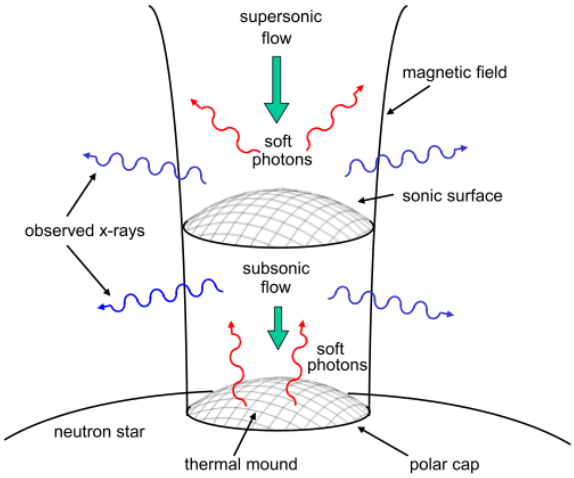

Figure 7.52: Schematic depiction of gas accreting onto the magnetic polar cap of a neutron star, from Becker & Wolff (2007)

They showed that the lower the accretion rate, the closer the thermal mound to the NS surface. In the low accretion rate/low-luminosity case we should thus detect a blackbody-like spectrum at low energies, below 2 keV according to Becker & Wolff (2007). This would explain the increase in the low-energy band and hence the decrease in the SC that we see in the HB. So, *the turning point would correspond to the transition from the standing shock to the thermal mound emission.* It is worth nothing that the significance of the presence of a blackbody component is larger in the HB than in the DB in support of this picture. However, given the

lack of sensitivity below 3 keV, this hypothesis is hard to verify and stands as mere speculation.

An alternative view of the origin of the emission during the DB would be an accretion disk instead of the standing shock. The possibility of the presence of an accretion disc was investigated with simulations by Hayasaki & Okazaki (2004) (see Fig. 7.53), and is in fact supported by the detection of spin-up in most Be/XRBs and of QPOs in some of them, during giant outbursts.

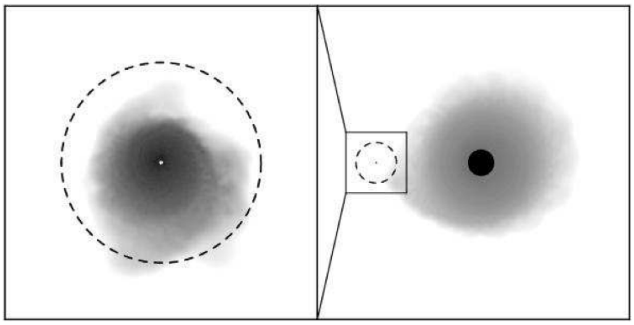

Figure 7.53: Illustrative diagram of a Be/X-ray binary according to the accretion-disc model. In this simulation, at the periastron passage, the gas in an outer part of the Be-star disc is transferred to the neutron star (right panel, from Okazaki et al. 2002) and forms an accretion disc (left panel from Hayasaki & Okazaki 2004).

The frequency of the QPO is interpreted as the Keplerian frequency at the inner edge of the disc and usually displays correlation with the spin-up rate and with the X-ray luminosity. The accretion disc is also indicated to exist between the outbursts in several systems (e.g., A 0535+26 Finger et al. 1996). On the other hand, Clark et al. (1999a) searched the optical/infrared contribution from the accretion disc in A 0535+26 during the X-ray quiescent phase, and found no signature of the accretion disc.

Obviously, more work is needed to determine the physical nature of the two branches.

7.6.3 Two classes of Be/XRBs?

Following the LMXBs classification, which subdivides neutron star systems into atoll and Z sources, it is interesting to attempt to identify subgroups of Be/XRBs, according to similarities and differences found with this study.

A two-branch pattern is traced in the CD/HID of all the four systems during giant outbursts, making it the best characterized, common feature of the whole class. As in low-mass systems, the sources do not jump through the diagram, but move smoothly along it, following the pattern. The HB corresponds to a low-intensity state and displays on average the higher fractional rms, similar to the island state in atolls and horizontal branch in Z sources. This represents the start and the end states of the source through the outburst. In the high-intensity DB the noise components display higher characteristic frequencies and lower rms than in the HB. The power law component of spectral fits shows a marked relation with flux, correlating in general with it during the DB and anti-correlating during the HB.

Differences among systems easily distinguishes two subgroups, with the slower pulsars, KS 1947+300 and EXO 2030+375, on one side, and the faster ones, 4U 0115+63 and V 0332+53, on the other. The first group is characterized by softer spectra in the HB compared with the other systems. This results in a clearer pattern in the CD of 4U 0115+63 and V 0332+53, in the same way as for atoll sources compared with Z sources. Hysteresis is not observed in the slower pulsars, while it is evident in V 0332+53 and, although with less intensity, 4U 0115+63. sCRSFs are crucial in the spectral shape of V 0332+53 and 4U 0115+63, where also a harmonic is observed in the energy range analyzed in this work. They are instead absent or very weak in the first group.

According to timing features, a strong difference among the two groups is the presence of QPOs in the faster pulsars. No narrow components are found in KS 1947+300 and EXO 2030+375, where a combination of only three broad noise Lorentzians are needed to fit PSD during the whole outburst. Instead, in 4U 0115+63 and V 0332+53, two more, peaked noise components are required,

that we referred to as QPOs since they represent a substantial concentration of power in a limited frequency range, although their Q values are not always lower than 2. In particular, $L_{\rm LF}$, with a characteristic frequency of 0.02–0.15 Hz, is common among the two systems. The other peaked component, $L_{\rm s}$, associated with the peaks of the periodic modulations, is only found in V 0332+53.

According to what we found, no evident correlations between spectral and timing parameters are present in Be/XRBs. This is an important difference compared to what is known on low-mass systems (see, for instance Kaaret et al. 1998; Bradshaw et al. 2007). The physical explanation of correlations observed in LMXBs is not clear, although some scenarios have been proposed. In general, the mechanism responsible for those correlations involves the presence of an accretion disk (Kaaret et al. 1998), which is considered responsible for the appearance of QPOs, and could also produce a blackbody flux. The blackbody spectral component would thus be related with the QPO frequency. The power law spectral component could instead arise from a corona. The flux of photons from the disk blackbody emission would cool the corona via Compton scattering, thus leading to a power-law spectrum that steepens as the blackbody flux increases. Both phenomena – correlation between QPO frequency and blackbody flux and between the photon index and the blackbody flux – are actually observed in LMXBs. The lack of this kind of relation in Be/XRBs is thus possibly related to the lack of an accretion disk. This is a merely speculative explanation, and only further investigation on both LMXBs and HMXBs outbursts will be able to solve the question.

Le vent se lève!... Il faut tenter de vivre!

Paul Valéry

8

Conclusions and future projects

8.1 Main results

- We have performed for the first time a systematic X-ray color, spectral and timing analysis on four Be/XRBs – KS 1947+300, EXO 2030+375, 4U 0115+63 and V 0332+53 – during giant outbursts.

- Two distinct spectral states emerged in the CD/HID of all the four systems, with specific spectral and timing features depending on the state. We dubbed them the horizontal branch, at low intensity, and the diagonal branch, at high intensity.

- We phenomenologically explained the transition between the two states, which is characterized by an extra emission at low energies, as due to the transition from the standing shock to the thermal mound emission.

- From marked differences in color, spectral and timing properties, we identified two subgroups in Be/XRBs, the fast pulsars on one side, and the slow ones on the other.

- The lack of correlations between spectral and timing parameters, differently from what is observed in low-mass systems, is possibly due to the lack of an accretion disk.

8.2 Future work

Our plans for the future foresee to extend the characterization of X-ray pulsar spectral states, including both more systems and more data from new X-ray emission. Results from this work are in fact limited by poor statistics, since the number of sources is not large enough to draw definite conclusions on the underlying physical parameters that may explain the differences between the two subgroups. The main difficulty is found in the transient nature of their X-ray emission and unpredictability of the type II outbursts.

In this context, we also mean to explore the properties of QPOs during giant outbursts. Several models have been proposed to explain the QPO generation mechanism in accretion-powered X-ray pulsars, among which the Keplerian frequency model and the beat-frequency model, but up to now there is no one unique paradigm able to describe the QPO frequencies observed. This research will constitute a firm starting point for the development of physical models for the giant outbursts of X-ray pulsars.

A

X-ray energy and power spectral fits

In this appendix, for each system, a table shows the spectral and timing parameters obtained from our best fits. For the spectral components, the width of the iron gaussian line was always fixed at 0.5 keV, and its value is not shown in the tables. Also, since the first harmonics of 4U 0115+63 and V 0332+53 CRSF are poorly constrained, they are not included in the results shown.

For the power spectral components, the frequency shown is the characteristic (or maximum) frequency of the Lorentzian.

Table A.1: Spectral parameters obtained for the KS 1947+300 outburst. When errors are not displayed, the corresponding parameter was fixed to the best-fit value during error calculation. The $N_{\rm H}$ was fixed at $4.3{\times}10^{21}$ cm^{-2} (Naik et al. 2006). The last column shows the retrieved reduced χ^2. Best fits were obtained with 73–74 DOF.

Obs. ID	MJD	$L_{\rm X}$ $\times10^{37}$ (erg s^{-1})	**Fe line** E (keV)	**Fe line** norm. (ph. cm^{-2} s^{-1})	**Powerlaw** Γ	**Powerlaw** Cutoff en. (keV)	**Powerlaw** norm.	$\chi^2_{\rm red}$
50425-01-05-00	51874.15	0.16	$6.17^{+0.32}_{-0.32}$	$0.0002^{+0.0001}_{-0.0001}$	$0.64^{+0.15}_{-0.15}$	$12.5^{+3.6}_{-2.4}$	$0.0039^{+0.0006}_{-0.0006}$	0.8
50425-01-06-00	51876.41	0.09	$6.04^{+0.34}_{-0.34}$	$0.0002^{+0.0001}_{-0.0001}$	$0.70^{+0.22}_{-0.24}$	$11.3^{+5.2}_{-3.0}$	$0.0031^{+0.0007}_{-0.0006}$	0.5
50425-01-07-00	51878.27	0.12	$6.39^{+0.27}_{-0.26}$	$0.0002^{+0.0001}_{-0.0001}$	$0.75^{+0.18}_{-0.19}$	$13.3^{+5.5}_{-3.3}$	$0.0037^{+0.0007}_{-0.0006}$	0.6
50425-01-08-01	51883.83	0.35	$6.45^{+0.30}_{-0.31}$	$0.0004^{+0.0002}_{-0.0001}$	$0.29^{+0.15}_{-0.16}$	$9.3^{+1.9}_{-1.4}$	$0.0055^{+0.0009}_{-0.0008}$	0.6
50425-01-08-00	51883.89	0.35	$6.45^{+0.23}_{-0.23}$	$0.0005^{+0.0001}_{-0.0001}$	$0.35^{+0.13}_{-0.13}$	$9.9^{+1.7}_{-1.3}$	$0.0059^{+0.0008}_{-0.0007}$	0.7
50425-01-09-00	51888.01	0.99	$6.28^{+0.18}_{-0.19}$	$0.0008^{+0.0002}_{-0.0002}$	$0.18^{+0.05}_{-0.05}$	$8.8^{+0.5}_{-0.4}$	$0.0130^{+0.0008}_{-0.0007}$	0.7
50425-01-09-01	51888.07	0.97	$6.23^{+0.15}_{-0.15}$	$0.0009^{+0.0002}_{-0.0002}$	$0.17^{+0.05}_{-0.05}$	$8.6^{+0.4}_{-0.4}$	$0.0128^{+0.0007}_{-0.0007}$	0.5
50425-01-10-00	51892.22	1.60	$6.46^{+0.16}_{-0.16}$	$0.0009^{+0.0002}_{-0.0002}$	$0.30^{+0.03}_{-0.03}$	$9.3^{+0.3}_{-0.3}$	$0.0259^{+0.0009}_{-0.0009}$	1.6
50425-01-11-00	51896.20	2.26	$6.60^{+0.20}_{-0.20}$	$0.0008^{+0.0002}_{-0.0002}$	$0.56^{+0.03}_{-0.03}$	$12.1^{+0.5}_{-0.4}$	$0.0496^{+0.0016}_{-0.0016}$	1.3
50425-01-11-01	51896.52	2.15	$6.37^{+0.22}_{-0.22}$	$0.0012^{+0.0003}_{-0.0003}$	$0.62^{+0.05}_{-0.05}$	$13.4^{+0.9}_{-0.8}$	$0.0496^{+0.0028}_{-0.0027}$	0.8
50425-01-12-00	51898.98	2.79	$6.48^{+0.18}_{-0.18}$	$0.0012^{+0.0002}_{-0.0002}$	$0.77^{+0.02}_{-0.02}$	$16.7^{+0.6}_{-0.6}$	$0.0754^{+0.0021}_{-0.0021}$	0.6
50425-01-13-00	51901.91	3.19	$6.60^{+0.31}_{-0.30}$	$0.0012^{+0.0004}_{-0.0004}$	$0.78^{+0.04}_{-0.04}$	$16.6^{+1.2}_{-1.1}$	$0.0887^{+0.0044}_{-0.0042}$	0.7
50425-01-13-01	51902.89	3.28	$6.42^{+0.20}_{-0.20}$	$0.0013^{+0.0004}_{-0.0004}$	$0.88^{+0.03}_{-0.03}$	$19.7^{+1.2}_{-1.1}$	$0.1010^{+0.0038}_{-0.0037}$	0.8
50425-01-14-00	51906.13	3.68	$6.47^{+0.23}_{-0.23}$	$0.0010^{+0.0003}_{-0.0003}$	$0.85^{+0.02}_{-0.02}$	$18.8^{+0.9}_{-0.8}$	$0.1110^{+0.0034}_{-0.0033}$	1.1
50425-01-14-01	51906.72	3.67	$6.31^{+0.45}_{-6.31}$	$0.0007^{+0.0005}_{-0.0005}$	$0.86^{+0.03}_{-0.04}$	$19.2^{+1.4}_{-1.2}$	$0.1120^{+0.0049}_{-0.0048}$	0.6
50425-01-15-00	51910.90	3.87	$6.45^{+0.17}_{-0.16}$	$0.0013^{+0.0003}_{-0.0003}$	$0.87^{+0.02}_{-0.02}$	$19.5^{+0.8}_{-0.7}$	$0.1180^{+0.0032}_{-0.0032}$	1.0
50425-01-16-00	51914.18	4.12	$6.36^{+0.18}_{-0.18}$	$0.0012^{+0.0003}_{-0.0003}$	$0.89^{+0.02}_{-0.02}$	$20.1^{+0.7}_{-0.7}$	$0.1300^{+0.0032}_{-0.0031}$	1.0
50425-01-17-00	51918.16	4.15	$6.54^{+0.39}_{-0.37}$	$0.0009^{+0.0004}_{-0.0005}$	$0.92^{+0.03}_{-0.03}$	$20.6^{+1.3}_{-1.1}$	$0.1380^{+0.0050}_{-0.0049}$	0.8
50425-01-18-00	51926.69	4.45	$6.32^{+0.24}_{-0.24}$	$0.0013^{+0.0005}_{-0.0005}$	$0.94^{+0.03}_{-0.03}$	$20.9^{+1.2}_{-1.1}$	$0.1520^{+0.0052}_{-0.0051}$	0.8
50425-01-19-00	51930.28	4.84	$6.24^{+0.18}_{-0.18}$	$0.0016^{+0.0005}_{-0.0005}$	$1.00^{+0.02}_{-0.02}$	$23.9^{+1.2}_{-1.1}$	$0.1760^{+0.0051}_{-0.0049}$	0.9
50425-01-20-00	51932.33	4.93	$6.27^{+0.22}_{-0.22}$	$0.0016^{+0.0005}_{-0.0005}$	$0.98^{+0.02}_{-0.02}$	$22.5^{+1.1}_{-1.0}$	$0.1770^{+0.0051}_{-0.0050}$	1.0
50425-01-21-01	51941.68	6.14	$6.15^{+0.18}_{-0.18}$	$0.0024^{+0.0006}_{-0.0006}$	$1.11^{+0.02}_{-0.02}$	$28.3^{+1.6}_{-1.5}$	$0.2700^{+0.0075}_{-0.0074}$	1.4
50425-01-21-00	51941.75	6.34	$6.13^{+0.19}_{-0.19}$	$0.0022^{+0.0006}_{-0.0006}$	$1.13^{+0.02}_{-0.02}$	$29.3^{+1.5}_{-1.4}$	$0.2890^{+0.0073}_{-0.0072}$	1.6
50425-01-22-00	51943.74	6.70	$6.12^{+0.16}_{-6.12}$	$0.0026^{+0.0006}_{-0.0006}$	$1.16^{+0.02}_{-0.02}$	$31.4^{+1.7}_{-1.6}$	$0.3170^{+0.0080}_{-0.0078}$	1.9
50425-01-23-01	51943.80	6.67	$6.13^{+0.17}_{-0.16}$	$0.0024^{+0.0006}_{-0.0006}$	$1.17^{+0.02}_{-0.02}$	$32.9^{+1.7}_{-1.6}$	$0.3170^{+0.0075}_{-0.0074}$	1.5
50425-01-23-00	51948.12	6.92	$6.23^{+0.17}_{-0.17}$	$0.0022^{+0.0005}_{-0.0005}$	$1.18^{+0.01}_{-0.01}$	$33.2^{+1.3}_{-1.2}$	$0.3330^{+0.0066}_{-0.0065}$	1.9
50425-01-17-01	51950.18	7.08	$6.25^{+0.20}_{-0.21}$	$0.0022^{+0.0006}_{-0.0006}$	$1.19^{+0.02}_{-0.02}$	$33.7^{+1.8}_{-1.7}$	$0.3480^{+0.0083}_{-0.0082}$	1.5
50425-01-24-00	51952.03	6.76	$6.22^{+0.15}_{-0.15}$	$0.0026^{+0.0006}_{-0.0006}$	$1.18^{+0.02}_{-0.02}$	$33.0^{+1.7}_{-1.5}$	$0.3250^{+0.0075}_{-0.0074}$	1.4

Continued on Next Page...

Table A.1 – Continued

Obs. ID	MJD	L_X $\times 10^{37}$ (erg s^{-1})	Fe line E (keV)	Fe line norm. (ph. cm^{-2} s^{-1})	Powerlaw Γ	Powerlaw Cutoff en. (keV)	Powerlaw norm.	χ^2_{red}
50425-01-25-00	51955.63	6.75	$6.30^{+0.24}_{-0.25}$	$0.0020^{+0.0006}_{-0.0006}$	$1.13^{+0.02}_{-0.02}$	$28.9^{+1.6}_{-1.4}$	$0.3060^{+0.0081}_{-0.0079}$	1.1
50425-01-26-00	51961.53	6.49	$6.26^{+0.18}_{-0.18}$	$0.0022^{+0.0006}_{-0.0006}$	$1.14^{+0.02}_{-0.02}$	$29.4^{+1.5}_{-1.3}$	$0.3040^{+0.0074}_{-0.0072}$	1.6
50425-01-27-00	51963.97	6.53	$6.12^{+0.24}_{-0.24}$	$0.0021^{+0.0008}_{-0.0007}$	$1.14^{+0.02}_{-0.02}$	$29.2^{+2.1}_{-1.8}$	$0.3040^{+0.0098}_{-0.0096}$	1.5
50425-01-29-00	51968.56	5.59	$6.37^{+0.22}_{-0.22}$	$0.0016^{+0.0005}_{-0.0005}$	$1.07^{+0.02}_{-0.02}$	$27.3^{+1.5}_{-1.4}$	$0.2290^{+0.0064}_{-0.0062}$	1.0
60402-01-01-00	51970.21	5.78	$6.35^{+0.24}_{-0.24}$	$0.0016^{+0.0006}_{-0.0006}$	$1.08^{+0.02}_{-0.02}$	$26.7^{+1.6}_{-1.5}$	$0.2430^{+0.0073}_{-0.0071}$	0.7
60402-01-02-00	51972.19	5.55	$6.21^{+0.25}_{-0.25}$	$0.0020^{+0.0007}_{-0.0007}$	$1.10^{+0.03}_{-0.03}$	$27.9^{+2.2}_{-1.9}$	$0.2410^{+0.0087}_{-0.0085}$	1.0
60402-01-03-00	51974.58	5.13	$6.25^{+0.20}_{-0.21}$	$0.0018^{+0.0005}_{-0.0005}$	$1.03^{+0.02}_{-0.02}$	$24.5^{+1.4}_{-1.2}$	$0.2010^{+0.0060}_{-0.0059}$	0.8
60402-01-04-00	51976.24	5.23	$6.16^{+0.27}_{-0.27}$	$0.0012^{+0.0005}_{-0.0005}$	$1.00^{+0.02}_{-0.02}$	$23.0^{+1.1}_{-1.0}$	$0.1980^{+0.0057}_{-0.0055}$	1.0
60402-01-05-00	51978.23	5.20	$6.31^{+0.25}_{-0.25}$	$0.0010^{+0.0005}_{-0.0005}$	$1.02^{+0.02}_{-0.02}$	$23.5^{+1.3}_{-1.2}$	$0.2050^{+0.0060}_{-0.0057}$	1.3
60402-01-06-00	51980.74	4.86	$6.24^{+0.25}_{-0.20}$	$0.0013^{+0.0004}_{-0.0005}$	$0.96^{+0.02}_{-0.02}$	$21.8^{+0.9}_{-0.9}$	$0.1710^{+0.0045}_{-0.0044}$	1.1
60402-01-07-00	51983.86	4.48	$6.34^{+0.21}_{-0.22}$	$0.0015^{+0.0005}_{-0.0005}$	$0.94^{+0.03}_{-0.03}$	$21.3^{+1.2}_{-1.1}$	$0.1510^{+0.0051}_{-0.0050}$	0.9
60402-01-08-00	51984.86	4.32	$6.28^{+0.27}_{-0.27}$	$0.0013^{+0.0004}_{-0.0004}$	$0.91^{+0.02}_{-0.02}$	$20.6^{+1.0}_{-0.9}$	$0.1400^{+0.0042}_{-0.0041}$	0.9
60402-01-09-00	51986.58	4.27	$6.52^{+0.26}_{-0.26}$	$0.0011^{+0.0004}_{-0.0004}$	$0.90^{+0.03}_{-0.03}$	$20.8^{+1.2}_{-1.1}$	$0.1340^{+0.0045}_{-0.0043}$	0.8
60402-01-10-00	51988.27	3.73	$6.47^{+0.44}_{-0.44}$	$0.0011^{+0.0006}_{-0.0007}$	$0.88^{+0.05}_{-0.05}$	$19.4^{+2.0}_{-1.7}$	$0.1170^{+0.0069}_{-0.0066}$	0.6
60402-01-11-00	51990.12	3.60	$6.37^{+0.42}_{-0.42}$	$0.0005^{+0.0005}_{-0.0005}$	$0.80^{+0.04}_{-0.04}$	$17.2^{+1.2}_{-1.0}$	$0.1010^{+0.0023}_{-0.0045}$	0.7
60402-01-12-00	51992.17	3.56	$6.48^{+0.48}_{-0.48}$	$0.0006^{+0.0007}_{-0.0006}$	$0.86^{+0.06}_{-0.06}$	$19.1^{+2.4}_{-2.0}$	$0.1070^{+0.0077}_{-0.0075}$	0.6
60402-01-13-00	51994.23	3.22	$6.52^{+0.43}_{-0.54}$	$0.0002^{+0.0006}_{-0.0003}$	$0.81^{+0.05}_{-0.05}$	$17.2^{+1.6}_{-1.3}$	$0.0927^{+0.0058}_{-0.0052}$	0.8
60402-01-14-00	51996.08	3.27	$6.58^{+0.42}_{-0.42}$	$0.0008^{+0.0004}_{-0.0004}$	$0.82^{+0.04}_{-0.04}$	$17.7^{+1.2}_{-1.1}$	$0.0956^{+0.0041}_{-0.0040}$	1.2
60402-01-15-00	51998.14	2.99	$6.46^{+0.46}_{-0.46}$	$0.0008^{+0.0006}_{-0.0005}$	$0.80^{+0.05}_{-0.05}$	$16.6^{+1.7}_{-1.4}$	$0.0861^{+0.0056}_{-0.0053}$	0.7
60402-01-15-01	51999.06	2.80	$6.49^{+0.50}_{-0.50}$	$0.0006^{+0.0005}_{-0.0002}$	$0.76^{+0.05}_{-0.05}$	$16.4^{+1.5}_{-1.3}$	$0.0746^{+0.0041}_{-0.0044}$	0.8
60402-01-16-01	51999.98	2.72	$6.44^{+0.31}_{-0.32}$	$0.0009^{+0.0003}_{-0.0004}$	$0.76^{+0.04}_{-0.04}$	$16.4^{+1.1}_{-1.0}$	$0.0714^{+0.0033}_{-0.0032}$	0.9
60402-01-16-00	52000.06	2.73	$6.37^{+0.31}_{-0.30}$	$0.0012^{+0.0005}_{-0.0005}$	$0.71^{+0.05}_{-0.05}$	$15.1^{+1.4}_{-1.2}$	$0.0684^{+0.0045}_{-0.0042}$	1.0
60402-01-16-02	52001.05	2.74	$6.58^{+0.34}_{-0.34}$	$0.0010^{+0.0005}_{-0.0004}$	$0.70^{+0.05}_{-0.05}$	$15.7^{+1.3}_{-1.1}$	$0.0659^{+0.0038}_{-0.0037}$	0.7
60402-01-17-00	52002.04	2.62	$6.36^{+0.37}_{-0.35}$	$0.0008^{+0.0005}_{-0.0005}$	$0.77^{+0.05}_{-0.05}$	$17.1^{+1.7}_{-1.4}$	$0.0687^{+0.0047}_{-0.0044}$	0.9
60402-01-18-00	52004.38	2.43	$6.21^{+0.23}_{-0.23}$	$0.0005^{+0.0005}_{-0.0002}$	$0.73^{+0.06}_{-0.03}$	$16.1^{+1.6}_{-1.4}$	$0.0617^{+0.0023}_{-0.0040}$	0.6
60402-01-19-00	52006.09	2.28	$6.51^{+0.27}_{-0.28}$	$0.0010^{+0.0004}_{-0.0003}$	$0.68^{+0.05}_{-0.05}$	$14.8^{+1.2}_{-1.0}$	$0.0543^{+0.0031}_{-0.0030}$	1.0
60402-01-20-00	52008.21	2.14	$6.40^{+0.19}_{-0.19}$	$0.0012^{+0.0003}_{-0.0003}$	$0.68^{+0.04}_{-0.04}$	$15.0^{+1.1}_{-1.0}$	$0.0502^{+0.0027}_{-0.0026}$	0.9
60402-01-21-00	52010.80	2.12	$6.93^{+0.93}_{-0.52}$	$0.0008^{+0.0004}_{-0.0005}$	$0.67^{+0.07}_{-0.07}$	$14.3^{+1.7}_{-1.4}$	$0.0509^{+0.0042}_{-0.0040}$	0.5
60402-01-22-00	52014.39	1.93	$6.43^{+0.29}_{-0.28}$	$0.0009^{+0.0003}_{-0.0003}$	$0.59^{+0.05}_{-0.05}$	$12.9^{+0.9}_{-0.8}$	$0.0429^{+0.0024}_{-0.0023}$	0.7
60402-01-23-00	52016.37	1.76	$6.67^{+0.24}_{-0.23}$	$0.0010^{+0.0003}_{-0.0003}$	$0.59^{+0.05}_{-0.05}$	$13.3^{+1.0}_{-0.9}$	$0.0378^{+0.0022}_{-0.0021}$	0.7
60402-01-24-00	52017.63	1.72	$6.44^{+0.25}_{-0.24}$	$0.0008^{+0.0003}_{-0.0003}$	$0.65^{+0.05}_{-0.05}$	$14.4^{+1.2}_{-1.0}$	$0.0392^{+0.0023}_{-0.0022}$	1.2
60402-01-25-00	52021.06	1.51	$6.43^{+0.39}_{-0.35}$	$0.0009^{+0.0003}_{-0.0004}$	$0.50^{+0.08}_{-0.08}$	$11.7^{+1.3}_{-1.1}$	$0.0295^{+0.0027}_{-0.0013}$	0.7

Continued on Next Page...

Table A.1 – Continued

Obs. ID	MJD	L_X $\times 10^{37}$ (erg s^{-1})	Fe line E (keV)	Fe line norm. (ph. cm^{-2} s^{-1})	Powerlaw Γ	Powerlaw Cutoff en. (keV)	Powerlaw norm.	χ^2_{red}
60402-01-26-00	52023.59	1.36	$6.85^{+0.26}_{-0.26}$	$0.0011^{+0.0003}_{-0.0004}$	$0.65^{+0.09}_{-0.09}$	$15.7^{+2.8}_{-2.1}$	$0.0288^{+0.0031}_{-0.0029}$	0.8
60402-01-27-00	52024.32	1.30	$6.53^{+0.27}_{-0.28}$	$0.0010^{+0.0003}_{-0.0003}$	$0.49^{+0.07}_{-0.07}$	$11.8^{+1.2}_{-1.0}$	$0.0248^{+0.0021}_{-0.0020}$	0.8
60402-01-28-00	52027.35	1.12	$6.31^{+0.31}_{-0.31}$	$0.0007^{+0.0002}_{-0.0002}$	$0.41^{+0.07}_{-0.07}$	$11.1^{+1.0}_{-0.9}$	$0.0189^{+0.0015}_{-0.0015}$	0.9
60402-01-29-00	52028.23	1.07	$6.36^{+0.20}_{-0.20}$	$0.0009^{+0.0002}_{-0.0002}$	$0.48^{+0.06}_{-0.06}$	$11.9^{+1.0}_{-0.9}$	$0.0197^{+0.0015}_{-0.0014}$	0.6
60402-01-30-00	52029.83	1.00	$6.49^{+0.31}_{-0.32}$	$0.0005^{+0.0003}_{-0.0002}$	$0.40^{+0.08}_{-0.08}$	$10.3^{+1.1}_{-0.9}$	$0.0178^{+0.0017}_{-0.0016}$	0.7
60402-01-31-00	52032.93	0.78	$6.37^{+0.18}_{-0.18}$	$0.0008^{+0.0002}_{-0.0001}$	$0.41^{+0.07}_{-0.07}$	$11.1^{+1.0}_{-0.9}$	$0.0129^{+0.0011}_{-0.0010}$	1.3
60402-01-32-00	52034.92	0.67	$6.28^{+0.32}_{-0.32}$	$0.0005^{+0.0002}_{-0.0002}$	$0.51^{+0.08}_{-0.08}$	$12.3^{+1.5}_{-1.3}$	$0.0127^{+0.0012}_{-0.0011}$	0.6
60402-01-33-00	52035.72	0.63	$6.36^{+0.40}_{-0.40}$	$0.0004^{+0.0002}_{-0.0002}$	$0.41^{+0.10}_{-0.09}$	$11.1^{+1.6}_{-1.3}$	$0.0107^{+0.0013}_{-0.0012}$	0.7
60402-01-34-00	52038.70	0.48	$6.48^{+0.30}_{-0.30}$	$0.0004^{+0.0002}_{-0.0002}$	$0.41^{+0.13}_{-0.13}$	$11.2^{+2.2}_{-1.6}$	$0.0080^{+0.0012}_{-0.0011}$	0.7
60402-01-35-00	52040.69	0.40	$6.65^{+0.50}_{-0.50}$	$0.0003^{+0.0002}_{-0.0001}$	$0.27^{+0.15}_{-0.16}$	$9.4^{+1.9}_{-1.4}$	$0.0058^{+0.0010}_{-0.0009}$	0.7
60402-01-36-00	52041.55	0.36	$6.34^{+0.27}_{-0.27}$	$0.0004^{+0.0002}_{-0.0002}$	$0.35^{+0.16}_{-0.17}$	$10.0^{+2.4}_{-1.7}$	$0.0060^{+0.0012}_{-0.0010}$	0.5
60402-01-37-00	52044.08	0.32	$6.21^{+0.34}_{-0.34}$	$0.0005^{+0.0002}_{-0.0002}$	$0.11^{+0.22}_{-0.24}$	$8.1^{+2.2}_{-1.5}$	$0.0040^{+0.0011}_{-0.0009}$	0.6
60402-01-38-01	52046.99	0.26	$6.40^{+0.46}_{-0.46}$	$0.0004^{+0.0002}_{-0.0002}$	$0.69^{+0.30}_{-0.31}$	$14.1^{+14.4}_{-5.2}$	$0.0065^{+0.0025}_{-0.0019}$	0.5
60402-01-38-00	52047.06	0.24	$6.03^{+0.35}_{-0.16}$	$0.0008^{+0.0004}_{-0.0003}$	$0.34^{+0.49}_{-0.52}$	$9.8^{+12.2}_{-3.7}$	$0.0038^{+0.0028}_{-0.0016}$	0.5
60402-01-39-00	52050.11	0.19	$6.02^{+0.31}_{-0.31}$	$0.0000^{+0.0003}_{-0.0000}$	$0.25^{+0.51}_{-0.51}$	$7.4^{+6.5}_{-2.3}$	$0.0040^{+0.0022}_{-0.0016}$	0.5
60402-01-39-01	52050.18	0.18	$6.30^{+0.52}_{-0.52}$	$0.0006^{+0.0004}_{-0.0004}$	$0.40^{+1.03}_{-0.38}$	$10.2^{+5.2}_{-5.8}$	$0.0034^{+0.0050}_{-0.0018}$	0.6
60402-01-40-00	52052.95	0.16	$6.32^{+0.34}_{-6.32}$	$0.0004^{+0.0002}_{-0.0002}$	$0.78^{+0.42}_{-0.39}$	$13.9^{+32.8}_{-5.9}$	$0.0051^{+0.0028}_{-0.0017}$	0.7
60402-01-41-00	52055.82	0.14	$6.99^{+0.62}_{-0.62}$	$0.0003^{+0.0002}_{-0.0002}$	$0.79^{+0.17}_{-0.16}$	$13.0^{+32.8}_{-5.9}$	$0.0048^{+0.0014}_{-0.0014}$	0.6
60402-01-41-01	52056.21	0.14	$6.32^{+0.60}_{-0.60}$	$0.0001^{+0.0002}_{-0.0001}$	$0.60^{+0.96}_{-0.66}$	$10.3^{+38.8}_{-5.1}$	$0.0040^{+0.0035}_{-0.0019}$	0.6
60402-01-42-00	52057.87	0.13	$6.32^{+0.70}_{-0.70}$	$0.0001^{+0.0001}_{-0.0001}$	$0.70^{+0.40}_{-0.56}$	$11.6^{+16.4}_{-5.3}$	$0.0040^{+0.0019}_{-0.0017}$	0.5
60402-01-43-00	52060.31	0.11	$6.04^{+0.95}_{-0.95}$	$0.0001^{+0.0001}_{-0.0001}$	$0.60^{+0.36}_{-0.37}$	$9.9^{+7.5}_{-3.2}$	$0.0032^{+0.0015}_{-0.0010}$	0.5
60402-01-44-01	52062.82	0.10	$6.65^{+0.65}_{-0.65}$	$0.0001^{+0.0001}_{-0.0001}$	$0.69^{+0.39}_{-0.58}$	$12.0^{+15.5}_{-5.4}$	$0.0029^{+0.0014}_{-0.0013}$	0.6
60402-01-44-02	52062.89	0.09	$6.00^{+0.50}_{-0.50}$	$0.0001^{+0.0001}_{-0.0001}$	$0.24^{+0.38}_{-0.42}$	$6.9^{+3.5}_{-1.9}$	$0.0019^{+0.0009}_{-0.0007}$	0.4
60402-01-45-00	52078.05	0.06	$6.30^{+0.35}_{-0.30}$	$0.0002^{+0.0001}_{-0.0001}$	$0.94^{+0.34}_{-0.38}$	$14.9^{+25.8}_{-6.4}$	$0.0027^{+0.0012}_{-0.0009}$	0.5

Table A.2: The same as Table A.1, for EXO 2030+375. Best fits were obtained with 47–72 DOF.

Obs. ID	MJD	L_X $\times 10^{37}$ (erg/s)	N_H cm^{-2}	Cyclotron line E (keV)	Cyclotron line σ (keV)	Cyclotron line τ	Fe line E (keV)	Fe line norm. (ph./cm^2/s)	Power law Γ	Power law cutoff (keV)	Power law norm.	χ^2_r
91089-01-07-00	53914.89	9.21	1.49	$8.6^{+1.4}_{-4.3}$	$4.5^{+6.4}_{-1.4}$	$1.18^{+7.45}_{-0.68}$	$6.44^{+0.11}_{-0.10}$	$0.0159^{+0.0060}_{-0.0031}$	$1.08^{+0.30}_{-0.09}$	$17.4^{+3.2}_{-1.1}$	$1.13^{+0.68}_{-0.21}$	1.0
91089-01-07-01	53915.83	9.17	1.01	$9.4^{+0.9}_{-3.2}$	$3.9^{+1.9}_{-1.0}$	$0.94^{+2.36}_{-0.45}$	$6.43^{+0.10}_{-0.10}$	$0.0167^{+0.0041}_{-0.0030}$	$1.04^{+0.17}_{-0.07}$	$17.4^{+1.8}_{-1.0}$	$0.98^{+0.50}_{-0.14}$	0.8
91089-01-08-00	53916.81	9.93	1.52	$8.4^{+1.4}_{-7.1}$	$4.4^{+3.1}_{-1.2}$	$1.31^{+8.86}_{-0.74}$	$6.49^{+0.10}_{-0.10}$	$0.0187^{+0.0058}_{-0.0034}$	$1.12^{+0.33}_{-0.09}$	$17.8^{+3.5}_{-1.2}$	$1.27^{+1.27}_{-0.25}$	0.7
91089-01-08-01	53917.76	9.99	0.84	$9.6^{+0.6}_{-1.2}$	$3.7^{+1.5}_{-0.8}$	$1.00^{+0.81}_{-0.33}$	$6.40^{+0.09}_{-0.09}$	$0.0178^{+0.0029}_{-0.0026}$	$1.05^{+0.08}_{-0.05}$	$16.8^{+0.8}_{-0.6}$	$1.09^{+0.25}_{-0.12}$	0.8
91089-01-08-02	53918.50	10.49	1.26	$9.1^{+1.0}_{-2.8}$	$4.5^{+2.6}_{-1.4}$	$1.48^{+3.73}_{-0.75}$	$6.40^{+0.10}_{-0.10}$	$0.0196^{+0.0054}_{-0.0035}$	$1.08^{+0.19}_{-0.08}$	$17.0^{+1.7}_{-1.0}$	$1.27^{+0.60}_{-0.22}$	0.8
91089-01-08-03	53919.61	10.90	1.54	$9.1^{+0.8}_{-1.6}$	$4.4^{+1.3}_{-0.8}$	$1.71^{+1.52}_{-0.61}$	$6.48^{+0.09}_{-0.08}$	$0.0208^{+0.0038}_{-0.0031}$	$1.12^{+0.12}_{-0.07}$	$17.3^{+1.2}_{-0.8}$	$1.43^{+0.49}_{-0.22}$	0.9
91089-01-08-06	53920.71	10.95	1.09	$9.6^{+0.5}_{-1.0}$	$3.7^{+1.0}_{-0.7}$	$1.18^{+0.74}_{-0.35}$	$6.43^{+0.09}_{-0.08}$	$0.0200^{+0.0032}_{-0.0028}$	$1.09^{+0.08}_{-0.05}$	$17.2^{+0.8}_{-0.6}$	$1.32^{+0.28}_{-0.15}$	0.8
91089-01-08-04	53921.07	10.67	1.03	$9.4^{+0.6}_{-1.6}$	$3.4^{+1.3}_{-0.7}$	$0.93^{+1.18}_{-0.35}$	$6.34^{+0.09}_{-0.09}$	$0.0214^{+0.0043}_{-0.0035}$	$1.10^{+0.12}_{-0.06}$	$17.7^{+1.4}_{-1.0}$	$1.26^{+0.43}_{-0.16}$	0.7
91089-01-08-05	53922.28	10.80	1.37	$9.2^{+0.8}_{-1.6}$	$4.2^{+1.4}_{-0.8}$	$1.47^{+1.40}_{-0.52}$	$6.45^{+0.09}_{-0.09}$	$0.0201^{+0.0037}_{-0.0030}$	$1.11^{+0.11}_{-0.07}$	$17.5^{+1.2}_{-0.8}$	$1.37^{+0.44}_{-0.20}$	0.9
91089-01-09-00	53923.33	11.21	1.53	$8.6^{+1.0}_{-2.8}$	$4.7^{+1.7}_{-1.0}$	$1.85^{+3.07}_{-0.80}$	$6.48^{+0.08}_{-0.08}$	$0.0226^{+0.0052}_{-0.0035}$	$1.17^{+0.17}_{-0.08}$	$18.3^{+1.8}_{-1.0}$	$1.60^{+1.25}_{-0.29}$	1.2
91089-01-09-01	53924.70	11.55	1.17	$9.8^{+0.5}_{-0.8}$	$3.5^{+1.0}_{-0.7}$	$1.12^{+0.66}_{-0.32}$	$6.42^{+0.09}_{-0.09}$	$0.0213^{+0.0036}_{-0.0033}$	$1.13^{+0.07}_{-0.05}$	$17.9^{+1.0}_{-0.9}$	$1.48^{+0.29}_{-0.16}$	0.9
91089-01-09-03	53926.63	11.88	1.25	$9.3^{+0.6}_{-1.1}$	$4.1^{+0.9}_{-0.6}$	$1.62^{+1.03}_{-0.48}$	$6.41^{+0.08}_{-0.08}$	$0.0245^{+0.0038}_{-0.0033}$	$1.13^{+0.09}_{-0.06}$	$17.3^{+0.9}_{-0.7}$	$1.58^{+0.40}_{-0.21}$	0.9
91089-01-09-04	53928.18	12.43	1.38	$9.4^{+0.7}_{-1.4}$	$4.3^{+1.5}_{-1.0}$	$1.86^{+1.59}_{-0.67}$	$6.43^{+0.09}_{-0.09}$	$0.0249^{+0.0049}_{-0.0041}$	$1.16^{+0.11}_{-0.07}$	$17.8^{+1.3}_{-1.0}$	$1.78^{+0.60}_{-0.28}$	0.9
91089-01-09-05	53928.64	11.40	1.02	$9.5^{+0.5}_{-1.0}$	$3.5^{+1.1}_{-0.7}$	$1.24^{+0.93}_{-0.40}$	$6.43^{+0.08}_{-0.08}$	$0.0242^{+0.0043}_{-0.0037}$	$1.11^{+0.09}_{-0.06}$	$17.4^{+1.1}_{-0.9}$	$1.44^{+0.38}_{-0.18}$	0.9
91089-01-09-06	53929.61	12.59	1.15	$9.9^{+0.4}_{-0.8}$	$3.9^{+0.7}_{-0.5}$	$1.46^{+0.79}_{-0.40}$	$6.43^{+0.09}_{-0.09}$	$0.0243^{+0.0039}_{-0.0035}$	$1.14^{+0.07}_{-0.05}$	$18.0^{+0.9}_{-0.8}$	$1.67^{+0.33}_{-0.19}$	0.8
91089-01-10-00	53930.79	13.01	1.21	$9.6^{+0.5}_{-1.0}$	$3.9^{+0.9}_{-0.6}$	$1.38^{+0.93}_{-0.42}$	$6.41^{+0.08}_{-0.08}$	$0.0257^{+0.0040}_{-0.0036}$	$1.17^{+0.08}_{-0.05}$	$19.0^{+1.0}_{-0.8}$	$1.80^{+0.42}_{-0.22}$	0.9
91089-01-10-01	53931.39	12.94	1.25	$9.8^{+0.4}_{-0.7}$	$3.3^{+0.6}_{-0.5}$	$1.03^{+0.47}_{-0.25}$	$6.47^{+0.08}_{-0.08}$	$0.0240^{+0.0036}_{-0.0034}$	$1.18^{+0.06}_{-0.05}$	$19.5^{+0.9}_{-0.8}$	$1.75^{+0.28}_{-0.17}$	0.8
91089-01-10-02	53932.24	13.35	1.31	$9.7^{+0.5}_{-0.7}$	$3.9^{+0.9}_{-0.6}$	$1.64^{+0.72}_{-0.41}$	$6.45^{+0.08}_{-0.08}$	$0.0274^{+0.0041}_{-0.0038}$	$1.16^{+0.07}_{-0.05}$	$18.4^{+1.0}_{-0.8}$	$1.86^{+0.36}_{-0.22}$	0.9
91089-01-10-03	53933.36	13.75	1.37	$9.7^{+0.5}_{-0.8}$	$4.0^{+0.9}_{-0.6}$	$1.71^{+0.87}_{-0.46}$	$6.44^{+0.08}_{-0.08}$	$0.0287^{+0.0044}_{-0.0039}$	$1.19^{+0.08}_{-0.06}$	$18.8^{+1.0}_{-0.8}$	$2.03^{+0.43}_{-0.25}$	0.7
91089-01-10-04	53934.26	13.36	1.35	$9.8^{+0.4}_{-0.7}$	$3.6^{+0.8}_{-0.5}$	$1.41^{+0.63}_{-0.35}$	$6.46^{+0.08}_{-0.08}$	$0.0266^{+0.0041}_{-0.0037}$	$1.19^{+0.07}_{-0.05}$	$19.1^{+1.0}_{-0.8}$	$1.92^{+0.35}_{-0.21}$	0.8
91089-01-10-05	53935.18	13.48	1.41	$9.8^{+0.4}_{-0.7}$	$3.6^{+0.7}_{-0.5}$	$1.51^{+0.73}_{-0.38}$	$6.47^{+0.09}_{-0.09}$	$0.0262^{+0.0045}_{-0.0040}$	$1.19^{+0.07}_{-0.05}$	$19.1^{+1.1}_{-1.0}$	$1.94^{+0.39}_{-0.23}$	0.7
91089-01-10-06	53936.30	13.85	1.53	$9.7^{+0.5}_{-0.8}$	$4.0^{+0.7}_{-0.5}$	$1.71^{+0.87}_{-0.45}$	$6.45^{+0.08}_{-0.08}$	$0.0296^{+0.0046}_{-0.0040}$	$1.24^{+0.08}_{-0.06}$	$19.9^{+1.1}_{-0.9}$	$2.19^{+0.48}_{-0.27}$	0.9
91089-01-11-00	53937.35	13.92	1.49	$9.6^{+0.4}_{-0.7}$	$3.9^{+0.7}_{-0.5}$	$1.66^{+0.76}_{-0.41}$	$6.46^{+0.08}_{-0.08}$	$0.0286^{+0.0043}_{-0.0038}$	$1.23^{+0.07}_{-0.05}$	$19.9^{+1.1}_{-0.9}$	$2.16^{+0.44}_{-0.26}$	0.9
91089-01-11-01	53938.17	12.19	0.86	$9.5^{+0.9}_{-3.2}$	$4.5^{+3.1}_{-1.4}$	$2.99^{+7.21}_{-1.46}$	$6.40^{+0.15}_{-0.14}$	$0.0310^{+0.0172}_{-0.0086}$	$1.05^{+0.30}_{-0.15}$	$14.9^{+2.6}_{-2.0}$	$1.62^{+1.79}_{-0.43}$	0.7
91089-01-11-02	53938.43	13.12	1.62	$9.2^{+0.7}_{-0.7}$	$4.2^{+1.1}_{-0.6}$	$2.04^{+2.58}_{-0.78}$	$6.44^{+0.09}_{-0.08}$	$0.0296^{+0.0076}_{-0.0049}$	$1.22^{+0.16}_{-0.08}$	$18.8^{+1.6}_{-1.1}$	$2.09^{+0.86}_{-0.38}$	0.9
91089-01-11-03	53939.25	13.85	1.22	$9.8^{+0.4}_{-0.7}$	$3.5^{+0.8}_{-0.6}$	$1.30^{+0.61}_{-0.34}$	$6.46^{+0.09}_{-0.09}$	$0.0261^{+0.0043}_{-0.0039}$	$1.20^{+0.07}_{-0.05}$	$19.4^{+1.0}_{-0.9}$	$1.98^{+0.36}_{-0.21}$	1.0
91089-01-11-04	53940.13	12.18	0.41	$10.0^{+0.5}_{-1.2}$	$3.7^{+1.3}_{-0.8}$	$1.69^{+1.68}_{-0.64}$	$6.44^{+0.13}_{-0.13}$	$0.0250^{+0.0071}_{-0.0056}$	$1.08^{+0.13}_{-0.07}$	$17.4^{+2.0}_{-1.7}$	$1.41^{+0.55}_{-0.20}$	1.0
91089-01-11-05	53941.44	14.73	1.59	$9.1^{+0.8}_{-2.4}$	$4.4^{+1.0}_{-0.6}$	$2.06^{+3.25}_{-0.84}$	$6.45^{+0.09}_{-0.08}$	$0.0326^{+0.0094}_{-0.0054}$	$1.30^{+0.19}_{-0.08}$	$21.2^{+2.5}_{-1.4}$	$2.65^{+1.23}_{-0.50}$	0.9
91089-01-11-06	53942.26	14.29	1.36	$9.6^{+0.5}_{-0.8}$	$4.0^{+1.0}_{-0.7}$	$1.71^{+0.89}_{-0.46}$	$6.43^{+0.08}_{-0.08}$	$0.0309^{+0.0048}_{-0.0042}$	$1.24^{+0.08}_{-0.06}$	$19.6^{+1.2}_{-1.0}$	$2.28^{+0.51}_{-0.29}$	1.0
91089-01-12-00	53944.05	11.91	1.03	$9.5^{+0.8}_{-6.0}$	$3.4^{+2.7}_{-0.8}$	$1.03^{+9.04}_{-0.55}$	$6.40^{+0.11}_{-0.11}$	$0.0312^{+0.0221}_{-0.0069}$	$1.26^{+0.39}_{-0.10}$	$22.8^{+6.6}_{-2.7}$	$1.76^{+2.93}_{-0.32}$	0.7
91089-01-12-01	53944.97	12.53	1.76	$9.7^{+0.5}_{-1.1}$	$4.3^{+1.0}_{-0.6}$	$2.81^{+2.14}_{-0.93}$	$6.36^{+0.10}_{-0.10}$	$0.0325^{+0.0083}_{-0.0062}$	$1.22^{+0.13}_{-0.09}$	$19.0^{+2.1}_{-1.7}$	$2.09^{+0.91}_{-0.40}$	1.1

Continued on Next Page...

Table A.2 – Continued

Obs. ID	MJD	L_X $\times 10^{37}$ (erg/s)	N_H cm^{-2}	Cyclotron line E (keV)	Cyclotron line σ (keV)	Cyclotron line τ	Fe line E (keV)	Fe line norm. (ph./cm^2/s)	Power law Γ	Power law cutoff (keV)	Power law norm.	χ^2_r
91089-01-12-02	53945.95	13.51	0.78	$9.9^{+0.5}_{-1.1}$	$3.6^{+0.9}_{-0.6}$	$1.73^{+1.56}_{-0.60}$	$6.41^{+0.10}_{-0.10}$	$0.0357^{+0.0087}_{-0.0066}$	$1.13^{+0.13}_{-0.09}$	$16.5^{+1.8}_{-1.5}$	$1.88^{+0.72}_{-0.31}$	0.8
91089-01-12-03	53946.86	12.79	1.05	$9.6^{+0.5}_{-0.9}$	$3.5^{+0.8}_{-0.5}$	$1.49^{+1.09}_{-0.47}$	$6.41^{+0.09}_{-0.09}$	$0.0286^{+0.0060}_{-0.0050}$	$1.20^{+0.11}_{-0.07}$	$19.2^{+1.6}_{-1.3}$	$1.87^{+0.57}_{-0.27}$	1.0
91089-01-12-05	53947.71	13.42	1.85	$8.7^{+1.2}_{-3.7}$	$5.3^{+1.6}_{-0.8}$	$3.80^{+8.32}_{-1.85}$	$6.45^{+0.09}_{-0.09}$	$0.0376^{+0.0179}_{-0.0079}$	$1.32^{+0.29}_{-0.12}$	$19.7^{+3.2}_{-1.9}$	$2.84^{+2.31}_{-0.80}$	1.0
91089-01-12-04	53948.82	13.43	1.59	$9.5^{+0.8}_{-2.9}$	$4.4^{+2.3}_{-0.9}$	$2.46^{+5.53}_{-1.13}$	$6.50^{+0.13}_{-0.13}$	$0.0289^{+0.0117}_{-0.0071}$	$1.27^{+0.26}_{-0.11}$	$22.0^{+3.7}_{-2.5}$	$2.24^{+1.89}_{-0.51}$	0.8
91089-01-12-06	53949.80	12.90	2.46	$8.0^{+1.1}_{-3.7}$	$5.3^{+1.8}_{-0.9}$	$4.31^{+8.25}_{-1.99}$	$6.54^{+0.08}_{-0.08}$	$0.0396^{+0.0128}_{-0.0080}$	$1.41^{+0.34}_{-0.15}$	$21.3^{+4.4}_{-2.2}$	$3.35^{+2.46}_{-1.09}$	1.0
91089-01-12-07	53950.92	12.87	1.49	$9.4^{+0.7}_{-1.4}$	$4.5^{+1.0}_{-0.6}$	$2.79^{+2.59}_{-1.02}$	$6.44^{+0.08}_{-0.08}$	$0.0384^{+0.0095}_{-0.0063}$	$1.27^{+0.15}_{-0.09}$	$20.0^{+2.1}_{-1.7}$	$2.29^{+1.17}_{-0.46}$	0.9
91089-01-13-00	53951.77	13.18	1.46	$9.3^{+0.9}_{-2.8}$	$4.7^{+2.9}_{-1.2}$	$2.63^{+4.38}_{-1.13}$	$6.45^{+0.12}_{-0.11}$	$0.0306^{+0.0068}_{-0.0064}$	$1.23^{+0.22}_{-0.11}$	$20.8^{+3.9}_{-2.2}$	$2.05^{+1.69}_{-0.46}$	0.8
91089-01-13-01	53952.82	13.48	1.85	$9.4^{+0.7}_{-1.6}$	$3.8^{+1.0}_{-0.6}$	$1.73^{+2.11}_{-0.66}$	$6.47^{+0.10}_{-0.10}$	$0.0302^{+0.0084}_{-0.0060}$	$1.30^{+0.16}_{-0.09}$	$21.6^{+2.7}_{-1.9}$	$2.35^{+1.25}_{-0.41}$	0.9
91089-01-13-02	53953.73	12.54	0.88	$9.4^{+0.9}_{-2.0}$	$4.9^{+2.0}_{-1.1}$	$3.02^{+3.53}_{-1.22}$	$6.44^{+0.09}_{-0.09}$	$0.0332^{+0.0095}_{-0.0061}$	$1.15^{+0.17}_{-0.10}$	$16.9^{+1.8}_{-1.5}$	$1.89^{+1.16}_{-0.40}$	1.1
91089-01-14-06	53958.60	13.20	0.93	$10.1^{+0.4}_{-0.7}$	$3.6^{+1.4}_{-0.9}$	$1.61^{+0.88}_{-0.47}$	$6.37^{+0.09}_{-0.09}$	$0.0306^{+0.0054}_{-0.0048}$	$1.16^{+0.08}_{-0.06}$	$19.0^{+1.5}_{-1.3}$	$1.75^{+0.37}_{-0.22}$	0.9
91089-01-14-00	53959.82	13.32	0.90	$10.0^{+0.7}_{-2.8}$	$2.9^{+1.7}_{-0.8}$	$0.99^{+3.21}_{-0.47}$	$6.42^{+0.23}_{-6.42}$	$0.0233^{+0.0122}_{-0.0089}$	$1.22^{+0.25}_{-0.12}$	$22.6^{+5.3}_{-3.7}$	$1.79^{+1.64}_{-0.35}$	0.6
91089-01-14-01	53960.60	12.96	0.96	$10.2^{+0.4}_{-0.7}$	$3.3^{+1.7}_{-0.8}$	$1.34^{+0.97}_{-0.44}$	$6.43^{+0.11}_{-0.11}$	$0.0300^{+0.0064}_{-0.0055}$	$1.19^{+0.09}_{-0.07}$	$19.4^{+2.0}_{-1.8}$	$1.82^{+0.43}_{-0.23}$	0.7
91089-01-14-02	53961.93	13.27	1.38	$9.8^{+0.5}_{-1.2}$	$3.8^{+1.3}_{-0.5}$	$1.76^{+1.66}_{-0.63}$	$6.42^{+0.10}_{-0.10}$	$0.0295^{+0.0073}_{-0.0056}$	$1.19^{+0.12}_{-0.08}$	$18.5^{+1.7}_{-1.4}$	$1.96^{+0.76}_{-0.31}$	0.9
91089-01-14-03	53962.50	13.31	1.79	$8.5^{+1.3}_{-3.7}$	$5.4^{+2.7}_{-1.1}$	$3.42^{+8.96}_{-1.75}$	$6.36^{+0.10}_{-0.09}$	$0.0335^{+0.0135}_{-0.0067}$	$1.31^{+0.30}_{-0.12}$	$20.8^{+3.8}_{-2.0}$	$2.62^{+1.53}_{-0.72}$	1.0
91089-01-14-04	53963.68	13.80	1.26	$10.1^{+0.4}_{-0.8}$	$3.6^{+0.8}_{-0.5}$	$1.51^{+0.99}_{-0.47}$	$6.47^{+0.10}_{-0.10}$	$0.0267^{+0.0055}_{-0.0048}$	$1.21^{+0.08}_{-0.06}$	$20.2^{+1.6}_{-1.4}$	$1.99^{+0.47}_{-0.25}$	0.8
91089-01-14-05	53964.55	14.21	1.54	$9.0^{+0.8}_{-1.0}$	$4.8^{+0.9}_{-0.6}$	$2.58^{+2.34}_{-0.90}$	$6.41^{+0.07}_{-0.07}$	$0.0367^{+0.0072}_{-0.0052}$	$1.25^{+0.14}_{-0.08}$	$19.7^{+1.7}_{-1.2}$	$2.42^{+1.08}_{-0.44}$	0.9
91089-01-15-00	53965.77	15.40	2.15	$9.1^{+0.9}_{-2.7}$	$4.6^{+2.3}_{-1.0}$	$2.53^{+4.22}_{-1.16}$	$6.51^{+0.12}_{-0.12}$	$0.0313^{+0.0111}_{-0.0073}$	$1.29^{+0.23}_{-0.11}$	$19.7^{+3.0}_{-1.9}$	$2.94^{+1.98}_{-0.67}$	0.9
91089-01-15-01	53966.85	13.81	1.21	$9.7^{+0.6}_{-1.2}$	$3.8^{+1.0}_{-0.7}$	$1.46^{+1.26}_{-0.50}$	$6.38^{+0.10}_{-0.10}$	$0.0276^{+0.0059}_{-0.0050}$	$1.22^{+0.11}_{-0.07}$	$19.9^{+1.7}_{-1.4}$	$2.08^{+0.65}_{-0.30}$	0.9
91089-01-15-02	53967.54	13.62	1.08	$9.8^{+0.5}_{-0.9}$	$3.7^{+1.4}_{-0.8}$	$1.60^{+1.13}_{-0.50}$	$6.40^{+0.09}_{-0.09}$	$0.0322^{+0.0058}_{-0.0049}$	$1.21^{+0.10}_{-0.07}$	$19.7^{+1.6}_{-1.3}$	$2.00^{+0.56}_{-0.27}$	0.6
91089-01-15-03	53968.66	14.75	1.41	$9.4^{+0.5}_{-1.0}$	$3.8^{+1.2}_{-0.7}$	$1.52^{+1.00}_{-0.45}$	$6.40^{+0.08}_{-0.07}$	$0.0333^{+0.0053}_{-0.0046}$	$1.26^{+0.09}_{-0.06}$	$20.7^{+1.4}_{-1.0}$	$2.36^{+0.63}_{-0.31}$	1.0
91089-01-15-04	53969.58	14.50	1.81	$9.3^{+0.6}_{-1.0}$	$4.0^{+1.0}_{-0.7}$	$1.73^{+0.97}_{-0.49}$	$6.45^{+0.09}_{-0.09}$	$0.0270^{+0.0048}_{-0.0043}$	$1.27^{+0.09}_{-0.06}$	$20.4^{+1.4}_{-1.1}$	$2.46^{+0.64}_{-0.34}$	0.7
91089-01-15-05	53970.48	13.48	1.13	$9.7^{+0.5}_{-0.8}$	$3.8^{+0.8}_{-0.6}$	$1.68^{+0.84}_{-0.45}$	$6.41^{+0.08}_{-0.08}$	$0.0315^{+0.0051}_{-0.0045}$	$1.18^{+0.08}_{-0.06}$	$19.5^{+1.4}_{-1.2}$	$1.87^{+0.43}_{-0.24}$	0.8
91089-01-15-06	53971.55	15.17	1.66	$9.8^{+0.4}_{-0.6}$	$3.4^{+0.7}_{-0.5}$	$1.20^{+0.52}_{-0.29}$	$6.48^{+0.09}_{-0.09}$	$0.0271^{+0.0045}_{-0.0041}$	$1.25^{+0.06}_{-0.05}$	$20.9^{+1.1}_{-0.9}$	$2.37^{+0.40}_{-0.24}$	0.9
91089-01-16-00	53972.19	14.26	1.40	$9.8^{+0.4}_{-0.7}$	$3.6^{+0.6}_{-0.5}$	$1.37^{+0.61}_{-0.33}$	$6.44^{+0.09}_{-0.09}$	$0.0266^{+0.0043}_{-0.0039}$	$1.22^{+0.07}_{-0.05}$	$20.0^{+1.1}_{-0.9}$	$2.11^{+0.39}_{-0.23}$	0.9
91089-01-16-01	53972.98	14.80	1.43	$9.8^{+0.5}_{-0.8}$	$3.9^{+0.9}_{-0.6}$	$1.46^{+0.77}_{-0.40}$	$6.38^{+0.09}_{-0.09}$	$0.0283^{+0.0047}_{-0.0042}$	$1.22^{+0.07}_{-0.05}$	$19.7^{+1.1}_{-1.0}$	$2.23^{+0.45}_{-0.26}$	0.7
91089-01-16-02	53974.48	13.23	1.21	$9.8^{+0.4}_{-0.6}$	$3.4^{+0.6}_{-0.5}$	$1.24^{+0.56}_{-0.30}$	$6.44^{+0.08}_{-0.08}$	$0.0260^{+0.0042}_{-0.0038}$	$1.18^{+0.07}_{-0.05}$	$18.8^{+1.0}_{-0.9}$	$1.86^{+0.33}_{-0.20}$	0.9
91089-01-16-03	53975.42	14.31	1.61	$9.5^{+0.5}_{-1.0}$	$3.7^{+1.2}_{-0.7}$	$1.28^{+0.86}_{-0.39}$	$6.41^{+0.09}_{-0.09}$	$0.0268^{+0.0047}_{-0.0043}$	$1.24^{+0.09}_{-0.06}$	$20.4^{+1.4}_{-1.1}$	$2.23^{+0.55}_{-0.28}$	0.8
91089-01-16-04	53976.12	13.95	1.27	$9.5^{+0.7}_{-1.3}$	$4.3^{+1.5}_{-0.9}$	$1.66^{+1.30}_{-0.56}$	$6.38^{+0.09}_{-0.08}$	$0.0281^{+0.0048}_{-0.0041}$	$1.20^{+0.10}_{-0.06}$	$19.3^{+1.2}_{-0.9}$	$2.07^{+0.58}_{-0.28}$	0.7
91089-01-16-05	53977.17	12.88	1.30	$9.5^{+0.5}_{-1.0}$	$3.6^{+1.0}_{-0.6}$	$1.13^{+0.74}_{-0.33}$	$6.44^{+0.09}_{-0.09}$	$0.0236^{+0.0040}_{-0.0036}$	$1.19^{+0.08}_{-0.05}$	$19.7^{+1.2}_{-0.9}$	$1.77^{+0.40}_{-0.21}$	0.9
91089-01-16-06	53978.15	13.67	1.25	$9.7^{+0.5}_{-0.9}$	$3.5^{+0.8}_{-0.5}$	$1.03^{+0.60}_{-0.29}$	$6.44^{+0.09}_{-0.09}$	$0.0239^{+0.0041}_{-0.0037}$	$1.20^{+0.07}_{-0.05}$	$20.0^{+1.2}_{-1.0}$	$1.90^{+0.36}_{-0.20}$	0.8
91089-01-17-00	53979.34	12.51	1.68	$8.9^{+0.9}_{-2.1}$	$4.0^{+1.3}_{-0.9}$	$1.32^{+1.84}_{-0.54}$	$6.49^{+0.10}_{-0.10}$	$0.0220^{+0.0050}_{-0.0039}$	$1.22^{+0.15}_{-0.08}$	$19.9^{+2.2}_{-1.2}$	$1.88^{+0.68}_{-0.30}$	1.1
91089-01-17-01	53980.39	12.75	1.43	$8.8^{+1.1}_{-2.6}$	$4.0^{+1.7}_{-0.9}$	$1.28^{+2.28}_{-0.55}$	$6.46^{+0.10}_{-0.09}$	$0.0225^{+0.0066}_{-0.0042}$	$1.20^{+0.19}_{-0.08}$	$19.7^{+2.6}_{-1.2}$	$1.84^{+0.76}_{-0.31}$	0.9

Continued on Next Page...

Table A.2 – Continued

Obs. ID	MJD	L_X $\times 10^{37}$ (erg/s)	N_H cm^{-2}	Cyclotron line E (keV)	Cyclotron line σ (keV)	Cyclotron line τ	Fe line E (keV)	Fe line norm. (ph./cm^2/s)	Power law Γ	Power law cutoff (keV)	Power law norm.	χ^2_r
91089-01-17-02	53981.36	12.29	0.88	$9.8^{+0.4}_{-0.8}$	$3.4^{+0.7}_{-0.5}$	$0.97^{+0.53}_{-0.26}$	$6.40^{+0.09}_{-0.09}$	$0.0218^{+0.0035}_{-0.0032}$	$1.12^{+0.06}_{-0.05}$	$17.9^{+0.8}_{-0.7}$	$1.51^{+0.26}_{-0.15}$	0.9
91089-01-17-03	53982.14	11.98	1.48	$8.5^{+1.0}_{-4.8}$	$4.3^{+1.2}_{-0.7}$	$1.53^{+5.95}_{-0.73}$	$6.44^{+0.09}_{-0.08}$	$0.0231^{+0.0063}_{-0.0039}$	$1.22^{+0.28}_{-0.08}$	$19.6^{+3.5}_{-1.1}$	$1.83^{+0.76}_{-0.34}$	0.8
91089-01-17-04	53983.20	11.58	1.19	$9.2^{+0.8}_{-2.1}$	$3.7^{+1.4}_{-0.8}$	$1.03^{+1.57}_{-0.42}$	$6.45^{+0.10}_{-0.10}$	$0.0197^{+0.0044}_{-0.0036}$	$1.14^{+0.14}_{-0.07}$	$18.1^{+1.1}_{-1.0}$	$1.48^{+0.47}_{-0.21}$	0.7
91089-01-17-05	53984.24	11.47	1.63	$8.4^{+1.0}_{-3.5}$	$4.0^{+1.1}_{-0.7}$	$1.27^{+3.34}_{-0.57}$	$6.44^{+0.09}_{-0.08}$	$0.0221^{+0.0063}_{-0.0037}$	$1.22^{+0.25}_{-0.09}$	$19.7^{+3.7}_{-1.2}$	$1.72^{+1.39}_{-0.31}$	0.9
91089-01-17-06	53985.22	11.46	1.61	$8.4^{+1.1}_{-3.0}$	$4.3^{+1.4}_{-0.8}$	$1.56^{+2.99}_{-0.68}$	$6.44^{+0.09}_{-0.08}$	$0.0217^{+0.0039}_{-0.0036}$	$1.17^{+0.21}_{-0.09}$	$18.2^{+2.5}_{-1.0}$	$1.66^{+0.91}_{-0.31}$	1.0
91089-01-18-01	53986.07	10.73	0.86	$9.0^{+0.8}_{-2.2}$	$3.7^{+1.3}_{-0.7}$	$0.95^{+1.56}_{-0.40}$	$6.38^{+0.09}_{-0.09}$	$0.0202^{+0.0042}_{-0.0033}$	$1.09^{+0.14}_{-0.07}$	$17.3^{+1.0}_{-0.9}$	$1.25^{+0.40}_{-0.17}$	0.8
91089-01-18-00	53986.99	10.57	1.04	$9.0^{+0.9}_{-2.8}$	$3.8^{+1.7}_{-0.9}$	$1.00^{+1.97}_{-0.45}$	$6.43^{+0.10}_{-0.10}$	$0.0186^{+0.0045}_{-0.0035}$	$1.09^{+0.17}_{-0.08}$	$17.2^{+1.9}_{-1.1}$	$1.27^{+0.51}_{-0.19}$	0.8
91089-01-18-02	53988.00	9.76	1.78	$5.6^{+9.7}_{-5.6}$	$6.4^{+8.2}_{-3.9}$	$2.69^{+12.08}_{-2.54}$	$6.46^{+0.18}_{-0.16}$	$0.0169^{+0.0076}_{-0.0088}$	$1.24^{+0.51}_{-0.21}$	$18.8^{+7.7}_{-3.1}$	$1.67^{+0.63}_{-0.65}$	0.9
91089-01-18-03	53989.16	9.57	1.51	$6.0^{+2.2}_{-6.8}$	$5.5^{+2.8}_{-1.4}$	$2.60^{+11.47}_{-1.89}$	$6.40^{+0.10}_{-0.09}$	$0.0196^{+0.0067}_{-0.0044}$	$1.20^{+0.36}_{-0.19}$	$17.7^{+5.1}_{-2.0}$	$1.55^{+0.79}_{-0.55}$	0.9
91089-01-18-04	53990.03	9.37	0.75	$4.8^{+5.3}_{-4.8}$	$8.7^{+7.9}_{-4.6}$	$7.27^{+15.01}_{-6.51}$	$6.38^{+0.16}_{-0.15}$	$0.0218^{+0.0209}_{-0.0080}$	$1.09^{+0.31}_{-0.24}$	$14.4^{+4.2}_{-2.7}$	$1.49^{+1.31}_{-0.64}$	0.7
91089-01-18-05	53991.12	9.45	0.97	$8.4^{+1.4}_{-8.0}$	$3.9^{+2.1}_{-0.8}$	$0.82^{+11.69}_{-0.52}$	$6.39^{+0.10}_{-0.10}$	$0.0168^{+0.0084}_{-0.0034}$	$1.05^{+0.43}_{-0.09}$	$16.7^{+5.1}_{-1.0}$	$1.04^{+0.42}_{-0.19}$	0.8
91089-01-18-06	53991.79	8.75	0.92	$8.4^{+1.4}_{-8.4}$	$3.3^{+1.1}_{0.6}$	$0.49^{+9.76}_{-0.30}$	$6.45^{+0.10}_{-0.10}$	$0.0143^{+0.0067}_{-0.0031}$	$1.02^{+0.44}_{-0.08}$	$16.6^{+4.9}_{-1.0}$	$0.89^{+0.44}_{-0.14}$	0.9
91089-01-19-00	53993.69	7.99	0.57	–	–	–	$6.27^{+0.14}_{-6.27}$	$0.0110^{+0.0023}_{-0.0023}$	$1.00^{+0.05}_{-0.05}$	$16.6^{+1.0}_{-0.9}$	$0.74^{+0.07}_{-0.07}$	0.9
91089-01-19-01	53995.01	7.78	0.22	–	–	–	$6.35^{+0.11}_{-0.11}$	$0.0128^{+0.0022}_{-0.0023}$	$0.95^{+0.06}_{-0.04}$	$15.6^{+1.0}_{-0.6}$	$0.67^{+0.07}_{-0.04}$	1.1
91089-01-19-02	53995.79	7.44	0.45	–	–	–	$6.36^{+0.08}_{-0.07}$	$0.0130^{+0.0016}_{-0.0016}$	$0.96^{+0.04}_{-0.04}$	$16.1^{+0.7}_{-0.6}$	$0.64^{+0.05}_{-0.04}$	1.3
91089-01-19-03	53997.04	7.65	0.04	–	–	–	$6.25^{+0.10}_{-6.25}$	$0.0161^{+0.0021}_{-0.0027}$	$0.90^{+0.07}_{-0.02}$	$15.4^{+1.1}_{-0.5}$	$0.58^{+0.08}_{-0.02}$	0.8
91089-01-19-04	53997.82	6.70	0.48	–	–	–	$6.38^{+0.11}_{-0.10}$	$0.0109^{+0.0019}_{-0.0019}$	$0.90^{+0.06}_{-0.06}$	$15.0^{+0.9}_{-0.8}$	$0.54^{+0.06}_{-0.05}$	1.1
91089-01-19-05	53998.66	6.15	0.40	–	–	–	$6.34^{+0.09}_{-0.09}$	$0.0102^{+0.0015}_{-0.0015}$	$0.89^{+0.05}_{-0.05}$	$14.7^{+0.7}_{-0.6}$	$0.49^{+0.04}_{-0.04}$	0.8
92067-01-04-10	53999.59	6.28	0.88	–	–	–	$6.34^{+0.10}_{-0.10}$	$0.0097^{+0.0016}_{-0.0016}$	$0.92^{+0.05}_{-0.05}$	$15.1^{+0.8}_{-0.7}$	$0.53^{+0.05}_{-0.05}$	1.3
92067-01-05-00	54000.62	5.94	0.69	–	–	–	$6.29^{+0.12}_{-6.29}$	$0.0099^{+0.0020}_{-0.0020}$	$0.88^{+0.07}_{-0.03}$	$14.2^{+0.9}_{-0.8}$	$0.47^{+0.06}_{-0.05}$	0.7
92067-01-05-01	54002.01	5.22	1.24	–	–	–	$6.36^{+0.13}_{-0.12}$	$0.0075^{+0.0015}_{-0.0015}$	$0.88^{+0.06}_{-0.06}$	$14.2^{+0.8}_{-0.7}$	$0.42^{+0.04}_{-0.04}$	0.6
92067-01-05-02	54002.72	4.65	1.30	–	–	–	$6.51^{+0.20}_{-0.18}$	$0.0064^{+0.0018}_{-0.0018}$	$0.91^{+0.09}_{-0.09}$	$14.2^{+1.3}_{-1.2}$	$0.41^{+0.06}_{-0.06}$	1.0
92067-01-05-03	54003.57	5.21	1.36	–	–	–	$6.41^{+0.18}_{-0.17}$	$0.0065^{+0.0018}_{-0.0018}$	$0.89^{+0.07}_{-0.07}$	$14.3^{+1.1}_{-0.9}$	$0.43^{+0.06}_{-0.05}$	1.1
92067-01-05-04	54004.44	5.13	1.27	–	–	–	$6.32^{+0.12}_{-0.11}$	$0.0082^{+0.0016}_{-0.0016}$	$0.85^{+0.06}_{-0.06}$	$13.7^{+0.8}_{-0.8}$	$0.41^{+0.05}_{-0.04}$	0.8
92067-01-05-05	54005.67	4.73	1.82	–	–	–	$6.58^{+0.25}_{-0.21}$	$0.0059^{+0.0018}_{-0.0018}$	$0.92^{+0.09}_{-0.09}$	$14.3^{+1.3}_{-1.2}$	$0.43^{+0.07}_{-0.06}$	0.9
92067-01-05-06	54006.58	5.05	0.88	–	–	–	$6.36^{+0.13}_{-0.12}$	$0.0090^{+0.0018}_{-0.0018}$	$0.84^{+0.07}_{-0.08}$	$13.9^{+1.0}_{-0.9}$	$0.38^{+0.05}_{-0.05}$	0.8
92067-01-06-00	54007.56	4.41	1.48	–	–	–	$6.40^{+0.21}_{-0.19}$	$0.0057^{+0.0017}_{-0.0017}$	$0.84^{+0.08}_{-0.09}$	$13.4^{+1.1}_{-1.0}$	$0.35^{+0.05}_{-0.05}$	1.0
92067-01-06-01	54008.43	3.97	2.32	–	–	–	$6.54^{+0.15}_{-0.14}$	$0.0052^{+0.0011}_{-0.0011}$	$0.91^{+0.06}_{-0.06}$	$14.3^{+0.9}_{-0.8}$	$0.35^{+0.04}_{-0.03}$	1.4
92067-01-06-02	54009.59	3.56	1.34	–	–	–	$6.38^{+0.20}_{-0.18}$	$0.0056^{+0.0017}_{-0.0016}$	$0.76^{+0.10}_{-0.11}$	$12.3^{+1.2}_{-1.1}$	$0.25^{+0.05}_{-0.04}$	1.1
92067-01-06-03	54010.37	3.37	2.32	–	–	–	$6.57^{+0.15}_{-0.14}$	$0.0048^{+0.0010}_{-0.0010}$	$0.87^{+0.06}_{-0.07}$	$13.3^{+0.8}_{-0.8}$	$0.29^{+0.03}_{-0.03}$	1.1
92067-01-06-04	54011.55	3.15	1.92	–	–	–	$6.34^{+0.17}_{-6.34}$	$0.0055^{+0.0015}_{-0.0015}$	$0.81^{+0.10}_{-0.10}$	$12.6^{+1.3}_{-1.1}$	$0.24^{+0.05}_{-0.04}$	1.0
92067-01-06-05	54012.73	2.80	3.18	–	–	–	$6.49^{+0.15}_{-0.13}$	$0.0044^{+0.0009}_{-0.0009}$	$0.91^{+0.07}_{-0.07}$	$13.5^{+1.0}_{-0.9}$	$0.26^{+0.03}_{-0.03}$	1.0

Continued on Next Page...

Table A.2 – Continued

Obs. ID	MJD	L_X $\times 10^{37}$ (erg/s)	N_H cm^{-2}	Cyclotron line E (keV)	Cyclotron line σ (keV)	Cyclotron line τ	Fe line E (keV)	Fe line norm. (ph./cm^2/s)	Power law Γ	Power law cutoff (keV)	Power law norm.	χ^2_r
92067-01-06-06	54013.71	2.54	3.12	–	–	–	$6.59^{+0.20}_{-0.17}$	$0.0032^{+0.0009}_{-0.0008}$	$0.93^{+0.07}_{-0.08}$	$13.5^{+1.1}_{-0.9}$	$0.25^{+0.03}_{-0.03}$	1.0
92067-01-07-00	54014.63	2.36	2.53	–	–	–	$6.20^{+0.56}_{-6.20}$	$0.0030^{+0.0023}_{-0.0025}$	$0.83^{+0.22}_{-0.21}$	$12.4^{+3.0}_{-2.0}$	$0.20^{+0.09}_{-0.06}$	0.7
92067-01-07-01	54015.44	2.07	3.15	–	–	–	$6.45^{+0.15}_{-0.14}$	$0.0038^{+0.0008}_{-0.0008}$	$0.90^{+0.09}_{-0.09}$	$13.2^{+1.2}_{-1.0}$	$0.20^{+0.03}_{-0.03}$	0.8
92067-01-07-02	54016.59	2.00	1.69	–	–	–	$6.26^{+0.56}_{-6.26}$	$0.0030^{+0.0020}_{-0.0020}$	$0.73^{+0.22}_{-0.23}$	$11.3^{+2.6}_{-1.8}$	$0.14^{+0.06}_{-0.05}$	0.6
92067-01-07-03	54017.47	1.77	3.18	–	–	–	$6.49^{+0.30}_{-0.24}$	$0.0022^{+0.0008}_{-0.0007}$	$0.88^{+0.10}_{-0.10}$	$12.8^{+1.3}_{-1.1}$	$0.17^{+0.03}_{-0.03}$	0.9
92067-01-07-04	54018.49	1.61	2.28	–	–	–	6.40	$0.0028^{+0.0013}_{-0.0007}$	$0.67^{+0.19}_{-0.19}$	$10.2^{+1.8}_{-1.4}$	$0.11^{+0.04}_{-0.03}$	1.1
92067-01-07-05	54019.43	1.50	3.03	–	–	–	6.40	$0.0020^{+0.0007}_{-0.0007}$	$0.91^{+0.10}_{-0.10}$	$12.3^{+1.3}_{-1.1}$	$0.16^{+0.03}_{-0.02}$	1.2
92067-01-07-06	54020.52	1.56	0.70	–	–	–	6.40	$0.0021^{+0.0018}_{-0.0021}$	$0.42^{+0.30}_{-0.18}$	$8.2^{+2.1}_{-1.3}$	$0.08^{+0.05}_{-0.02}$	0.8
92067-01-08-00	54021.31	1.32	3.14	–	–	–	6.40	$0.0017^{+0.0006}_{-0.0006}$	$1.04^{+0.11}_{-0.11}$	$14.8^{+2.1}_{-1.7}$	$0.16^{+0.03}_{-0.03}$	1.6
92067-01-08-01	54022.31	1.17	3.11	–	–	–	6.40	$0.0014^{+0.0006}_{-0.0006}$	$0.99^{+0.11}_{-0.12}$	$13.6^{+1.9}_{-1.5}$	$0.14^{+0.03}_{-0.02}$	1.4
92067-01-08-02	54023.46	0.99	2.24	–	–	–	6.40	$0.0005^{+0.0011}_{-0.0005}$	$0.66^{+0.28}_{-0.29}$	$9.7^{+2.8}_{-1.8}$	$0.07^{+0.04}_{-0.03}$	1.0
92067-01-08-03	54024.58	0.94	3.06	–	–	–	6.40	$0.0012^{+0.0005}_{-0.0005}$	$1.04^{+0.12}_{-0.12}$	$14.9^{+2.5}_{-1.9}$	$0.11^{+0.02}_{-0.02}$	1.0
92067-01-08-04	54025.39	0.87	3.18	–	–	–	6.40	$0.0014^{+0.0005}_{-0.0005}$	$1.18^{+0.13}_{-0.13}$	$17.9^{+4.0}_{-2.8}$	$0.13^{+0.03}_{-0.02}$	1.0
92067-01-08-05	54026.42	0.74	3.26	–	–	–	6.40	$0.0012^{+0.0004}_{-0.0005}$	$1.14^{+0.14}_{-0.14}$	$16.4^{+3.7}_{-2.6}$	$0.10^{+0.03}_{-0.02}$	1.1
92067-01-08-06	54027.65	0.67	2.48	–	–	–	6.40	$0.0007^{+0.0004}_{-0.0005}$	$1.27^{+0.15}_{-0.16}$	$18.7^{+5.6}_{-3.6}$	$0.12^{+0.03}_{-0.03}$	0.8
92067-01-09-00	54028.77	0.58	2.76	–	–	–	6.40	$0.0008^{+0.0004}_{-0.0004}$	$1.18^{+0.15}_{-0.15}$	$16.6^{+4.2}_{-2.8}$	$0.09^{+0.02}_{-0.02}$	0.9
92067-01-09-01	54029.68	0.55	2.82	–	–	–	6.40	$0.0010^{+0.0004}_{-0.0004}$	$0.95^{+0.19}_{-0.19}$	$12.2^{+3.0}_{-2.0}$	$0.06^{+0.02}_{-0.02}$	0.9
92067-01-09-03	54031.78	0.48	2.50	–	–	–	6.40	$0.0006^{+0.0004}_{-0.0004}$	$1.17^{+0.18}_{-0.18}$	$15.2^{+4.6}_{-2.9}$	$0.08^{+0.02}_{-0.02}$	0.6
92067-01-09-05	54033.50	0.39	2.52	–	–	–	6.40	$0.0006^{+0.0004}_{-0.0004}$	$1.01^{+0.22}_{-0.22}$	$12.3^{+3.7}_{-2.4}$	$0.05^{+0.02}_{-0.01}$	0.6
92067-01-09-06	54034.79	0.33	2.20	–	–	–	6.40	$0.0007^{+0.0005}_{-0.0004}$	$1.19^{+0.24}_{-0.25}$	$14.9^{+6.8}_{-3.6}$	$0.06^{+0.03}_{-0.02}$	0.8
92067-01-10-00	54035.77	0.30	2.44	–	–	–	6.40	$0.0007^{+0.0004}_{-0.0004}$	$1.08^{+0.28}_{-0.30}$	$12.5^{+5.8}_{-3.2}$	$0.04^{+0.02}_{-0.02}$	0.9
92067-01-10-01	54036.79	0.24	2.70	–	–	–	6.40	$0.0003^{+0.0004}_{-0.0003}$	$1.16^{+0.44}_{-0.46}$	$10.9^{+8.4}_{-3.5}$	$0.05^{+0.05}_{-0.03}$	0.5
92067-01-10-02	54037.87	0.29	2.83	–	–	–	6.40	$0.0004^{+0.0003}_{-0.0003}$	$1.45^{+0.26}_{-0.27}$	$19.6^{+15.7}_{-6.3}$	$0.08^{+0.04}_{-0.02}$	0.8
92067-01-10-03	54038.82	0.25	2.87	–	–	–	6.40	$0.0003^{+0.0005}_{-0.0003}$	$1.35^{+0.41}_{-0.41}$	$15.0^{+19.3}_{-5.5}$	$0.06^{+0.06}_{-0.03}$	0.6
92067-01-10-04	54039.87	0.24	2.14	–	–	–	6.40	$0.0003^{+0.0005}_{-0.0003}$	$1.26^{+0.54}_{-0.59}$	$14.7^{+37.3}_{-6.7}$	$0.05^{+0.06}_{-0.03}$	0.6
92067-01-10-05	54040.88	0.30	2.23	–	–	–	6.40	$0.0004^{+0.0003}_{-0.0004}$	$1.14^{+0.27}_{-0.25}$	$13.3^{+5.9}_{-3.1}$	$0.05^{+0.02}_{-0.02}$	0.5
92067-01-10-06	54041.90	0.36	2.81	–	–	–	6.40	$0.0006^{+0.0007}_{-0.0006}$	$1.22^{+0.43}_{-0.44}$	$14.2^{+16.2}_{-5.1}$	$0.07^{+0.06}_{-0.03}$	0.9
92067-01-11-00	54042.42	0.44	2.85	–	–	–	6.40	$0.0009^{+0.0004}_{-0.0004}$	$1.14^{+0.21}_{-0.21}$	$14.2^{+4.8}_{-2.9}$	$0.07^{+0.03}_{-0.02}$	0.9
92067-01-11-01	54043.72	0.44	3.05	–	–	–	6.40	$0.0010^{+0.0005}_{-0.0005}$	$1.08^{+0.28}_{-0.28}$	$13.5^{+6.3}_{-3.4}$	$0.06^{+0.03}_{-0.02}$	0.9
92067-01-11-02	54044.98	0.49	3.21	–	–	–	6.40	$0.0011^{+0.0004}_{-0.0004}$	$1.09^{+0.18}_{-0.18}$	$13.6^{+3.5}_{-2.4}$	$0.07^{+0.02}_{-0.02}$	0.9
92067-01-11-03	54045.82	0.47	3.56	–	–	–	6.40	$0.0009^{+0.0007}_{-0.0007}$	$1.15^{+0.35}_{-0.34}$	$16.1^{+13.5}_{-5.1}$	$0.07^{+0.05}_{-0.03}$	0.7

Table A.3: The same as Table A.1, for 4U 0115+63. The photoabsorption was fixed at the average value of 0.9×10^{22} cm^{-2} during error calculation. Best fits were obtained with 68–71 DOF.

Obs. ID	MJD	L_X $\times10^{37}$ (erg/s)	Cyclotron line τ	Cyclotron line E (keV)	Cyclotron line Width (keV)	Fe line E (keV)	Fe line norm. (ph./cm^2/s)	Power law Γ	Power law norm.	Power law cutoff e. (keV)	Power law fold. en. (keV)	χ^2_r
90089-01-01-00	53254.07	6.78	$0.36^{+0.04}_{-0.03}$	$11.4^{+0.7}_{-0.2}$	$10.6^{+1.0}_{-1.5}$	$6.5^{+0.2}_{-0.2}$	$0.0064^{+0.0014}_{-0.0013}$	$0.24^{+0.03}_{-0.03}$	$0.102^{+0.004}_{-0.004}$	$9.0^{+0.2}_{-0.2}$	$7.7^{+0.4}_{-0.3}$	0.8
90089-01-02-00	53256.43	8.99	$0.37^{+0.02}_{-0.02}$	$11.4^{+0.2}_{-0.2}$	$7.3^{+0.4}_{-0.4}$	$6.5^{+0.1}_{-0.1}$	$0.0100^{+0.0016}_{-0.0016}$	$0.28^{+0.02}_{-0.02}$	$0.147^{+0.005}_{-0.004}$	$8.9^{+0.1}_{-0.1}$	$7.7^{+0.1}_{-0.1}$	0.8
90089-01-03-01	53260.15	12.66	$0.32^{+0.02}_{-0.02}$	$11.1^{+0.2}_{-0.2}$	$5.5^{+0.3}_{-0.2}$	$6.3^{+0.1}_{-0.1}$	$0.0166^{+0.0021}_{-0.0023}$	$0.38^{+0.02}_{-0.02}$	$0.247^{+0.001}_{-0.001}$	$8.7^{+0.2}_{-0.2}$	$7.8^{+0.1}_{-0.1}$	1.0
90089-01-03-03	53260.56	12.69	$0.32^{+0.02}_{-0.02}$	$11.2^{+0.1}_{-0.1}$	$5.2^{+0.2}_{-0.2}$	$6.4^{+0.1}_{-0.1}$	$0.0161^{+0.0022}_{-0.0024}$	$0.38^{+0.02}_{-0.02}$	$0.241^{+0.008}_{-0.008}$	$8.7^{+0.2}_{-0.2}$	$7.8^{+0.1}_{-0.1}$	0.9
90089-01-03-00	53262.15	13.67	$0.28^{+0.04}_{-0.04}$	$11.0^{+0.2}_{-0.1}$	$4.4^{+0.3}_{-0.2}$	$6.3^{+0.1}_{-6.3}$	$0.0183^{+0.0026}_{-0.0029}$	$0.42^{+0.03}_{-0.03}$	$0.275^{+0.011}_{-0.011}$	$8.7^{+0.2}_{-0.3}$	$7.6^{+0.2}_{-0.2}$	0.9
90089-01-04-06	53265.07	12.58	$0.31^{+0.03}_{-0.03}$	$11.0^{+0.1}_{-0.1}$	$3.8^{+0.2}_{-0.1}$	$6.3^{+0.1}_{-6.3}$	$0.0164^{+0.0024}_{-0.0027}$	$0.38^{+0.02}_{-0.03}$	$0.242^{+0.009}_{-0.009}$	$8.5^{+0.2}_{-0.2}$	$7.6^{+0.1}_{-0.1}$	1.4
90089-01-04-01	53267.17	11.49	$0.28^{+0.04}_{-0.04}$	$11.0^{+0.2}_{-0.2}$	$3.0^{+0.3}_{-0.4}$	$6.3^{+0.1}_{-6.3}$	$0.0143^{+0.0034}_{-0.0038}$	$0.36^{+0.04}_{-0.04}$	$0.209^{+0.013}_{-0.013}$	$8.2^{+0.3}_{-0.3}$	$7.6^{+0.3}_{-0.2}$	0.9
90089-01-04-04	53267.24	11.73	$0.37^{+0.13}_{-0.06}$	$10.6^{+0.2}_{-0.3}$	$3.5^{+0.3}_{-0.3}$	$6.3^{+0.3}_{-6.3}$	$0.0117^{+0.0041}_{-0.0044}$	$0.31^{+0.05}_{-0.08}$	$0.203^{+0.016}_{-0.021}$	$8.4^{+0.6}_{-0.4}$	$7.2^{+0.3}_{-0.4}$	0.7
90089-01-04-05	53267.30	12.05	$0.29^{+0.04}_{-0.03}$	$10.9^{+0.1}_{-0.1}$	$3.2^{+0.2}_{-0.3}$	$6.2^{+0.1}_{-6.2}$	$0.0163^{+0.0032}_{-0.0033}$	$0.37^{+0.03}_{-0.03}$	$0.221^{+0.012}_{-0.010}$	$8.2^{+0.3}_{-0.2}$	$7.7^{+0.2}_{-0.2}$	1.0
90089-01-04-02	53269.10	11.92	$0.31^{+0.03}_{-0.02}$	$10.9^{+0.1}_{-0.1}$	$3.3^{+0.1}_{-0.1}$	$6.2^{+0.1}_{-6.2}$	$0.0133^{+0.0024}_{-0.0029}$	$0.34^{+0.02}_{-0.03}$	$0.209^{+0.008}_{-0.009}$	$8.3^{+0.2}_{-0.2}$	$7.7^{+0.1}_{-0.1}$	1.9
90089-01-04-03	53271.95	9.96	$0.36^{+0.04}_{-0.03}$	$10.7^{+0.1}_{-0.1}$	$3.4^{+0.1}_{-0.1}$	$6.4^{+0.1}_{-0.1}$	$0.0123^{+0.0018}_{-0.0019}$	$0.32^{+0.02}_{-0.03}$	$0.167^{+0.006}_{-0.006}$	$8.7^{+0.2}_{-0.2}$	$7.5^{+0.1}_{-0.1}$	1.4
90089-01-05-00	53272.79	9.55	$0.36^{+0.03}_{-0.03}$	$10.8^{+0.1}_{-0.1}$	$3.6^{+0.1}_{-0.1}$	$6.4^{+0.1}_{-0.1}$	$0.0109^{+0.0017}_{-0.0018}$	$0.30^{+0.02}_{-0.02}$	$0.156^{+0.006}_{-0.006}$	$8.6^{+0.2}_{-0.2}$	$7.5^{+0.1}_{-0.1}$	1.4
90089-01-05-05	53272.95	9.56	$0.41^{+0.04}_{-0.04}$	$10.7^{+0.1}_{-0.1}$	$3.6^{+0.1}_{-0.1}$	$6.5^{+0.1}_{-0.2}$	$0.0092^{+0.0022}_{-0.0021}$	$0.30^{+0.08}_{-0.05}$	$0.162^{+0.035}_{-0.016}$	$8.8^{+0.2}_{-0.2}$	$7.4^{+0.2}_{-0.2}$	1.1
90089-01-05-01	53274.83	8.60	$0.38^{+0.03}_{-0.03}$	$10.7^{+0.1}_{-0.1}$	$4.2^{+0.1}_{-0.1}$	$6.4^{+0.1}_{-0.1}$	$0.0092^{+0.0017}_{-0.0017}$	$0.26^{+0.02}_{-0.02}$	$0.134^{+0.005}_{-0.005}$	$8.5^{+0.2}_{-0.2}$	$7.6^{+0.1}_{-0.1}$	1.0
90089-01-05-02	53275.67	8.00	$0.39^{+0.03}_{-0.03}$	$10.7^{+0.1}_{-0.1}$	$4.5^{+0.2}_{-0.1}$	$6.5^{+0.1}_{-0.1}$	$0.0081^{+0.0015}_{-0.0015}$	$0.23^{+0.02}_{-0.02}$	$0.119^{+0.004}_{-0.004}$	$8.7^{+0.2}_{-0.2}$	$7.6^{+0.1}_{-0.1}$	1.4
90089-01-05-03	53276.73	7.38	$0.37^{+0.03}_{-0.03}$	$10.6^{+0.1}_{-0.1}$	$4.9^{+0.2}_{-0.2}$	$6.5^{+0.1}_{-0.1}$	$0.0074^{+0.0015}_{-0.0015}$	$0.23^{+0.02}_{-0.02}$	$0.110^{+0.004}_{-0.004}$	$8.6^{+0.2}_{-0.2}$	$7.5^{+0.1}_{-0.1}$	1.1
90089-01-05-04	53278.62	6.62	$0.40^{+0.02}_{-0.02}$	$10.7^{+0.1}_{-0.1}$	$6.8^{+0.5}_{-0.4}$	$6.6^{+0.2}_{-0.2}$	$0.0054^{+0.0014}_{-0.0014}$	$0.19^{+0.02}_{-0.02}$	$0.097^{+0.004}_{-0.003}$	$8.7^{+0.2}_{-0.2}$	$7.4^{+0.1}_{-0.1}$	1.1
90089-01-06-00	53280.69	5.72	$0.52^{+0.03}_{-0.03}$	$11.0^{+0.2}_{-0.2}$	$10.7^{+0.8}_{-0.8}$	$6.7^{+0.2}_{-0.2}$	$0.0041^{+0.0012}_{-0.0012}$	$0.12^{+0.02}_{-0.02}$	$0.079^{+0.003}_{-0.003}$	$9.1^{+0.1}_{-0.1}$	$7.7^{+0.3}_{-0.3}$	0.9
90014-02-01-02	53284.61	3.52	$0.51^{+0.08}_{-0.08}$	$15.4^{+0.5}_{-0.7}$	$8.8^{+1.4}_{-1.3}$	$6.8^{+0.2}_{-0.2}$	$0.0035^{+0.0009}_{-0.0009}$	$0.38^{+0.04}_{-0.04}$	$0.070^{+0.003}_{-0.004}$	$8.8^{+0.2}_{-0.2}$	$7.4^{+0.5}_{-0.4}$	0.9
90014-02-01-01	53285.98	2.86	$0.50^{+0.17}_{-0.17}$	$15.4^{+0.8}_{-0.8}$	$7.8^{+2.1}_{-2.5}$	$6.7^{+0.2}_{-0.2}$	$0.0024^{+0.0011}_{-0.0012}$	$0.35^{+0.07}_{-0.08}$	$0.055^{+0.005}_{-0.006}$	$8.7^{+0.2}_{-0.2}$	$7.0^{+0.9}_{-0.7}$	0.8
90014-02-02-00	53287.81	2.35	$0.51^{+0.11}_{-0.11}$	$15.2^{+0.7}_{-0.8}$	$8.3^{+1.7}_{-1.7}$	$6.8^{+0.2}_{-0.2}$	$0.0021^{+0.0006}_{-0.0006}$	$0.40^{+0.04}_{-0.06}$	$0.050^{+0.003}_{-0.003}$	$9.1^{+0.2}_{-0.2}$	$6.9^{+0.6}_{-0.5}$	1.0
90014-02-02-01	53289.52	1.89	$0.31^{+0.19}_{-0.09}$	$16.0^{+0.4}_{-0.4}$	$4.9^{+3.3}_{-1.9}$	$6.7^{+0.3}_{-0.3}$	$0.0015^{+0.0005}_{-0.0005}$	$0.52^{+0.03}_{-0.06}$	$0.049^{+0.002}_{-0.004}$	$9.1^{+0.2}_{-0.1}$	$6.2^{+0.8}_{-0.4}$	0.7
90014-02-02-02	53290.64	1.49	$0.30^{+0.18}_{-0.09}$	$16.9^{+0.4}_{-0.5}$	$4.0^{+3.2}_{-1.7}$	$6.5^{+0.4}_{-0.4}$	$0.0009^{+0.0004}_{-0.0004}$	$0.58^{+0.03}_{-0.05}$	$0.043^{+0.002}_{-0.003}$	$9.4^{+0.2}_{-0.1}$	$6.1^{+0.7}_{-0.4}$	0.7
90014-02-02-03	53291.81	1.15	$0.40^{+0.25}_{-0.21}$	$17.5^{+0.8}_{-0.9}$	$6.5^{+3.9}_{-3.3}$	$6.6^{+0.5}_{-0.5}$	$0.0002^{+0.0004}_{-0.0002}$	$0.64^{+0.04}_{-0.07}$	$0.037^{+0.002}_{-0.003}$	$9.7^{+0.2}_{-0.2}$	$6.6^{+1.1}_{-0.8}$	0.8
90014-02-03-00	53293.44	0.71	$0.16^{+0.11}_{-0.08}$	$15.9^{+0.8}_{-1.0}$	$3.1^{+2.7}_{-1.7}$	$6.6^{+0.5}_{-0.5}$	$0.0002^{+0.0002}_{-0.0002}$	$0.76^{+0.02}_{-0.03}$	$0.028^{+0.001}_{-0.001}$	$10.2^{+0.2}_{-0.2}$	$6.1^{+0.5}_{-0.3}$	0.7

Table A.4: The same as Table A.1, for V 0332+53 using Model I. The photoabsorption was fixed to 1.5×10^{22} cm^{-2} (Pottschmidt 2005). Best fits were obtained with 68–70 DOF.

Obs. ID	MJD	L_X $\times 10^{37}$ (erg/s)	Cyclotron line τ	Cyclotron line E (keV)	Cyclotron line Width (keV)	Fe line E (keV)	Fe line norm. (ph./cm^2/s)	Power law Γ	Power law cutoff en. (keV)	Power law norm.	χ^2_r
90089-11-01-02	53340.29	11.02	$2.22^{+0.05}_{-0.07}$	$27.6^{+0.1}_{-0.1}$	$7.5^{+0.3}_{-0.5}$	$6.4^{+0.1}_{-0.1}$	$0.0087^{+0.0026}_{-0.0027}$	$0.03^{+0.03}_{-0.05}$	$15.5^{+1.1}_{-1.8}$	$0.149^{+0.004}_{-0.007}$	1.2
90089-11-01-03	53341.14	12.51	$2.09^{+0.05}_{-0.06}$	$27.3^{+0.1}_{-0.1}$	$7.3^{+0.3}_{-0.3}$	$6.4^{+0.1}_{-0.1}$	$0.0085^{+0.0021}_{-0.0017}$	$-0.03^{+0.03}_{-0.03}$	$13.6^{+1.0}_{-0.9}$	$0.163^{+0.005}_{-0.006}$	1.8
90089-11-01-04	53341.80	13.33	$2.09^{+0.05}_{-0.05}$	$27.1^{+0.1}_{-0.1}$	$7.2^{+0.3}_{-0.3}$	$6.4^{+0.1}_{-0.1}$	$0.0088^{+0.0025}_{-0.0020}$	$-0.06^{+0.03}_{-0.04}$	$13.1^{+0.8}_{-0.8}$	$0.169^{+0.004}_{-0.007}$	1.5
90089-11-02-05	53343.04	13.83	$2.05^{+0.05}_{-0.06}$	$26.8^{+0.1}_{-0.1}$	$7.3^{+0.3}_{-0.3}$	$6.5^{+0.1}_{-0.1}$	$0.0094^{+0.0025}_{-0.0016}$	$-0.14^{+0.04}_{-0.04}$	$11.8^{+0.9}_{-0.8}$	$0.164^{+0.006}_{-0.006}$	1.6
90089-11-02-06	53343.11	14.35	$1.97^{+0.05}_{-0.03}$	$26.7^{+0.1}_{-0.1}$	$7.0^{+0.3}_{-0.3}$	$6.5^{+0.1}_{-0.1}$	$0.0078^{+0.0021}_{-0.0012}$	$-0.16^{+0.04}_{-0.04}$	$11.3^{+0.4}_{-0.7}$	$0.168^{+0.005}_{-0.006}$	1.9
90089-11-02-01	53343.24	14.44	$2.07^{+0.04}_{-0.08}$	$26.6^{+0.1}_{-0.1}$	$7.5^{+0.3}_{-0.4}$	$6.5^{+0.1}_{-0.2}$	$0.0085^{+0.0022}_{-0.0018}$	$-0.13^{+0.04}_{-0.05}$	$12.0^{+0.9}_{-1.0}$	$0.176^{+0.005}_{-0.005}$	1.4
90089-11-02-02	53343.39	14.90	$2.05^{+0.04}_{-0.08}$	$26.7^{+0.1}_{-0.1}$	$7.3^{+0.2}_{-0.5}$	$6.5^{+0.1}_{-0.1}$	$0.0099^{+0.0019}_{-0.0015}$	$-0.16^{+0.02}_{-0.05}$	$11.4^{+0.5}_{-1.0}$	$0.174^{+0.003}_{-0.003}$	1.9
90089-11-02-07	53344.02	15.07	$2.00^{+0.05}_{-0.04}$	$26.5^{+0.1}_{-0.1}$	$6.9^{+0.3}_{-0.2}$	$6.5^{+0.1}_{-0.1}$	$0.0089^{+0.0021}_{-0.0017}$	$-0.19^{+0.02}_{-0.03}$	$10.7^{+0.6}_{-0.6}$	$0.177^{+0.005}_{-0.006}$	1.5
90089-11-02-09	53345.73	17.74	$1.97^{+0.04}_{-0.05}$	$26.3^{+0.1}_{-0.1}$	$7.1^{+0.3}_{-0.3}$	$6.4^{+0.1}_{-0.1}$	$0.0098^{+0.0020}_{-0.0017}$	$-0.20^{+0.03}_{-0.03}$	$10.5^{+0.5}_{-0.5}$	$0.207^{+0.006}_{-0.006}$	1.8
90089-11-02-08	53346.71	18.88	$2.02^{+0.06}_{-0.08}$	$26.4^{+0.1}_{-0.1}$	$7.5^{+0.3}_{-0.5}$	$6.4^{+0.1}_{-0.2}$	$0.0131^{+0.0041}_{-0.0025}$	$-0.18^{+0.03}_{-0.05}$	$11.1^{+0.6}_{-0.9}$	$0.220^{+0.006}_{-0.010}$	1.2
90089-11-03-03	53352.77	27.05	$1.91^{+0.07}_{-0.04}$	$25.1^{+0.1}_{-0.1}$	$7.4^{+0.5}_{-0.3}$	$6.4^{+0.1}_{-0.1}$	$0.0211^{+0.0048}_{-0.0035}$	$-0.07^{+0.04}_{-0.05}$	$10.7^{+0.8}_{-0.8}$	$0.448^{+0.016}_{-0.020}$	0.7
90089-11-03-04	53353.73	27.67	$1.99^{+0.04}_{-0.12}$	$24.9^{+0.1}_{-0.1}$	$8.4^{+0.4}_{-0.7}$	$6.4^{+0.1}_{-0.1}$	$0.0296^{+0.0062}_{-0.0060}$	$0.03^{+0.04}_{-0.07}$	$12.7^{+1.3}_{-1.7}$	$0.506^{+0.017}_{-0.025}$	0.7
90089-11-03-01	53354.62	28.71	$1.79^{+0.04}_{-0.08}$	$24.9^{+0.1}_{-0.1}$	$8.0^{+0.3}_{-0.4}$	$6.4^{+0.1}_{-0.1}$	$0.0251^{+0.0054}_{-0.0039}$	$-0.10^{+0.02}_{-0.05}$	$10.3^{+0.5}_{-0.8}$	$0.474^{+0.010}_{-0.014}$	1.2
90089-11-03-02	53354.86	28.04	$1.87^{+0.06}_{-0.10}$	$25.0^{+0.1}_{-0.1}$	$8.0^{+0.4}_{-0.6}$	$6.4^{+0.1}_{-0.1}$	$0.0253^{+0.0061}_{-0.0048}$	$-0.06^{+0.04}_{-0.08}$	$10.9^{+0.8}_{-1.1}$	$0.478^{+0.015}_{-0.029}$	0.8
90089-11-03-05	53355.10	29.01	$1.95^{+0.19}_{-0.23}$	$24.5^{+0.3}_{-0.3}$	$9.0^{+1.2}_{-1.5}$	$6.5^{+0.2}_{-0.2}$	$0.0282^{+0.0121}_{-0.0077}$	$0.01^{+0.09}_{-0.14}$	$13.0^{+3.8}_{-3.1}$	$0.516^{+0.033}_{-0.053}$	0.9
90089-11-04-00	53356.49	30.45	$1.69^{+0.03}_{-0.03}$	$24.4^{+0.0}_{-0.0}$	$7.8^{+0.2}_{-0.2}$	$6.4^{+0.1}_{-0.1}$	$0.0283^{+0.0045}_{-0.0043}$	$-0.11^{+0.02}_{-0.02}$	$9.7^{+0.3}_{-0.3}$	$0.530^{+0.009}_{-0.009}$	1.9
90089-11-04-01	53357.07	32.72	$1.66^{+0.15}_{-0.14}$	$24.6^{+0.2}_{-0.2}$	$7.7^{+1.0}_{-0.9}$	$6.5^{+0.2}_{-0.2}$	$0.0281^{+0.0120}_{-0.0073}$	$-0.20^{+0.08}_{-0.08}$	$8.8^{+1.3}_{-0.9}$	$0.503^{+0.031}_{-0.030}$	0.9
90089-11-04-02	53358.59	31.12	$1.65^{+0.03}_{-0.03}$	$24.3^{+0.0}_{-0.0}$	$7.8^{+0.2}_{-0.2}$	$6.4^{+0.1}_{-0.1}$	$0.0332^{+0.0052}_{-0.0052}$	$-0.08^{+0.02}_{-0.02}$	$9.8^{+0.3}_{-0.1}$	$0.571^{+0.009}_{-0.010}$	1.6
90089-11-04-04	53360.00	32.33	$1.74^{+0.12}_{-0.12}$	$24.1^{+0.2}_{-0.2}$	$8.3^{+0.8}_{-0.7}$	$6.5^{+0.1}_{-0.1}$	$0.0464^{+0.0098}_{-0.0102}$	$0.01^{+0.06}_{-0.07}$	$11.4^{+1.8}_{-1.3}$	$0.636^{+0.032}_{-0.030}$	1.0
90089-11-04-05	53361.12	32.36	$1.57^{+0.03}_{-0.03}$	$24.1^{+0.1}_{-0.1}$	$7.9^{+0.2}_{-0.2}$	$6.4^{+0.1}_{-0.1}$	$0.0367^{+0.0059}_{-0.0058}$	$-0.12^{+0.02}_{-0.02}$	$9.2^{+0.3}_{-0.3}$	$0.586^{+0.006}_{-0.012}$	1.6
90089-11-05-01	53364.91	33.92	$1.43^{+0.08}_{-0.11}$	$23.3^{+0.1}_{-0.1}$	$8.2^{+0.6}_{-1.0}$	$6.4^{+0.1}_{-0.1}$	$0.0490^{+0.0077}_{-0.0093}$	$-0.10^{+0.04}_{-0.06}$	$8.7^{+0.7}_{-0.8}$	$0.686^{+0.022}_{-0.030}$	0.9
90089-11-05-02	53365.91	32.90	$1.57^{+0.07}_{-0.10}$	$23.3^{+0.1}_{-0.1}$	$9.0^{+0.5}_{-0.8}$	$6.5^{+0.1}_{-0.1}$	$0.0460^{+0.0075}_{-0.0088}$	$-0.02^{+0.04}_{-0.06}$	$10.0^{+0.9}_{-1.0}$	$0.712^{+0.024}_{-0.027}$	0.8
90427-01-01-00	53367.23	32.89	$1.51^{+0.03}_{-0.03}$	$23.7^{+0.0}_{-0.1}$	$8.0^{+0.2}_{-0.2}$	$6.4^{+0.1}_{-0.1}$	$0.0461^{+0.0059}_{-0.0071}$	$-0.12^{+0.02}_{-0.02}$	$8.6^{+0.2}_{-0.2}$	$0.640^{+0.011}_{-0.012}$	1.5
90427-01-01-01	53368.24	32.38	$1.53^{+0.03}_{-0.03}$	$23.7^{+0.1}_{-0.1}$	$8.0^{+0.2}_{-0.2}$	$6.4^{+0.1}_{-0.1}$	$0.0421^{+0.0041}_{-0.0069}$	$-0.10^{+0.02}_{-0.02}$	$8.9^{+0.2}_{-0.2}$	$0.642^{+0.011}_{-0.012}$	1.7
90427-01-01-02	53368.91	32.47	$1.52^{+0.03}_{-0.04}$	$23.6^{+0.1}_{-0.1}$	$8.3^{+0.2}_{-0.1}$	$6.4^{+0.1}_{-0.1}$	$0.0441^{+0.0060}_{-0.0072}$	$-0.09^{+0.02}_{-0.02}$	$9.0^{+0.3}_{-0.3}$	$0.657^{+0.011}_{-0.012}$	1.7
90427-01-02-00	53374.03	30.18	$1.67^{+0.06}_{-0.05}$	$24.4^{+0.1}_{-0.1}$	$7.8^{+0.3}_{-0.3}$	$6.4^{+0.1}_{-0.1}$	$0.0332^{+0.0063}_{-0.0053}$	$-0.11^{+0.03}_{-0.03}$	$9.4^{+0.5}_{-0.4}$	$0.541^{+0.015}_{-0.015}$	1.0
90014-01-01-06	53378.60	27.51	$1.87^{+0.04}_{-0.02}$	$25.0^{+0.1}_{-0.1}$	$7.6^{+0.3}_{-0.2}$	$6.4^{+0.1}_{-0.1}$	$0.0289^{+0.0046}_{-0.0050}$	$-0.05^{+0.01}_{-0.03}$	$10.4^{+0.5}_{-0.4}$	$0.501^{+0.009}_{-0.012}$	1.2
90014-01-01-07	53378.74	26.44	$1.80^{+0.03}_{-0.03}$	$25.1^{+0.1}_{-0.1}$	$7.4^{+0.2}_{-0.3}$	$6.4^{+0.1}_{-0.1}$	$0.0229^{+0.0046}_{-0.0035}$	$-0.10^{+0.01}_{-0.03}$	$9.6^{+0.3}_{-0.4}$	$0.459^{+0.007}_{-0.013}$	1.8
90014-01-01-02	53381.04	24.10	$2.14^{+0.32}_{-0.32}$	$26.3^{+0.7}_{-0.6}$	$7.1^{+2.9}_{-1.6}$	$6.6^{+0.1}_{-0.1}$	$0.0096^{+0.0111}_{-0.0096}$	$-0.12^{+0.25}_{-0.17}$	$10.2^{+4.3}_{-2.2}$	$0.365^{+0.075}_{-0.033}$	0.8
90014-01-01-01	53381.35	23.73	$2.01^{+0.08}_{-0.14}$	$25.5^{+0.2}_{-0.2}$	$7.9^{+0.8}_{-0.8}$	$6.5^{+0.2}_{-0.1}$	$0.0248^{+0.0061}_{-0.0064}$	$-0.05^{+0.09}_{-0.08}$	$11.1^{+2.2}_{-1.4}$	$0.400^{+0.029}_{-0.024}$	0.7

Continued on Next Page...

Table A.4 – Continued

Obs. ID	MJD	L_X $\times 10^{37}$ (erg/s)	Cyclotron line τ	Cyclotron line E (keV)	Cyclotron line Width (keV)	Fe line E (keV)	Fe line norm. (ph./cm^2/s)	Power law Γ	Power law cutoff en. (keV)	Power law norm.	χ^2_r
90014-01-02-03	53385.87	19.39	$1.98^{+0.06}_{-0.11}$	$26.1^{+0.1}_{-0.1}$	$7.7^{+0.3}_{-0.6}$	$6.4^{+0.1}_{-0.1}$	$0.0147^{+0.0033}_{-0.0025}$	$-0.12^{+0.03}_{-0.07}$	$10.2^{+0.5}_{-1.0}$	$0.293^{+0.009}_{-0.017}$	1.2
90014-01-02-10	53387.12	18.33	$1.92^{+0.05}_{-0.05}$	$26.2^{+0.1}_{-0.1}$	$7.2^{+0.3}_{-0.3}$	$6.4^{+0.1}_{-0.1}$	$0.0141^{+0.0024}_{-0.0020}$	$-0.17^{+0.03}_{-0.04}$	$9.6^{+0.4}_{-0.5}$	$0.258^{+0.007}_{-0.008}$	1.4
90014-01-02-15	53389.08	16.88	$1.95^{+0.05}_{-0.06}$	$26.4^{+0.1}_{-0.1}$	$7.4^{+0.2}_{-0.2}$	$6.5^{+0.1}_{-0.1}$	$0.0151^{+0.0029}_{-0.0026}$	$-0.15^{+0.03}_{-0.04}$	$10.0^{+0.6}_{-0.5}$	$0.235^{+0.007}_{-0.008}$	1.8
90014-01-03-01	53393.21	14.44	$1.95^{+0.04}_{-0.05}$	$26.6^{+0.1}_{-0.1}$	$7.2^{+0.2}_{-0.3}$	$6.5^{+0.1}_{-0.1}$	$0.0147^{+0.0023}_{-0.0028}$	$-0.14^{+0.03}_{-0.04}$	$10.5^{+0.3}_{-0.7}$	$0.192^{+0.004}_{-0.009}$	1.8
90014-01-03-02	53394.59	14.10	$1.95^{+0.05}_{-0.05}$	$26.7^{+0.1}_{-0.1}$	$7.0^{+0.3}_{-0.3}$	$6.4^{+0.1}_{-0.1}$	$0.0122^{+0.0022}_{-0.0022}$	$-0.19^{+0.03}_{-0.04}$	$9.8^{+0.4}_{-0.5}$	$0.181^{+0.005}_{-0.006}$	1.9
90014-01-04-00	53398.46	11.69	$2.03^{+0.05}_{-0.06}$	$26.9^{+0.1}_{-0.1}$	$6.5^{+0.2}_{-0.3}$	$6.5^{+0.1}_{-0.1}$	$0.0125^{+0.0014}_{-0.0021}$	$-0.13^{+0.03}_{-0.04}$	$10.9^{+0.6}_{-0.6}$	$0.151^{+0.004}_{-0.006}$	1.7
90014-01-04-01	53399.60	11.56	$2.07^{+0.07}_{-0.09}$	$26.9^{+0.2}_{-0.2}$	$7.2^{+0.4}_{-0.6}$	$6.5^{+0.1}_{-0.1}$	$0.0114^{+0.0023}_{-0.0024}$	$-0.08^{+0.04}_{-0.07}$	$12.3^{+1.1}_{-1.4}$	$0.151^{+0.006}_{-0.008}$	1.2
90014-01-04-02	53401.37	10.63	$2.06^{+0.08}_{-0.07}$	$26.9^{+0.2}_{-0.1}$	$7.3^{+0.4}_{-0.4}$	$6.6^{+0.1}_{-0.1}$	$0.0119^{+0.0025}_{-0.0026}$	$-0.07^{+0.05}_{-0.06}$	$12.8^{+1.0}_{-1.3}$	$0.137^{+0.005}_{-0.004}$	1.5
90014-01-04-03	53403.34	9.94	$2.07^{+0.07}_{-0.08}$	$27.0^{+0.2}_{-0.2}$	$7.0^{+0.4}_{-0.4}$	$6.6^{+0.1}_{-0.1}$	$0.0097^{+0.0023}_{-0.0026}$	$-0.09^{+0.05}_{-0.07}$	$12.9^{+1.0}_{-1.4}$	$0.120^{+0.004}_{-0.007}$	1.2
90014-01-05-00	53405.24	9.94	$2.16^{+0.08}_{-0.09}$	$27.1^{+0.2}_{-0.2}$	$7.0^{+0.4}_{-0.5}$	$6.6^{+0.1}_{-0.1}$	$0.0099^{+0.0021}_{-0.0023}$	$-0.05^{+0.04}_{-0.07}$	$13.5^{+1.2}_{-1.7}$	$0.127^{+0.005}_{-0.007}$	0.9
90014-01-05-04	53407.76	8.92	$2.25^{+0.07}_{-0.09}$	$27.2^{+0.2}_{-0.2}$	$7.4^{+0.4}_{-0.4}$	$6.5^{+0.1}_{-0.1}$	$0.0091^{+0.0022}_{-0.0018}$	$0.02^{+0.04}_{-0.06}$	$15.8^{+1.7}_{-1.9}$	$0.120^{+0.005}_{-0.005}$	1.2
90014-01-05-05	53407.96	8.63	$2.26^{+0.07}_{-0.06}$	$27.4^{+0.1}_{-0.1}$	$7.5^{+0.3}_{-0.4}$	$6.5^{+0.1}_{-0.1}$	$0.0064^{+0.0015}_{-0.0010}$	$-0.00^{+0.05}_{-0.04}$	$15.5^{+1.0}_{-1.4}$	$0.111^{+0.004}_{-0.003}$	1.4
90014-01-05-03	53410.75	7.20	$2.43^{+0.24}_{-0.20}$	$27.5^{+0.5}_{-0.4}$	$7.8^{+1.3}_{-1.0}$	$6.6^{+0.3}_{-0.3}$	$0.0061^{+0.0050}_{-0.0029}$	$0.17^{+0.17}_{-0.11}$	$26.1^{+1.3}_{-8.3}$	$0.104^{+0.015}_{-0.009}$	1.0
90014-01-05-06	53411.62	6.86	$2.47^{+0.12}_{-0.14}$	$27.7^{+0.3}_{-0.2}$	$7.4^{+0.4}_{-0.6}$	$6.3^{+0.1}_{-0.3}$	$0.0036^{+0.0013}_{-0.0007}$	$0.10^{+0.05}_{-0.06}$	$21.1^{+4.6}_{-3.7}$	$0.092^{+0.004}_{-0.005}$	0.9
90014-01-06-00	53414.04	5.99	$2.88^{+0.11}_{-0.09}$	$27.8^{+0.3}_{-0.2}$	$9.4^{+0.4}_{-0.3}$	$6.6^{+0.1}_{-0.2}$	$0.0047^{+0.0010}_{-0.0009}$	$0.35^{+0.01}_{-0.01}$	–	$0.090^{+0.002}_{-0.002}$	1.2
90014-01-06-01	53416.07	4.66	$2.86^{+0.10}_{-0.11}$	$27.8^{+0.2}_{-0.2}$	$8.3^{+0.3}_{-0.3}$	$6.4^{+0.2}_{-0.1}$	$0.0032^{+0.0006}_{-0.0006}$	$0.37^{+0.01}_{-0.01}$	–	$0.073^{+0.002}_{-0.001}$	1.3
90014-01-06-02	53417.58	4.08	$2.82^{+0.01}_{-0.01}$	$28.1^{+0.3}_{-0.2}$	$8.4^{+0.3}_{-0.3}$	$6.5^{+0.4}_{-0.2}$	$0.0026^{+0.0002}_{-0.0002}$	$0.39^{+-0.01}_{-0.01}$	–	$0.065^{+0.001}_{-0.001}$	1.1
90014-01-06-03	53418.47	3.42	$2.63^{+0.12}_{-0.12}$	$27.8^{+0.3}_{-0.3}$	$7.9^{+0.3}_{-0.4}$	6.4	$0.0018^{+0.0005}_{-0.0006}$	$0.40^{+0.01}_{-0.01}$	–	$0.055^{+0.001}_{-0.001}$	1.1
90014-01-07-01	53419.41	2.96	$2.66^{+0.17}_{-0.16}$	$27.9^{+0.3}_{-0.3}$	$7.0^{+0.4}_{-0.4}$	6.4	$0.0018^{+0.0005}_{-0.0006}$	$0.45^{+0.01}_{-0.01}$	–	$0.053^{+0.001}_{-0.002}$	1.1
90014-01-07-02	53420.64	2.57	$2.64^{+0.11}_{-0.11}$	$28.4^{+0.2}_{-0.3}$	$7.6^{+0.4}_{-0.5}$	$6.2^{+0.4}_{-0.2}$	$0.0011^{+0.0002}_{-0.0002}$	$0.46^{+0.01}_{-0.01}$	–	$0.047^{+0.001}_{-0.001}$	1.9
90014-01-07-03	53420.71	2.63	$2.56^{+0.14}_{-0.14}$	$27.8^{+0.3}_{-0.3}$	$6.9^{+0.3}_{-0.4}$	6.4	$0.0016^{+0.0005}_{-0.0005}$	$0.46^{+0.01}_{-0.01}$	–	$0.047^{+0.001}_{-0.001}$	1.3
90014-01-07-04	53422.61	1.80	$2.62^{+0.01}_{-0.10}$	$28.1^{+0.4}_{-0.2}$	$5.6^{+0.3}_{-0.4}$	$6.2^{+0.4}_{-0.2}$	$0.0011^{+0.0002}_{-0.0002}$	$0.57^{+0.01}_{-0.01}$	–	$0.041^{+0.001}_{-0.001}$	1.6
90014-01-08-00	53426.47	0.69	$2.40^{+0.81}_{-0.45}$	$27.8^{+0.7}_{-0.7}$	$4.1^{+0.5}_{-0.7}$	6.4	$0.0004^{+0.0002}_{-0.0002}$	$0.74^{+0.02}_{-0.02}$	–	$0.023^{+0.000}_{-0.001}$	1.2
90014-01-08-01	53428.50	0.45	$2.60^{+0.01}_{-0.01}$	$28.0^{+0.4}_{-0.5}$	$3.4^{+0.5}_{-0.6}$	6.4	$0.0003^{+0.0002}_{-0.0002}$	$0.82^{+0.01}_{-0.01}$	–	$0.010^{+0.001}_{-0.001}$	1.0

Table A.5: The same as Table A.1, for V 0332+53 using Model II. The photoabsorption was fixed to 1.5×10^{22} cm^{-2} (Pottschmidt 2005). Best fits were obtained with 47–48 DOF.

Obs. ID	MJD	L_X $\times 10^{37}$ (erg/s)	Cyclotron line τ	Cyclotron line E (keV)	Cyclotron line Width (keV)	Fe line E (keV)	Fe line norm. (ph./cm^2/s)	Power law Γ	Power law norm.	χ^2_r
90089-11-01-02	53340.29	11.02	$5.80^{+3.03}_{-0.82}$	$34.2^{+4.1}_{-1.5}$	$15.7^{+1.9}_{-1.1}$	$6.4^{+0.1}_{-0.1}$	$0.0133^{+0.0016}_{-0.0015}$	$0.34^{+0.01}_{-0.02}$	$0.183^{+0.004}_{-0.004}$	1.5
90089-11-01-03	53341.14	12.51	$5.27^{+1.05}_{-0.48}$	$33.1^{+1.9}_{-1.0}$	$15.4^{+1.5}_{-1.1}$	$6.5^{+0.1}_{-0.1}$	$0.0139^{+0.0016}_{-0.0034}$	$0.37^{+0.04}_{-0.04}$	$0.226^{+0.019}_{-0.018}$	0.9
90089-11-01-04	53341.80	13.33	$6.03^{+1.71}_{-0.81}$	$34.1^{+2.6}_{-1.6}$	$17.2^{+1.5}_{-1.4}$	$6.5^{+0.1}_{-0.1}$	$0.0167^{+0.0019}_{-0.0018}$	$0.31^{+0.02}_{-0.02}$	$0.214^{+0.005}_{-0.004}$	1.2
90089-11-02-05	53343.04	13.83	$5.44^{+1.72}_{-0.53}$	$32.8^{+3.0}_{-1.1}$	$17.7^{+2.3}_{-1.1}$	$6.5^{+0.1}_{-0.1}$	$0.0187^{+0.0020}_{-0.0019}$	$0.28^{+0.01}_{-0.02}$	$0.214^{+0.004}_{-0.005}$	1.6
90089-11-02-06	53343.11	14.35	$5.45^{+1.29}_{-0.50}$	$32.8^{+2.4}_{-1.1}$	$17.7^{+1.9}_{-1.1}$	$6.5^{+0.1}_{-0.1}$	$0.0179^{+0.0020}_{-0.0019}$	$0.28^{+0.01}_{-0.02}$	$0.222^{+0.004}_{-0.003}$	1.4
90089-11-02-01	53343.24	14.44	$5.30^{+1.38}_{-0.54}$	$32.3^{+2.5}_{-1.2}$	$17.5^{+2.1}_{-1.3}$	$6.5^{+0.1}_{-0.1}$	$0.0176^{+0.0022}_{-0.0022}$	$0.28^{+0.02}_{-0.02}$	$0.228^{+0.005}_{-0.005}$	1.3
90089-11-02-02	53343.39	14.90	$5.73^{+1.80}_{-0.69}$	$33.2^{+3.0}_{-1.4}$	$18.5^{+2.2}_{-1.4}$	$6.5^{+0.1}_{-0.1}$	$0.0201^{+0.0022}_{-0.0021}$	$0.26^{+0.02}_{-0.02}$	$0.227^{+0.005}_{-0.005}$	1.5
90089-11-02-10	53344.75	16.39	$5.09^{+0.75}_{-0.32}$	$31.7^{+1.5}_{-0.8}$	$17.9^{+1.7}_{-1.0}$	$6.5^{+0.1}_{-0.1}$	$0.0208^{+0.0024}_{-0.0022}$	$0.26^{+0.01}_{-0.02}$	$0.252^{+0.005}_{-0.004}$	1.8
90089-11-02-08	53346.71	18.88	$5.00^{+0.79}_{-0.42}$	$31.5^{+1.6}_{-1.1}$	$18.2^{+1.7}_{-1.4}$	$6.4^{+0.1}_{-0.1}$	$0.0264^{+0.0029}_{-0.0029}$	$0.25^{+0.02}_{-0.02}$	$0.286^{+0.008}_{-0.006}$	1.3
90089-11-03-03	53352.77	27.05	$3.81^{+0.15}_{-0.11}$	$27.6^{+0.4}_{-0.3}$	$14.7^{+1.0}_{-0.8}$	$6.4^{+0.1}_{-0.1}$	$0.0445^{+0.0052}_{-0.0052}$	$0.39^{+0.02}_{-0.02}$	$0.599^{+0.018}_{-0.016}$	1.6
90089-11-03-04	53353.73	27.67	$3.60^{+0.11}_{-0.10}$	$27.0^{+0.3}_{-0.3}$	$14.5^{+0.8}_{-0.8}$	$6.4^{+0.1}_{-0.1}$	$0.0484^{+0.0054}_{-0.0052}$	$0.40^{+0.02}_{-0.02}$	$0.637^{+0.020}_{-0.016}$	1.1
90089-11-03-02	53354.86	28.04	$2.06^{+0.14}_{-0.08}$	$25.2^{+0.4}_{-0.3}$	$11.3^{+1.0}_{-0.7}$	$6.4^{+0.1}_{-0.1}$	$0.0458^{+0.0053}_{-0.0052}$	$0.36^{+0.01}_{-0.02}$	$0.608^{+0.014}_{-0.016}$	1.1
90089-11-03-05	53355.10	29.01	$2.01^{+0.34}_{-0.19}$	$24.8^{+1.1}_{-0.7}$	$11.9^{+2.3}_{-1.5}$	$6.4^{+0.2}_{-0.2}$	$0.0465^{+0.0092}_{-0.0092}$	$0.33^{+0.03}_{-0.03}$	$0.608^{+0.027}_{-0.029}$	0.8
90089-11-03-05	53356.49	30.45	$2.01^{+0.34}_{-0.19}$	$24.8^{+1.1}_{-0.7}$	$11.9^{+2.3}_{-1.5}$	$6.4^{+0.2}_{-0.2}$	$0.0465^{+0.0092}_{-0.0092}$	$0.33^{+0.03}_{-0.03}$	$0.608^{+0.027}_{-0.029}$	0.8
90089-11-04-01	53357.07	32.72	$2.87^{+0.21}_{-0.11}$	$24.6^{+0.5}_{-0.4}$	$15.1^{+1.7}_{-1.2}$	$6.5^{+0.1}_{-0.1}$	$0.0592^{+0.0085}_{-0.0087}$	$0.36^{+0.03}_{-0.03}$	$0.720^{+0.032}_{-0.031}$	1.7
90089-11-04-04	53360.00	32.33	$3.15^{+0.08}_{-0.08}$	$25.5^{+0.3}_{-0.2}$	$14.2^{+0.9}_{-1.0}$	$6.5^{+0.1}_{-0.1}$	$0.0664^{+0.0075}_{-0.0075}$	$0.44^{+0.02}_{-0.02}$	$0.831^{+0.033}_{-0.025}$	1.7
90089-11-04-05	53361.12	32.36	$3.15^{+0.08}_{-0.08}$	$25.5^{+0.3}_{-0.2}$	$14.2^{+0.9}_{-1.0}$	$6.5^{+0.1}_{-0.1}$	$0.0664^{+0.0075}_{-0.0075}$	$0.44^{+0.02}_{-0.02}$	$0.831^{+0.033}_{-0.025}$	1.7
90089-11-05-01	53364.91	33.92	$2.73^{+0.03}_{-0.02}$	$23.5^{+0.2}_{-0.2}$	$15.5^{+0.8}_{-0.5}$	$6.4^{+0.1}_{-0.1}$	$0.0813^{+0.0073}_{-0.0073}$	$0.45^{+0.02}_{-0.02}$	$0.954^{+0.024}_{-0.035}$	1.6
90089-11-05-02	53365.91	32.90	$2.67^{+0.03}_{-0.02}$	$23.3^{+0.2}_{-0.2}$	$15.3^{+0.7}_{-0.5}$	$6.4^{+0.1}_{-0.1}$	$0.0735^{+0.0067}_{-0.0068}$	$0.46^{+0.02}_{-0.02}$	$0.942^{+0.023}_{-0.032}$	1.4
90427-01-01-00	53367.23	32.89	$2.76^{+0.01}_{-0.01}$	$23.8^{+0.1}_{-0.1}$	$14.5^{+0.2}_{-0.3}$	$6.4^{+0.1}_{-0.1}$	$0.0806^{+0.0056}_{-0.0051}$	$0.46^{+0.01}_{-0.01}$	$0.920^{+0.023}_{-0.016}$	1.6
90427-01-01-01	53368.24	32.38	$2.89^{+0.02}_{-0.01}$	$24.2^{+0.1}_{-0.1}$	$15.0^{+0.4}_{-0.3}$	$6.4^{+0.1}_{-0.1}$	$0.0740^{+0.0055}_{-0.0053}$	$0.46^{+0.01}_{-0.02}$	$0.907^{+0.016}_{-0.023}$	1.8
90427-01-01-02	53368.91	32.47	$2.77^{+0.02}_{-0.01}$	$23.8^{+0.1}_{-0.1}$	$15.2^{+0.4}_{-0.3}$	$6.4^{+0.1}_{-0.1}$	$0.0750^{+0.0056}_{-0.0055}$	$0.45^{+0.01}_{-0.02}$	$0.914^{+0.017}_{-0.023}$	1.7
90427-01-02-00	53374.03	30.18	$1.83^{+0.05}_{-0.04}$	$24.1^{+0.2}_{-0.2}$	$10.8^{+0.5}_{-0.5}$	$6.4^{+0.1}_{-0.1}$	$0.0604^{+0.0053}_{-0.0053}$	$0.39^{+0.01}_{-0.01}$	$0.730^{+0.016}_{-0.016}$	1.4
90427-01-02-03	53376.64	28.74	$1.90^{+0.03}_{-0.02}$	$24.6^{+0.1}_{-0.1}$	$10.1^{+0.4}_{-0.2}$	$6.4^{+0.1}_{-0.1}$	$0.0557^{+0.0046}_{-0.0045}$	$0.40^{+0.01}_{-0.01}$	$0.688^{+0.012}_{-0.012}$	1.6
90014-01-01-06	53378.60	27.51	$2.03^{+0.05}_{-0.05}$	$25.0^{+0.2}_{-0.1}$	$10.3^{+0.4}_{-0.4}$	$6.4^{+0.1}_{-0.1}$	$0.0522^{+0.0044}_{-0.0044}$	$0.41^{+0.01}_{-0.01}$	$0.663^{+0.013}_{-0.013}$	1.7
90014-01-01-07	53378.74	26.44	$2.08^{+0.05}_{-0.05}$	$25.3^{+0.2}_{-0.2}$	$10.9^{+0.4}_{-0.4}$	$6.5^{+0.1}_{-0.1}$	$0.0483^{+0.0042}_{-0.0042}$	$0.40^{+0.01}_{-0.01}$	$0.625^{+0.012}_{-0.012}$	1.8
90014-01-01-02	53381.04	24.10	$3.51^{+0.15}_{-0.13}$	$27.0^{+0.2}_{-0.2}$	$13.9^{+2.5}_{-1.9}$	$6.6^{+0.1}_{-0.1}$	$0.0258^{+0.0139}_{-0.0140}$	$0.39^{+0.06}_{-0.06}$	$0.517^{+0.050}_{-0.049}$	0.8
90014-01-01-01	53381.35	23.73	$2.40^{+0.46}_{-0.27}$	$26.3^{+1.3}_{-0.8}$	$11.9^{+2.0}_{-1.4}$	$6.5^{+0.1}_{-0.1}$	$0.0395^{+0.0057}_{-0.0057}$	$0.37^{+0.02}_{-0.02}$	$0.515^{+0.018}_{-0.018}$	0.9
90014-01-02-03	53385.87	19.39	$3.61^{+1.07}_{-0.56}$	$29.8^{+2.3}_{-1.4}$	$16.3^{+2.7}_{-1.9}$	$6.4^{+0.1}_{-0.1}$	$0.0296^{+0.0034}_{-0.0034}$	$0.32^{+0.02}_{-0.02}$	$0.377^{+0.010}_{-0.010}$	1.0
90014-01-02-10	53387.12	18.33	$2.84^{+0.35}_{-0.25}$	$28.2^{+0.9}_{-0.7}$	$13.5^{+1.3}_{-1.0}$	$6.4^{+0.1}_{-0.1}$	$0.0304^{+0.0028}_{-0.0028}$	$0.32^{+0.01}_{-0.01}$	$0.349^{+0.008}_{-0.008}$	1.9

Continued on Next Page...

Table A.5 – Continued

Obs. ID	MJD	L_X $\times 10^{37}$ (erg/s)	Cyclotron line τ	Cyclotron line E (keV)	Cyclotron line Width (keV)	Fe line E (keV)	Fe line norm. (ph./cm^2/s)	Power law Γ	Power law norm.	χ^2_r
90014-01-02-08	53388.03	17.21	$3.05^{+0.40}_{-0.28}$	$28.9^{+1.0}_{-0.7}$	$13.8^{+1.3}_{-1.0}$	$6.5^{+0.1}_{-0.1}$	$0.0287^{+0.0026}_{-0.0026}$	$0.32^{+0.01}_{-0.01}$	$0.322^{+0.007}_{-0.007}$	1.1
90014-01-02-15	53389.08	16.88	$3.06^{+0.53}_{-0.34}$	$29.0^{+1.3}_{-0.9}$	$14.4^{+1.7}_{-1.3}$	$6.5^{+0.1}_{-0.1}$	$0.0285^{+0.0026}_{-0.0026}$	$0.32^{+0.01}_{-0.01}$	$0.312^{+0.007}_{-0.007}$	1.2
90014-01-02-13	53390.33	16.08	$3.06^{+0.29}_{-0.22}$	$29.1^{+0.7}_{-0.6}$	$13.9^{+1.0}_{-0.9}$	$6.5^{+0.1}_{-0.1}$	$0.0283^{+0.0023}_{-0.0022}$	$0.32^{+0.01}_{-0.01}$	$0.294^{+0.006}_{-0.006}$	1.2
90014-01-03-00	53391.32	15.50	$3.84^{+1.09}_{-0.60}$	$31.0^{+2.2}_{-1.4}$	$15.8^{+2.3}_{-1.6}$	$6.5^{+0.1}_{-0.1}$	$0.0269^{+0.0023}_{-0.0023}$	$0.31^{+0.01}_{-0.01}$	$0.278^{+0.006}_{-0.006}$	1.6
90014-01-03-01	53393.21	14.44	$3.58^{+0.98}_{-0.54}$	$30.6^{+2.1}_{-1.3}$	$15.0^{+2.1}_{-1.6}$	$6.5^{+0.1}_{-0.1}$	$0.0250^{+0.0021}_{-0.0021}$	$0.30^{+0.01}_{-0.01}$	$0.252^{+0.006}_{-0.006}$	1.6
90014-01-03-02	53394.59	14.10	$2.94^{+0.03}_{-0.03}$	$29.0^{+2.1}_{-1.3}$	$13.1^{+0.4}_{-0.4}$	$6.5^{+0.1}_{-0.1}$	$0.0241^{+0.0021}_{-0.0021}$	$0.31^{+0.01}_{-0.01}$	$0.249^{+0.005}_{-0.005}$	1.8
90014-01-04-00	53398.46	11.69	$3.22^{+0.04}_{-0.04}$	$30.0^{+1.3}_{-0.9}$	$12.2^{+0.4}_{-0.4}$	$6.5^{+0.1}_{-0.1}$	$0.0209^{+0.0017}_{-0.0017}$	$0.32^{+0.01}_{-0.01}$	$0.202^{+0.004}_{-0.004}$	1.5
90014-01-04-01	53399.60	11.56	$3.29^{+0.07}_{-0.06}$	$30.2^{+1.3}_{-0.9}$	$12.6^{+0.6}_{-0.5}$	$6.5^{+0.1}_{-0.1}$	$0.0181^{+0.0019}_{-0.0019}$	$0.30^{+0.01}_{-0.01}$	$0.191^{+0.005}_{-0.005}$	0.9
90014-01-04-02	53401.37	10.63	$3.69^{+2.74}_{-0.89}$	$31.2^{+4.7}_{-2.0}$	$13.4^{+3.3}_{-2.0}$	$6.6^{+0.1}_{-0.1}$	$0.0170^{+0.0017}_{-0.0017}$	$0.29^{+0.01}_{-0.01}$	$0.171^{+0.004}_{-0.004}$	1.4
90014-01-04-03	53403.34	9.94	$3.39^{+3.48}_{-0.87}$	$30.7^{+5.7}_{-2.0}$	$12.2^{+3.7}_{-2.0}$	$6.6^{+0.1}_{-0.1}$	$0.0145^{+0.0016}_{-0.0016}$	$0.28^{+0.01}_{-0.02}$	$0.151^{+0.004}_{-0.004}$	1.4
90014-01-05-00	53405.24	9.94	$2.94^{+1.72}_{-0.60}$	$29.5^{+3.4}_{-1.5}$	$10.8^{+2.6}_{-1.5}$	$6.6^{+0.1}_{-0.1}$	$0.0146^{+0.0016}_{-0.0016}$	$0.30^{+0.01}_{-0.01}$	$0.158^{+0.004}_{-0.004}$	1.2
90014-01-05-01	53407.56	8.78	$2.92^{+0.43}_{-0.29}$	$29.6^{+1.0}_{-0.7}$	$10.4^{+0.9}_{-0.7}$	$6.5^{+0.1}_{-0.1}$	$0.0117^{+0.0011}_{-0.0011}$	$0.28^{+0.01}_{-0.01}$	$0.134^{+0.002}_{-0.002}$	1.5
90014-01-05-04	53407.76	8.92	$2.80^{+0.95}_{-0.46}$	$29.3^{+2.0}_{-1.1}$	$10.2^{+1.7}_{-1.2}$	$6.5^{+0.1}_{-0.1}$	$0.0122^{+0.0013}_{-0.0013}$	$0.30^{+0.01}_{-0.01}$	$0.141^{+0.003}_{-0.003}$	0.9
90014-01-05-05	53407.96	8.63	$2.88^{+0.94}_{-0.47}$	$29.6^{+2.0}_{-1.1}$	$10.4^{+1.6}_{-1.1}$	$6.5^{+0.1}_{-0.1}$	$0.0107^{+0.0012}_{-0.0012}$	$0.29^{+0.01}_{-0.01}$	$0.131^{+0.003}_{-0.003}$	1.0
90014-01-05-02	53409.28	8.11	$2.50^{+0.42}_{-0.27}$	$28.7^{+1.0}_{-0.7}$	$9.0^{+0.9}_{-0.7}$	$6.5^{+0.1}_{-0.1}$	$0.0095^{+0.0011}_{-0.0011}$	$0.28^{+0.01}_{-0.01}$	$0.120^{+0.002}_{-0.002}$	1.5
90014-01-05-03	53410.75	7.20	$2.48^{+3.58}_{-0.63}$	$28.7^{+5.8}_{-1.7}$	$8.3^{+3.3}_{-1.7}$	$6.5^{+0.3}_{-0.3}$	$0.0064^{+0.0019}_{-0.0019}$	$0.31^{+0.02}_{-0.02}$	$0.110^{+0.004}_{-0.004}$	1.0
90014-01-05-06	53411.62	6.86	$2.58^{+1.80}_{-0.54}$	$29.0^{+3.1}_{-1.3}$	$7.7^{+1.9}_{-1.1}$	$6.4^{+0.2}_{-0.2}$	$0.0057^{+0.0012}_{-0.0012}$	$0.27^{+0.01}_{-0.01}$	$0.099^{+0.002}_{-0.002}$	0.7
90014-01-06-00	53414.04	5.99	$2.67^{+1.02}_{-0.48}$	$29.0^{+1.9}_{-1.1}$	$8.2^{+1.3}_{-1.0}$	$6.5^{+0.2}_{-0.2}$	$0.0040^{+0.0009}_{-0.0009}$	$0.27^{+0.01}_{-0.01}$	$0.081^{+0.002}_{-0.002}$	1.0
90014-01-06-01	53416.07	4.66	$2.73^{+0.63}_{-0.38}$	$28.6^{+1.2}_{-0.8}$	$7.8^{+0.8}_{-0.7}$	$6.4^{+0.2}_{-0.4}$	$0.0029^{+0.0007}_{-0.0007}$	$0.34^{+0.01}_{-0.01}$	$0.069^{+0.001}_{-0.001}$	1.6
90014-01-06-02	53417.58	4.08	$2.96^{+0.64}_{-0.38}$	$28.6^{+1.3}_{-0.9}$	$8.7^{+0.8}_{-0.7}$	$6.5^{+0.2}_{-0.2}$	$0.0025^{+0.0007}_{-0.0007}$	$0.39^{+0.01}_{-0.02}$	$0.065^{+0.002}_{-0.002}$	1.1
90014-01-06-03	53418.47	3.42	$2.69^{+0.48}_{-0.31}$	$28.0^{+1.0}_{-0.8}$	$8.0^{+0.7}_{-0.6}$	$6.4^{+0.2}_{-0.2}$	$0.0019^{+0.0005}_{-0.0006}$	$0.40^{+0.01}_{-0.01}$	$0.055^{+0.002}_{-0.001}$	1.4
90014-01-07-01	53419.41	2.96	$2.56^{+0.58}_{-0.32}$	$27.7^{+1.1}_{-0.7}$	$6.8^{+0.7}_{-0.6}$	6.4	$0.0018^{+0.0006}_{-0.0006}$	$0.45^{+0.01}_{-0.01}$	$0.052^{+0.002}_{-0.001}$	1.3
90014-01-07-02	53420.64	2.57	$2.79^{+1.33}_{-0.64}$	$28.6^{+2.2}_{-1.5}$	$7.5^{+1.1}_{-1.0}$	6.4	$0.0010^{+0.0006}_{-0.0006}$	$0.47^{+0.02}_{-0.02}$	$0.048^{+0.001}_{-0.002}$	1.9
90014-01-07-03	53420.71	2.63	$2.52^{+0.66}_{-0.32}$	$27.8^{+1.3}_{-0.8}$	$6.8^{+0.7}_{-0.6}$	6.4	$0.0016^{+0.0005}_{-0.0005}$	$0.46^{+0.01}_{-0.01}$	$0.047^{+0.001}_{-0.001}$	1.8
90014-01-08-00	53426.47	0.69	$9.15^{+-9.15}_{-4.77}$	$30.2^{+1.5}_{-3.0}$	$3.4^{+1.4}_{-2.2}$	6.4	$0.0005^{+0.0002}_{-0.0002}$	$0.76^{+0.02}_{-0.02}$	$0.024^{+0.001}_{-0.001}$	1.3
90014-01-08-01	53428.50	0.45	$2.21^{+-2.21}_{-0.79}$	$27.3^{+6.4}_{-1.1}$	$2.9^{+1.1}_{-0.9}$	6.4	$0.0003^{+0.0002}_{-0.0002}$	$0.83^{+0.02}_{-0.02}$	$0.018^{+0.001}_{-0.000}$	1.1

Table A.6: Power spectral fit parameters obtained for the KS 1947+300 outburst.

Obs. ID	MJD	L_X	$\mathbf{L_b}$		$\mathbf{L_l}$		$\mathbf{L_u}$		χ^2_r
		(10^{37} erg s^{-1})	ν_b (Hz)	rms (%)	ν_l (Hz)	rms (%)	ν_u (Hz)	rms (%)	
50425-01-05-00	51874.15	0.16	–	–	$0.04^{+0.01}_{-0.01}$	$49.6^{+2.5}_{-2.4}$	–	–	1.6
50425-01-06-00	51876.41	0.09	–	–	$0.03^{+0.01}_{-0.00}$	$52.7^{+2.5}_{-2.3}$	–	–	2.2
50425-01-07-00	51878.27	0.12	–	–	$0.04^{+0.01}_{-0.01}$	$56.2^{+2.4}_{-2.2}$	–	–	2.2
50425-01-08-01	51883.83	0.35	–	–	$0.07^{+0.02}_{-0.02}$	$28.3^{+2.5}_{-2.6}$	–	–	0.7
50425-01-08-00	51883.89	0.35	–	–	$0.05^{+0.01}_{-0.01}$	$31.6^{+1.9}_{-2.0}$	–	–	1.5
50425-01-09-00	51888.01	0.99	–	–	$0.18^{+0.06}_{-0.03}$	$19.0^{+2.0}_{-2.2}$	–	–	1.2
50425-01-09-01	51888.07	0.97	–	–	$0.15^{+0.04}_{-0.02}$	$22.1^{+1.7}_{-2.4}$	–	–	1.2
50425-01-10-00	51892.22	1.60	–	–	$0.18^{+0.04}_{-0.03}$	$19.5^{+1.6}_{-1.7}$	–	–	1.3
50425-01-11-00	51896.20	2.26	–	–	$0.40^{+0.07}_{-0.10}$	$16.1^{+2.0}_{-1.4}$	–	–	1.0
50425-01-11-01	51896.52	2.15	–	–	$0.28^{+0.13}_{-0.07}$	$19.0^{+3.1}_{-3.4}$	–	–	1.0
50425-01-12-00	51898.98	2.79	–	–	$0.14^{+0.01}_{-0.00}$	$19.5^{+2.4}_{-1.7}$	$0.7^{+0.5}_{-0.2}$	$13.0^{+1.6}_{-3.2}$	1.3
50425-01-13-00	51901.91	3.28	–	–	$0.31^{+0.04}_{-0.03}$	$20.5^{+0.7}_{-0.7}$	–	–	1.9
50425-01-14-00	51906.13	3.68	–	–	$0.21^{+0.07}_{-0.08}$	$18.7^{+1.9}_{-1.6}$	$1.1^{+0.7}_{-0.4}$	$10.0^{+2.7}_{-2.5}$	1.3
50425-01-14-01	51906.72	3.67	–	–	$0.18^{+0.02}_{-0.02}$	$20.5^{+1.2}_{-1.1}$	$2.3^{+1.2}_{-0.7}$	$9.5^{+1.2}_{-1.3}$	1.5
50425-01-15-00	51910.90	3.87	–	–	$0.12^{+0.02}_{-0.01}$	$20.5^{+1.1}_{-1.3}$	$1.0^{+0.2}_{-0.1}$	$11.8^{+1.2}_{-1.4}$	1.5
50425-01-16-00	51914.18	4.12	–	–	$0.22^{+0.10}_{-0.03}$	$18.7^{+1.3}_{-1.9}$	$1.1^{+0.5}_{-0.2}$	$10.5^{+1.8}_{-2.1}$	1.8
50425-01-17-00	51918.16	4.15	–	–	$0.27^{+0.11}_{-0.04}$	$20.0^{+1.5}_{-3.5}$	$2.9^{+2.8}_{-1.5}$	$7.7^{+2.2}_{-0.8}$	0.9
50425-01-18-00	51926.69	4.45	–	–	$0.19^{+0.06}_{-0.03}$	$21.2^{+1.5}_{-1.9}$	$1.6^{+0.8}_{-0.4}$	$9.5^{+1.6}_{-1.5}$	1.7
50425-01-19-00	51930.28	4.84	–	–	$0.27^{+0.03}_{-0.06}$	$21.2^{+1.5}_{-1.4}$	$2.5^{+2.4}_{-1.0}$	$7.7^{+3.1}_{-1.6}$	0.8
50425-01-20-00	51932.33	4.93	–	–	$0.24^{+0.04}_{-0.05}$	$20.2^{+1.4}_{-0.9}$	$2.1^{+0.4}_{-0.3}$	$10.0^{+0.6}_{-0.8}$	2.4
50425-01-21-01	51941.68	6.14	–	–	$0.24^{+0.06}_{-0.03}$	$20.0^{+1.3}_{-1.3}$	$1.2^{+0.1}_{-0.1}$	$12.6^{+0.6}_{-2.5}$	1.7
50425-01-21-00	51941.75	6.34	–	–	$0.21^{+0.07}_{-0.03}$	$20.0^{+2.1}_{-1.9}$	$1.3^{+0.3}_{-0.2}$	$12.2^{+1.8}_{-1.6}$	1.9
50425-01-22-00	51943.74	6.70	–	–	$0.26^{+0.03}_{-0.05}$	$19.5^{+1.4}_{-0.8}$	$1.4^{+0.2}_{-0.2}$	$11.8^{+1.1}_{-1.6}$	1.6
50425-01-23-01	51943.80	6.67	–	–	$0.28^{+0.07}_{-0.04}$	$20.7^{+1.6}_{-1.3}$	$1.7^{+0.5}_{-0.5}$	$10.0^{+2.5}_{-1.4}$	1.5
50425-01-23-00	51948.12	6.92	–	–	$0.27^{+0.04}_{-0.06}$	$18.4^{+1.3}_{-0.7}$	$1.4^{+0.2}_{-0.1}$	$13.0^{+1.3}_{-0.9}$	1.5
50425-01-17-01	51950.18	7.08	–	–	$0.23^{+0.05}_{-0.04}$	$21.9^{+1.3}_{-1.5}$	$1.9^{+0.4}_{-0.4}$	$10.9^{+1.4}_{-1.1}$	1.3
50425-01-24-00	51952.03	6.76	–	–	$0.20^{+0.04}_{-0.06}$	$21.4^{+2.1}_{-2.1}$	$1.4^{+0.4}_{-0.3}$	$13.0^{+2.6}_{-1.6}$	1.9
50425-01-25-00	51955.63	6.75	–	–	$0.20^{+0.08}_{-0.14}$	$20.0^{+3.4}_{-1.7}$	$1.3^{+0.5}_{-0.2}$	$13.8^{+4.6}_{-2.1}$	0.9
50425-01-26-00	51961.53	6.49	–	–	$0.35^{+0.24}_{-0.15}$	$19.0^{+2.2}_{-4.0}$	$1.4^{+1.1}_{-0.5}$	$10.5^{+4.1}_{-4.0}$	1.7
50425-01-27-00	51963.97	6.53	–	–	$0.27^{+0.08}_{-0.07}$	$19.5^{+1.9}_{-2.2}$	$1.4^{+0.6}_{-0.4}$	$12.2^{+2.4}_{-2.3}$	0.9
50425-01-28-00	51965.37	6.10	–	–	$0.31^{+0.14}_{-0.08}$	$18.4^{+1.7}_{-2.2}$	$1.5^{+0.6}_{-0.4}$	$10.9^{+2.8}_{-2.0}$	1.6
50425-01-29-00	51968.56	5.59	–	–	$0.24^{+0.04}_{-0.07}$	$20.5^{+1.6}_{-1.2}$	$1.4^{+0.3}_{-0.4}$	$10.5^{+2.9}_{-2.1}$	1.4

Continued on Next Page...

Table A.6 – Continued

Obs. ID	MJD	L_X (10^{37} erg s^{-1})	$\mathbf{L_b}$ ν_b (Hz)	$\mathbf{L_b}$ rms (%)	$\mathbf{L_l}$ ν_l (Hz)	$\mathbf{L_l}$ rms (%)	$\mathbf{L_u}$ ν_u (Hz)	$\mathbf{L_u}$ rms (%)	χ^2_r
60402-01-01-00	51970.21	5.78	–	–	$0.24^{+0.04}_{-0.09}$	$20.2^{+2.0}_{-2.8}$	$1.2^{+0.5}_{-0.4}$	$11.4^{+4.6}_{-2.2}$	1.2
60402-01-02-00	51972.19	5.55	–	–	$0.20^{+0.06}_{-0.03}$	$20.0^{+1.6}_{-2.6}$	$1.1^{+0.2}_{-0.1}$	$12.6^{+1.3}_{-1.5}$	1.2
60402-01-03-00	51974.58	5.13	–	–	$0.24^{+0.06}_{-0.05}$	$21.0^{+1.5}_{-1.8}$	$1.5^{+0.4}_{-0.4}$	$10.5^{+2.4}_{-1.8}$	1.1
60402-01-04-00	51976.24	5.23	–	–	$0.20^{+0.07}_{-0.05}$	$22.1^{+1.8}_{-1.5}$	$1.5^{+1.0}_{-0.6}$	$10.0^{+3.6}_{-1.8}$	1.1
60402-01-05-00	51978.23	5.20	–	–	$0.22^{+0.05}_{-0.05}$	$20.2^{+1.5}_{-1.5}$	$1.5^{+0.3}_{-0.3}$	$10.9^{+1.5}_{-1.4}$	1.6
60402-01-06-00	51980.74	4.86	–	–	$0.18^{+0.06}_{-0.04}$	$20.5^{+1.6}_{-1.6}$	$1.3^{+0.2}_{-0.3}$	$11.8^{+1.6}_{-1.5}$	1.8
60402-01-07-00	51983.86	4.48	–	–	$0.17^{+0.04}_{-0.02}$	$19.0^{+1.7}_{-1.7}$	$1.1^{+0.4}_{-0.2}$	$12.6^{+2.3}_{-2.1}$	1.8
60402-01-08-00	51984.86	4.32	–	–	$0.24^{+0.08}_{-0.06}$	$21.4^{+1.5}_{-1.2}$	$1.9^{+3.4}_{-1.0}$	$8.4^{+2.0}_{-1.8}$	1.6
60402-01-09-00	51986.58	4.27	$0.0032^{+0.0040}_{-0.0022}$	$15.2^{+5.6}_{-3.1}$	$0.33^{+0.06}_{-0.04}$	$20.2^{+1.1}_{-1.1}$	$2.6^{+1.3}_{-0.8}$	$8.4^{+1.4}_{-1.3}$	2.8
60402-01-10-00	51988.27	3.73	$0.0006^{+0.0048}_{-0.0006}$	$28.4^{+5.6}_{-11.7}$	$0.26^{+0.03}_{-0.04}$	$22.1^{+1.6}_{-1.2}$	–	–	0.9
60402-01-11-00	51990.12	3.60	$0.0114^{+0.0210}_{-0.0114}$	$12.3^{+2.6}_{-2.3}$	$0.16^{+0.16}_{-0.11}$	$20.0^{+3.6}_{-6.5}$	$0.8^{+1.4}_{-0.7}$	$11.5^{+8.2}_{-4.3}$	0.8
60402-01-12-00	51992.17	3.56	$0.0339^{+0.0297}_{-0.0198}$	$14.1^{+5.0}_{-3.6}$	$0.29^{+0.11}_{-0.10}$	$18.4^{+3.0}_{-2.2}$	–	–	1.7
60402-01-13-00	51994.23	3.22	$0.0054^{+0.0051}_{-0.0021}$	$14.2^{+2.7}_{-2.1}$	$0.18^{+0.06}_{-0.03}$	$22.0^{+1.4}_{-2.9}$	–	–	1.7
60402-01-14-00	51996.08	3.27	$0.0015^{+0.0041}_{-0.0015}$	$17.8^{+16.9}_{-5.8}$	$0.27^{+0.03}_{-0.04}$	$21.3^{+1.1}_{-10.7}$	–	–	1.4
60402-01-15-00	51998.14	2.99	$0.0009^{+0.0213}_{-0.0008}$	$8.9^{+1785.2}_{-3.3}$	$0.10^{+0.08}_{-0.04}$	$19.8^{+3.1}_{-1.6}$	$0.9^{+0.4}_{-0.3}$	$14.1^{+0.9}_{-1.3}$	1.8
60402-01-15-01	51999.06	2.80	$0.0092^{+0.0149}_{-0.0065}$	$9.7^{+1.6}_{-1.9}$	$0.17^{+0.06}_{-0.03}$	$22.0^{+1.8}_{-1.9}$	–	–	0.8
60402-01-16-01	51999.98	2.72	$0.0070^{+0.0037}_{-0.0043}$	$15.8^{+4.3}_{-1.9}$	$0.22^{+0.05}_{-0.08}$	$19.9^{+2.2}_{-1.4}$	$2.9^{+3.1}_{-1.6}$	$7.7^{+8.1}_{-1.8}$	1.4
60402-01-16-00	52000.06	2.73	$0.0134^{+0.0271}_{-0.0134}$	$9.1^{+4.6}_{-1.4}$	$0.22^{+0.07}_{-0.22}$	$19.9^{+1.2}_{-10.0}$	$1.8^{+1.8}_{-1.8}$	$5.0^{+48.1}_{-2.5}$	1.4
60402-01-16-02	52001.05	2.74	$0.0007^{+0.0034}_{-0.0007}$	$26.8^{+4.6}_{-2.3}$	$0.28^{+0.08}_{-0.03}$	$21.3^{+1.0}_{-1.4}$	–	–	2.4
60402-01-17-00	52002.04	2.62	$0.0037^{+0.0024}_{-0.0017}$	$11.9^{+2.3}_{-1.8}$	$0.24^{+0.08}_{-0.05}$	$20.4^{+1.8}_{-2.0}$	–	–	1.9
60402-01-18-00	52004.38	2.43	$0.0207^{+0.0120}_{-0.0065}$	$37.2^{+4.4}_{-5.3}$	$0.36^{+0.19}_{-0.15}$	$17.1^{+4.4}_{-2.3}$	–	–	1.1
60402-01-19-00	52006.09	2.28	$0.0010^{+0.0039}_{-0.0010}$	$15.8^{+8.6}_{-5.0}$	$0.19^{+0.03}_{-0.03}$	$21.6^{+1.2}_{-1.2}$	–	–	1.2
60402-01-20-00	52008.21	2.14	$0.0001^{+0.0018}_{-0.0001}$	$59.9^{+285.7}_{-19.0}$	$0.19^{+0.03}_{-0.02}$	$22.5^{+1.1}_{-0.8}$	–	–	1.3
60402-01-22-00	52014.39	1.93	$0.0065^{+0.0063}_{-0.0036}$	$12.0^{+2.1}_{-2.2}$	$0.19^{+0.04}_{-0.04}$	$19.2^{+1.6}_{-1.2}$	–	–	2.2
60402-01-23-00	52016.37	1.76	$0.0024^{+0.0033}_{-0.0023}$	$14.0^{+25.9}_{-3.5}$	$0.21^{+0.06}_{-0.04}$	$20.3^{+1.6}_{-1.7}$	–	–	1.1
60402-01-24-00	52017.63	1.72	$0.0253^{+0.0420}_{-0.0184}$	$12.5^{+2.1}_{-1.9}$	$0.19^{+0.17}_{-0.06}$	$20.5^{+3.5}_{-5.7}$	–	–	0.7
60402-01-25-00	52021.06	1.51	$0.0012^{+0.0150}_{-0.0146}$	$16.6^{+1.6}_{-1.5}$	$0.14^{+0.03}_{-0.02}$	$21.3^{+1.3}_{-1.8}$	–	–	1.0
60402-01-26-00	52023.59	1.36	$0.0026^{+0.0140}_{-0.0019}$	$9.0^{+43.2}_{-2.7}$	$0.14^{+0.03}_{-0.04}$	$21.3^{+1.5}_{-1.7}$	–	–	1.1
60402-01-27-00	52024.32	1.30	$0.0001^{+0.3672}_{-0.0001}$	$22.5^{+149.8}_{-11.2}$	$0.17^{+0.05}_{-0.03}$	$18.8^{+1.5}_{-1.8}$	–	–	1.2
60402-01-29-00	52028.23	1.07	$0.0371^{+0.0175}_{-0.0130}$	$14.9^{+1.4}_{-2.8}$	$0.27^{+0.16}_{-0.09}$	$16.5^{+3.3}_{-2.9}$	–	–	1.0
60402-01-30-00	52029.83	1.00	$0.0029^{+0.0096}_{-0.0012}$	$10.9^{+5.8}_{-2.6}$	$0.13^{+0.03}_{-0.02}$	$21.8^{+1.2}_{-2.0}$	–	–	1.1
60402-01-31-00	52032.93	0.78	$0.0109^{+0.0073}_{-0.0047}$	$13.8^{+1.5}_{-1.6}$	$0.18^{+0.16}_{-0.05}$	$19.6^{+2.5}_{-3.0}$	–	–	1.0
60402-01-32-00	52034.92	0.67	$0.0179^{+0.0217}_{-0.0102}$	$11.9^{+1.9}_{-2.0}$	$0.18^{+0.12}_{-0.06}$	$19.4^{+3.1}_{-3.5}$	–	–	0.9

Continued on Next Page...

Table A.6 – Continued

Obs. ID	MJD	L_X (10^{37} erg s^{-1})	$\mathbf{L_b}$ ν_b (Hz)	$\mathbf{L_b}$ rms (%)	$\mathbf{L_l}$ ν_l (Hz)	$\mathbf{L_l}$ rms (%)	$\mathbf{L_u}$ ν_u (Hz)	$\mathbf{L_u}$ rms (%)	χ^2_r
60402-01-33-00	52035.72	0.63	$0.0104^{+0.0124}_{-0.0066}$	$11.1^{+2.3}_{-2.5}$	$0.12^{+0.06}_{-0.06}$	$18.7^{+2.7}_{-3.4}$	–	–	1.9
60402-01-34-00	52038.70	0.48	$0.0008^{+1.4742}_{-0.0007}$	$16.2^{+13.4}_{-4.0}$	$0.04^{+0.75}_{-0.04}$	$23.3^{+2.6}_{-11.3}$	–	–	1.7
60402-01-35-00	52040.69	0.40	$0.0589^{+0.0589}_{-0.0589}$	$27.7^{+3.0}_{-13.8}$	$0.14^{+0.29}_{-0.29}$	$67.4^{+51.0}_{-3.8}$	–	–	1.2
60402-01-36-00	52041.55	0.36	–	–	$0.08^{+0.02}_{-0.02}$	$26.3^{+2.7}_{-2.9}$	–	–	1.9
60402-01-37-00	52044.08	0.32	–	–	$0.05^{+0.02}_{-0.02}$	$25.8^{+3.1}_{-2.9}$	–	–	1.6
60402-01-38-01	52046.99	0.26	–	–	$0.06^{+0.02}_{-0.02}$	$28.4^{+3.0}_{-3.1}$	–	–	1.4
60402-01-38-00	52047.06	0.24	–	–	$0.09^{+0.03}_{-0.03}$	$26.5^{+3.3}_{-3.4}$	–	–	1.0
60402-01-39-00	52050.11	0.19	–	–	$0.04^{+0.01}_{-0.01}$	$31.1^{+3.1}_{-2.8}$	–	–	2.0
60402-01-39-01	52050.18	0.18	–	–	$0.06^{+0.01}_{-0.01}$	$35.9^{+3.2}_{-3.1}$	–	–	4.5
60402-01-40-00	52052.95	0.16	–	–	$0.06^{+0.01}_{-0.01}$	$41.1^{+3.5}_{-3.9}$	–	–	1.8
60402-01-41-00	52055.82	0.14	–	–	$0.04^{+0.01}_{-0.01}$	$38.0^{+3.9}_{-3.8}$	–	–	2.2
60402-01-41-01	52056.21	0.14	–	–	$0.05^{+0.01}_{-0.01}$	$47.7^{+2.9}_{-3.8}$	–	–	1.5
60402-01-42-00	52057.87	0.13	–	–	$0.04^{+0.01}_{-0.01}$	$52.1^{+3.9}_{-4.1}$	–	–	1.6
60402-01-43-00	52060.31	0.11	–	–	$0.04^{+0.01}_{-0.01}$	$50.2^{+3.6}_{-3.5}$	–	–	2.1
60402-01-44-00	52062.68	0.11	–	–	$0.04^{+0.01}_{-0.01}$	$57.8^{+3.0}_{-2.9}$	–	–	1.3
60402-01-44-01	52062.82	0.10	–	–	$0.04^{+0.01}_{-0.01}$	$57.2^{+5.0}_{-4.8}$	–	–	1.9
60402-01-44-02	52062.89	0.09	–	–	$0.05^{+0.01}_{-0.01}$	$65.7^{+3.9}_{-4.0}$	–	–	1.9
60402-01-45-00	52078.05	0.06	–	–	$0.03^{+0.01}_{-0.01}$	$62.7^{+4.6}_{-4.8}$	–	–	1.7

Table A.7: Power spectral fit parameters obtained for the EXO 2030+375 outburst.

Obs. ID	MJD	L_X (10^{37} erg s^{-1})	$\mathbf{L_l}$ ν_l (Hz)	$\mathbf{L_l}$ rms (%)	$\mathbf{L_u}$ ν_u (Hz)	$\mathbf{L_u}$ rms (%)	$\mathbf{L_{u'}}$ $\nu_{u'}$ (Hz)	$\mathbf{L_{u'}}$ rms (%)	χ^2_r
91089-01-07-00	53914.89	9.21	$0.135^{+0.035}_{-0.026}$	36±2	$0.99^{+0.17}_{-0.14}$	$19.9^{+2.4}_{-2.1}$	–	–	1.8
91089-01-07-01	53915.83	9.17	$0.198^{+0.053}_{-0.041}$	32±2	$1.34^{+0.38}_{-0.28}$	$16.4^{+3.0}_{-2.4}$	–	–	1.3
91089-01-08-00	53916.81	9.93	$0.130^{+0.052}_{-0.031}$	36±3	$1.23^{+0.28}_{-0.22}$	$18.8^{+2.4}_{-2.1}$	–	–	1.9
91089-01-08-01	53917.76	9.99	$0.161^{+0.038}_{-0.029}$	32±2	$0.87^{+0.14}_{-0.11}$	$21.0^{+2.3}_{-2.3}$	–	–	1.3
91089-01-08-02	53918.50	10.49	$0.110^{+0.026}_{-0.021}$	38±3	$1.10^{+0.24}_{-0.19}$	$18.5^{+2.4}_{-2.0}$	–	–	1.5
91089-01-08-03	53919.61	10.90	$0.160^{+0.041}_{-0.033}$	34±2	$0.93^{+0.17}_{-0.13}$	$20.9^{+2.8}_{-2.5}$	–	–	1.8
91089-01-08-06	53920.71	10.95	$0.178^{+0.056}_{-0.039}$	33±2	$1.01^{+0.26}_{-0.16}$	$18.9^{+2.8}_{-2.9}$	–	–	2.2
91089-01-08-04	53921.07	10.67	$0.160^{+0.031}_{-0.028}$	34±2	$1.16^{+0.33}_{-0.25}$	$18.7^{+3.2}_{-2.4}$	–	–	2.2
91089-01-08-05	53922.28	10.80	$0.242^{+0.034}_{-0.026}$	36±1	$2.45^{+0.43}_{-0.38}$	$9.3^{+2.1}_{-1.5}$	–	–	1.9
91089-01-09-00	53923.33	11.21	$0.176^{+0.036}_{-0.026}$	36±2	$1.46^{+0.23}_{-0.16}$	$15.5^{+2.2}_{-2.4}$	–	–	1.3
91089-01-09-01	53924.70	11.55	$0.320^{+0.036}_{-0.043}$	34±1	$2.68^{+0.30}_{-0.55}$	$8.0^{+2.4}_{-1.0}$	–	–	2.1
91089-01-09-03	53926.63	11.88	$0.241^{+0.022}_{-0.026}$	36±1	$2.21^{+0.23}_{-0.32}$	$10.6^{+2.4}_{-1.1}$	–	–	1.7
91089-01-09-04	53928.18	12.43	$0.241^{+0.072}_{-0.046}$	35^{+3}_{-4}	$1.33^{+1.56}_{-0.42}$	$14.9^{+5.4}_{-6.2}$	–	–	1.7
91089-01-09-07	53928.32	11.69	$0.309^{+0.043}_{-0.040}$	35±1	$2.93^{+0.62}_{-0.92}$	$7.5^{+3.4}_{-1.5}$	–	–	1.3
91089-01-09-05	53928.64	11.40	$0.292^{+0.032}_{-0.034}$	37±1	$3.21^{+0.51}_{-0.95}$	$6.7^{+3.0}_{-1.1}$	–	–	1.8
91089-01-09-06	53929.61	12.59	$0.341^{+0.037}_{-0.045}$	37±1	$3.05^{+0.38}_{-0.55}$	$9.5^{+2.7}_{-1.2}$	–	–	1.6
91089-01-10-00	53930.79	13.01	$0.269^{+0.040}_{-0.037}$	38^{+1}_{-2}	$1.88^{+0.32}_{-0.29}$	$14.9^{+3.6}_{-2.4}$	–	–	1.4
91089-01-10-01	53931.39	12.94	$0.338^{+0.050}_{-0.064}$	37±1	$2.80^{+0.56}_{-0.74}$	$9.6^{+5.8}_{-1.9}$	–	–	3.0
91089-01-10-02	53932.24	13.35	$0.334^{+0.039}_{-0.046}$	37±1	$2.97^{+0.66}_{-0.79}$	$8.5^{+5.3}_{-1.7}$	–	–	1.9
91089-01-10-03	53933.36	13.75	$0.425^{+0.035}_{-0.032}$	39±1	$4.18^{+0.59}_{-0.77}$	$5.5^{+1.5}_{-1.0}$	–	–	2.3
91089-01-10-04	53934.26	13.36	$0.282^{+0.033}_{-0.034}$	38±1	$2.20^{+0.32}_{-0.36}$	$12.3^{+3.3}_{-1.8}$	–	–	1.6
91089-01-10-05	53935.18	13.48	$0.301^{+0.031}_{-0.033}$	37±1	$2.91^{+0.54}_{-0.58}$	$9.9^{+3.0}_{-1.6}$	–	–	1.4
91089-01-10-06	53936.30	13.85	$0.411^{+0.030}_{-0.032}$	41±1	$4.08^{+0.47}_{-0.73}$	$6.7^{+1.7}_{-0.9}$	–	–	2.1
91089-01-11-00	53937.35	13.92	$0.318^{+0.031}_{-0.032}$	37±1	$2.97^{+0.40}_{-0.48}$	$9.9^{+2.3}_{-1.2}$	–	–	1.5
91089-01-11-01	53938.17	12.19	$0.291^{+0.043}_{-0.046}$	37^{+1}_{-2}	$2.68^{+0.51}_{-0.56}$	$10.3^{+3.6}_{-1.7}$	–	–	1.5
91089-01-11-02	53938.43	13.12	$0.317^{+0.046}_{-0.046}$	37±1	$3.33^{+0.70}_{-0.86}$	$9.7^{+4.3}_{-1.8}$	–	–	1.6
91089-01-11-03	53939.25	13.85	$0.274^{+0.037}_{-0.033}$	38±1	$2.87^{+0.36}_{-0.39}$	$10.3^{+1.7}_{-1.2}$	–	–	1.9
91089-01-11-04	53940.13	12.18	$0.335^{+0.032}_{-0.032}$	37±1	$3.22^{+0.36}_{-0.41}$	$9.0^{+1.5}_{-1.0}$	–	–	1.9
91089-01-11-05	53941.44	14.73	$0.282^{+0.036}_{-0.031}$	38±1	$5.84^{+0.86}_{-1.50}$	$5.1^{+3.6}_{-1.4}$	$2.25^{+0.44}_{-0.67}$	$9.0^{+2.6}_{-3.0}$	1.5
91089-01-12-00	53944.05	11.91	$0.288^{+0.038}_{-0.035}$	37±1	$4.58^{+1.29}_{-1.03}$	$8.5^{+2.8}_{-2.7}$	–	–	1.4
91089-01-12-01	53944.97	12.53	$0.364^{+0.032}_{-0.034}$	36±1	$2.40^{+0.46}_{-0.57}$	$6.8^{+3.0}_{-1.7}$	$5.83^{+0.52}_{-0.57}$	6.8±1.0	2.2
91089-01-12-02	53945.95	13.51	$0.426^{+0.038}_{-0.034}$	36±1	$4.12^{+2.02}_{-0.72}$	$8.0^{+4.0}_{-0.1}$	–	–	1.7

Continued on Next Page...

Table A.7 – Continued

Obs. ID	MJD	L_X (10^{37} erg s^{-1})	$\mathbf{L_l}$ ν_l (Hz)	$\mathbf{L_l}$ rms (%)	$\mathbf{L_u}$ ν_u (Hz)	$\mathbf{L_u}$ rms (%)	$\mathbf{L_{u'}}$ $\nu_{u'}$ (Hz)	$\mathbf{L_{u'}}$ rms (%)	χ^2_r
91089-01-12-03	53946.86	12.79	$0.375^{+0.034}_{-0.019}$	37±1	$0.01^{+0.01}_{-0.01}$	$7.6^{+2.0}_{-0.1}$	$3.75^{+0.34}_{-0.32}$	$8.6^{+0.4}_{-0.3}$	1.0
91089-01-12-05	53947.71	13.42	$0.366^{+0.040}_{-0.038}$	36±1	$2.63^{+0.73}_{-1.20}$	$7.3^{+4.8}_{-2.1}$	–	–	2.2
91089-01-12-04	53948.82	13.43	$0.348^{+0.039}_{-0.024}$	35±1	$1.95^{+0.45}_{-0.35}$	$9.3^{+2.7}_{-1.5}$	–	–	3.2
91089-01-12-06	53949.80	12.90	$0.323^{+0.033}_{-0.038}$	36±1	$2.11^{+0.56}_{-0.79}$	$6.6^{+8.7}_{-2.7}$	$4.52^{+1.62}_{-0.87}$	$7.8^{+2.5}_{-3.4}$	1.0
91089-01-12-07	53950.92	12.87	$0.343^{+0.029}_{-0.023}$	30±1	$2.26^{+0.11}_{-0.10}$	$7.8^{+2.5}_{-3.4}$	$7.02^{+0.54}_{-0.61}$	$3.7^{+0.4}_{-0.3}$	2.0
91089-01-13-01	53952.82	13.48	$0.27^{+0.08}_{-0.08}$	$26.1^{+8.1}_{-5.9}$	$0.97^{+0.36}_{-0.40}$	22±6	$4.06^{+0.79}_{-1.01}$	$7.0^{+4.5}_{-1.8}$	2.4
91089-01-13-02	53953.73	12.54	$0.357^{+0.030}_{-0.026}$	30±1	$2.50^{+0.15}_{-0.17}$	$21.6^{+6.0}_{-6.3}$	$7.94^{+0.73}_{-0.79}$	$2.8^{+0.3}_{-0.3}$	1.7
91089-01-14-06	53958.60	13.20	$0.374^{+0.048}_{-0.041}$	36±1	$3.19^{+0.55}_{-0.55}$	$8.9^{+1.3}_{-1.5}$	–	–	1.1
91089-01-14-00	53959.82	13.32	$0.340^{+0.051}_{-0.044}$	34±1	$3.29^{+0.88}_{-0.59}$	$9.8^{+1.9}_{-2.5}$	–	–	1.3
91089-01-14-01	53960.60	12.96	$0.389^{+0.057}_{-0.072}$	30±5	$2.29^{+0.48}_{-0.33}$	$13.8^{+3.8}_{-3.4}$	–	–	1.8
91089-01-14-02	53961.93	13.27	$0.373^{+0.044}_{-0.044}$	36±1	$3.31^{+0.56}_{-0.76}$	$6.7^{+2.2}_{-1.7}$	$7.70^{+1.39}_{-1.81}$	$3.2^{+2.2}_{-1.0}$	1.2
91089-01-14-03	53962.50	13.31	$0.431^{+0.034}_{-0.035}$	35±1	$3.65^{+0.42}_{-0.47}$	$5.4^{+2.9}_{-1.5}$	$7.05^{+1.10}_{-1.21}$	$3.7^{+1.5}_{-1.5}$	1.1
91089-01-14-04	53963.68	13.80	$0.348^{+0.038}_{-0.038}$	36±1	$2.93^{+0.31}_{-1.60}$	$11.1^{+1.7}_{-0.8}$	–	–	0.9
91089-01-14-05	53964.55	14.21	$0.336^{+0.043}_{-0.043}$	37±1	$2.73^{+0.57}_{-0.69}$	$11.1^{+2.7}_{-2.1}$	–	–	1.1
91089-01-15-00	53965.77	15.40	$0.355^{+0.041}_{-0.039}$	35±1	$2.70^{+0.52}_{-0.65}$	$7.3^{+3.1}_{-2.0}$	$6.20^{+0.97}_{-1.04}$	$4.8^{+1.7}_{-1.4}$	1.0
91089-01-15-01	53966.85	13.81	$0.379^{+0.049}_{-0.047}$	36±1	$2.88^{+0.61}_{-0.77}$	$8.2^{+3.3}_{-2.1}$	$7.66^{+1.03}_{-1.51}$	$3.8^{+1.8}_{-1.2}$	1.8
91089-01-15-02	53967.54	13.62	$0.276^{+0.036}_{-0.022}$	26±1	$1.06^{+0.09}_{-0.10}$	$3.8^{+1.8}_{-1.2}$	$3.45^{+0.41}_{-0.30}$	$13.3^{+1.1}_{-1.4}$	1.5
91089-01-15-03	53968.66	14.75	$0.263^{+0.027}_{-0.030}$	31±1	$1.11^{+0.09}_{-0.08}$	$2.0^{+1.8}_{-1.2}$	$4.00^{+0.32}_{-0.27}$	$10.5^{+1.3}_{-0.5}$	0.9
91089-01-15-04	53969.58	14.50	$0.362^{+0.033}_{-0.030}$	30±1	$1.64^{+0.15}_{-0.42}$	$4.0^{+1.8}_{-1.2}$	$5.08^{+0.45}_{-0.61}$	$6.5^{+2.3}_{-0.3}$	2.1
91089-01-15-05	53970.48	13.48	$0.323^{+0.023}_{-0.036}$	27±1	$1.11^{+0.12}_{-0.13}$	$2.0^{+1.8}_{-1.2}$	$3.55^{+0.25}_{-0.22}$	$11.8^{+0.4}_{-0.4}$	0.8
91089-01-15-06	53971.55	15.17	$0.291^{+0.026}_{-0.025}$	33±1	$1.78^{+0.18}_{-0.30}$	$1.0^{+1.8}_{-1.2}$	$4.88^{+0.46}_{-0.58}$	$6.2^{+1.8}_{-0.9}$	1.8
91089-01-16-00	53972.19	14.26	$0.318^{+0.035}_{-0.042}$	28±1	$1.27^{+0.10}_{-0.08}$	$5.0^{+1.8}_{-1.2}$	$4.34^{+0.25}_{-0.20}$	$9.1^{+0.2}_{-0.5}$	1.5
91089-01-16-01	53972.98	14.80	$0.408^{+0.028}_{-0.038}$	30±1	$2.82^{+0.16}_{-0.17}$	$3.3^{+1.8}_{-1.2}$	$8.04^{+0.39}_{-0.22}$	$2.0^{+0.4}_{-0.4}$	1.2
91089-01-16-02	53974.48	13.23	$0.352^{+0.025}_{-0.026}$	31^{+2}_{-1}	$2.25^{+0.30}_{-0.19}$	$4.5^{+1.8}_{-1.2}$	$6.10^{+1.32}_{-1.39}$	$4.4^{+1.5}_{-1.3}$	2.1
91089-01-16-03	53975.42	14.31	$0.369^{+0.035}_{-0.036}$	29±1	$2.22^{+0.20}_{-0.41}$	$4.1^{+1.8}_{-1.2}$	$6.13^{+0.55}_{-0.61}$	$4.4^{+0.4}_{-0.5}$	1.6
91089-01-16-04	53976.12	13.95	$0.350^{+0.028}_{-0.038}$	34^{+3}_{-1}	$1.71^{+0.51}_{-0.46}$	$4.0^{+1.8}_{-1.2}$	$5.80^{+1.16}_{-1.44}$	$5.5^{+1.2}_{-1.5}$	1.0
91089-01-16-05	53977.17	12.88	$0.324^{+0.042}_{-0.024}$	32±1	$1.71^{+0.17}_{-0.33}$	$4.2^{+1.8}_{-1.2}$	$4.75^{+0.35}_{-0.60}$	$6.7^{+2.2}_{-0.3}$	1.7
91089-01-16-06	53978.15	13.67	$0.377^{+0.036}_{-0.048}$	29±1	$1.93^{+0.16}_{-0.28}$	$4.0^{+1.8}_{-1.2}$	$5.85^{+0.67}_{-0.67}$	$5.3^{+1.7}_{-0.4}$	1.9
91089-01-17-00	53979.34	12.51	$0.345^{+0.036}_{-0.049}$	29±1	$1.85^{+0.15}_{-0.18}$	$3.8^{+1.8}_{-1.2}$	$5.61^{+0.49}_{-0.90}$	$6.1^{+1.7}_{-1.0}$	1.4
91089-01-17-01	53980.39	12.75	$0.289^{+0.038}_{-0.028}$	36±1	$1.85^{+0.38}_{-0.41}$	$3.5^{+1.8}_{-1.2}$	$5.53^{+1.13}_{-1.66}$	$4.5^{+3.1}_{-1.5}$	1.4
91089-01-17-02	53981.36	12.29	$0.397^{+0.036}_{-0.034}$	37±1	–	–	$3.49^{+0.50}_{-0.53}$	$8.6^{+1.7}_{-1.2}$	0.9
91089-01-17-03	53982.14	11.98	$0.367^{+0.037}_{-0.036}$	37±1	–	–	$3.63^{+0.64}_{-0.67}$	$8.3^{+2.0}_{-1.3}$	1.1
91089-01-17-04	53983.20	11.58	$0.435^{+0.040}_{-0.037}$	39±1	–	–	$5.29^{+0.91}_{-1.30}$	$5.0^{+1.8}_{-1.0}$	1.7

Continued on Next Page...

Table A.7 – Continued

Obs. ID	MJD	L_X (10^{37} erg s^{-1})	$\mathbf{L_l}$ ν_l (Hz)	rms (%)	$\mathbf{L_u}$ ν_u (Hz)	rms (%)	$\mathbf{L_{u'}}$ $\nu_{u'}$ (Hz)	rms (%)	χ^2_r
91089-01-17-05	53984.24	11.47	$0.433^{+0.039}_{-0.038}$	37 ± 1	–	–	$4.30^{+1.03}_{-1.09}$	$6.9^{+2.4}_{-1.4}$	1.7
91089-01-17-06	53985.22	11.46	$0.371^{+0.029}_{-0.028}$	37 ± 1	–	–	$3.36^{+0.39}_{-0.41}$	$9.2^{+1.4}_{-1.0}$	2.1
91089-01-18-01	53986.07	10.73	$0.382^{+0.035}_{-0.034}$	37 ± 1	–	–	$3.95^{+0.71}_{-0.73}$	$9.5^{+2.2}_{-1.4}$	1.4
91089-01-18-00	53986.99	10.57	$0.459^{+0.055}_{-0.051}$	36 ± 1	–	–	$3.76^{+0.63}_{-0.78}$	$6.2^{+2.0}_{-1.3}$	1.6
91089-01-18-02	53988.00	9.76	$0.416^{+0.060}_{-0.064}$	38 ± 1	–	–	$3.54^{+0.96}_{-1.14}$	$7.9^{+4.6}_{-2.0}$	1.2
91089-01-18-03	53989.16	9.57	$0.359^{+0.057}_{-0.053}$	34 ± 1	–	–	$3.26^{+0.76}_{-0.72}$	$10.4^{+3.7}_{-2.1}$	1.2
91089-01-18-04	53990.03	9.37	$0.327^{+0.051}_{-0.048}$	36 ± 1	–	–	$2.90^{+0.67}_{-0.64}$	$10.3^{+3.6}_{-2.0}$	1.2
91089-01-18-05	53991.12	9.45	$0.324^{+0.078}_{-0.078}$	34 ± 2	–	–	$2.12^{+0.54}_{-0.61}$	$14.7^{+7.9}_{-3.3}$	1.3
91089-01-18-06	53991.79	8.75	$0.374^{+0.064}_{-0.062}$	34^{+1}_{-2}	–	–	$2.30^{+0.58}_{-0.61}$	$12.5^{+6.0}_{-2.9}$	1.4
91089-01-19-00	53993.69	7.99	$0.391^{+0.048}_{-0.044}$	36 ± 1	–	–	$3.60^{+0.79}_{-1.02}$	$7.1^{+2.5}_{-1.5}$	1.8
91089-01-19-01	53995.01	7.78	$0.434^{+0.044}_{-0.044}$	36 ± 1	–	–	$4.67^{+1.54}_{-1.77}$	$6.2^{+4.1}_{-1.5}$	1.1
91089-01-19-02	53995.79	7.44	$0.396^{+0.042}_{-0.041}$	36 ± 1	–	–	$3.80^{+0.80}_{-0.93}$	$7.9^{+2.6}_{-1.4}$	2.1
91089-01-19-03	53997.04	7.65	$0.374^{+0.053}_{-0.054}$	35 ± 1	–	–	$3.45^{+1.05}_{-1.21}$	$8.6^{+6.8}_{-2.0}$	1.4
91089-01-19-04	53997.82	6.70	$0.342^{+0.052}_{-0.051}$	35 ± 1	–	–	$3.04^{+0.66}_{-0.60}$	$9.8^{+3.0}_{-1.8}$	1.3
91089-01-19-05	53998.66	6.15	$0.409^{+0.045}_{-0.046}$	36 ± 1	–	–	$4.38^{+1.13}_{-1.84}$	$6.5^{+3.7}_{-1.3}$	1.8
92067-01-04-10	53999.59	6.28	$0.484^{+0.058}_{-0.055}$	34 ± 1	–	–	$4.12^{+0.74}_{-0.93}$	$5.3^{+2.0}_{-1.2}$	1.4
92067-01-05-00	54000.62	5.94	$0.486^{+0.063}_{-0.071}$	35^{+1}_{-2}	–	–	$4.98^{+2.77}_{-2.64}$	$6.2^{+8.3}_{-2.0}$	1.8
92067-01-05-01	54002.01	5.22	$0.388^{+0.048}_{-0.052}$	35 ± 1	–	–	$4.22^{+1.60}_{-1.19}$	$7.7^{+4.5}_{-1.9}$	1.0
92067-01-05-02	54002.72	4.65	$0.283^{+0.077}_{-0.077}$	35 ± 2	–	–	$2.43^{+1.81}_{-1.04}$	$13.2^{+4.8}_{-4.6}$	1.1
92067-01-05-03	54003.57	5.21	$0.213^{+0.076}_{-0.050}$	32^{+3}_{-4}	–	–	$1.23^{+0.49}_{-0.32}$	$19.1^{+5.1}_{-4.9}$	0.9
92067-01-05-04	54004.44	5.13	$0.312^{+0.073}_{-0.070}$	33 ± 2	–	–	$3.03^{+0.91}_{-0.89}$	$10.6^{+7.2}_{-2.3}$	1.8
92067-01-05-05	54005.67	4.73	$0.364^{+0.086}_{-0.077}$	32 ± 2	–	–	$2.35^{+0.65}_{-0.71}$	$10.4^{+6.1}_{-2.6}$	1.3
92067-01-05-06	54006.58	5.05	$0.295^{+0.071}_{-0.059}$	34^{+2}_{-3}	–	–	$1.78^{+0.94}_{-0.67}$	$13.8^{+4.8}_{-4.5}$	1.4
92067-01-06-00	54007.56	4.41	$0.459^{+0.076}_{-0.081}$	33 ± 1	–	–	$4.08^{+1.20}_{-1.78}$	$7.0^{+5.1}_{-1.8}$	1.2
92067-01-06-01	54008.43	3.97	$0.202^{+0.161}_{-0.130}$	25^{+9}_{-7}	–	–	$1.02^{+0.44}_{-0.34}$	$22.2^{+8.9}_{-5.9}$	0.9
92067-01-06-02	54009.59	3.56	$0.310^{+0.083}_{-0.087}$	29^{+3}_{-6}	–	–	$1.84^{+0.85}_{-0.64}$	$14.8^{+6.2}_{-3.2}$	1.4
92067-01-06-03	54010.37	3.37	$0.231^{+0.071}_{-0.064}$	26^{+5}_{-4}	–	–	$1.59^{+0.51}_{-0.34}$	$19.3^{+3.1}_{-3.1}$	1.6
92067-01-06-04	54011.55	3.15	$0.182^{+0.065}_{-0.052}$	22^{+4}_{-3}	–	–	$0.99^{+0.37}_{-0.22}$	$23.4^{+3.0}_{-3.8}$	1.0
92067-01-06-05	54012.73	2.80	$0.162^{+0.097}_{-0.087}$	22^{+8}_{-4}	–	–	$0.99^{+0.93}_{-0.24}$	$22.8^{+2.7}_{-6.1}$	1.2
92067-01-06-06	54013.71	2.54	$0.167^{+0.042}_{-0.031}$	32 ± 4	–	–	$2.42^{+0.85}_{-0.60}$	$15.2^{+2.1}_{-1.8}$	2.5
92067-01-07-00	54014.63	2.36	$0.168^{+0.226}_{-0.114}$	31^{+3}_{-11}	–	–	$1.33^{+4.62}_{-1.00}$	$16.0^{+8.2}_{-5.9}$	1.4
92067-01-07-01	54015.44	2.07	$0.220^{+0.066}_{-0.068}$	24^{+6}_{-4}	–	–	$1.84^{+1.71}_{-0.69}$	$13.2^{+3.5}_{-3.0}$	1.6
92067-01-07-02	54016.59	2.00	$0.211^{+0.060}_{-0.048}$	30^{+3}_{-4}	–	–	$4.01^{+4.21}_{-2.51}$	$7.8^{+3.0}_{-1.5}$	1.1

Continued on Next Page...

Table A.7 – Continued

Obs. ID	MJD	L_X (10^{37} erg s^{-1})	$\mathbf{L_l}$ ν_l (Hz)	$\mathbf{L_l}$ rms (%)	$\mathbf{L_u}$ ν_u (Hz)	$\mathbf{L_u}$ rms (%)	$\mathbf{L_{u'}}$ $\nu_{u'}$ (Hz)	$\mathbf{L_{u'}}$ rms (%)	χ^2_r
92067-01-07-03	54017.47	1.77	$0.228^{+0.072}_{-0.066}$	26 ± 5	–	–	$2.04^{+2.12}_{-1.07}$	$10.1^{+5.5}_{-3.0}$	1.0
92067-01-07-04	54018.49	1.61	$0.312^{+0.080}_{-0.140}$	16^{+8}_{-4}	–	–	$1.79^{+2.47}_{-0.96}$	$15.0^{+4.0}_{-4.0}$	1.7
92067-01-07-05	54019.43	1.50	$0.142^{+0.046}_{-0.089}$	27^{+4}_{-6}	–	–	$1.71^{+1.60}_{-1.17}$	$11.0^{+9.2}_{-2.4}$	1.1
92067-01-07-06	54020.52	1.56	$0.102^{+0.051}_{-0.018}$	19^{+4}_{-6}	–	–	$0.25^{+0.18}_{-0.09}$	$19.5^{+11.5}_{-3.4}$	1.9
92067-01-08-00	54021.31	1.32	$0.108^{+0.034}_{-0.020}$	30 ± 3	–	–	–	–	0.8
92067-01-08-01	54022.31	1.17	$0.252^{+0.063}_{-0.053}$	22 ± 2	–	–	–	–	1.9
92067-01-08-02	54023.46	0.99	$0.127^{+0.035}_{-0.024}$	25 ± 2	–	–	–	–	2.1
92067-01-08-03	54024.58	0.94	$0.105^{+0.021}_{-0.017}$	26 ± 2	–	–	–	–	3.0
92067-01-08-04	54025.39	0.87	$0.116^{+0.062}_{-0.030}$	25 ± 3	–	–	–	–	2.2
92067-01-08-05	54026.42	0.74	$0.034^{+0.012}_{-0.012}$	32^{+6}_{-3}	–	–	–	–	1.9
92067-01-08-06	54027.65	0.67	$0.085^{+0.041}_{-0.024}$	27 ± 4	–	–	–	–	1.1
92067-01-09-01	54029.68	0.55	$0.142^{+0.093}_{-0.105}$	18^{+10}_{-2}	–	–	–	–	1.7
92067-01-09-02	54030.93	0.47	$0.052^{+0.033}_{-0.020}$	24 ± 3	–	–	–	–	2.4
92067-01-09-03	54031.78	0.48	$0.045^{+0.015}_{-0.011}$	25 ± 3	–	–	–	–	1.8
92067-01-09-04	54032.73	0.42	$0.053^{+0.033}_{-0.021}$	23^{+5}_{-4}	–	–	–	–	0.9
92067-01-09-06	54034.79	0.33	$0.028^{+0.023}_{-0.012}$	35^{+10}_{-7}	–	–	–	–	1.3
92067-01-10-00	54035.77	0.30	$0.018^{+0.028}_{-0.015}$	36^{+51}_{-10}	–	–	–	–	1.6
92067-01-10-01	54036.79	0.24	$0.051^{+0.030}_{-0.016}$	27^{+3}_{-4}	–	–	–	–	1.5
92067-01-10-02	54037.87	0.29	$0.031^{+0.015}_{-0.010}$	33 ± 5	–	–	–	–	1.2
92067-01-10-04	54039.87	0.24	$0.047^{+0.035}_{-0.024}$	30^{+10}_{-5}	–	–	–	–	0.8
92067-01-10-05	54040.88	0.30	$0.041^{+0.018}_{-0.012}$	24 ± 4	–	–	–	–	1.2
92067-01-10-06	54041.90	0.36	$0.126^{+0.058}_{-0.035}$	21 ± 3	–	–	–	–	1.4
92067-01-11-01	54043.72	0.44	$0.037^{+0.022}_{-0.017}$	27^{+8}_{-5}	–	–	–	–	1.0
92067-01-11-02	54044.98	0.49	$0.050^{+0.021}_{-0.016}$	25 ± 3	–	–	–	–	1.1

Table A.8: Power spectral fit parameters obtained for the 4U 0115+63 outburst.

Obs. ID	MJD	L_X	$\mathbf{L_b}$		$\mathbf{L_{LF}}$		$\mathbf{L_l}$		$\mathbf{L_u}$		χ^2_r
		(10^{37} erg s^{-1})	ν_b (Hz)	rms (%)	ν_{LF} (Hz)	rms (%)	ν_l (Hz)	rms (%)	ν_u (Hz)	rms (%)	
90089-01-01-00	53254.07	6.78	$0.007^{+0.000}_{-0.000}$	$6.9^{+3.4}_{-3.5}$	$0.068^{+0.020}_{-0.027}$	$15.7^{+1.8}_{-4.4}$	$0.96^{+0.23}_{-0.25}$	$11.6^{+4.3}_{-1.7}$	–	–	1.0
90089-01-02-00	53256.43	8.99	$0.005^{+0.012}_{-0.002}$	$27.6^{+5.0}_{-5.0}$	$0.123^{+0.059}_{-0.065}$	$14.2^{+2.1}_{-3.1}$	$1.06^{+0.30}_{-0.21}$	$10.7^{+1.5}_{-2.2}$	–	–	0.8
90089-01-03-01	53260.15	12.66	$0.003^{+0.002}_{-0.001}$	$27.7^{+6.7}_{-6.4}$	$0.155^{+0.032}_{-0.042}$	$12.8^{+1.2}_{-0.7}$	$1.12^{+0.40}_{-0.24}$	$10.1^{+2.9}_{-2.1}$	–	–	1.3
90089-01-03-03	53260.56	12.69	$0.001^{+0.002}_{-0.001}$	$64.0^{+20.2}_{-24.0}$	$0.104^{+0.034}_{-0.028}$	$10.9^{+0.9}_{-0.6}$	$0.73^{+0.17}_{-0.11}$	$14.0^{+1.4}_{-1.5}$	–	–	1.6
90089-01-03-00	53262.15	13.67	$0.001^{+0.002}_{-0.001}$	$122.7^{+30.8}_{-49.7}$	$0.050^{+0.011}_{-0.007}$	$5.7^{+0.7}_{-0.9}$	$1.21^{+0.09}_{-0.08}$	$22.6^{+0.7}_{-0.7}$	–	–	1.7
90089-01-04-06	53265.07	12.58	$0.002^{+0.001}_{-0.001}$	$121.8^{+88.1}_{-57.6}$	$0.035^{+0.007}_{-0.006}$	$15.6^{+0.9}_{-0.8}$	$0.62^{+0.04}_{-0.05}$	$14.9^{+0.6}_{-0.7}$	–	–	1.2
90089-01-04-01	53267.17	11.49	$0.013^{+0.036}_{-0.006}$	$5.1^{+1.1}_{-1.2}$	$0.045^{+0.050}_{-0.012}$	$10.8^{+0.9}_{-1.1}$	$0.57^{+0.06}_{-0.04}$	$16.7^{+0.7}_{-0.6}$	–	–	1.3
90089-01-04-02	53269.10	11.92	$0.002^{+0.001}_{-0.000}$	$21.1^{+5.3}_{-1.5}$	$0.034^{+0.006}_{-0.004}$	$12.0^{+0.5}_{-0.4}$	$0.55^{+0.15}_{-0.03}$	$16.0^{+0.6}_{-1.1}$	$0.8^{+0.1}_{-0.1}$	$12.6^{+0.7}_{-2.0}$	1.2
90089-01-04-00	53270.39	11.25	$0.002^{+0.000}_{-0.001}$	$18.4^{+2.2}_{-1.8}$	$0.040^{+0.008}_{-0.011}$	$12.0^{+1.2}_{-0.3}$	$0.60^{+0.02}_{-0.11}$	$15.0^{+0.5}_{-2.3}$	$1.1^{+0.1}_{-0.5}$	$10.0^{+5.3}_{-0.3}$	1.4
90089-01-04-03	53271.95	9.96	$0.002^{+0.000}_{-0.001}$	$12.9^{+3.0}_{-1.0}$	$0.068^{+0.012}_{-0.011}$	$14.0^{+0.6}_{-0.7}$	$0.69^{+0.13}_{-0.08}$	$14.0^{+5.6}_{-2.1}$	$1.3^{+0.4}_{-0.4}$	$9.6^{+1.8}_{-2.2}$	1.6
90089-01-05-00	53272.79	9.55	$0.003^{+0.003}_{-0.003}$	$14.2^{+6.3}_{-2.7}$	$0.063^{+0.007}_{-0.009}$	$9.0^{+1.2}_{-0.8}$	$0.52^{+0.13}_{-0.17}$	$15.6^{+1.1}_{-1.3}$	$2.1^{+1.0}_{-1.2}$	$4.2^{+7.1}_{-1.8}$	1.0
90089-01-05-05	53272.95	9.56	$0.008^{+0.005}_{-0.004}$	$9.5^{+1.1}_{-1.6}$	$0.083^{+0.060}_{-0.011}$	$8.9^{+0.7}_{-0.6}$	$0.52^{+0.07}_{-0.25}$	$14.6^{+0.8}_{-0.8}$	$2.1^{+0.4}_{-0.5}$	$4.8^{+4.6}_{-0.8}$	2.0
90089-01-05-01	53274.83	8.60	$0.003^{+0.001}_{-0.001}$	$13.8^{+1.5}_{-2.9}$	$0.065^{+0.007}_{-0.008}$	$8.7^{+0.5}_{-0.5}$	$0.36^{+0.06}_{-0.05}$	$12.1^{+0.7}_{-0.7}$	$1.5^{+0.2}_{-0.2}$	$7.7^{+0.7}_{-0.7}$	1.6
90089-01-05-02	53275.67	8.00	$0.002^{+0.001}_{-0.000}$	$15.2^{+1.6}_{-3.0}$	$0.064^{+0.007}_{-0.005}$	$8.8^{+0.5}_{-0.5}$	$0.36^{+0.04}_{-0.04}$	$13.8^{+0.9}_{-0.8}$	$1.3^{+0.2}_{-0.2}$	$8.3^{+1.0}_{-0.7}$	1.0
90089-01-05-03	53276.73	7.38	$0.002^{+0.004}_{-0.002}$	$15.6^{+45.6}_{-3.8}$	$0.057^{+0.008}_{-0.006}$	$8.7^{+0.7}_{-1.2}$	$0.35^{+0.26}_{-0.05}$	$14.6^{+1.2}_{-1.0}$	$1.6^{+1.2}_{-1.1}$	$6.8^{+0.8}_{-2.7}$	1.7
90089-01-05-04	53278.62	6.62	$0.003^{+0.003}_{-0.002}$	$16.9^{+13.2}_{-3.6}$	$0.062^{+0.007}_{-0.007}$	$8.0^{+0.6}_{-0.7}$	$0.40^{+0.11}_{-0.07}$	$14.7^{+0.8}_{-0.9}$	$2.0^{+0.6}_{-0.6}$	$5.3^{+1.7}_{-1.5}$	1.7
90089-01-06-00	53280.69	5.72	$0.001^{+0.002}_{-0.001}$	$70.9^{+17.1}_{-13.1}$	$0.062^{+0.011}_{-0.009}$	$8.0^{+1.0}_{-1.1}$	$0.56^{+0.08}_{-0.05}$	$15.0^{+0.6}_{-0.8}$	–	–	1.4
90014-02-01-02	53284.61	3.52	$-0.001^{+0.002}_{-0.001}$	$55.0^{+6.8}_{-8.1}$	$0.084^{+0.007}_{-0.010}$	$8.6^{+2.2}_{-1.9}$	$0.31^{+0.08}_{-0.06}$	$19.4^{+1.9}_{-1.8}$	–	–	1.3
90014-02-01-01	53285.98	2.86	$0.001^{+0.002}_{-0.001}$	$52.5^{+11.0}_{-10.5}$	$0.069^{+0.021}_{-0.066}$	$7.9^{+1.0}_{-1.1}$	$0.29^{+0.03}_{-0.03}$	$20.9^{+0.9}_{-0.8}$	–	–	1.3
90014-02-02-00	53287.81	2.35	$0.006^{+0.006}_{-0.004}$	$10.2^{+2.4}_{-2.2}$	–	–	$0.17^{+0.02}_{-0.01}$	$25.0^{+0.8}_{-0.9}$	–	–	1.2
90014-02-02-01	53289.52	1.89	$0.025^{+0.021}_{-0.012}$	$14.9^{+1.6}_{-2.6}$	–	–	$0.19^{+0.04}_{-0.03}$	$23.4^{+1.8}_{-2.5}$	–	–	1.3
90014-02-02-02	53290.64	1.49	$0.009^{+0.023}_{-0.009}$	$8.8^{+2.1}_{-3.1}$	–	–	$0.15^{+0.02}_{-0.01}$	$30.3^{+1.2}_{-1.1}$	–	–	1.1
90014-02-02-03	53291.81	1.15	$0.010^{+0.003}_{-0.002}$	$20.3^{+2.0}_{-1.8}$	–	–	$0.21^{+0.02}_{-0.02}$	$26.1^{+0.9}_{-0.9}$	–	–	1.5
90014-02-03-00	53293.44	0.71	$0.012^{+0.003}_{-0.003}$	$30.8^{+2.4}_{-2.5}$	–	–	$0.20^{+0.02}_{-0.01}$	$29.3^{+1.2}_{-1.2}$	–	–	1.0
90014-02-03-01	53295.68	0.32	$0.007^{+0.001}_{-0.002}$	$36.0^{+2.8}_{-3.0}$	–	–	$0.18^{+0.01}_{-0.01}$	$31.0^{+1.4}_{-0.9}$	–	–	1.3
90014-02-03-02	53297.60	0.16	$0.001^{+0.001}_{-0.001}$	$139.3^{+69.9}_{-44.2}$	–	–	$0.20^{+0.02}_{-0.02}$	$29.3^{+1.5}_{-2.1}$	–	–	1.7

Table A.9: Power spectral fit parameters obtained for the V 0332+53 outburst.

Obs. ID	MJD	L_X	$\mathbf{L_b}$		$\mathbf{L_{LF}}$		$\mathbf{L_s}$		$\mathbf{L_l}$		χ^2_r
		(10^{37} erg s^{-1})	ν_b (Hz)	rms (%)	ν_{LF} (Hz)	rms (%)	ν_s (Hz)	rms (%)	ν_l (Hz)	rms (%)	
90089-11-01-02	53340.29	11.00	$0.0001^{+0.0006}_{-0.0001}$	$70.0^{+29.3}_{-34.9}$	$0.045^{+0.008}_{-0.005}$	$6.3^{+0.5}_{-0.6}$	–	–	$0.26^{+0.01}_{-0.01}$	$16.4^{+0.3}_{-0.3}$	1.4
90089-11-01-03	53341.14	12.50	$0.0001^{+0.0001}_{-0.0001}$	$295.2^{+113.4}_{-108.2}$	$0.046^{+0.006}_{-0.005}$	$5.0^{+0.5}_{-0.5}$	–	–	$0.26^{+0.01}_{-0.01}$	$15.8^{+0.2}_{-0.2}$	1.5
90089-11-01-04	53341.80	13.30	$0.0003^{+0.0021}_{-0.0003}$	$12.9^{+6.6}_{-5.5}$	$0.042^{+0.040}_{-0.020}$	$4.0^{+2.1}_{-1.0}$	–	–	$0.25^{+0.01}_{-0.01}$	$15.0^{+0.5}_{-0.3}$	1.0
90089-11-02-00	53342.79	14.10	$0.0032^{+0.0010}_{-0.0009}$	$7.2^{+1.2}_{-0.9}$	$0.050^{+0.004}_{-0.005}$	$4.7^{+0.7}_{-0.3}$	$0.22^{+0.01}_{-0.01}$	$5.0^{+0.8}_{-0.3}$	$0.38^{+0.01}_{-0.02}$	$12.0^{+0.1}_{-0.3}$	1.5
90089-11-02-05	53343.04	13.80	$0.0018^{+0.0158}_{-0.0011}$	$8.6^{+3.8}_{-2.2}$	$0.065^{+0.046}_{-0.016}$	$5.9^{+6.0}_{-0.8}$	$0.23^{+0.02}_{-0.02}$	$6.0^{+1.1}_{-0.6}$	$0.48^{+0.05}_{-0.07}$	$10.5^{+1.3}_{-1.3}$	1.4
90089-11-02-06	53343.11	14.40	$0.0002^{+0.0078}_{-0.0001}$	$18.7^{+10.5}_{-7.6}$	$0.054^{+0.010}_{-0.019}$	$3.4^{+0.5}_{-0.7}$	$0.21^{+0.02}_{-0.03}$	$3.1^{+1.0}_{-0.5}$	$0.31^{+0.06}_{-0.06}$	$13.3^{+0.2}_{-0.2}$	1.3
90089-11-02-01	53343.24	14.40	$0.0004^{+0.0002}_{-0.0003}$	$16.9^{+5.2}_{-7.4}$	$0.049^{+0.004}_{-0.005}$	$3.3^{+0.4}_{-0.5}$	$0.21^{+0.03}_{-0.03}$	$4.3^{+1.0}_{-0.9}$	$0.29^{+0.04}_{-0.01}$	$13.7^{+0.4}_{-0.3}$	1.4
90089-11-02-02	53343.39	14.90	$0.0033^{+0.0022}_{-0.0016}$	$6.5^{+1.9}_{-1.3}$	$0.058^{+0.007}_{-0.006}$	$4.3^{+0.5}_{-0.7}$	$0.22^{+0.02}_{-0.01}$	$7.4^{+0.8}_{-1.1}$	$0.59^{+0.13}_{-0.07}$	$9.6^{+1.2}_{-0.3}$	1.4
90089-11-02-03	53343.76	15.00	$0.0014^{+0.0005}_{-0.0005}$	$9.7^{+4.0}_{-1.9}$	$0.046^{+0.005}_{-0.005}$	$6.6^{+0.4}_{-0.2}$	$0.22^{+0.02}_{-0.01}$	$5.7^{+0.3}_{-0.3}$	$0.43^{+0.02}_{-0.02}$	$10.9^{+0.1}_{-0.3}$	1.8
90089-11-02-07	53344.02	15.10	$0.0036^{+0.0014}_{-0.0011}$	$7.7^{+1.9}_{-1.2}$	$0.041^{+0.003}_{-0.002}$	$3.3^{+0.3}_{-0.5}$	$0.22^{+0.02}_{-0.01}$	$7.5^{+0.4}_{-0.5}$	$0.57^{+0.06}_{-0.04}$	$9.6^{+0.3}_{-0.5}$	1.6
90089-11-02-04	53344.55	15.80	$0.0001^{+0.0001}_{-0.0001}$	$519.2^{+0.0}_{0.0}$	$0.041^{+0.004}_{-0.006}$	$5.2^{+0.4}_{-0.3}$	$0.24^{+0.04}_{-0.02}$	$7.3^{+0.5}_{-0.7}$	$0.48^{+0.04}_{-0.04}$	$9.7^{+0.3}_{-0.6}$	0.9
90089-11-02-10	53344.75	16.40	$0.0001^{+0.0004}_{-0.0001}$	$53.8^{+8.1}_{-18.3}$	$0.055^{+0.008}_{-0.021}$	$2.8^{+0.4}_{-0.4}$	$0.28^{+0.03}_{-0.02}$	$1.5^{+0.9}_{-0.5}$	$0.32^{+0.01}_{-0.02}$	$13.0^{+0.2}_{-0.2}$	1.5
90089-11-02-09	53345.73	17.70	$0.0001^{+0.0006}_{-0.0001}$	$53.1^{+14.3}_{-26.3}$	$0.058^{+0.021}_{-0.013}$	$5.9^{+1.6}_{-0.6}$	$0.28^{+0.11}_{-0.04}$	$1.9^{+2.7}_{-0.6}$	$0.34^{+0.05}_{-0.05}$	$11.9^{+0.6}_{-1.6}$	0.6
90089-11-02-08	53346.71	18.90	$0.0001^{+0.0006}_{-0.0001}$	$41.5^{+18.4}_{-33.7}$	$0.068^{+0.070}_{-0.042}$	$4.3^{+3.0}_{-0.9}$	$0.26^{+0.09}_{-0.07}$	$5.4^{+5.8}_{-2.0}$	$0.52^{+0.49}_{-0.19}$	$9.8^{+3.1}_{-4.6}$	1.0
90089-11-03-03	53352.77	27.00	$0.0021^{+0.0051}_{-0.0016}$	$3.5^{+3.0}_{-1.3}$	$0.043^{+0.041}_{-0.010}$	$3.2^{+0.3}_{-0.5}$	$0.24^{+0.01}_{-0.01}$	$6.8^{+0.7}_{-2.1}$	$0.51^{+0.04}_{-0.03}$	$11.9^{+0.7}_{-0.7}$	1.3
90089-11-03-04	53353.73	27.70	$0.0001^{+0.0001}_{-0.0001}$	$60.0^{+15.0}_{-26.0}$	$0.058^{+0.015}_{-0.013}$	$6.8^{+0.4}_{-0.4}$	$0.24^{+0.01}_{-0.01}$	$5.0^{+0.4}_{-0.5}$	$0.72^{+0.24}_{-0.04}$	$9.5^{+0.3}_{-1.2}$	1.2
90089-11-03-00	53354.51	29.20	$0.0001^{+0.0001}_{-0.0001}$	$15.3^{+6.6}_{-7.3}$	$0.047^{+0.007}_{-0.008}$	$7.8^{+0.4}_{-0.5}$	$0.23^{+0.01}_{-0.01}$	$6.2^{+1.4}_{-1.2}$	$0.71^{+0.12}_{-0.09}$	$10.1^{+0.9}_{-1.0}$	1.1
90089-11-03-01	53354.62	28.70	$0.0001^{+0.0001}_{-0.0001}$	$23.4^{+5.4}_{-5.0}$	$0.048^{+0.010}_{-0.007}$	$7.3^{+0.4}_{-0.4}$	$0.23^{+0.01}_{-0.01}$	$6.0^{+0.6}_{-1.4}$	$0.69^{+0.10}_{-0.07}$	$10.8^{+0.6}_{-1.0}$	1.1
90089-11-03-02	53354.86	28.00	$0.0001^{+0.0001}_{-0.0001}$	$20.3^{+10.3}_{-7.6}$	$0.033^{+0.015}_{-0.011}$	$7.4^{+0.5}_{-0.8}$	$0.23^{+0.01}_{-0.01}$	$5.8^{+1.5}_{-1.4}$	$0.64^{+0.13}_{-0.08}$	$11.1^{+0.9}_{-1.3}$	1.2
90089-11-03-05	53355.10	29.00	$0.0001^{+0.0001}_{-0.0001}$	$505.1^{+0.0}_{0.0}$	$0.035^{+0.003}_{-0.005}$	$3.3^{+0.3}_{-0.5}$	$0.30^{+0.15}_{-0.02}$	$10.5^{+0.5}_{-0.4}$	$1.20^{+0.12}_{-0.11}$	$6.6^{+1.6}_{-0.2}$	1.9
90089-11-04-00	53356.49	30.40	$0.0001^{+0.0001}_{-0.0001}$	$27.5^{+0.0}_{0.0}$	$0.087^{+0.051}_{-0.037}$	$8.8^{+2.2}_{-1.1}$	$0.25^{+0.08}_{-0.06}$	$5.1^{+6.8}_{-1.5}$	$0.86^{+0.14}_{-0.12}$	$9.9^{+1.2}_{-2.0}$	1.0
90089-11-04-01	53357.07	32.70	$0.0001^{+0.0001}_{-0.0001}$	$94.9^{+0.0}_{0.0}$	$0.047^{+0.036}_{-0.025}$	$6.5^{+1.6}_{-1.0}$	$0.23^{+0.03}_{-0.03}$	$6.2^{+1.7}_{-1.1}$	$1.13^{+0.21}_{-0.11}$	$9.1^{+2.0}_{-1.3}$	1.6
90089-11-04-02	53358.59	31.10	$0.0001^{+0.0001}_{-0.0001}$	$94.9^{+0.0}_{0.0}$	$0.088^{+0.028}_{-0.030}$	$8.4^{+0.9}_{-1.2}$	$0.24^{+0.02}_{-0.01}$	$6.1^{+1.4}_{-1.2}$	$1.09^{+0.17}_{-0.19}$	$9.6^{+1.8}_{-1.1}$	0.9
90089-11-04-04	53360.00	32.30	–	–	$0.044^{+0.011}_{-0.009}$	$8.1^{+0.6}_{-0.7}$	$0.26^{+0.04}_{-0.02}$	$5.1^{+1.4}_{-1.9}$	$0.93^{+0.20}_{-0.19}$	$9.8^{+2.2}_{-1.3}$	1.5
90089-11-04-05	53361.12	32.40	$0.0001^{+0.0067}_{-0.0061}$	$32.7^{+14.0}_{-15.7}$	$0.065^{+0.023}_{-0.021}$	$8.3^{+0.9}_{-1.1}$	$0.27^{+0.04}_{-0.02}$	$6.8^{+2.1}_{-1.0}$	$1.84^{+0.19}_{-0.21}$	$7.3^{+0.9}_{-0.6}$	0.9
90089-11-05-00	53363.23	33.00	$0.0001^{+0.0056}_{-0.0041}$	$24.4^{+4.7}_{-4.9}$	$0.071^{+0.022}_{-0.018}$	$8.4^{+0.7}_{-0.8}$	$0.25^{+0.02}_{-0.01}$	$6.3^{+1.2}_{-0.8}$	$1.94^{+0.16}_{-0.16}$	$6.5^{+0.5}_{-0.4}$	2.0
90089-11-05-01	53364.91	33.90	$0.0039^{+0.0050}_{-0.0039}$	$4.1^{+1.7}_{-1.0}$	$0.073^{+0.024}_{-0.008}$	$8.4^{+0.4}_{-0.4}$	$0.27^{+0.02}_{-0.01}$	$6.5^{+1.1}_{-0.9}$	$1.85^{+0.15}_{-0.10}$	$6.5^{+0.3}_{-0.3}$	2.2
90089-11-05-02	53365.91	32.90	$0.0001^{+0.0050}_{-0.0009}$	$35.6^{+7.1}_{-8.2}$	$0.056^{+0.017}_{-0.017}$	$7.3^{+0.7}_{-0.9}$	$0.25^{+0.02}_{-0.02}$	$6.7^{+1.3}_{-0.6}$	$1.79^{+0.18}_{-0.23}$	$6.6^{+0.7}_{-0.4}$	1.4
90427-01-01-00	53367.23	32.90	$0.0001^{+0.0050}_{-0.0029}$	$51.2^{+12.3}_{-11.8}$	$0.043^{+0.005}_{-0.009}$	$7.4^{+0.4}_{-0.4}$	$0.25^{+0.01}_{-0.01}$	$7.0^{+0.3}_{-0.3}$	$1.60^{+0.17}_{-0.09}$	$7.3^{+0.2}_{-0.5}$	1.4
90427-01-01-01	53368.24	32.40	$0.0001^{+0.0050}_{-0.0031}$	$57.3^{+13.1}_{-14.2}$	$0.064^{+0.045}_{-0.026}$	$8.0^{+1.6}_{-1.4}$	$0.27^{+0.06}_{-0.04}$	$7.4^{+3.2}_{-1.8}$	$1.88^{+0.19}_{-0.22}$	$6.4^{+0.6}_{-0.9}$	0.6
90427-01-01-02	53368.91	32.50	$0.0001^{+0.0050}_{-0.0037}$	$44.1^{+15.1}_{-16.2}$	$0.049^{+0.044}_{-0.025}$	$5.2^{+1.5}_{-1.3}$	$0.27^{+0.06}_{-0.03}$	$8.4^{+2.5}_{-1.4}$	$1.71^{+0.23}_{-0.27}$	$7.0^{+1.2}_{-1.0}$	1.8
90427-01-02-00	53374.03	30.20	–	–	$0.035^{+0.016}_{-0.021}$	$6.5^{+1.3}_{-1.2}$	$0.27^{+0.14}_{-0.09}$	$7.5^{+4.0}_{-2.6}$	$1.43^{+0.75}_{-0.40}$	$6.8^{+1.7}_{-2.4}$	1.0

Continued on Next Page...

Table A.9 – Continued

Obs. ID	MJD	L_X (10^{37} erg s^{-1})	$\mathbf{L_b}$ ν_b (Hz)	$\mathbf{L_b}$ rms (%)	$\mathbf{L_{LF}}$ ν_{LF} (Hz)	$\mathbf{L_{LF}}$ rms (%)	$\mathbf{L_s}$ ν_s (Hz)	$\mathbf{L_s}$ rms (%)	$\mathbf{L_l}$ ν_l (Hz)	$\mathbf{L_l}$ rms (%)	χ^2_r
90427-01-02-03	53376.64	28.70	–	–	$0.031^{+0.007}_{-0.004}$	$7.2^{+0.4}_{-0.4}$	$0.28^{+0.02}_{-0.02}$	$5.7^{+0.3}_{-0.5}$	$0.62^{+0.07}_{-0.03}$	$10.1^{+0.7}_{-0.7}$	1.1
90014-01-01-00	53378.42	28.40	–	–	$0.032^{+0.005}_{-0.008}$	$7.0^{+0.5}_{-0.3}$	$0.28^{+0.03}_{-0.03}$	$6.4^{+2.0}_{-0.5}$	$0.74^{+0.12}_{-0.33}$	$8.9^{+0.7}_{-1.1}$	1.6
90014-01-01-06	53378.60	27.50	$0.0001^{+0.0045}_{-0.0078}$	$34.1^{+5.6}_{-6.6}$	$0.053^{+0.766}_{-0.026}$	$4.6^{+1.5}_{-0.3}$	$0.25^{+0.02}_{-0.02}$	$6.0^{+1.3}_{-1.5}$	$0.68^{+0.16}_{-0.22}$	$10.0^{+0.4}_{-0.8}$	1.3
90014-01-01-07	53378.74	26.40	–	–	$0.026^{+0.018}_{-0.010}$	$5.4^{+0.5}_{-0.6}$	–	–	$0.37^{+0.02}_{-0.02}$	$12.7^{+0.7}_{-0.4}$	1.3
90014-01-01-02	53381.04	24.10	–	–	$0.064^{+0.088}_{-0.025}$	$5.3^{+5.1}_{-1.8}$	–	–	$0.32^{+0.04}_{-0.04}$	$14.2^{+1.1}_{-1.2}$	1.6
90014-01-01-01	53381.35	23.70	–	–	$0.051^{+0.015}_{-0.015}$	$10.7^{+1.0}_{-1.4}$	$0.28^{+0.10}_{-0.08}$	$5.4^{+7.5}_{-1.9}$	$0.50^{+0.37}_{-0.14}$	$10.8^{+2.3}_{-2.3}$	1.5
90014-01-02-03	53385.87	19.40	–	–	$0.029^{+0.010}_{-0.006}$	$3.9^{+0.3}_{-0.6}$	$0.23^{+0.02}_{-0.03}$	$6.6^{+0.8}_{-1.1}$	$0.44^{+0.05}_{-0.02}$	$14.1^{+0.4}_{-0.5}$	1.2
90014-01-02-00	53386.40	18.30	$0.0072^{+0.0019}_{-0.0026}$	$6.5^{+0.4}_{-0.5}$	$0.052^{+0.003}_{-0.003}$	$4.6^{+0.2}_{-0.3}$	$0.24^{+0.01}_{-0.01}$	$7.2^{+0.3}_{-0.3}$	$0.46^{+0.01}_{-0.01}$	$13.4^{+0.2}_{-0.1}$	2.4
90014-01-02-10	53387.12	18.30	$0.0001^{+0.0003}_{-0.0001}$	$31.0^{+58.5}_{-15.2}$	$0.047^{+0.008}_{-0.013}$	$5.3^{+0.9}_{-0.5}$	$0.24^{+0.02}_{-0.02}$	$7.8^{+1.1}_{-0.8}$	$0.49^{+0.03}_{-0.08}$	$13.2^{+1.4}_{-1.2}$	1.6
90014-01-02-08	53388.03	17.20	$0.0235^{+0.0572}_{-0.0060}$	$8.0^{+0.6}_{-1.0}$	$0.052^{+0.002}_{-0.008}$	$2.9^{+0.4}_{-0.4}$	$0.23^{+0.01}_{-0.01}$	$5.8^{+0.4}_{-0.5}$	$0.40^{+0.01}_{-0.02}$	$14.9^{+0.3}_{-0.2}$	1.6
90014-01-02-15	53389.08	16.90	$0.0116^{+0.0043}_{-0.0052}$	$6.4^{+0.7}_{-0.6}$	$0.049^{+0.007}_{-0.010}$	$5.1^{+0.4}_{-0.7}$	$0.23^{+0.01}_{-0.01}$	$7.6^{+1.0}_{-1.0}$	$0.45^{+0.03}_{-0.07}$	$13.5^{+0.4}_{-0.3}$	0.8
90014-01-02-13	53390.33	16.10	$0.0034^{+0.0011}_{-0.0011}$	$7.9^{+1.5}_{-1.0}$	$0.053^{+0.004}_{-0.004}$	$5.6^{+0.2}_{-0.2}$	$0.23^{+0.01}_{-0.01}$	$6.8^{+0.3}_{-0.5}$	$0.38^{+0.01}_{-0.01}$	$14.4^{+0.2}_{-1.3}$	2.5
90014-01-03-00	53391.32	15.50	$0.0013^{+0.0009}_{-0.0005}$	$9.7^{+3.0}_{-2.3}$	$0.053^{+0.003}_{-0.002}$	$5.4^{+0.2}_{-0.4}$	$0.24^{+0.01}_{-0.01}$	$6.9^{+0.6}_{-0.5}$	$0.39^{+0.02}_{-0.01}$	$14.4^{+0.3}_{-0.2}$	1.9
90014-01-03-01	53393.21	14.40	$0.0049^{+0.0030}_{-0.0033}$	$10.6^{+1.9}_{-1.7}$	$0.050^{+0.004}_{-0.004}$	$4.8^{+0.6}_{-0.5}$	$0.24^{+0.01}_{-0.01}$	$7.0^{+0.5}_{-0.5}$	$0.39^{+0.02}_{-0.02}$	$14.5^{+0.3}_{-0.3}$	1.1
90014-01-03-02	53394.59	14.10	$0.0001^{+0.0043}_{-0.0052}$	$45.8^{+6.9}_{-9.0}$	$0.068^{+0.026}_{-0.030}$	$6.8^{+3.0}_{-1.4}$	$0.26^{+0.05}_{-0.02}$	$5.2^{+2.2}_{-1.6}$	$0.37^{+0.09}_{-0.06}$	$15.0^{+1.5}_{-1.3}$	1.7
90014-01-03-03	53395.31	13.40	$0.0001^{+0.0043}_{-0.0052}$	$49.4^{+5.9}_{-5.5}$	$0.060^{+0.012}_{-0.010}$	$6.1^{+1.1}_{-1.2}$	$0.25^{+0.02}_{-0.01}$	$5.6^{+1.6}_{-0.9}$	$0.34^{+0.08}_{-0.03}$	$15.6^{+0.8}_{-1.3}$	1.7
90014-01-04-00	53398.46	11.70	$0.0001^{+0.0043}_{-0.0052}$	$42.4^{+6.0}_{-6.3}$	$0.050^{+0.021}_{-0.020}$	$4.9^{+0.4}_{-0.6}$	$0.21^{+0.06}_{-0.07}$	$15.2^{+1.3}_{-3.3}$	$0.40^{+0.05}_{-0.07}$	$9.0^{+2.4}_{-1.0}$	1.0
90014-01-04-01	53399.60	11.60	$0.0001^{+0.0001}_{-0.0001}$	$208.5^{+115.3}_{-103.1}$	$0.054^{+0.007}_{-0.011}$	$5.7^{+0.7}_{-0.5}$	–	–	$0.36^{+0.03}_{-0.03}$	$15.0^{+0.7}_{-0.6}$	1.2
90014-01-04-02	53401.37	10.60	$0.0001^{+0.0001}_{-0.0001}$	$123.2^{+35.9}_{-38.3}$	$0.057^{+0.013}_{-0.014}$	$7.9^{+2.3}_{-1.5}$	–	–	$0.32^{+0.04}_{-0.03}$	$15.3^{+1.7}_{-1.6}$	1.5
90014-01-04-03	53403.34	9.94	$0.0001^{+0.0043}_{-0.0052}$	$45.6^{+12.3}_{-14.8}$	$0.029^{+0.003}_{-0.004}$	$6.1^{+0.4}_{-1.4}$	$0.26^{+0.01}_{-0.01}$	$4.1^{+0.9}_{-1.0}$	$0.26^{+0.02}_{-0.02}$	$17.4^{+0.7}_{-0.5}$	1.3
90014-01-05-00	53405.24	9.94	$0.0117^{+0.0076}_{-0.0046}$	$8.8^{+1.3}_{-1.3}$	$0.062^{+0.006}_{-0.004}$	$4.8^{+0.9}_{-0.8}$	$0.21^{+0.02}_{-0.02}$	$8.2^{+0.9}_{-1.5}$	$0.41^{+0.04}_{-0.04}$	$13.6^{+0.5}_{-0.7}$	1.2
90014-01-05-01	53407.56	8.78	$0.0002^{+0.0011}_{-0.0001}$	$30.8^{+8.5}_{-14.0}$	$0.052^{+0.002}_{-0.002}$	$9.2^{+0.3}_{-0.3}$	–	–	$0.28^{+0.01}_{-0.01}$	$17.5^{+0.4}_{-0.4}$	1.7
90014-01-05-04	53407.76	8.92	–	–	$0.050^{+0.004}_{-0.004}$	$9.8^{+0.7}_{-0.7}$	–	–	$0.32^{+0.04}_{-0.02}$	$16.6^{+0.9}_{-1.1}$	1.4
90014-01-05-05	53407.96	8.63	$0.0001^{+0.0066}_{-0.0033}$	$104.5^{+34.6}_{-36.3}$	$0.046^{+0.004}_{-0.003}$	$8.5^{+0.8}_{-0.8}$	–	–	$0.29^{+0.02}_{-0.02}$	$17.5^{+0.6}_{-0.9}$	1.3
90014-01-05-02	53409.28	8.11	$0.0001^{+0.0066}_{-0.0033}$	$222.6^{+37.0}_{-38.3}$	$0.056^{+0.003}_{-0.003}$	$8.7^{+0.6}_{-0.7}$	–	–	$0.26^{+0.02}_{-0.01}$	$18.7^{+0.9}_{-0.9}$	1.1
90014-01-05-03	53410.75	7.20	–	–	$0.049^{+0.007}_{-0.005}$	$10.7^{+1.1}_{-1.0}$	–	–	$0.25^{+0.04}_{-0.02}$	$18.6^{+0.6}_{-0.8}$	2.4
90014-01-05-06	53411.62	6.86	–	–	$0.043^{+0.006}_{-0.007}$	$11.1^{+0.8}_{-1.2}$	–	–	$0.22^{+0.03}_{-0.01}$	$21.3^{+0.9}_{-1.3}$	1.1
90014-01-06-00	53414.04	5.99	$0.0001^{+0.0003}_{-0.0001}$	$92.2^{+67.0}_{-32.9}$	$0.049^{+0.003}_{-0.003}$	$10.3^{+0.7}_{-0.8}$	–	–	$0.16^{+0.01}_{-0.01}$	$22.9^{+0.4}_{-0.4}$	1.4
90014-01-06-01	53416.07	4.66	$0.0001^{+0.0013}_{-0.0001}$	$80.2^{+164.1}_{-40.1}$	–	–	–	–	$0.11^{+0.01}_{-0.01}$	$29.1^{+0.9}_{-0.8}$	1.1
90014-01-06-02	53417.58	4.08	$0.0001^{+0.0002}_{-0.0001}$	$160.6^{+73.1}_{-60.2}$	$0.041^{+0.003}_{-0.002}$	$5.8^{+1.3}_{-1.1}$	–	–	$0.11^{+0.01}_{-0.01}$	$29.2^{+0.5}_{-0.5}$	1.1
90014-01-06-03	53418.47	3.42	$0.0001^{+0.0003}_{-0.0001}$	$77.1^{+107.8}_{-38.6}$	$0.044^{+0.004}_{-0.004}$	$8.6^{+1.8}_{-1.7}$	–	–	$0.13^{+0.01}_{-0.01}$	$27.8^{+0.6}_{-1.0}$	1.3
90014-01-07-01	53419.41	2.96	–	–	–	–	–	–	$0.09^{+0.01}_{-0.01}$	$31.9^{+1.0}_{-1.0}$	0.8
90014-01-07-02	53420.64	2.57	$0.0046^{+0.0051}_{-0.0032}$	$13.5^{+3.0}_{-2.6}$	$0.040^{+0.002}_{-0.004}$	$9.4^{+1.7}_{-1.9}$	–	–	$0.12^{+0.01}_{-0.01}$	$28.2^{+0.8}_{-3.0}$	0.9

Continued on Next Page...

Table A.9 – Continued

Obs. ID	MJD	L_X (10^{37} erg s^{-1})	$\mathbf{L_b}$ ν_b (Hz)	$\mathbf{L_b}$ rms (%)	$\mathbf{L_{LF}}$ ν_{LF} (Hz)	$\mathbf{L_{LF}}$ rms (%)	$\mathbf{L_s}$ ν_s (Hz)	$\mathbf{L_s}$ rms (%)	$\mathbf{L_l}$ ν_l (Hz)	$\mathbf{L_l}$ rms (%)	χ^2_r
90014-01-07-03	53420.71	2.63	$0.0082^{+0.0079}_{-0.0037}$	$11.8^{+2.4}_{-1.9}$	$0.052^{+0.074}_{-0.011}$	$12.2^{+1.2}_{-1.4}$	–	–	$0.13^{+0.01}_{-0.01}$	$26.9^{+1.0}_{-5.8}$	1.4
90014-01-07-04	53422.61	1.80	$0.0070^{+0.0041}_{-0.0028}$	$15.7^{+2.9}_{-1.9}$	$0.057^{+0.020}_{-0.017}$	$15.7^{+1.1}_{-2.0}$	–	–	$0.13^{+0.01}_{-0.01}$	$25.1^{+1.6}_{-3.6}$	1.8
90014-01-07-00	53424.37	1.17	$0.0118^{+0.0488}_{-0.0050}$	$18.8^{+2.3}_{-2.1}$	$0.052^{+0.021}_{-0.003}$	$16.8^{+1.7}_{-1.6}$	–	–	$0.15^{+0.01}_{-0.01}$	$22.6^{+2.4}_{-2.2}$	2.0
90014-01-08-00	53426.47	0.69	$0.0002^{+0.0063}_{-0.0002}$	$47.0^{+58.3}_{-20.7}$	$0.034^{+0.007}_{-0.007}$	$19.5^{+2.1}_{-1.9}$	–	–	$0.13^{+0.01}_{-0.01}$	$24.2^{+1.9}_{-1.3}$	1.1
90014-01-08-01	53428.50	0.45	$0.0001^{+0.0065}_{-0.0073}$	$83.7^{+25.8}_{-23.5}$	$0.083^{+0.015}_{-0.035}$	$13.3^{+1.9}_{-3.9}$	–	–	$0.16^{+0.02}_{-0.05}$	$7.2^{+7.7}_{-2.7}$	1.8

B

Resumen del trabajo de tesis

B.1 Binarias de rayos X

Las binarias de rayos X se encuentran entre los más brillantes objetos extra-solares del cielo y están caracterizadas por intensa variabilidad en escalas temporales de milisegundos hasta meses y años. Su principal fuente de energía es de tipo gravitacional, la cual se libera como consecuencia de un proceso de acrecimiento de materia procedente de la estrella masiva sobre la superficie de la estrella de neutrones. Estos sistemas representan, por tanto, laboratorios únicos para el estudio de las propiedades de la materia bajo condiciones extremas.

Gracias a los observatorios en banda X, lanzados en años recientes, sabemos que en nuestra galaxia hay más de 200 fuentes X brillantes, con flujo $> 10^{-10}$ erg cm^{-2} s^{-1}. Estas fuentes se distribuyen por el Centro Galáctico y por el Plano Galáctico.

Más del 90% de fuentes X galácticas son binarias de rayos X. Tradicionalmente, estos sistemas se dividen en dos subgrupos, las binarias de rayos X de alta masa (HMXBs) y las binarias de rayos X de baja masa (LMXBs). Este trabajo se centra en el estudio del primer subgupo. En las siguientes secciones se dará una descripcíon de las dos componentes de estos sistemas, es decir objetos compactos, incluyendo a las enanas blancas por completitud, y estrellas OB calientes.

B.1.1 Objetos compactos

El colapso gravitacional produce los objetos más exóticos del Universo: agujeros negros y estrellas de neutrones. Este tipo de estrellas representan el estado final de la evolución estelar y conforman hoy en día los constituyentes fundamentales de las galaxias.

Las enanas blancas son estrellas de aproximadamente una masa solar y un radio característico de 5 000 km, con una densidad media de 10^6 g cm^{-3}. Son objetos en estado de enfriamiento estacionario, ya que en su interior las fuerzas gravitacionales están equilibradas por la presión de degeneración de los electrones. Las enanas blancas no participan en la formación de binarias de rayos X.

Las estrellas de neutrones poseen un diámetro de aproximadamente 20 km y tienen un masa de 1.4 $M_\odot$. Debido a su pequeño tamaño y alta densidad, una estrella de neutrones presenta un campo gravitacional superficial muy intenso. Estos objetos representan la evolución final de estrellas masivas, con M >6–8 $M_\odot$. Después de explotar como supernova, el núcleo de la estrella colapsa bajo su gravedad a tal punto que protones y electrones se combinan para formar neutrones.

La existencia de agujeros negros está predicha por la teoría de la relatividad general de Einstein. Hay agujeros negros de tipo estelar, que se supone se forman a partir de una explosión de supernova, y otros supermasivos, encontrados en galaxias y núcleos galácticos activos.

B.1.2 Estrellas OB masivas

Estrellas masivas de tipo espectral temprano son las típicas contrapartidas en HMXBs. Existen dos formas de transferencia de materia desde la compañera masiva a la estrella compacta en las HMXBs: viento estelar y disco circunestelar (originario del llamado “fenómeno Be”).

Todas las estrellas calientes presentan un viento radiativo intenso. La materia del viento estelar contribuye a enriquecer el medio interestelar y, en caso de sistemas binarios, puede participar en el proceso de acrecimiento o producir shocks de vientos en colisión, generando en ambos casos emisión X.

Las estrellas Be clásicas son estrellas de tipo OB, no supergigantes, que presentan o han presentado emisión en las líneas del hidrógeno. Están caracterizadas por

exceso infrarrojo, rotación rápida y alta tasa de pérdida de materia. Las líneas de emisión y el exceso infrarrojo se originan en un disco circunestelar. Varias hipótesis han sido formuladas para explicar la formación del disco circunestelar, aunque en todas ellas la rápida rotación de la estrella B juega un papel destacado.

B.1.3 Binarias de rayos X de alta masa

Las HMXBs se dividen en dos clases: aquéllas que contienen a una estrella supergigante (SGXBs) y aquéllas que contienen a una estrella Be (Be/XRBs). Los dos grupos tienen contrapartida de tipo OB y se encuentran en el Plano Galáctico y en las Nubes de Magallanes.

En las SGXBs el proceso de acrecimiento tiene lugar en forma de viento estelar u, ocasionalmente, rebosamiento del lóbulo de Roche. Son sistemas persistentes en la banda X y muestran fuertes variaciones en escalas temporales breves. Su luminosidad X varía entre $10^{36} - 10^{38}$ erg s^{-1}, según la forma de acrecimiento.

Las Be/XRBs son sistemas excéntricos, en general transitorios. Representan la mayoría de HMXBs. La emisión X es muy variable, desde total ausencia hasta outbursts gigantes de duración de semanas y meses. Los outbursts están clasificados en dos tipos, siendo unos breves y recurrentes, separados por el periodo orbital (Tipo I, con $L_{\rm X} \sim 10^{36} - 10^{37}$ erg s^{-1}) y otros ocasionales, y muy intensos (Tipo II, $L_{\rm X} \geq 10^{37}$ erg s^{-1}.)

Recientemente, gracias a observaciones de *INTEGRAL*, otra subclase ha sido definida, los SFXTs, caracterizados por la ocurrencia de outbursts de rayos X muy cortos e intensos. La razón física para estos outbursts es todavía desconocida, aunque especulaciones teóricas los conectarían a alguna forma de eyección discreta de masa desde la supergigante, o a variabilidad del viento. Este grupo se considera una subclase de SGXBs debido a que su contrapartida es una supergigante, aunque estos sistemas son de tipo transitorio.

B.2 Búsqueda de contrapartidas infrarrojas de HMXBs oscurecidas

B.2.1 Justificación científica

En los últimos siete años la misión *INTEGRAL* de la Agencia Espacial Europea ha revelado la presencia de una importante población de HMXBs en los brazos galácticos de Scutum y Norma, regiones ambas ricas en nubes moleculares densas. La gran profundidad óptica de estas nubes produce una importante extinción en la banda óptica, ultravioleta y de rayos X, que constituyen las ventanas observacionales clásicas en las que la gran mayoría de HMXBs han sido descubiertas y sus contrapartidas identificadas. Las únicas ventanas practicables para buscar binarias de rayos X en las regiones más internas de las nubes moleculares masivas son el infrarrojo y los rayos gamma, donde la fotoabsorción es significativamente más baja.

En efecto, la mayoría de las nuevas HMXBs descubiertas por *INTEGRAL* están fuertemente absorbidas, con fotoabsorción de $N_{\rm H} \sim 10^{23}$ cm^{-2} o mayor, virtualmente inobservables a energías inferiores a los 4 keV. Eso explica como no fueron detectadas por las misiones de rayos X anteriores a *INTEGRAL*. Las contrapartidas ópticas de estas fuentes son difícilmente observables a causa de la elevada extinción interestelar, con A_V superior a 20 mag. Debido a esto, la contrapartida de la gran mayoría de estas fuentes todavía no se ha encontrado. La identificación de contrapartidas ópticas/IR es un paso necesario para realizar un estudio detallado de estos sistemas. Con datos limitados al rango de las altas energías, la comprensión de su compleja estructura y dinámica no puede ser completa.

B.2.2 Observaciones y ánalisis de datos

En este contexto, hemos desarrollado una técnica fotométrica apta para seleccionar estrellas con líneas de emisión en el círculo de error de las fuentes X detectadas por *INTEGRAL*, las cuales serían las naturales candidatas a contrapartidas

en sistemas Be/XRBs. Las carácteristicas más notables de las estrellas Be en el infrarrojo son las líneas de emision de hidrógeno y helio I. Nuestra técnica prevé la construcción de diagramas color-color utilizando dos filtros de banda ancha, H y $K_{\rm s}$, y dos de banda estrecha, Brγ y He I. En diagramas del tipo (Brγ - $K_{\rm s}$)–(H - $K_{\rm s}$) y (He I - $K_{\rm s}$)–(H-$K_{\rm s}$), estrellas con emisión deberían destacarse debajo de la secuencia de estrellas con líneas de absorción. Esta técnica fue aplicada en el IR a estrellas de campo por primera vez en este trabajo.

Las observaciones fueron tomadas en el observatorio de ESO, en Chile, durante dos noches en modo visita. El instrumento empleado fue SOFI, en el New Technology Telescope, en La Silla. Los datos fueron reducidos según el proceso estándar, con rutinas de IRAF. Primero se corrigió el interquadrant-raw cross talk, una característica que afecta a los detectores IR; las imágenes se combinaron obteniendo la mediana para crear una imagen de cielo, que se sustrajo de cada una; se corrigió de flat-field; se alinearon y combinaron las imágenes reducidas para obtener la imagen final.

El paso más crítico de la reducción fue obtener fotometría PSF, para lo cual se desarrolló una rutina iterativa. En el primer paso, el modelo de PSF se computó utilizando sólo una función analítica, eligiendo entre varios perfiles el que producía la menor desviación estándar en el ajuste. El radio de la PSF se disminuyó para excluir posibles contribuciones desde objetos diferentes de las estrellas elegidas para determinar la PSF. El perfil de la estrellas de PSF y sus vecinos fueron ajustados y los vecinos restados de la imagen. Desde la imagen con los vecinos restados se construyó un modelo mejorado de PSF, aumentando de nuevo el radio de ajuste en su valor original (se utilizaron 11 pixeles). En este paso se empleó, junto con la función analítica, una tabla con las desviaciones de los perfiles reales de luminosidad desde el modelo. Se ajustaron y restaron de nuevo las estrellas de PSF y sus vecinos y, si el resultado era satisfactorio, se siguió bajando el radio de PSF y obteniendo el perfil final de PSF. Al final, se aplicó el ajuste de PSF simultáneamente a todas las estrellas del campo.

La corrección de apertura fue estimada como diferencia entre la fotometría de apertura y la fotometría PSF obtenida. La calibración fue realizada en dos

pasos, determinando los coeficientes de extinción a través de la recta de Bouguer, y luego resolviendo las ecuaciones de trasformacion estándar.

B.2.3 Resultados

La técnica fue aplicada a 14 campos de fuentes descubiertas por *INTEGRAL*. Para todos los campos menos uno hemos podido seleccionar candidatos a contrapartida. Entre ellos, consideramos como candidatos más probables los que destacan en ambos diagramas color-color.

Para testar nuestra técnica fotométrica, la aplicamos a una Be/XRB conocida, 1A1118–615. Tomamos un espectro K_s de su contrapartida, que claramente muestra He I y Brγ en emisión. Tomamos también imágenes en los cuatro filtros, H, K_s, Brγ y He I; obtuvimos fotometría PSF y los diagramas color-color. El resultado de la prueba fue que la contrapartida de este sistema fue correctamente identificada en ambos diagramas. Esta prueba es una primera validación de nuestro trabajo.

Además, tomamos espectroscopía K_s con el instrumento NICS del Telescopio Nazionale Galileo del candidato a contrapartida más brillante de IGR J18307–1322, 2MASS J18304334–1233504. La única característica detectada es He I en emisión. En nuestros diagramas, el objeto debería también mostrar Brγ en emisión. Como la mayoría de las estrellas de campo muestra Brγ en absorción, mientras el espectro obtenido no muestra Brγ ni en absorción ni en emisión, esto justifica que sea seleccionado en el diagrama (Brγ-K_s)–(H-K_s). Nuestros datos entonces apuntan a este objeto como posible contrapartida de IGR J18307–1322, ya que varias Be/XRBs, aún teniendo He I en emisión, no presentan la línea Brγ.

B.3 Análisis y clasificación espectral NIR de HMXBs identificadas por INTEGRAL

B.3.1 Objetivo científico

Como se ha mencionado en la sección anterior, muchas de las nuevas fuentes de rayos X descubiertas por *INTEGRAL* presentan un elevado nivel de absorción.

Las recientes técnicas de espectroscopía infrarroja emergen entonces como herramientas útiles para caracterizar estos sistemas y, junto con datos de alta energía, revelar la clase a la que pertenecen. En particular, en el caso de los SFXTs, los datos de baja energía son de importancia crucial para su clasificación, ya que sus propiedades en la banda X son comunes a otros objetos (binarias RS CVn y LMXBs).

B.3.2 Observaciones y ánalisis de datos

Observaciones de contrapartidas propuestas para fuentes descubiertas por *INTEGRAL* fueron tomadas a lo largo de varios turnos, en 2006, 2007 y 2008 en los observatorios de ESO, en La Silla y Paranal, en Chile. Se utilizó, en modo visita, el instrumento SOFI en el NTT, y, en modo servicio, ISAAC en el VLT. Según el instrumento, las observaciones se hicieron en media o baja resolución respectivamente. Para el análisis y clasificación se utilizó la banda $K_{\rm s}$. Las fuentes observadas fueron IGR J16207–5129, IGR J16465–4507, IGR J16479–4514, IGR J16493–4348, AX J1841.0–0536 and IGR J19140+0951. También se incluyó 4U 1907+09 porque su clasificación ha sido un tema muy discutido en el pasado, y todavía no existen espectros IR de esta fuente.

Los datos fueron reducidos según el procesado estándar, con rutinas de IRAF. Primero se corrigió por el inter-quadrant row cross-talk, que afecta a los espectros tanto como a las imágenes de detectores IR; se combinaron las imágenes para obtener una imagen de cielo, que se restó; se corrigió por flat-field; se extrajeron los espectros monodimensionales de manera interactiva; se calibraron en longitud de onda utilizando espectros de lámparas; se corrigió la absorción telúrica. El último paso es el más crítico en la reducción de espectros IR. En la región infrarroja, entre 1 y 5 μm, el espectro de la atmósfera está dominado por transiciones de agua telúrica y CO_2. Estas líneas varían rápidamente con el tiempo y la elevación. En particular para estrellas calientes, una línea muy importante para la clasificación es la de He I en 2.058 μm, la cual se encuentra en un rango espectral donde bandas de absorción de CO_2 dominan el espectro. Para nuestro objetivo, esto vuelve de crucial importancia la correcta sustracción de las bandas telúricas.

La técnica que se utilizó fue observar, para cada espectro científico, espectros

de una estrella de tipo A0-A3 III-V y de una de tipo G2-3 V. Para obtener diferencias pequeñas en masa de aire, la primera se observaba inmediatamente antes o después del objeto científico, mientras que la segunda en un intervalo de una hora. Las estrellas de tipo A poseen como carácteristica propia sólo una línea de Brγ en absorción, pudiendose considerar el rango restante de la banda K_s un puro espectro telúrico. En la región de Brγ, utilizamos el espectro de la estrella G dividido por el espectro solar; insertamos la relación obtenida en el espectro de la estrella A, obteniendo un espectro final telúrico. Esto se repitió para cada objeto científico, obteniendo un espectro telúrico para cada uno. La corrección se hizo de manera interactiva, dividiendo el espectro científico por el correspondiente espectro telúrico, después de aplicar un factor de corrección de escala y desplazamiento para corregir diferencias en masa de aire y alineado.

B.3.3 Resultados

Los espectros se analizaron y clasificaron en comparación con atlas IR. Las líneas espectrales detectadas en los espectros fueron, en general, He I 20 581 Å, He I 21 120 Å, N III 21 155 Å y Brγ 21 661 Å. Todas las fuentes fueron clasificadas como HMXBs. Los resultados obtenidos son los siguientes:

IGR J16207–5129: la contrapartida fue clasificada B1 Ia; el sistema es entonces una SGXB;

IGR J16465–4507: la contrapartida fue clasificada O9.5 Ia; junto con informacion de datos X, nuestro análisis confirmió la inclusión del sistema en la clase de SFXTs, ya propuesta a partir de espectros ópticos;

IGR J16479–4514: la contrapartida fue clasificada O9.5 Iab, y el sistema como SFXT;

IGR J16493–4348: la contrapartida fue clasificada B0.5 Ib, y el sistema como SGXB;

AX J1841.0–0536: la contrapartida fue clasificada B1 Ib; junto con informacion de datos X, nuestro análisis confirmió la inclusión del sistema en la clase de SFXTs, ya propuesta desde espectros ópticos;

IGR J19140+0951: la contrapartida fue clasificada O8.5 Iab, y el sistema como SGXB;

4U 1907+09: la contrapartida fue clasificada O8.5 Iab, y se confirmió el sistema como SGXB.

Para cada fuente se estimó el reddening y la distancia, y se comparó la extinción interestelar obtenida con el valor de $N_{\rm H}$ conocido a partir de los datos X. En particular, para cuatro objetos – IGR J16465–4507, IGR J16479–4514, AX J1841.0–0536 y IGR J19140+0951 – la extinción obtenida con nuestros datos IR resultó una o dos magnitudes inferior a la derivada con los datos X. Esto significa que la fuente de absorción en la banda X se encuentra concentrada alrededor de la estrella de neutrones. Esto es consistente con la observación de la línea de fluorescencia del hierro en 6.4 keV en los espectros X de las cuatro fuentes, ya que ésta se considera una traza de la capa esférica de material alrededor del objeto compacto. Los sistemas que fueron clasificados como SFXTs presentan un elevado nivel de absorción intrínseco, sugeriendo que ésta podría ser una propiedad de la clase.

Nuestros resultados sobre la estimación de la distancia, aunque afectados por incertidumbres importantes, son compatibles con los brazos galácticos de Norma, Scutum o Sagitario, según la fuente.

Parte de estos resultados se publicaron en Nespoli et al. (2008b).

B.4 Espectroscopía en la banda K revela dos nuevas SyXBs

B.4.1 Binarias simbióticas de rayos X

Las binarias simbióticas de rayos X (SyXBs) son una subclase, recientemente introducida, de LMXBs, caracterizada por la presencia de una contrapartida de tipo gigante tardío. Se trata de una clase rara, llamada así por analogía con las binarias simbióticas, sistemas constituidos por una enana blanca y una gigante

de tipo M. Hasta ahora, solo seis sistemas conocidos pertenecen a este grupo, lo cual vuelve su estudio de gran interés.

B.4.2 IGR J16358–4726 y IGR J16393–4643,

Durante la campaña de epectroscopía IR de contrapartidas de HMXBs, se tomaron datos de IGR J16358–4726 y IGR J16393–4643, dos fuentes descubiertas por *INTEGRAL*, supuestas HMXBs.

En el caso de la primera fuente, IGR J16358–4726, trabajos con datos X revelaron la presencia de una estrella de neutrones. A partir de espectroscopía NIR, Chaty et al. (2008) sugirieron que la contrapartida es una sgB[e], y el sistema entonces una HMXBs, perteneciente a una clase peculiar de SGXBs.

Respecto a IGR J16393–4643, la fuente de rayos X fue identificada como un púlsar; el estudio de los parámetros orbitales del sistema, a partir del análisis temporal de las pulsaciones, produjo cuatro soluciones matemáticas, entre las cuales Thomson et al. (2006) propusieron como más probable la que propone un periodo orbital de 3.7 días y una función de masa de $6.5\pm1\ M_{\odot}$. Esto correspondería a una HMXB. Además de la contrapartida inicialmente propuesta, fotometría reciente de Chaty et al. (2008) descubrió tres candidatos más, que se descartaron por su magnitud débil. Resultados de ajuste de SED, utlizando observaciones desde el rango óptico hasta el MIR, sugirieron un tipo espectral BIV-V.

B.4.3 Observaciones, análisis y resultados

Las contrapartidas propuestas fueron observadas en 2007 con el espectrógrafo ISAAC, en el telescopio UT1, en Paranal (ESO). Los datos fueron tomados en baja resolución. La reducción se hizo con IRAF, utilizando los métodos estándares. La corrección de absorción telúrica se hizo de la misma forma que se describió en la sección precedente.

El análisis y la clasificación espectral utilizaron los atlas NIR disponibles. Los dos espectros que presentamos son, para IGR J16358–4726, el primer espectro infrarrojo, y, para IGR J16393–4643, el primero que incluye el rango más allá de 2.3 μm. Los espectros de las dos fuentes son muy parecidos, siendo su característica más evidente las intensas bandas de CO en absorción entre 2.29 y 2.40 μm, típicas

de estrellas tardías. Se pueden reconocer también varias líneas metálicas, aunque en general no se puedan resolver.

Detectamos también He I 20 281 Å y Brγ en débil emisión en ambos espectros: como éstas no son características propias de estrellas de tipo tardío, podrían ser la traza de un disco de acrecimiento alrededor de un objeto compacto. Sin embargo, dada su debilidad, ésta es sólo una hipótesis y de hecho podrían ser incluso el residuo de la corrección telúrica, que en esas regiones es muy crítica. En cualquier caso, las líneas de emisión típicas de las binarias de rayos X parecen no estar presentes en los espectros ópticos de las otras SyXBs conocidas. La razón se debería a la elevada luminosidad total de las compañeras gigantes, que deslumbraría la emisión derivada del reprocesado de la radiación X.

Nuestros espectros K claramente indican que ambos objetos son de tipo tardío, y excluyen que los sistemas sean HMXBs con compañeras de tipo OB. La morfología general de los espectros y la comparación entre las intensidades relativas de CO 22 900 Å y de las líneas de Na I y Ca I, que son indicadores de luminosidad, revelan que ambas estrellas son gigantes o supergigantes.

Lamentablemente, un ajuste de SED no pudo mejorar la clasificación espectral debido a la degeneración entre la dirección del vector de reddening y la variación de la temperatura efectiva en el rango espectral empleado.

B.4.4 Conclusiones

Nuestra clasificación espectral apunta a gigantes o supergigantes tardías. Junto con las características conocidas a partir de estudios en la banda X, nos permite proponer que ambos sistemas pertenecen a la clase de SyXBs.

En el caso de IGR J16393–4643, la solución orbital propuesta como más probable por Thompson et al. (2006), no resulta compatible con nuestra clasificación espectral. Entre las otras soluciones matemáticas, excluyendo la solución 3 por su debilidad estadística, sólo la solución 2 es aceptable. Ésta consiste en una función de masa de 0.092 $M_\odot$ y un periodo orbital de 50.2 días. Derivamos un límite a la masa de una gigante roja que quepa en la órbita prevista por la solución 2, obteniendo un valor de 7 $M_\odot$.

Los resultados obtenidos para IGR J16393–4643 son válidos siempre que la contrapartida sea confirmada, excluyendo como possibles compañeras los otros objetos que se encuentran en el círculo de error de *XMM/Newton*.

B.5 Análisis espectral/temporal de BeXRBs durante outbursts gigantes

Con este trabajo investigamos la variabilidad espectral y temporal de cuatro púlsares de rayos X con compañera Be durante outbursts de tipo gigante. Por outbursts gigantes nos referimos a outbursts de tipo II, donde la luminosidad en la banda X llega al límite de Eddington. Nuestro objetivo es definir y caracterizar posibles estados espectrales, tal y como se ha hecho para las LMXBs y agujeros negros. Para ello haremos uso de las propiedades espectrales y temporales, la posición de las fuentes en el diagrama color-color a lo largo del outburst y de las correlaciones de esas propiedades entre ellas.

B.5.1 Técnicas de análisis de datos X

Fotometría en multibanda

En analogía con la fotometría óptica, en la banda X es posible caracterizar la forma espectral definiendo colores X. El color se define como el cociente entre el número de cuentas (fotones) en dos bandas de energía. También se le suele denominar razón de "dureza" (harness ratio). Dado que el continuo X entre 2–30 keV de virtualmente todas las HMXBs puede ser representado por una ley de potencia, es decir, una línea recta en los diagramas log-log, un color corresponde a una medida aproximada de la pendiente espectral. Un *diagrama color-color* es el gráfico de un color en función de otro, calculado en una banda de energía diferente. El color en el rango de energía más alto, se le denomina color "duro", mientras que el de rango de energía más bajo se le denomina color "blando". Un *diagrama intensidad-color* es el gráfico de un color en función de la intensidad en un determinado rango espectral.

Estos tipos de diagramas son independientes del modelo de ajuste espectral empleado y reflejan las propiedades intrínsecas de los sistemas. En el estudio de las

LMXBs se han convertido en una herramienta esencial de análisis introduciendo el concepto de estados espectrales. Un estado se define a partir de la aparición de una componente espectral o temporal asociada con una posición bien reconocible en el CD/HID.

Ajuste espectral

Las variaciones espectrales se pueden describir de una manera más detallada en términos de una combinación de una o más funciones matemáticas motivadas físicamente, o modelos, ajustados a los espectros observados. El análisis del comportamiento de los parámetros del modelo mientras la fuente evoluciona en el CD/HID, junto con la identificación de correlaciones entre parámetros, es una herramienta muy útil para caracterizar los estados del sistema y estudiar las transiciones entre dichos estados.

Análisis temporal

Las observaciones de las binarias de rayos X muestran una gran variabilidad en un amplio rango de escalas temporales en todas las longitudes de onda y hasta el milisegundo en la banda X. La herramienta principal utilizada para estudiar las propiedades temporales de una fuente X es el espectro de potencia de Fourier, o Power Spectral Density (PSD), de las series temporales de la intensidad de la radiación X, o curvas de luz. Esta técnica es particularmente importante cuando el ruido domina sobre la señal y sólo es posible estudiar las propiedades promediadas de los fenómenos temporales. Al igual que en los espectros en energía, los espectros de potencia son modelizados mediante el ajuste de funciones matemáticas o componentes del espectro de potencia. Desgraciadamente no existe un modelo físico capaz de describir las componentes temporales de forma consistente, dado que los procesos que determinan la variabilidad en banda X son todavía de difícil interpretación. Las componentes anchas se denominan *ruido* y las estrechas *oscilaciones casi-periódicas* (QPOs).

B.5.2 Este trabajo

Mientras existen numerosos estudios sobre la aplicación de CD/HID y técnicas de análisis espectral a binarias de rayos X de baja masa, muy poco trabajo de

este tipo se ha hecho sobre binarias de rayos X de alta masa. El objetivo de este trabajo es realizar por primera vez un estudio sistemático de cuatro Be/XRBs durante outbursts gigantes, utilizando las tres técnicas introducidas antes, simultáneamente, y empleando los resultados y las correlaciones obtenidos para intentar definir y caracterizar estados espectrales para esta clase de sistemas.

B.5.3 Estados espectrales

En esta sección presentamos las actuales definiciones de estados en LMXBs, sea que contengan estrellas de neutrones, sea agujeros negros.

Estados en LMXBs con estrellas de neutrones

Según la forma de los trazados que dibujan en el CD/HID, con escalas temporales de horas hasta días, se distinguen dos subclases, las *fuentes Z* y las *fuentes atoll*. Las fuentes Z son la subclase más brillante, caracterizada por una trazado de tres ramas in los CDs/HIDs, que en algunos casos parece una "Z", en otros una "ν". Las tres ramas se denominan "horizontal branch" (HB), "normal branch" (NB) y "flaring branch" (FB). Los espectros de potencia de las fuentes Z muestran varios tipos de QPOs así como de componentes de ruido. Su presencia y propiedades están fuertemente correlacionadas con la posición de la fuente a lo largo del trazado de Z.

Las fuentes atoll cubren un rango mucho más amplio de luminosidades y suelen tener un espectro más duro y variabilidad de mayor amplitud. En alta luminosidad, siguen en el CD/HID un trazado denominado "banana branch", que está a su vez subdividido en "upper banana", "lower banana", dominados por componentes de ruido, y "lower left banana", donde se observan QPOs gemelas en el rango de los kHz. En baja luminosidad, la emisión X es, en general, más dura y la fuente se encuentra en el "island state" (IS). El estado correspondiente al nivel más bajo de luminosidad se le denomina "extreme island state" (EIS).

Estados en agujeros negros

Los espectros X de agujeros negros en LMXBs en el rango 3-30 keV se pueden representar utilizando dos componentes principales, una ley de potencias, que ajusta

el espectro a altas energías (> 10 keV) y la ley de Planck que representa la intensidad de la radiación emitida por un cuerpo negro, la cual cuando está presenta ajusta el espectro a bajas energías. Cuando una ley de potencias, de naturaleza no térmica, con índice espectral en el rango 1.5–2 domina el espectro, la fuente se encuentra en el "low/hard state" (LS); cuando una componente blanda, térmica, de cuerpo negro con temperatura $kT \lesssim 1$ keV domina, la fuente se encuentra en el "high/soft state" (HS). Entre ellos, se define el "intermediate state", que a su vez se subdivide en "soft intermediate state" (SIMS) y "hard intermediate state" (HIMS). Durante el LS y el HIMS, el espectro de potencias está dominado por intensas componentes de ruido y a veces QPOs. El SIMS muestra espectros de potencias dominados por una débil ley de potencias y varias QPOs. Durante el HS los espectros de potencias son parecidos a los del SIMS, pero con variabilidad menos intensa y ausencia en general de QPOs.

En general, a partir de características espectrales y temporales, el LS en agujeros negros se parece a EIS/IS de sistemas atoll con estrellas de neutrones. Además, algunas correlaciones entre frecuencias encontradas en las componentes temporales son similares para agujeros negros y estrellas de neutrones de tipo atoll, sugiriendo que resultan del el mismo proceso físico.

B.5.4 Las fuentes analizadas

Los sistemas estudiados en este trabajo son las siguientes Be/XRBs:

- KS 1947+300: el sistema muestra pulsaciones X con periodo de 18.7 s. y su periodo orbital es de 40.4 días. El espectro de energía entre 0.1–100 keV fue ajustado a partir de datos de BeppoSAX utilizando tres componentes: una componente de comptonización, una componente de cuerpo negro en $\sim$0.6 keV y una débil línea de emisión de hierro en 6.7 keV, con una débil absorción. La contrapartida fue identificada como una estrella enrojecida de tipo B0Ve, situada a una distancia de $\sim$10 kpc.

- EXO 2030+375: desde su descubrimiento en 1985, el sistema mostró su primer outburst gigante en junio de 2006. En este trabajo analizamos datos de ese evento. El sistema, situado a una distancia de 7.1 kpc, está constituido por

un púlsar de $P_{\rm spin} = 41.7$ s y una estrella de tipo B0Ve. El continuo del espectro X puede ser ajustado con una ley de potencias con cutoff exponencial, y eventualmente una componente de cuerpo negro, en fases de muy alta o baja luminosidad. Una línea de ciclotrón (CRSF) fue detectada en 11 keV durante el pico más brillante del outburst de 2006.

- 4U 0115+63 Este sistema muy activo y estudiado presenta pulsaciones de periodo ∼3.6 s. Desde el lanzamiento de RXTE, se ha observado tres outbursts gigantes, en 1999, 2000 y 2004 respectivamente. En este trabajo analizamos datos del evento de 2004. La contrapartida es una estrella de tipo B0.2 Ve, y su distancia se estima en 7–8 kpc. El espectro X del sistema muestra hasta cinco CRSFs.

- V 0332+53 La fuente fue descubierta en 1984. Su periodo de spin es de 4.4 s. y su periodo orbital de 34.25 días. La contrapartida óptica, BQ Cam, es de tipo O8-9 Ve, situada a una distancia de ∼7 kpc. Una CRSF con pico fundamental y dos harmonicos fue detectada en el espectro X de la fuente durante el outburst gigante de 2004–2005, el mismo analizado en este trabajo.

B.5.5 Observaciones, reducción de datos y análisis

Los datos analizados en este trabajo provienen del satélite RXTE. Se utilizó el instrumento PCA, con dos configuraciones diferentes de datos: para el análisis espectral, se emplearon datos de un solo detector, el PCU2, de tipo "Standard 2", es decir con alta resolución espectral (129 canales y resolución temporal de 16 s); para el análisis temporal, se emplearon datos de todos los detectores, en general de tipo "Good Xenon", con 256 canales.

Análisis espectral

Para cada observación, se obtuvo un espectro utilizando el paquete FTOOLS de Heasarc, versión 6.6.3. Los espectros fueron corregidos de la intensidad del fondo y del tiempo muerto del detector. Cada espectro fue ajustado en el rango 3–50 keV, con XSPEC, versión 12.4, incluyendo un error sistemático de 0.6%. En general, el modelo empleado está constituido por absorción fotoeléctrica, una ley de poten-

cias con cutoff exponencial en alta energía y un perfil gaussiano en ∼6.5 keV que corresponde a una línea de emisión del hierro. Además, para tres fuentes, EXO 2030+375, 4U 0115+63 y V 0332+53, se incluyó una línea de ciclotrón con perfil gaussiano. En particular, para V 0332+53, se obtuvieron dos ajustes buenos con dos modelos diferentes, incluyendo en uno el cutoff y excluyendolo en el otro. Los resultados obtenidos, con similitudes y diferencias, serán comentado en la sección siguiente.

Los diagramas CD/HID se obtuvieron directamente desde la intensidad de la radiación X, a partir de curvas de luz.

Análisis temporal

Se extrajeron espectros de potencias de cada observación, a partir de una curva de luz en el rango 2–20 keV, con una resolución final de 256 s. Los ajustes emplearon perfiles lorentzianos sea en el caso de QPOs, sea para componentes de ruido. Esto nos permitió identificar y estudiar las características de las componentes temporales utilizando un solo tipo de función, y comparar las diferentes componentes entre ellas y entre los diferentes sistemas. Los picos de pulsaciones se ajustaron con Lorentzianas de frecuencia fijada en el valor esperado y anchura fijada a 0.001 Hz.

B.5.6 Resultados

Colores

En los cuatro sistemas estudiados, se pueden distinguir dos ramas diferentes, o estados espectrales, en el HID/CD. Según la forma que éstas dibujan en los diagramas, las nombramos *rama horizontal* (HB) y *rama diagonal* (DB). La primera, breve, corresponde a bajo flujo, la segunda, más larga, a alto flujo. La transición de uno a otro estado ocurre en $L_{\rm X}$ ∼10% del valor del pico para KS 1947+300, EXO 2030+375 y V 0332+53, mientras para 4U 0115+63 ese cambio se observa en $L_{\rm X} = 25\%$ del valor del pico.

El color blando muestra el mismo comportamiento en todos los cuatro sistemas, en anti-correlación con el flujo durante la DB y en correlación durante la HB. El color duro en general correlaciona con el flujo, con la excepción de V

0332+53. Otra importante diferencia es que la HB es más dura que la DB en V 0332+53, mientras que es más blanda en las demás fuentes. En este sentido, para KS 1947+300, EXO 2030+375 y 4U 0115+63, la HB representa una rama de tipo "low-soft" (bajo flujo y emisión blanda), un estado que no se observa en las LMXBs o en agujeros negros.

4U 0115+63 y V 0332+53 muestran histéresis en sus CD/HID. Esto significa que observaciones de la fase de subida del outburst están desplazadas respecto a las de flujo parecido en la fase de bajada. Durante la bajada la emisión es más blanda.

Los dos estados están definidos a partir del cambio de tendencia del SC. Su disminución en la HB indica que el espectro se vuelve más blando mientras la fuente progresa en este estado. Es decir, se produce emisión adicional en baja energía. Suponemos que durante la DB la emisión X provenga desde el "standing shock" arriba de la superficie de la estrella de neutrones en la columna de acrecimiento, como resultado de Comptonización de fotones de baja energía desde el casquete polar por parte de electrones de alta energía desde el flujo de acreción. Con luminosidades cerca del límite de Eddington, la materia acrecida es parada a una cierta distancia desde la superficie de la estrella de neutrones debido a la presión de radiación. En algún momento la tasa de acrecimiento de masa es lo suficientemente baja como para que empecemos a ver el espectro resultante del reprocesado de la radiación de cuerpo negro inyectada en la columna de acrecimiento desde el casquete polar. En ese momento estamos entrando en la HB. El punto de inversión correspondería entonces a la transición desde la emisión del "standing shock" a la del casquete polar.

Características espectrales

Las dos ramas se pueden distinguir también desde el punto de vista espectral. En todos los sistemas el índice espectral muestra una fuerte relación con el flujo, correlacionando en general con él durante la DB y anti-correlacionando durante la HB, en acuerdo con lo que enseña el análisis de los colores. El cutoff exponencial no muestra ninguna tendencia común en los sistemas analizados en este trabajo.

La línea del hierro es una componente necesaria para ajustar los espectros de todas las cuatro fuentes durante la DB. Su intensidad disminuye mucho durante

la HB, y en varios espectros de ese estado no es necesario incluirla. En general, su energía central es constante a lo largo del outburst en todos los sistemas; su intensidad correlaciona con el flujo calculado entre 3–30 keV.

Tres sistemas – EXO 2030+375, 4U 0115+63 y V 0332+53 – entre los cuatro analizados en este trabajo muestran evidencia de una línea de ciclotrón. Sin embargo, los espectros de EXO 2030+375 sólo la requieren en la fase más brillante del outburst y sus parámetros característicos no varían dentro de los errores a lo largo del outburst. En 4U 0115+63 y V 0332+53, la energía central de la línea es mayor en la HB que en la DB, en anti-correlación con el flujo total. En promedio la profundidad óptica muestra un comportamiento parecido. Ambos sistemas requieren, además del pico fundamental, también el primer armónico. Para V 0332+53 se obtuvieron buenos ajustes empleando dos modelos diferentes, es decir incluyendo en el primero un cutoff, y excluyendolo en el segundo. Con el primer modelo, la energía de la línea de ciclotrón correlaciona con el flujo total durante todo el outburst; con el segundo modelo, su comportamiento es muy diferente, de correlación en baja luminosidad (HB) y de anti-correlación en alta luminosidad (DB). Lo que se observa con el segundo modelo se puede explicar si suponemos que el acrecimiento tiene lugar en régimen de luminosidad sub-Eddington en la HB y super-Eddington en la DB. Calculamos la luminosidad crítica que define el umbral entre los dos regímenes, obteniendo valores comparables con el punto de inversión entre DB y HB ($L_{\rm E} \sim 5 \times 10^{37}$ erg s^{-1}) en el límite de baja energía de los fotones producidos y valores del semi-ángulo de las líneas del campo magnético en los polos $\theta_{\rm c} < 0.1$.

Sin embargo las diferencias entre los resultados del primer modelo y el segundo son todavía materia de debate y serán investigadas en un estudio futuro.

Características temporales

Después de ajustar los picos de las componentes de pulsaciones, los espectros de potencia de las Be/XRBs son caracterizados por ruido limitado (BLN). Todos los espectros analizados en este trabajo se ajustaron con la suma de 2–4 Lorentzianas. Considerando todos los sistemas, identificamos seis tipos diferentes de componentes temporales, de las cuales, cuatro son de ruido limitado ($L_{\rm b}$, $L_{\rm l}$, $L_{\rm u}$, $L_{\rm u'}$, con frecuencia característica creciente) y dos son QPOs ($L_{\rm LF}$ y $L_{\rm s}$).

La componente mejor caracterizada es $L_{\rm l}$, que cubre un rango de frecuencias entre 0.1–2 Hz. En todos los sistemas su frecuencia máxima, ν_l correlaciona con el flujo, mientras que su intensidad muestra tendencias diferentes según la fuente.

Las dos componentes estrechas sólo se observan en 4U 0115+63 y V 0332+53. $L_{\rm LF}$, con frecuencia característica entre 0.02–0.15 Hz, es común entre los dos sistemas, mientras que $L_{\rm s}$ sólo se observa en V 0332+53 en la DB: su frecuencia característica varía entre 0.2–0.3 Hz, que corresponde aproximadamente a la frecuencia del pico fundamental de las pulsaciones.

¿Dos clases de Be/XRBs?

Cómo las LMXBs están divididas en fuentes "atoll" y fuentes Z, es interesante intentar definir subgrupos en las Be/XRBs.

Un patrón de dos ramas es trazado en el CD/HID de los cuatro sistemas durante outbursts gigantes, siendo éste el rasgo común mejor caracterizado. Como en los sistemas de baja masa, las fuentes no saltan por el diagrama, sino se mueven de manera continua y progresiva en él, siguiendo el patrón. La HB corresponde a un estado de baja intensidad y muestra en promedio la rms fraccional más alta, así como el "island state" en los atolls y la rama horizontal en las fuentes Z. La HB representa el estadio inicial y final de la fuente en el outburst. En la DB, correspondiente a alta intensidad, las componentes de ruido muestran frecuencias características más altas y rms más bajas que en la HB. La ley de potencia en los ajustes espectrales muestra una firme relación con el flujo, correlacionando con él en la DB y anti-correlacionando en la HB.

Las diferencias entre los sistemas identifican claramente dos subgrupos, con los púlsares más lentos, KS 1947+300 y EXO 2030+375, por un lado, y los más rápidos, 4U 0115+63 y V 0332+53, por el otro. El primer grupo se caracteriza por espectros más blandos en la HB respecto a los otros sistemas. Se observa histéresis sólo en los púlsares rápidos. Las CRSFs, muy evidentes en los espectros de 4U 0115+63 y V 0332+53, no se observan o son muy débiles en los otros sistemas.

Desde el punto de vista del análisis temporal, la principal diferencia entre los dos grupos es la presencia de QPOs, que son típicas en los PSD de lós púlsares rápidos, mientras que no se observan en los otros sistemas.

Ninguna evidente correlación se encontró entre los parámetros espectrales y temporales de las Be/XRBs. Esto representa una diferencia importante respecto a los sistemas de baja masa. Para las LMXBs la razón de tales correlaciones es todavía desconocida, pero una posible explicación encuentra su origen en la presencia de un disco de acrecimiento. La falta de correlaciones en Be/XRBs se podría entonces deber a la falta de un disco de acrecimiento en esta clase de sistemas. Esta descripción es puramente especulativa, y sólo ulterior investigación de outbursts de ambas clases, LMXBs y HMXBs, podrá resolver la cuestión.

E quindi uscimmo a riveder le stelle.

Dante Alighieri

Acknowledgments

Quiero agradecer a mis dos directores de tesis, Juan y Pablo, porque este trabajo es el resultado de un esfuerzo conjunto por parte de los tres. Gracias por vuestro apoyo, paciencia (o incluso impaciencia, cuando hacía falta), y sobre todo por ser siempre guías, y conducirme hacia los resultados de forma excelente y rigurosa. Gracias también a Ronald, cuya colaboración fue desde el principio preciosa para acercarme al entonces desconocido mundo de la espectroscopía infrarroja. E, sul versante scientifico, un grazie enorme a Tomaso, che per primo destò il mio interesse nei confronti delle Binarie X, ben otto anni or sono, e che con grande ottimismo mi ha sempre appoggiato e confortato, da lontano, in questi anni.

Un agradecimiento especial va a Alberto y Amelia, porque sin vuestra ayuda todo esto nunca hubiera podido siquiera empezar. Gracias por el apoyo del principio, por el soporte práctico con el papeleo para la matrícula (y las becas), cuando la burocracia española todavía era todo un mundo incomprensible (bueno, esto poco ha cambiado desde entonces), por los emails/llamadas/fax (¿y qué más?) a todo el mundo, para que se aceptara la documentación italiana, por acogernos incluso por un tiempo en vuestra casa :), por ... de verdad, mil gracias por todo lo que habéis hecho por Mauro y por mí, desde mucho antes de que llegaramos aquí.

En estos años tuve la suerte de trabajar en un entorno absolutamente positivo como él del OAUV. Gracias a todos los que habéis compartido este tiempo conmigo, por hacer que la atmósfera del día a día fuese la más relajada y amistosa que un estudiante puede esperar haciendo su tesis. Y gracias a Feli, por hacer que la burocracia no hundiese a mi tesis (y a mí con ella).

El nivel científico de mi tesis se ha beneficiado ciertamente de las sugerencias y correcciones de los tres evaluadores, Pere Blay, Jorge Casares, José Miguel Torrejón, con quienes hubo un muy interesante intercambio de ideas. Mil gracias por vuestra paciencia y detenimiento en la lectura de este largo trabajo.

Voglio ringraziare la mia famiglia, mia madre, mio padre e mio fratello, per il sostegno che non avete mai smesso di darmi, per l'appoggio incondizionato alle mie scelte, anche quelle rischiose, o che implicavano un oceano di troppo tra me e voi, per l'incoraggiamento costante nei momenti difficili (e ne avrò ancora bisogno, ma già lo sapete . . .).

Ma, soprattutto, un grazie tutto speciale a Mauro, dolce compagno, guida intelligente da cui ho tratto tante idee e soluzioni, costante punto fermo di questi anni della mia vita. Questa tesi è un'avventura comune, ha comportato scelte comuni, rinunce e speranze comuni. Grazie per l'incrollabile fiducia in me, per il sostegno di ogni giorno, per il tuo smisurato affetto e per la tenerezza, che mi danno la gioia di alzarmi ogni mattina.

Bibliography

Alpar, M. A., Cheng, A. F., Ruderman, M. A., & Shaham, J. 1982, Nat, 300, 728

Angelini, L., Stella, L., & Parmar, A. N. 1989, ApJ, 346, 906

Arnaud, K. A. 1996, in Astronomical Society of the Pacific Conference Series, Vol. 101, Astronomical Data Analysis Software and Systems V, ed. G. H. Jacoby & J. Barnes, 17–+

Backer, D. C., Kulkarni, S. R., Heiles, C., Davis, M. M., & Goss, W. M. 1982, Nat, 300, 615

Bamba, A., Ueno, M., Koyama, K., & Yamauchi, S. 2003, ApJ, 589, 253

Bamba, A., Yokogawa, J., Ueno, M., Koyama, K., & Yamauchi, S. 2001, PASJ, 53, 1179

Barret, D. & Olive, J.-F. 2002, ApJ, 576, 391

Becker, P. A. & Wolff, M. T. 2007, ApJ, 654, 435

Belloni, T. & Hasinger, G. 1990, A&A, 230, 103

Belloni, T., Homan, J., Casella, P., et al. 2005, A&A, 440, 207

Belloni, T., Psaltis, D., & van der Klis, M. 2002, ApJ, 572, 392

Belloni, T. M. 2010, in Lecture Notes in Physics, Berlin Springer Verlag, Vol. 794, Lecture Notes in Physics, Berlin Springer Verlag, ed. T. Belloni, 53–+

Bessell, M. S. & Brett, J. M. 1988, PASP, 100, 1134

Bird, A. J., Barlow, E. J., Bassani, L., et al. 2004, ApJL, 607, L33

Bird, A. J., Malizia, A., Bazzano, A., et al. 2007, ApJS, 170, 175

Bjorkman, J. E. & Cassinelli, J. P. 1993, ApJ, 409, 429

Blay, P., Martínez-Núñez, S., Negueruela, I., et al. 2008, A&A, 489, 669

Bodaghee, A., Courvoisier, T. J.-L., Rodriguez, J., et al. 2007, A&A, 467, 585

Bodaghee, A., Walter, R., Zurita Heras, J. A., et al. 2006, A&A, 447, 1027

Borozdin, K., Gilfanov, M., Sunyaev, R., et al. 1990, Soviet Astronomy Letters, 16, 345

Bradshaw, C. F., Titarchuk, L., & Kuznetsov, S. 2007, ApJ, 663, 1225

Bradt, H. V., Rothschild, R. E., & Swank, J. H. 1993, A&AS, 97, 355

Burnard, D. J., Arons, J., & Klein, R. I. 1991, ApJ, 367, 575

Butler, S. C., Tomsick, J. A., Chaty, S., et al. 2009, ApJ, 698, 502

Camenzind, M. 2007, Compact objects in astrophysics : white dwarfs, neutron stars, and black holes (Compact objects in astrophysics : white dwarfs, neutron stars and black holes, Astronomy and astrophysics library. Edited by M. Camenzind. ISBN 9783540257707 Berlin: Springer-Verlag, 2007)

Carpenter, J. M. 2001, AJ, 121, 2851

Casella, P., Belloni, T., & Stella, L. 2006, A&A, 446, 579

Chakrabarty, D., Koh, T., Bildsten, L., et al. 1995, ApJ, 446, 826

Chakrabarty, D. & Roche, P. 1997, ApJ, 489, 254

Chandrasekhar, S. 1931, ApJ, 74, 81

Chaty, S. 2007, ArXiv e-prints, 710

Chaty, S., Rahoui, F., Foellmi, C., et al. 2008, A&A, 484, 783

Churchwell, E., Babler, B. L., Meade, M. R., et al. 2009, PASP, 121, 213

Clark, J. S., Lyuty, V. M., Zaitseva, G. V., et al. 1999a, MNRAS, 302, 167

Clark, J. S. & Steele, I. A. 2000, A&AS, 141, 65

Clark, J. S., Steele, I. A., Fender, R. P., & Coe, M. J. 1999b, A&A, 348, 888

Coburn, W., Kalemci, E., Kretschmar, P., et al. 2004, The Astronomer's Telegram, 337, 1

Coburn, W., Kretschmar, P., Kreykenbohm, I., et al. 2005, The Astronomer's Telegram, 381, 1

Cominsky, L., Clark, G. W., Li, F., Mayer, W., & Rappaport, S. 1978, Nat, 273, 367

Cook, M. C. & Page, C. G. 1987, MNRAS, 225, 381

Corbet, R. H. D., Hannikainen, D. C., & Remillard, R. 2004, The Astronomer's Telegram, 269, 1

Corbet, R. H. D. & Levine, A. M. 2006, The Astronomer's Telegram, 843, 1

Cox, N. L. J., Kaper, L., & Mokiem, M. R. 2005, A&A, 436, 661

Davidsen, A., Malina, R., & Bowyer, S. 1977, ApJ, 211, 866

Davidson, K. & Ostriker, J. P. 1973, ApJ, 179, 585

Dieters, S. W. & van der Klis, M. 2000, MNRAS, 311, 201

Domiciano de Souza, A., Kervella, P., Jankov, S., et al. 2003, A&A, 407, L47

Draine, B. T. 1989, in ESA Special Publication, Vol. 290, Infrared Spectroscopy in Astronomy, ed. E. Böhm-Vitense, 93–+

Drew, J. E., Greimel, R., Irwin, M. J., et al. 2005, MNRAS, 362, 753

Dunn, R. J. H., Fender, R. P., Körding, E. G., Belloni, T., & Cabanac, C. 2010, MNRAS, 403, 61

Eggleton, P. P. 1983, ApJ, 268, 368

Ekström, S., Meynet, G., Maeder, A., & Barblan, F. 2008, A&A, 478, 467

Ferrigno, C., Becker, P. A., Segreto, A., Mineo, T., & Santangelo, A. 2009, A&A, 498, 825

Figer, D. F., MacKenty, J. W., Robberto, M., et al. 2006, ApJ, 643, 1166

Finger, G. & Nicolini, G. 1998, Interquadrant raw crosstalk (European Southern Observatory)

Finger, M. H., Wilson, R. B., & Harmon, B. A. 1996, ApJ, 459, 288

Förster Schreiber, N. M. 2000, AJ, 120, 2089

Frank, J., King, A., & Raine, D. J. 2002, Accretion Power in Astrophysics: Third Edition, ed. Frank, J., King, A., & Raine, D. J.

Galloway, D. K., Morgan, E. H., & Levine, A. M. 2004, ApJ, 613, 1164

García, M., Baliunas, S. L., Elvis, M., et al. 1983, ApJ, 267, 291

Giacconi, R., Kellogg, E., Gorenstein, P., Gursky, H., & Tananbaum, H. 1971, ApJL, 165, L27+

Giacconi, R., Murray, S., Gursky, H., et al. 1972, ApJ, 178, 281

Gierliński, M. & Done, C. 2002, MNRAS, 331, L47

Golenetskii, S., Aptekar, R., Frederiks, D., et al. 2003, ApJ, 596, 1113

González-Solares, E. A., Walton, N. A., Greimel, R., et al. 2008, MNRAS, 388, 89

Goranskii, V. P., Esipov, V. F., Lyutyi, V. M., & Shugarov, S. Y. 1991, Soviet Astronomy Letters, 17, 399

Grankin, K. N., Shevchenko, V. S., & Yakubov, S. D. 1991, Soviet Astronomy Letters, 17, 415

Grebel, E. K., Richtler, T., & de Boer, K. S. 1992, A&A, 254, L5+

Grebenev, S. A., Bird, A. J., Molkov, S. V., et al. 2005, The Astronomer's Telegram, 457, 1

Groh, J. H., Damineli, A., Teodoro, M., & Barbosa, C. L. 2006, A&A, 457, 591

Halpern, J. P. & Gotthelf, E. V. 2004, The Astronomer's Telegram, 341, 1

Halpern, J. P., Gotthelf, E. V., Helfand, D. J., Gezari, S., & Wegner, G. A. 2004, The Astronomer's Telegram, 289, 1

Hannikainen, D. C., Rawlings, M. G., Muhli, P., et al. 2007, ArXiv e-prints, 706

Hannikainen, D. C., Rodriguez, J., Cabanac, C., et al. 2004, A&A, 423, L17

Hannikainen, D. C., Rodriguez, J., & Pottschmidt, K. 2003, IAUC, 8088, 4

Hanson, M. M., Conti, P. S., & Rieke, M. J. 1996, ApJS, 107, 281

Hanson, M. M., Kudritzki, R.-P., Kenworthy, M. A., Puls, J., & Tokunaga, A. T. 2005a, ApJS, 161, 154

Hanson, M. M., Puls, J., & Repolust, T. 2005b, in IAU Symposium, Vol. 227, Massive Star Birth: A Crossroads of Astrophysics, ed. R. Cesaroni, M. Felli, E. Churchwell, & M. Walmsley, 376–382

Harding, A. K. & Lai, D. 2006, Reports on Progress in Physics, 69, 2631

Hasinger, G. & van der Klis, M. 1989, A&A, 225, 79

Hayasaki, K. & Okazaki, A. T. 2004, MNRAS, 350, 971

Heindl, W. A., Coburn, W., Gruber, D. E., et al. 1999, ApJL, 521, L49

Heindl, W. A., Rothschild, R. E., Coburn, W., et al. 2004, in American Institute of Physics Conference Series, Vol. 714, X-ray Timing 2003: Rossi and Beyond, ed. P. Kaaret, F. K. Lamb, & J. H. Swank, 323–330

Hill, A. B., Dean, A. J., Landi, R., et al. 2008, MNRAS, 385, 423

Homan, J. & Belloni, T. 2005, APSS, 300, 107

Hubert, A. M., Floquet, M., Hao, J. X., et al. 1997, A&A, 324, 929

Hutchings, J. B. & Crampton, D. 1981, ApJ, 247, 222

Iben, Jr., I. 1974, ARA&A, 12, 215

Iben, Jr., I. & Renzini, A. 1983, ARA&A, 21, 271

in't Zand, J. J. M. 2005, A&A, 441, L1

in't Zand, J. J. M., Jonker, P. G., Nelemans, G., Steeghs, D., & O'Brien, K. 2006, A&A, 448, 1101

Ivanov, V. D., Rieke, M. J., Engelbracht, C. W., et al. 2004, ApJS, 151, 387

Iye, M. 1986, PASJ, 38, 463

Jernigan, J. G., Klein, R. I., & Arons, J. 2000, ApJ, 530, 875

Kaaret, P., Yu, W., Ford, E. C., & Zhang, S. N. 1998, ApJL, 497, L93+

Kaper, L. 1998, in ESA Special Publication, Vol. 413, Ultraviolet Astrophysics Beyond the IUE Final Archive, ed. W. Wamsteker, R. Gonzalez Riestra, & B. Harris, 149–+

Kaplan, D. L., Levine, A. M., Chakrabarty, D., et al. 2007, ApJ, 661, 437

Keller, S. C., Wood, P. R., & Bessell, M. S. 1999, A&AS, 134, 489

Kennea, J. A., Pagani, C., Markwardt, C., et al. 2005, The Astronomer's Telegram, 599, 1

Kleinmann, S. G. & Hall, D. N. B. 1986, ApJS, 62, 501

Klochkov, D., Horns, D., Santangelo, A., et al. 2007, A&A, 464, L45

Koornneef, J. 1983, A&A, 128, 84

Kouveliotou, C., Patel, S., Tennant, A., et al. 2003, IAUC, 8109, 2

Krimm, H., Barthelmy, S., Gehrels, N., et al. 2006, The Astronomer's Telegram, 861, 1

Kudritzki, R.-P. & Puls, J. 2000, ARA&A, 38, 613

Kuiper, L., Jonker, P., Hermsen, W., & O'Brien, K. 2005, The Astronomer's Telegram, 654, 1

Kuulkers, E. 2005, in American Institute of Physics Conference Series, Vol. 797, Interacting Binaries: Accretion, Evolution, and Outcomes, ed. L. Burderi, L. A. Antonelli, F. D'Antona, T. di Salvo, G. L. Israel, L. Piersanti, A. Tornambè, & O. Straniero, 402–409

Kuulkers, E., van der Klis, M., & Vaughan, B. A. 1996, A&A, 311, 197

Levine, A. & Corbet, R. 2000, IAUC, 7523, 2

Liu, Q. Z., van Paradijs, J., & van den Heuvel, E. P. J. 2006, A&A, 455, 1165

Liu, Q. Z., van Paradijs, J., & van den Heuvel, E. P. J. 2007, A&A, 469, 807

Lucy, L. B. & Solomon, P. M. 1970, ApJ, 159, 879

Lutovinov, A., Revnivtsev, M., Gilfanov, M., et al. 2005, A&A, 444, 821

Lutovinov, A., Rodrigues, J., Budtz-Jorgensen, C., Grebenev, S., & Winkler, C. 2004, The Astronomer's Telegram, 329, 1

Makishima, K., Kawai, N., Koyama, K., et al. 1984, PASJ, 36, 679

Makishima, K., Mihara, T., Ishida, M., et al. 1990, ApJL, 365, L59

Malizia, A., Bassani, L., di Cocco, G., et al. 2004, The Astronomer's Telegram, 227, 1

Maraschi, L., Treves, A., & van den Heuvel, E. P. J. 1976, Nat, 259, 292

Markwardt, C. B., Swank, J. H., & Smith, E. 2005, The Astronomer's Telegram, 465, 1

Marlborough, J. M., Zijlstra, J.-W., & Waters, L. B. F. M. 1997, A&A, 321, 867

Marshall, N. & Ricketts, M. J. 1980, MNRAS, 193, 7P

Masetti, N., Dal Fiume, D., Cusumano, G., et al. 2002, A&A, 382, 104

Masetti, N., Landi, R., Pretorius, M. L., et al. 2007, A&A, 470, 331

Masetti, N., Morelli, L., Palazzi, E., et al. 2006a, A&A, 459, 21

Masetti, N., Orlandini, M., Palazzi, E., Amati, L., & Frontera, F. 2006b, A&A, 453, 295

Massey, P., Silva, D. R., Levesque, E. M., et al. 2009, ApJ, 703, 420

Mattana, F., Götz, D., Falanga, M., et al. 2006, A&A, 460, L1

McCollough, M. L., Turler, M., Willis, D., & Shaw, S. E. 2006, The Astronomer's Telegram, 868, 1

Mereghetti, S., Esposito, P., Tiengo, A., et al. 2006, ApJ, 653, 1423

Mihara, T., Makishima, K., & Nagase, F. 1998, Advances in Space Research, 22, 987

Mihara, T., Makishima, K., Ohashi, T., Sakao, T., & Tashiro, M. 1990, Nat, 346, 250

Miyamoto, S., Kimura, K., Kitamoto, S., Dotani, T., & Ebisawa, K. 1991, ApJ, 383, 784

Molkov, S., Mowlavi, N., Goldwurm, A., et al. 2003, The Astronomer's Telegram, 176, 1

Moorwood, A., Cuby, J.-G., Biereichel, P., et al. 1998a, The Messenger, 94, 7

Moorwood, A., Cuby, J.-G., Biereichel, P., et al. 1998b, The Messenger, 94, 7

Moorwood, A., Cuby, J.-G., & Lidman, C. 1998c, The Messenger, 91, 9

Motch, C. & Janot-Pacheco, E. 1987, A&A, 182, L55

Muno, M. P., Remillard, R. A., & Chakrabarty, D. 2002, ApJL, 568, L35

Naik, S., Callanan, P. J., Paul, B., & Dotani, T. 2006, ApJ, 647, 1293

Negueruela, I. 1998, A&A, 338, 505

Negueruela, I. 2009, ArXiv e-prints

Negueruela, I., Israel, G. L., Marco, A., Norton, A. J., & Speziali, R. 2003, A&A, 397, 739

Negueruela, I. & Okazaki, A. T. 2001, A&A, 369, 108

Negueruela, I., Roche, P., Fabregat, J., & Coe, M. J. 1999, MNRAS, 307, 695

Negueruela, I. & Schurch, M. P. E. 2007, A&A, 461, 631

Negueruela, I., Smith, D. M., Reig, P., Chaty, S., & Torrejón, J. M. 2006, in ESA Special Publication, ed. A. Wilson, Vol. 604, 165–170

Negueruela, I., Smith, D. M., Torrejon, J. M., & Reig, P. 2007, ArXiv e-prints, 704

Nelson, R. W., Salpeter, E. E., & Wasserman, I. 1993, ApJ, 418, 874

Nespoli, E., Fabregat, J., & Mennickent, R. 2007, The Astronomer's Telegram, 983, 1

Nespoli, E., Fabregat, J., & Mennickent, R. E. 2008a, The Astronomer's Telegram, 1396, 1

Nespoli, E., Fabregat, J., & Mennickent, R. E. 2008b, A&A, 486, 911

Nowak, M. A., Vaughan, B. A., Wilms, J., Dove, J. B., & Begelman, M. C. 1999, ApJ, 510, 874

Nucita, A. A., Carpano, S., & Guainazzi, M. 2007, A&A, 474, L1

Okazaki, A. T. 2000, in Astronomical Society of the Pacific Conference Series, Vol. 214, IAU Colloq. 175: The Be Phenomenon in Early-Type Stars, ed. M. A. Smith, H. F. Henrichs, & J. Fabregat, 409–+

Okazaki, A. T. & Negueruela, I. 2001, A&A, 377, 161

Ostriker, J. P., Weaver, R., Yahil, A., & McCray, R. 1976, ApJL, 208, L61

Owocki, S. P. 1994, in IAU Symposium, Vol. 162, Pulsation; Rotation; and Mass Loss in Early-Type Stars, ed. L. A. Balona, H. F. Henrichs, & J. M. Le Contel, 475–+

Paczyǹski, B. 1976, in IAU Symposium, Vol. 73, Structure and Evolution of Close Binary Systems, ed. P. Eggleton, S. Mitton, & J. Whelan, 75–+

Parmar, A. N., White, N. E., Stella, L., Izzo, C., & Ferri, P. 1989, ApJ, 338, 359

Patel, S. K., Kouveliotou, C., Tennant, A., et al. 2004, ApJL, 602, L45

Patel, S. K., Zurita, J., Del Santo, M., et al. 2007, ApJ, 657, 994

Pellizza, L. J., Chaty, S., & Negueruela, I. 2006, A&A, 455, 653

Persson, S. E., Murphy, D. C., Krzeminski, W., Roth, M., & Rieke, M. J. 1998, AJ, 116, 2475

Pickles, A. J. 1998, PASP, 110, 863

Pigulski, A., Kopacki, G., & Kołaczkowski, Z. 2001, A&A, 376, 144

Porter, J. M. & Rivinius, T. 2003, PASP, 115, 1153

Pottschmidt, K., Kreykenbohm, I., Wilms, J., et al. 2005, ApJL, 634, L97

Predehl, P. & Schmitt, J. H. M. M. 1995, A&A, 293, 889

Priedhorsky, W., Hasinger, G., Lewin, W. H. G., et al. 1986, ApJL, 306, L91

Psaltis, D., Belloni, T., & van der Klis, M. 1999, ApJ, 520, 262

Qu, J. L., Zhang, S., Song, L. M., & Falanga, M. 2005, ApJL, 629, L33

Radhakrishnan, V. & Srinivasan, G. 1982, Current Science, 51, 1096

Rahoui, F., Chaty, S., Lagage, P.-O., & Pantin, E. 2008, A&A, 484, 801

Ramírez, S. V., Depoy, D. L., Frogel, J. A., Sellgren, K., & Blum, R. D. 1997, AJ, 113, 1411

Rappaport, S., Clark, G. W., Cominsky, L., Li, F., & Joss, P. C. 1978, ApJL, 224, L1

Reig, P. 2008, A&A, 489, 725

Reig, P. & Coe, M. J. 1998, MNRAS, 294, 118

Reig, P. & Coe, M. J. 1999, MNRAS, 302, 700

Reig, P. & Roche, P. 1999, MNRAS, 306, 100

Reig, P., van Straaten, S., & van der Klis, M. 2004, ApJ, 602, 918

Revnivtsev, M. G., Sazonov, S. Y., Gilfanov, M. R., & Sunyaev, R. A. 2003, Astronomy Letters, 29, 587

Reynolds, A. P., Parmar, A. N., & White, N. E. 1993, ApJ, 414, 302

Rieke, G. H. & Lebofsky, M. J. 1985, ApJ, 288, 618

Rodriguez, J., Cabanac, C., Hannikainen, D. C., et al. 2005, A&A, 432, 235

Runacres, M. C. & Owocki, S. P. 2005, A&A, 429, 323

Schaller, G., Schaerer, D., Meynet, G., & Maeder, A. 1992, A&AS, 96, 269

Schwartz, D. A., Griffiths, R. E., Bowyer, S., Thorstensen, J. R., & Charles, P. A. 1980, AJ, 85, 549

Sguera, V., Barlow, E. J., Bird, A. J., et al. 2005, A&A, 444, 221

Smarr, L. L. & Blandford, R. 1976, ApJ, 207, 574

Smith, D. M., Bezayiff, N., & Negueruela, I. 2006a, The Astronomer's Telegram, 766, 1

Smith, D. M., Heindl, W. A., Markwardt, C. B., et al. 2006b, ApJ, 638, 974

Staubert, R., Shakura, N. I., Postnov, K., et al. 2007, A&A, 465, L25

Stee, P. & de Araujo, F. X. 1994, A&A, 292, 221

Stella, L., White, N. E., Davelaar, J., et al. 1985, ApJL, 288, L45

Sugizaki, M., Mitsuda, K., Kaneda, H., et al. 2001, ApJS, 134, 77

Sun, X.-J., Li, T.-P., Wu, M., & Cheng, L.-X. 1994, A&A, 289, 127

Sutantyo, W. 1975, A&A, 41, 47

Swank, J. & Morgan, E. 2000, IAUC, 7531, 4

Swank, J. H. & Markwardt, C. B. 2003, The Astronomer's Telegram, 128, 1

Telting, J. H., Waters, L. B. F. M., Roche, P., et al. 1998, MNRAS, 296, 785

Terrell, J. & Priedhorsky, W. C. 1984, ApJL, 285, L15

Thompson, T. W. J., Tomsick, J. A., Rothschild, R. E., in't Zand, J. J. M., & Walter, R. 2006, ApJ, 649, 373

Tomsick, J. A., Chaty, S., Rodriguez, J., et al. 2006, ApJ, 647, 1309

Tomsick, J. A., Chaty, S., Rodriguez, J., Walter, R., & Kaaret, P. 2009, ApJ, 701, 811

Tsygankov, S., Lutovinov, A., & Serber, A. 2009, ArXiv e-prints

Tsygankov, S. S., Lutovinov, A. A., Churazov, E. M., & Sunyaev, R. A. 2006, MNRAS, 371, 19

Tsygankov, S. S., Lutovinov, A. A., Churazov, E. M., & Sunyaev, R. A. 2007, Astronomy Letters, 33, 368

Vallée, J. P. 2008, AJ, 135, 1301

van den Heuvel, E. P. J. & de Loore, C. 1973, A&A, 25, 387

van den Heuvel, E. P. J. & Heise, J. 1972, Nat, 239, 67

van der Klis, M. 1989, in Timing Neutron Stars, ed. H. Ögelman & E. P. J. van den Heuvel, 27–+

van der Klis, M. 1994, A&A, 283, 469

van der Klis, M. 2000, ARA&A, 38, 717

van der Klis, M. 2006, in Compact stellar X-ray sources, ed. M. van der Klis & W. H. G. Lewin (Cambridge University Press)

van der Klis, M., Swank, J. H., Zhang, W., et al. 1996, ApJL, 469, L1+

van Kerkwijk, M. H., van Oijen, J. G. J., & van den Heuvel, E. P. J. 1989, A&A, 209, 173

van Straaten, S., van der Klis, M., & Méndez, M. 2003, ApJ, 596, 1155

Wainscoat, R. J. & Cowie, L. L. 1992, AJ, 103, 332

Walter, R. & Zurita Heras, J. 2007, A&A, 476, 335

Walter, R., Zurita Heras, J., Bassani, L., et al. 2006, A&A, 453, 133

Wasserman, I. & Shapiro, S. L. 1983, ApJ, 265, 1036

Wegner, W. 1994, MNRAS, 270, 229

Wegner, W. 2006, MNRAS, 371, 185

Wheaton, W. A., Doty, J. P., Primini, F. A., et al. 1979, Nat, 282, 240

Wijnands, R. & van der Klis, M. 1998, Nat, 394, 344

Wijnands, R. & van der Klis, M. 1999, ApJ, 514, 939

Wijnands, R. A. D., van der Klis, M., Kuulkers, E., Asai, K., & Hasinger, G. 1997, A&A, 323, 399

Wilson, C. A., Fabregat, J., & Coburn, W. 2005, ApJL, 620, L99

Wilson, C. A. & Finger, M. H. 2006, The Astronomer's Telegram, 877, 1

Wilson, C. A., Finger, M. H., & Camero-Arranz, A. 2008, ApJ, 678, 1263

Wilson, C. A., Finger, M. H., Coe, M. J., Laycock, S., & Fabregat, J. 2002, ApJ, 570, 287

Wright, N. J., Greimel, R., Barlow, M. J., et al. 2008, MNRAS, 390, 929

Zurita, J. & Walter, R. 2004, The Astronomer's Telegram, 336, 1